THE UNIVERSITY *of* EDINBURGH

Immobilised Semiconductors for Photocatalytic Water Purification

Gylen Odling

Thesis submitted for the degree of PhD

The University of Edinburgh

PhD - The University of Edinburgh - 2018

Declaration

I declare that this thesis has been composed solely by myself and that it has not been submitted, in whole or in part, in any previous application for a degree. Except where states otherwise by reference or acknowledgment, the work presented is entirely my own.

Gylen Odling

November 2018

Acknowledgements

Foremost I thank my supervisor Professor Neil Robertson for his tireless support and guidance throughout the enclosed work. He has brought a level of enthusiasm and engagement to this project which has been fundamental to its success and my enjoyment of my time as a PhD student. As we were both newcomers to the field academically, my achievements as part of this project are a direct result of constructive and friendly environment which Neil cultivates.

In moving beyond my own discipline, the support of those whose expertise differs from my own has been key. Dr. Efthalia Chatzisymeon has been an excellent supervisor in the field of environmental engineering, with her input and guidance in an area completely new to me has been highly valuable. Despite her own very full schedule Thalia has always been available with advice and direction, for which I am hugely thankful, being somewhat lost on anything biological.

Despite having a very different background, Dr. Kevin Jones has also been a key contributor over the course of my work. He has without fail been around for a chat whenever I happened to be in St. Andrews, and his encouragement and interest in my work is something for which I am greatly thankful.

Professor Satishchandra Ogale must be thanked for being a kind and welcoming host during my time in India. In addition, I must thank his group, in particular Reshma and Sachin for making me feel welcome in both their laboratory and country.

In the UK, there are a huge number of PhD students, academics and support staff which have helped me. Firstly, I would like to thank every member of the Robertson group past and present, who have helped me in innumerable ways during my PhD. I would also like to thank the various students and staff members of the CRITICAT CDT who made the training period and subsequent events enjoyable, and for making a broad community of great people across the three host institutions. Beyond these groups, there are several people who should be thanked specifically for their contributions. I would like to thank Dr. Lorna Eades for her help in running ICP-OES and ICP-MS analyses, Drs. Nicola Cayzer and John Craven for their support in operating the SEM,

Dr. Steve Francis for helping with XPS, and Ross Blackley and Dr. David Miller for taking the time to assist with TEM analyses. Every one of these people has given their time and effort to provide excellent support in their areas and have ensured the measurements contained within this thesis are of the best quality possible.

I have been lucky to be well funded throughout my work, and would like to thank the bodies which have contributed, namely the EPSRC CRITICAT Centre for Doctoral Training, and Energy Technology Partnership Post-Graduate and Early Career Researcher Exchange program

Finally, I would like to thank my family, to my parents who have been a constant source of advice and support and continue to amaze and amuse me, to my sister who often gives me far too much credit, and lastly to Rachel without whom I would not have made it.

List of Abbreviations

Abbreviation	Meaning
4CP	4-Chlorophenol
4NP	4-Nitrophenol
ATCC	American Type Culture Collection
BTO	Bismuth Titanate
CFU	Colony Forming Unit
CNT	Carbon Nanotube
COD	Chemical Oxygen Demand
DE	Degradation Efficiency
EDTA	Ethylenediamine Tetraacetic Acid
EDX	Energy Dispersive X-ray Spectroscopy
EUWFD	European Union Water Framework Directive
FFT	Fast Fourier Transform
FTO	Fluorine Tin Oxide
HAADF	High Angle Annular Dark Field
ICP-MS	Inductively Coupled Plasma Mass Spectrometry
ICP-OES	Inductively Coupled Plasma Optical Emission Spectroscopy
JCPDS	Joint Committee on Powder Diffraction Standards
LED	Light Emitting Diode
LMB	Leuco-Methylene Blue
LVO	Lanthanum Vanadate
MB	Methylene Blue
MO	Methyl Orange
M-S	Mott-Schottky
NHE	Normal Hydrogen Electrode
NP	Nonylphenol
NTO	Nitrotriazolone
PC	Paracetamol
PCP	Pentachlorophenol
PEC	Photoelectrocatalysis

PL	Photoluminescence
Rh6G	Rhodamine 6G
RhB	Rhodamine B
ROS	Reactive Oxygen Species
SEM	Scanning Electron Microscopy
SILAR	Sequential Ionic Layer Adsorption Reaction
STEM	Scanning Transmission Electron Microscopy
TC	Tetracycline
TEM	Transmission Electron Microscopy
TNT	Trinitrotoluene
WHO	World Health Organisation
XPS	X-Ray Photoelectron Spectroscopy
XRD	X-Ray Diffraction

Lay Summary

Drinking water is a commodity of increasing value in the modern world. A combination of larger numbers of people needing more drinking water and greater amounts of drinking water being polluted to the point of being unfit for consumption means that shortages are becoming increasingly common. Removing hazardous material from water thereby making it safe to drink has been identified as a key strategy to increase the amount of clean drinking water available.

The work enclosed within this thesis focuses on one emerging method to remove pollution from drinking water. This method uses solids which can destroy pollutants when a light is shone upon them, and work in a way which allows the process to be repeated multiple times. A convenient use of this process for many of the worst affected by poor water quality is the use of sunlight as a light source, but opportunities exist to use this method to remove specific problem pollutants from water sources in locations across the globe using lamps to drive the process.

In this area, loose powders of a material known as titanium dioxide are the most commonly studied. However, removing the powder from the water after use is difficult to achieve, and the speed with which the pollutants are removed from water are typically slow. The work enclosed within proposes several ways in which this material can be modified to improve on both of these factors. Materials containing a mixture of titanium dioxide and other materials have been prepared and stuck to large scale glass supports which can be easily removed from water. The materials chosen for combination with titanium dioxide were picked based on their complementary characteristics to titanium dioxide, and the resulting composites have shown promising activity to destroy several pollutants which have been identified as hazardous materials which are difficult to remove from water by other methods.

Abstract

TiO_2 based nanomaterials are currently the most widely studied for photocatalytic water purification. Despite high stability and low environmental impact, instances of water treatment applications using TiO_2 photocatalysis are few due to modest activity only under high energy ultraviolet light. Another drawback is the nanoscale nature of such materials, posing a problem in the separation and re-use of the photocatalytic material. This work aims to overcome these problems by forming nanocomposites between TiO_2 and other semiconductors with favourable properties such as visible light harvesting or improved charge separation, and to generate these materials immobilised upon macroscopic supports.

Composites of bismuth titanate (BTO) and lanthanum vanadate (LVO) on TiO_2 have been prepared immobilised on glass beads using a sequential ionic layer adsorption (SILAR) method. Modification of TiO_2 with these wide band gap semiconductors gives little to no extension of the TiO_2 absorption into the visible but allows for charge separation between the two materials due to off-set band energies. This improved charge separation and, in the case of BTO-TiO_2, modest absorption extension is demonstrated to be effective for the photocatalytic degradation of a variety of different chemical pollutants and bacteria in water. An extensive photocatalytic scope using these materials is presented, in addition to re-use tests and mechanistic investigations.

Attempts were made to narrow the band gap and as such harvest a greater portion of visible light by forming composites of BiOI and $BiVO_4$ with TiO_2 on glass slides using SILAR. Through electronic and optical characterisation methods these materials were shown to have both the off-set band alignment of the BTO and LVO composites, but with a narrower band gap. Using visible only light the BiOI and $BiVO_4$ materials were applied to the degradation of dyes successfully, however only BiOI was found to have any activity against colourless 4CP. This difference was investigated using comparisons to a ZrO_2 model system and was determined to arise from a sensitisation effect of the dye pollutant used.

The use of two separate modifications to impart the charge separation and visible light harvesting was investigated. Chlorine doped TiO_2 particles were deposited on the TiO_2

surface, giving a visible active composite. It was found that this could be improved by the addition of a carbon coating process, allowing photogenerated charges to rapidly move apart and react. This composite was found to be highly stable, particularly under acidic conditions in contrast to the other materials developed. As such its activity was not only tested against the typical organic pollutants, but also for the photocatalytic reduction of Cr(VI) to Cr(III) under acidic conditions.

Contents

Chapter 1 Introduction

1.1 Drinking Water: A Critical Resource

Purification of drinking water sources is one of the greatest challenges facing the world today. The scope of the problem of water contamination is extreme, with huge areas of the planet suffering from poor water quality. The World Health Organisation (WHO) estimate that 844 million people currently lack any form of drinking water purification, with around 159 million people relying on water from surface sources[1]. As great in scope as this problem currently is, it is expected to grow due to increased population growth and industrialisation putting greater pressure on current drinking water sources, with water consumption rates about double of the global population growth over the past century[2]. The United Nations has predicted that in 2030 there will be a global shortfall of fresh water of 40%[3], putting a large proportion of the global population under water stressed conditions.

In addition to the clear humanitarian issues surrounding poor water quality, there is a strong economic case for improvements in water purification technologies. It has been estimated that around 50% of the global workforce works in an industry which is heavily dependent on water[4]. Matching the scale of the potential economic problems that arise from poor water quality is the required investment in water treatment technologies. The United States is estimated to need around $322 to $600 billion in investment over the next 20 years to overcome water purification issues[5], while the United Kingdom estimated that it would cost around £27 billion over the same period to meet the EU Water Framework Directive targets[6]. The development of improved methods to decontaminate water is therefore not only of humanitarian importance, but also key in the global economic future.

The need for improvements to drinking water sources is summarised by the Global Goal for Sustainable Development[7], which states that work should be undertaken to "By 2030, achieve universal and equitable access to safe and affordable drinking water for all". To this end, this global goal aims to increase efforts to remediate polluted water, making it fit for consumption. Indeed, a key aim of much work in the field of

water technologies considers contaminated wastewaters as a valuable asset to combat water scarcity[8].

The nature of contaminated water however can itself be a complicating factor, vast differences in both the levels and types of contaminant present can occur when aiming to tackle this problem in different locations. Water in, for example, Bangladesh can be highly contaminated with textile wastes containing contaminants such as aliphatic oils and grease, heavy metals and dye molecules[9]. In contrast, relatively low concentrations of endocrine disruptors such as alkyl phenols have been found to be present in water sources in Europe[10]. These two situations require fundamentally different approaches for remediation, and thus work on new treatment materials and methods should take this into account.

Furthermore, consideration of the local environment to which a water treatment strategy is applied is also complex, and oft overlooked. In the development of new reactor systems for photocatalysis, there is a place for both the complex high efficiency systems and simpler ones. However, care should be taken that the new materials and system are designed and tested in such a way that is appropriate for the target application. For example, flow systems are ideal for water purification in developed nations where they may be maintained but may be ill-suited to villages in developing countries. In these areas, simplicity of operation and maintenance is key; for instance, a recent report by MacMahon *et al.*[11] of a pilot solar water disinfection project in Kenya noted that even a relatively simple gravity fed solar water disinfection scheme was not immune from enough damage from local natural events to render it non-functional (Figure 1.1).

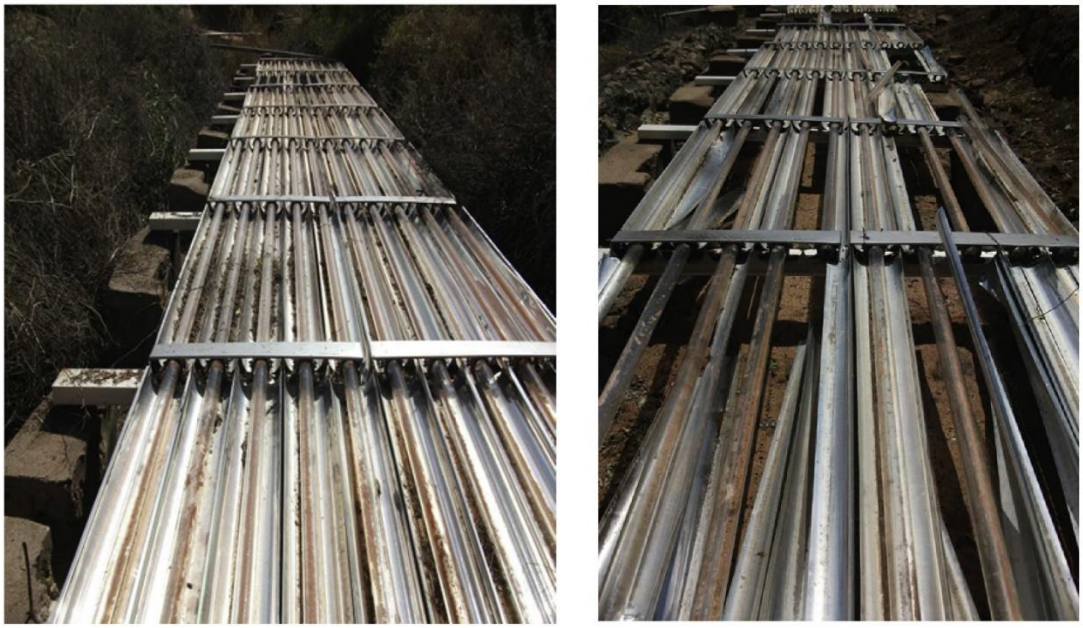

Figure 1.1. Left) Solar disinfection system developed by MacMahon et al. Right) Damage to the system discovered after flash flooding. Image adapted with permission from reference [11]

It was determined that flash flooding in the local area had caused damage to the system, which was not immediately repaired. While this example takes place in a particularly challenging locale, it demonstrates a key consideration; robustness of the proposed solution, ease of operation and maintenance should be at the forefront of the design of new materials and systems. Other parameters such as the use of appropriate target test pollutants and light sources for the application in question should also be evaluated, with thought given to their level of appropriateness for application.

With these factors in mind, one emergent treatment method is that of photocatalytic water purification using semiconductors, the subject of this review. Under irradiation, semiconducting materials may, if certain conditions are met, destroy organic and bacterial contaminants. Much work has been carried out in this area on the development of high efficiency materials for this purpose, with many high-quality reviews of such existing in the literature[12–14]. This chapter aims to draw attention to points of improvement in the applicability of materials and testing methodologies which have arisen in recent years. A brief introduction to photocatalytic water purification is given, with a discussion of the various processes which must be considered when designing a photocatalytic material. Advances in the applicability of

photocatalytic materials are highlighted, with a focus on ease of separation and re-use, factors which have to date been somewhat overlooked in favour of pursuing higher efficacy. Interesting recent examples of reactor systems are also considered, with emphasis on potential matching of design to use beyond the laboratory. Finally, issues in the reported literature of unreliable or inappropriate testing methods are discussed thoroughly, and examples where these inconsistencies are overcome provided. This chapter aims to give a general introduction to photocatalysis, and to bring attention to somewhat overlooked examples where photocatalytic materials are designed with applicability in mind. In addition, possible points of improvement and collaboration with a view to increasing the presence of photocatalytic water treatment beyond the laboratory are also suggested.

1.2 An Introduction to Photocatalytic Pollutant Degradation

Photocatalysis on semiconductors can be thought of as a photoinduced production of reactive species. The general process is described schematically in Figure 1.2.

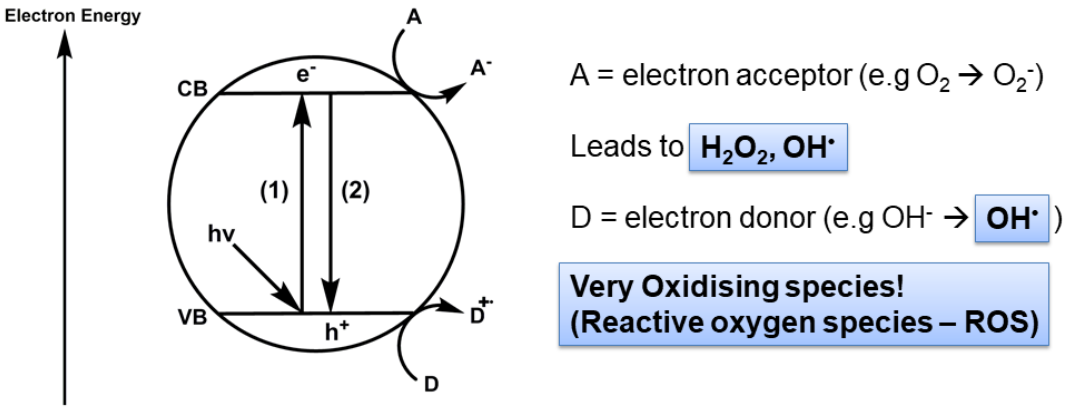

Figure 1.2. Generation of reactive oxygen species (ROS) on a semiconductor photocatalyst under irradiation.

Upon absorption of a photon with sufficient energy, electrons may be excited across the band gap (1) giving high energy electrons in the conduction band (e_{cb}) and leaving high energy holes in the valence band (h_{vb}). These high energy species can then undergo surface reactions with electron donors (D) or acceptors (A) thereby closing the cycle and returning the semiconductor to its original state. A major barrier to

overcome in photocatalysis is that of recombination (2), where charges do not reach the surface to react and conduction band electrons simply returns to holes in the valence band[15]. Much work has been undertaken in overcoming this problem, generally focusing on designing materials such that there are short routes and quick transport of charges to the particle surface[16,17] or mechanisms by which the lifetime of charges are increased by separation across multiple materials[18]. Indeed, the standard materials in this field are typically TiO_2 based nanomaterials, with the mass produced P25 nanopowder being the most common. This material, comprised of ~20 nm TiO_2 particles, has been widely studied and is known to destroy a variety of pollutants under UV irradiation. P25 typically displays good efficiencies owing to charge separation across the anatase/rutile phase interface[19], however activity under visible light is negligible, which has been the focus of much recent work[20].

When designing a photocatalyst for water purification, the aim is usually to use the semiconductor to produce reactive oxygen species (ROS) which carry out the degradation of organic or bacteriological contaminants[21–23]. It is key therefore to understand the energetics of the redox processes which allow ROS to form at semiconductors surfaces, a summary of which is given in table 1.1.

Table 1.1 – Key redox processes in photocatalytic water treatment on semiconductors

Number	ROS Generating Redox Reaction	Redox Potential (V vs NHE) [21,24]
1	$O_2 + e_{cb}^- \rightarrow O_2^-$	-0.33
2	$O_2 + H^+ + e_{cb}^- \rightarrow HO_2^\bullet$	-0.05
3	$HO_2^\bullet + H^+ + e_{cb}^- \rightarrow H_2O_2$	1.44
4	$O_2 + 2e_{cb}^- + 2H^+ \rightarrow H_2O_2$	0.70
5	$H_2O_2 + H^+ + e_{cb}^- \rightarrow OH^\bullet + H_2O$	1.14
6	$OH^-_{adsorbed} + h_{vb}^+ \rightarrow OH^\bullet_{adsorbed}$	1.60
7	$OH^-_{free} + h_{vb}^+ \rightarrow OH^\bullet_{free}$	2.72

It is worthwhile to note the upper and lower extremes of these processes and keep them in mind when designing a new photocatalytic material. For instance, the reduction of oxygen (1) is a key step in scavenging photogenerated electrons from the excited semiconductor, which may occur at potentials more negative than the conduction band minima of some semiconductors. In such cases, lowering the pH can be used to promote the reduction of oxygen to the hydroperoxyl radical (2)[21], or loading with a noble metal co-catalyst to allow the 2-electron reduction of oxygen to hydrogen peroxide (4)[25]. When considering the valence band holes, hydroxyl radicals can be generated from surface hydroxide groups. For complete mineralisation of organic material, hydroxyl radicals are generally required due to their high oxidising power[26], and as such there has been considerable interest in the literature upon their generation[27]. While producing hydroxyl radicals adsorbed onto the surface (6) requires only a moderately oxidising hole, to generate free hydroxyl radicals desorbed from the surface (7) requires a significantly deeper valence band[28], with implications for the degradation of adsorbing vs non-adsorbing pollutants[29]. This highlights an important factor which should be considered when designing new photocatalytic materials; there is a trade-off between electrochemical driving force for surface redox reactions and the desire to reduce the energy of light used. Materials which use cheap visible light sources and/or solar irradiation are attractive but may be unable to form the more oxidising ROS species effectively. It is perhaps noteworthy however that in some cases complete mineralisation may not be needed, but only if the degradation products are sufficiently innocuous compared to the parent pollutant. Accessing such highly oxidising species as ROS has been noted as a viable route to degrade persistent micropollutants[30], toxic organic contaminants which are not removed by current water treatment strategies. Hence, at the nanoscale, the process can be understood relatively simply, however to apply these processes in practice implementation barriers must be overcome, which will be the focus of the remainder of this review.

1.3 Designing Applicable Materials

A huge number of novel materials have been developed in the field of photocatalytic water purification[12,31,32], with new papers being published frequently describing new ways of improving photocatalytic performances. Sometimes overlooked however is

the coupling of improved photocatalytic performance with methods by which the material may be applied easily in practice. Much of the published work overlooks this and is carried out without consideration of a target use. Such a disconnect between laboratory and real-world application in a field so closely aligned with a clear potential case for implementation is detrimental and should be addressed going forward.

High efficiency photocatalysts are typically nanoscale materials due to the aforementioned short lifetimes of photogenerated charges requiring short path lengths to the particle surface[15]. Separation of such materials on the laboratory scale is simple enough, with centrifugation being the most commonly applied technique[33,34]. However, when looking to applying such materials on a larger scale this becomes impractical. Removal of nanomaterials from drinking water is key not only for material recovery and re-use, but also from an environmental perspective. While many of the semiconductors used in photocatalysis are considered non-toxic, there are questions being raised as to their toxicity when present in nanoparticulate forms[35]. Simple methods of separation and re-use should therefore be an integral part of material design in this area. What follows is a discussion of recent developments in the production of easily recoverable materials with high photocatalytic performance.

1.3.1 Magnetically Separable Nanoparticles

One way in which simple separation of nanomaterials from solution can be achieved is to use either a photocatalyst with magnetic properties, or to form a composite of the active photocatalyst with such a material. Separation of such materials from solution can be simply achieved using an inexpensive bar magnet as shown in Figure 1.3.

Figure 1.3. Magnetic separation of a magnetic nanocomposite post use. Image adapted from Reference 36.

In this way the good mass transport of a suspension is retained during photocatalytic treatment, but the impractical separation step is simplified somewhat. As magnetisation must be possible under ambient conditions, the most widely reported materials for this purpose are iron based in nature, typically magnetite[36–38] or ferrite type[39–41] materials. A selection of recently reported materials is given in Table 1.2.

Table 1.2 – Recently Published Magnetic Photocatalyst Materials

Material (Magnetic component in bold)	Model Pollutant	Light Source	Photocatalytic Degradation Measure
ZnO/AgBr/**Fe_3O_4**/Ag_3VO_4[36]	Rhodamine B	50 W LED	0.029 min^{-1}
NiAl Layered Double Hydroxide/**Fe_3O_4**–Reduced Graphene Oxide[37]	Ciprofloxacin	500 W Xe Lamp (>420 nm filter)	0.0235 min^{-1}
Fe_3O_4-TiO_2[38]	Reactive Brilliant Red 3	300 W Xe Lamp	0.03-0.035 min^{-1}
Bi_2MoO_6/**$ZnFe_2O_4$**[39]	Rhodamine B	150 W Xe Lamp	0.0034 min^{-1}
$CoFe_2O_4$–PANI[40]	Methyl Orange	10 W LED	85% degradation in 2 hours
C_3N_4@**$MnFe_2O_4$**-graphene[41]	Various antibiotics	300 W Xe Lamp (>400 nm filter)	0.017-0.042 min^{-1}

These examples demonstrate the various levels of nanoparticle engineering required to arrive at a highly efficient photocatalyst system. Although magnetite and ferrite materials have the potential to be photocatalytically active in their own rights[42,43], the efficiency of these materials alone is low due to rapid charge recombination in the pure semiconductor. The work of Shekofteh-Gohari *et al.*[36] demonstrated that magnetite may be incorporated simply as support material for a photocatalytic ZnO, AgBr and Ag_3VO_4 composite, and may not necessarily take part in the photocatalytic mechanism.

Examples exist in the literature where the inclusion of a magnetic semiconductor reduces activity[44] due to the light filtering or migration of charges from the active photocatalysts to an inert magnetic material. Successes in overcoming this unfavourable charge migration have been achieved by introduction of barrier layers between active and inactive magnetic support materials[45] as shown in Figure 1.4.

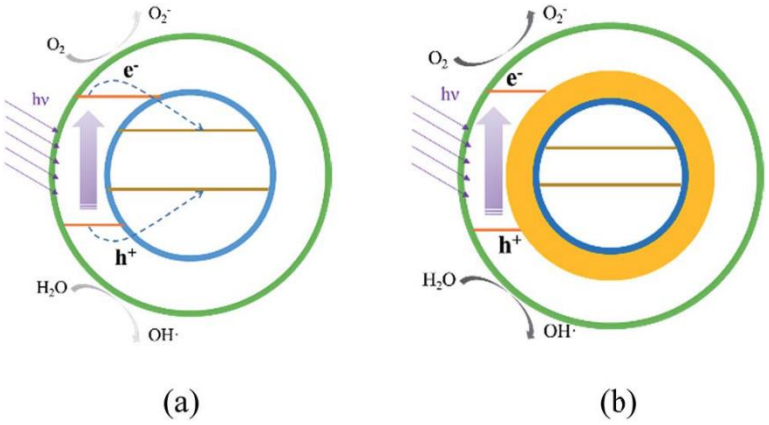

Figure 1.4. Charge transfer in a magnetic composite without (a) and with (b) a blocking interlayer Image adapted from reference 45.

Without using a barrier (Figure 1.4a), charges can migrate to the magnetic support, where they may be unable to take part in useful surface reactions either due to mismatching of conduction and valence band energy levels, or simply due to being blocked from solution by the outer layers. When an interlayer is introduced (Figure 1.4b), this charge migration is suppressed and photocatalytic ROS generation on the active material surface can go ahead.

Parasitic light filtering is fundamentally more difficult to engineer against, but it has been demonstrated that it is possible to make use of the light harvesting properties of magnetic materials, rather than having an inactive material filtering out light from the reaction. Zhao *et al.*[39] postulated such a sensitisation effect of zinc ferrite on bismuth molybdate as shown in Figure 1.5.

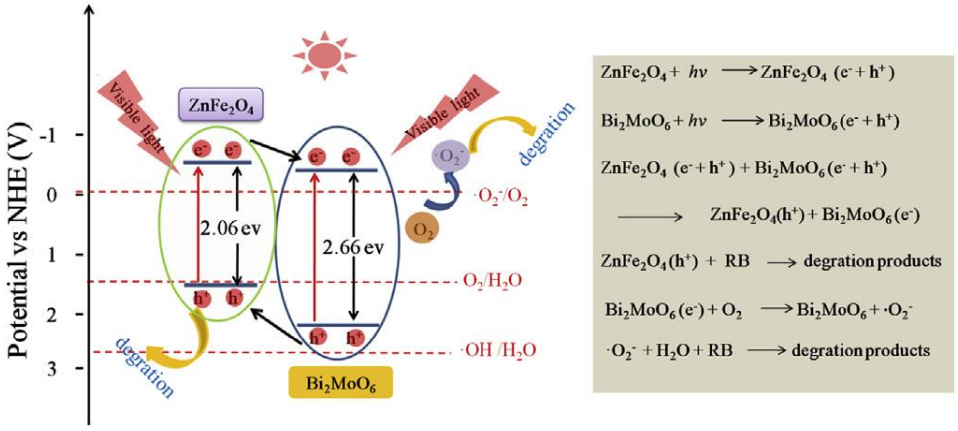

Figure 1.5. Mechanism of action of the $ZnFe_2O_4$-Bi_2MoO_6 magnetic composite postulated by Zhao et al. Image adapted from reference 39.

Thus, the authors suggest that the zinc ferrite assists the photocatalytic degradation rather than acting as a simple support. It is noteworthy that as magnetite and ferrite materials typically have relatively narrow band gaps, which will therefore have low reductive and oxidative potential of photoexcited electrons and holes respectively Using this example, holes generated on Bi_2MoO_6 will migrate to $ZnFe_2O_4$, losing some oxidising potential, with the opposite true for photogenerated electrons on $ZnFe_2O_4$. Care should be taken when designing magnetic composites for this reason.

Where magnetite and ferrite materials are used as light harvesting materials, they are often combined in a composite with conductive carbonaceous materials to allow a degree of charge separation between the two materials. A recent report by Xiao et al[46] has suggested that carbon nitride (C_3N_4), a material commonly used in this manner, may be itself degraded by ROS generated in the photocatalytic reaction as shown in Figure 1.6.

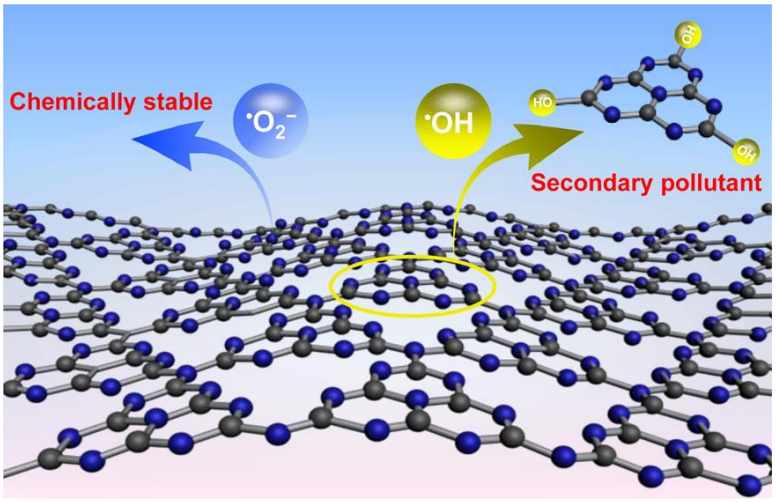

Figure 1.6. ROS attack on C_3N_4 as proposed by Xiao et al. Image adapted from reference 46.

While good stability of photocatalyst systems containing C_3N_4 have been noted[47], the results of Xiao *et al.* suggest that low levels of secondary pollutants may be introduced into the treated water in this way, suggesting that this may be a material to avoid for water treatment. The degradation fragments identified by the authors involve the breaking of C-N bonds, suggesting that degradation in this manner may be specific to C_3N_4. Therefore, it may be the case that this does not occur when the related materials graphene or reduced graphene oxide are used, however detailed studies on photocatalytic stabilities of such systems have not been undertaken to date.

One avenue that may be exploited in magnetically separable nanocomposites for water treatment is the use of photo-Fenton chemistry due to the presence of iron in most magnetic materials. A large number of reactions are involved in the Fenton and photo-Fenton processes; however, the overall process is typically described as[48]:

$$Fe(II) + H_2O_2 \rightarrow OH^{\bullet} + Fe(III) + OH^-$$

$$Fe(III)L + h\nu \rightarrow Fe(II) + L^{\bullet}$$

Addition of H_2O_2 in the presence of Fe(II) in the material reductively produces hydroxyl radicals, with the possibility of this reduction being encouraged by irradiation. The oxidised Fe(III) can then be photoreduced back to Fe(II) through the photooxidation of an electron donor (L), typically an organic carboxylate or alcohol,

allowing the process to repeat[49]. Using addition of H_2O_2 in conjunction with a magnetic nanocomposite, Nguyen et al[50] recently demonstrated a large improvement in photodegradation of rhodamine B and Cephalexin over photocatalysis alone. It is noteworthy however that some authors suggest that photo-Fenton like chemistry is always present in photocatalytic degradation reactions using iron containing species[41,51], due to photoproduction of H_2O_2 as described earlier in this chapter. Indeed, an avenue of interest could be to couple a material with a high efficiency for H_2O_2 production with a photo-Fenton material such as the magnetic photocatalysts described here. Electro-Fenton processes are well known in the literature[52], where H_2O_2 is electrochemically generated and then catalytically consumed by Fe(II), however there is a gap in the established work where a fully photocatalytic system could be investigated.

While magnetic materials can be an effective way in which photocatalytic water treatment may be achieved with a simple separation method post-use, they do fundamentally require the inclusion of magnetic materials. This restricts the choice of materials available, which may be to the detriment of the materials photocatalytic activity. Therefore, more versatile methods of producing photocatalyst systems with simple separation from solution have been investigated.

1.3.2 Immobilised Nanomaterials

Immobilisation of a nanomaterial on a macroscopic support gives a simple route to separation of the photocatalyst from solution. Supports such as glass, plastic, or metals have been described in the literature for this purpose[53,54]. Post-use separation in such cases is achieved trivially by filtering or decanting the treated water. While a great many reports have arisen focusing on vacuum techniques for this purpose, these methods are well established and recent reviews have been published describing such processes[55,56]. This chapter will instead focus on recent developments in simple solution processing techniques for immobilisation of photocatalysts. In table 1.3 is given a selection of immobilised photocatalyst systems including the support material and method of deposition.

Table 1.3 – Recently Reported Immobilised Photocatalysts

Photocatalytic Material	Support	Photocatalyst Deposition Method	Model Pollutant	Light source / Applied Bias	Photocatalytic Degradation Measure
ZnO[75]	Polypropylene Plates	Epoxy Sealer Method	Compost Leachate	32 W UV_C Lamps	61 % COD Removal in 4 hours
TiO_2[79]	Optical Fibres	Dip Coating	Chlorobenzoic Acid	365 nm LEDs	5.2×10^{-5} s^{-1}
TiO_2-SiO_2[57]	Microscope Glass Slides	Dip Coating	Methylisoborneol	350 nm Lamps	3.22×10^{-2} min^{-1} 2.72×10^{-2} min^{-1}
			Geosmin		
BiOCl-TiO_2[120]	FTO Glass	Hydrothermal	Rhodamine B	150 W Xenon Lamp	2.59 h^{-1}
TiO_2[61]	FTO Glass	Hydrothermal	Methylene Blue	Sim. Solar Light / 1 V vs RHE	94 % Removal in 90 mins
			Orange II		77% Removal in 4 hours

C_3N_4-TiO_2[63]	Ti Foil	Anodisation	Phenol	500 W Xe Lamp / 1-4 V vs RHE	100% Removal in 150 mins
Au-Polydopamine-Bi_2MoO_6-TiO_2[71]	Ti Foil	Anodisation	Methylene Blue	300 W Hg Lamp + 300 W Xe lamp	0.0203 min^{-1}
			Phenol		0.0126 min^{-1}
			Bisphenol A		0.0197 min^{-1}
TiO_2-polydopamine[74]	Glass Rod & Capillary Fibres	*In-situ* polymerisation	Geosmin	350 W Xe Lamp	Up to 91.5% removal in 2 hours
			Fluorene		Up to 99% removal in 2 hours
Cu_2O-CNT-Si Nanopillars[69]	Si	Electrodeposition	Methylene Blue	100 W Halogen (>400 nm)	86% Removal in 2 hours
Bi-TiO_2[70]	Ti Foil	Electrodeposition	Acid Orange II	1000 W Xe Lamp (>400 nm)	30 % removal in 2 hours
Bi_2O_3-TiO_2					45% removal in 2 hours
BiOI-TiO_2					60% removal in 2 hours

Immobilisation on glass slides is a commonly applied method, where a glass substrate is coated with a sol precursor to a photocatalytic material, which becomes the active phase on heat treatment. Yaparatne et al[57] recently used such a method to prepare TiO_2-SiO_2 films on glass slides. Coating suspensions containing sols have been found to improve the film robustness greatly by controlling aggregation[58]. While SiO_2 and other such binders may not be photocatalytically active material under normal conditions, their inclusion is hugely beneficial when designing a well-adhered film photocatalyst. SiO_2 or TiO_2 are the most commonly applied binder sols, however other materials with superior or complementary photocatalytic action are known to be prepared by sol-gel routes[59], which could impart both a robust film and improved photocatalytic activity.

A somewhat lower temperature method by which TiO_2 photocatalysts can be immobilised on glass substrates is by hydrothermal synthesis. Fluorine doped tin oxide (FTO) is used in such cases due to lattice matching between TiO_2 and FTO[60], typically giving rod or wire type morphologies. While interesting from a crystal growth perspective, the immobilisation of photocatalysts on FTO also affords opportunities to perform photoelectrocatalysis (PEC) due to the conductive nature of FTO. PEC processes allow control over the reactive species present at the semiconductor surface by applying a typically anodic bias potential, thus charge recombination is suppressed and the quantity of photogenerated holes able to react is increased. Recently Woo An *et al*[61] investigated PEC performances of hydrothermally grown TiO_2 nanorod arrays. The authors concluded that the aspect ratio of the prepared nanorods was key in the PEC activity by controlling the degree of light trapping and charge transport in the film as shown in Figure 1.7.

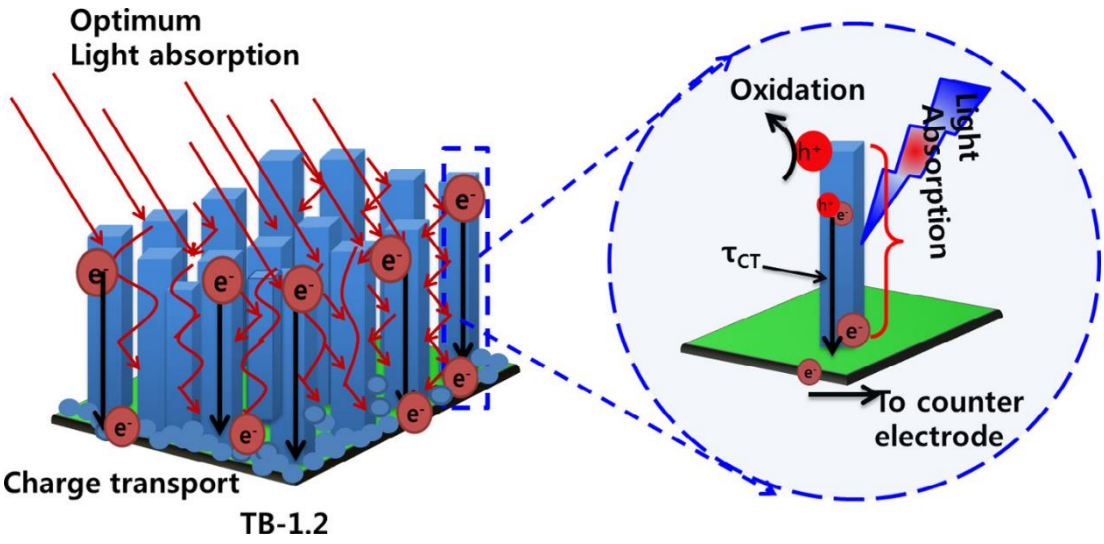

Figure 1.7. Light trapping and charge transport mechanism proposed by Woo An et al. Image adapted from reference 61.

This mechanism was proposed to result in an improvement of the PEC process over the photocatalytic and electrocatalytic processes individually. To improve light trapping and increase surface area further, nanomaterials with tube-like morphologies can be prepared. Recently much work has been undertaken in producing TiO_2 nanotubes by anodisation of Ti foils[62]. Employing high potentials and corrosive solvents, etching of the Ti substrate and subsequent annealing leaves tubes of TiO_2 immobilised on the foil surface. Such materials are enabled as PEC electrodes due to the conducting metal underlayer, which has been capitalised upon by work such as that of Wang *et al.*[63] to degrade phenol. While PEC processes have been studied thoroughly, questions have arisen as to the energy efficiency of such methods. Cardoso *et al.*[64] recently evaluated the energy efficiency of PEC and other light driven processes finding them to be considerably more energy intensive than ozonation for textile waste decolourisation. It has been suggested that PEC may be well suited to synthesis of high value chemicals[65], where this increased energy cost is off-set by the smaller quantities required and higher financial margins. PEC fits this niche well also due to the selectivity that may be applied through the bias potential, giving control where pure photocatalysis may give several species. This also would allow the use of rarer or more-costly metals to be applied in this way. While the vast majority of anodisation work in the literature focuses upon titania, it is also possible when starting from an

alloy of titanium and other metals, which upon anodisation gives composite materials. Mazierski *et al.*[66] demonstrated this in the fabrication of TiO_2-Ag_2O nanotube arrays interlaced with Ag nanoparticles. While the use of Ag does not lend itself to cheap applications, this work shows the potential for the use of alloys to generate photocatalytic materials in this way, and may be well suited to generation of higher margin products.

While applying a potential to assist during photocatalytic degradation can be advantageous, the conductive nature of substrates can be applied in producing new photocatalyst materials. Techniques such as electropolymerisation[67] and electrodeposition[68] have been used to produce new composite materials on conducting photocatalytic films.

Electrodeposition methods use the controlled precipitation of insoluble nanoparticles under oxidative or reductive potentials on the electrode surface, and can give close control over the particle morphologies and interconnection by changing the potentials used, and the way in which the potential is applied. A recent report by Sun *et al.*[69] demonstrates the fine control of such a method, where a pulsed electrodeposition method is used to grow nanocubes of Cu_2O onto carbon nanotube (CNT) fibres suspended between Si nanopillars as shown in Figure 1.8.

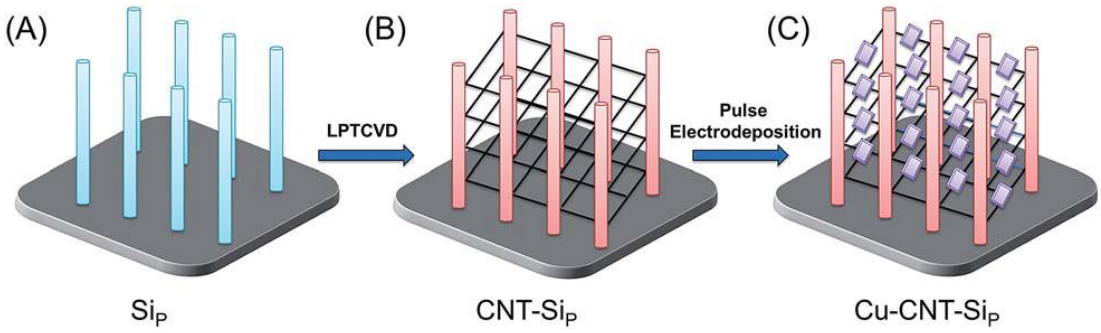

Figure 1.8. Schematic representation of the fabrication process including electrodeposition of suspended CuO on CNT fibres by Sun et al. Image adapted from reference 69.

This technique may also give rise to divergent synthetic strategies, where electrodeposition of a common precursor can lead to multiple products. As Sun *et al.* noted, their method has been found to produce CuO in some systems rather than Cu_2O,

however in other cases a more varied product scope has been demonstrated. Yuan *et al.*[70] found that they were able to deposit Bi nanoparticles on TiO_2 nanotubes, which, while active in their own right for the degradation of Acid Orange II, could be converted by simple solution processing or thermal treatments to give BiOI-TiO_2 or Bi_2O_3-TiO_2 composites with better photocatalytic activity.

Cai *et al.*[71] recently used electropolymerisation to produce a polydopamine layer in a composite of Au-Bi_2MoO_6 on TiO_2 nanotube arrays. Similar to electrodeposition of inorganic materials, electropolymerisation uses a surface potential to produce material, in this case the conducting polymer polydopamine, on the electrode surface in a controlled manner. In the work of Cai *et al.*, the polydopamine was used as an anchoring material and also to facilitate the growth of the Au NP, however it has been suggested that polydopamine may contribute to the photocatalytic production of hydroxyl radicals[72], and may sensitise semiconductors such as TiO_2 in addition[73]. Polydopamine has also been used as an immobilisation method of TiO_2 on glass substrates in its own right by Liu *et al* as shown in Figure 1.9[74].

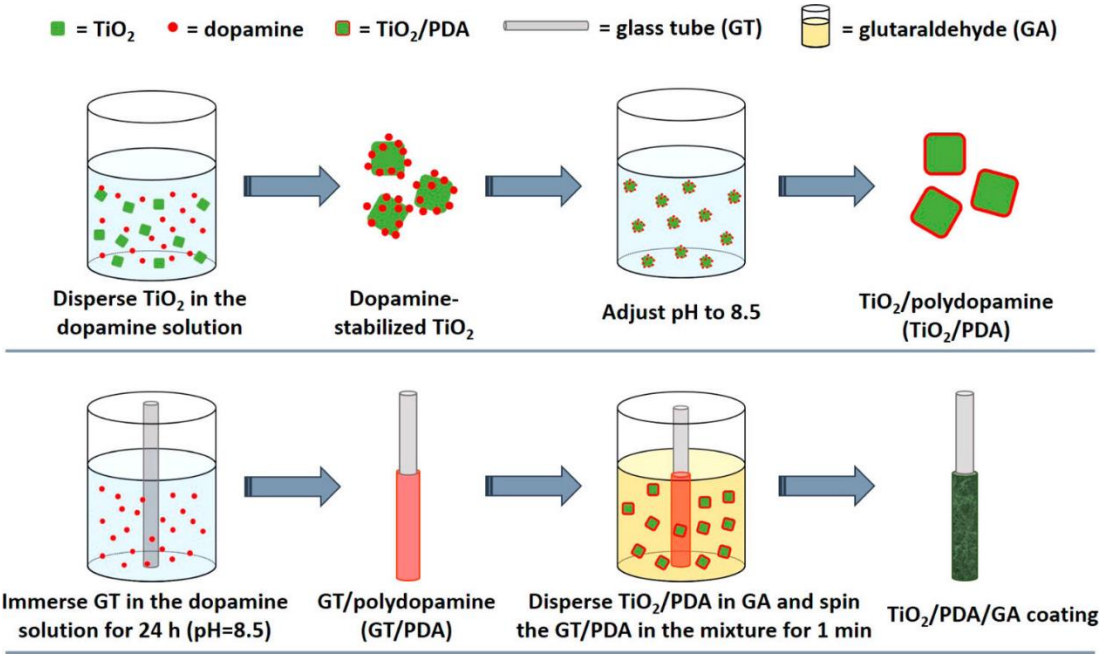

Figure 1.9. Polymerisation coating of glass tubes by polydopamine coating of TiO_2 as reported by Liu et al. Image adapted from reference 74.

The authors apply an *in situ* polymerisation coating technique to coat glass rods and capillary fibres with TiO_2-polydopamine composites, where the TiO_2 is firstly coated with polydopamine and then "caught" on the surface of the substrate during polymerisation. This material was found to be highly effective for the degradation of fluorene and geosmin under visible and UV irradiation.

Incorporation of polymers into photocatalytic materials has been studied thoroughly, however the use of simple polymeric substrates has also gained attention in recent years. Use of plastic is somewhat complicated by the inability to heat most plastics to the temperatures required for most deposition methods of common photocatalysts. The work of Ranjbari *et al.*[75] exemplifies a way in which this thermal instability may be overcome. They use a method by which pre-synthesised ZnO particles are immobilised through use of an adhesive layer, thereby avoiding any calcination or annealing steps. Their work demonstrates that it is possible to retain the favourable characteristics of high temperature syntheses (i.e. high crystallinity, porosity, morphologies, desirable phases) and immobilise the material post-synthesis in a simple manner.

Many different polymers in the literature have been reported as inactive supports, or to contribute to the photocatalytic activity of another material by introducing mechanisms for charge separation, or to act as photocatalysts in their own right[76,77]. However, organic materials are highly unlikely to be stable in the presence of photocatalytically generated ROS. As such, thorough stability testing should be undertaken upon such materials when ascertaining their practical utility, alongside determination whether secondary pollutants are being introduced during photocatalytic treatment.

In addition to being easily separable, immobilised photocatalyst systems have been shown to improve light delivery to the photocatalyst surface through reducing the inner filtering which occurs in slurry reactors[78]. The work of Tugaoen *et al.*[79] has recently demonstrated the direct deposition of photocatalytic TiO_2 onto the surface of optical fibres, providing a route for direct excitation from within the support as shown in Figure 1.10.

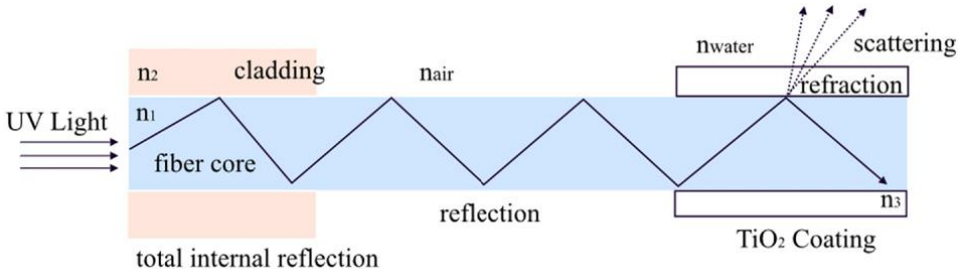

Figure 1.10. Light delivery mechanism in a TiO_2 coated fibre optic developed by Tugaoen et al. Image adapted from reference 79.

By capitalising on the difference in refractive index at the optical fibre/TiO_2 interface, the fibre optic acts as both a support and a route by which light can be introduced into the system. Such a system removes any potential shadowing or parasitic absorption by the pollutant solution, and as light is introduced directly into the fibre, less is leaked into the surroundings.

1.4 Reactor Systems

Immobilisation of novel photocatalyst materials is still relatively uncommon in the literature, where batch slurry systems are favoured, however reports exist of a variety of photoreactor types using industry standard TiO_2 or ZnO materials. A selection of recent reports on photocatalytic reactor designs is given in Table 1.4.

Table 1.4 – Photocatalytic Reactor Reports

Photocatalytic Material	Reactor Design	Model Pollutant	Light Source	Degradation Measure	Notes
ZnO[81]	Microfluidic	Methyl Orange	100 W UV Lamp	Up to ~1.2 min^{-1}	2 order of magnitude improvement over batch
TiO_2[82]	Fixed Bed	Clofibric acid	Hg Lamp	1.12 min^{-1}	Efficiency lower, but comparable, to slurry
	Fixed Film			1.28 min^{-1}	
ZnO-TiO_2[84]	Fixed Film	Methyl Orange	UV Lamp (2.61 mW cm^{-2})	0.0072 $hour^{-1}$	Photoleaching under UV irradiation
TiO_2[85]	Rotating disk	Phenol	UV Light (1.782 mW cm^{-2})	0.01313 min^{-1}	Jet stream impinging onto photocatalyst surface

C_3N_4-TiO_2[88]	Membrane	Sulfamethoxazole	300 W Xe Lamp	69% Removal in 30 hours	Recirculating system
C_3N_4[89]	Membrane	Rhodamine B	300 W Xe Lamp (>400 nm filter)	18% to 92% Removal after 1 to 7 passes	Multiple stage system
CuO-TiO_2[91]	Foam	Methyl Orange	Xe Lamp (100 mW cm^{-2})	0.1487 min^{-1}	Addition of H_2O_2, “Fenton-like” reactivity on Cu
BiOBr-TiO_2[92]	Unpowered Fixed Bed	Rhodamine	Real Solar (30–60 mW cm^{-2})	305.6 L h^{-1} m^{-2}	Flow produced by capillary force

Microfluidic devices have gained a significant amount of attention in recent years due to the improvements in mass transport and reduction in parasitic light filtering which exists in larger systems[80]. In such a system a pollutant solution is pumped through micro-scale channels coated with photocatalysts while irradiating through a transparent glass or plastic face. Devices may be single channel, but more commonly multi-channel systems such as that shown in Figure 1.11 are used.

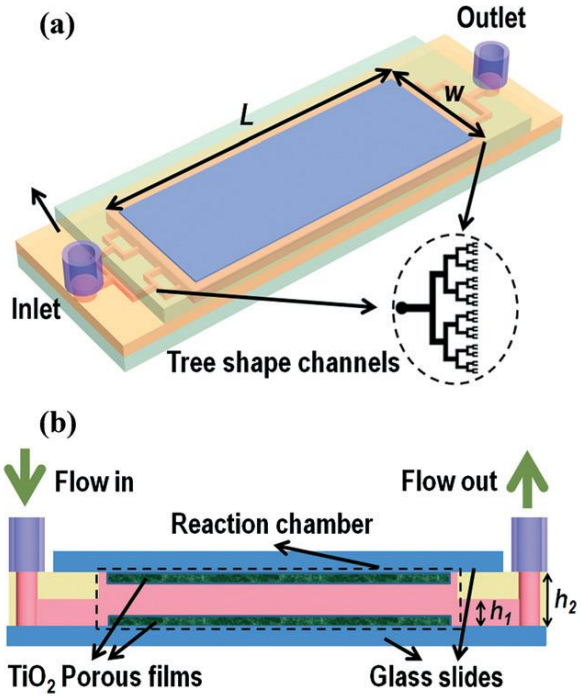

Figure 1.11. Schematic of a typical microfluidic device with multiple channels in a tree like distribution. Image adapted from reference 80.

Zhao *et al.*[81] recently studied the effectiveness of a ZnO nanorod based system formed using a combination of sol gel and hydrothermal syntheses in a microfluidic chamber type reactor. The authors of this work observed a large improvement over the batch type process, ascribing this to improved mass transport when run in flow. While the use of micro-scale fluidic devices has gained popularity due to these reasons, success has been achieved with larger scale flow systems. The use of fixed bed and fixed film reactors using TiO_2 has been proven to be effective for pollutant degradation, with examples existing of comparable activity being displayed versus slurry reactors[82]. Even larger monolithic type reactor designs have been reported, where the

photocatalyst is deposited upon a porous macroscopic support built around light source housings as shown in Figure 1.12[83].

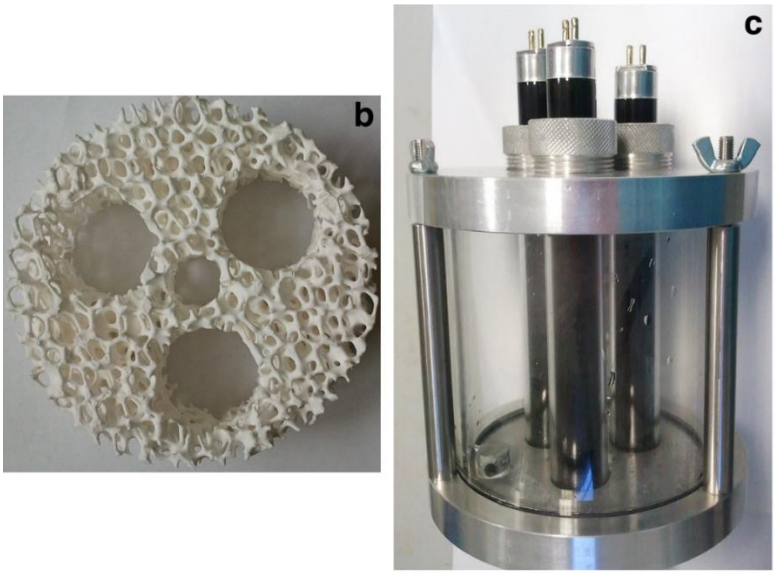

Figure 1.12. Photocatalytic monolith developed by Kete et al (b) and reactor design showing light source positioning (c). Image adapted from reference 83.

In using such a large-scale system, light distribution must be taken into account, with large monoliths such as that which is shown in Figure 1.12 likely suffering from severe shadowing issues. Using multiple smaller light sources such as LEDs or decreasing the monolith size can have a beneficial effect on light distribution in such cases.

An important aspect of such flow systems which may sometimes be overlooked in the literature is the stability of the photocatalytic material under the test conditions. İkizler *et al.*[84] found that Zn from ZnO nanorods could be leached into the test solution under irradiation due to photodissolution of Zn, but were able to abate this somewhat by introduction of a protective TiO_2 layer. While the possibility of leaching or flaking from a film surface is always present in any immobilised photocatalytic test system, under flow this can be exacerbated by the rate of water being passed over the film. A recent example from Jafarikojour *et al.*[85] applied an impinging jet stream of pollutant, with the aim of improving mass transfer rates. This technique involves introducing the pollutant rapidly in a jet of water onto the photocatalyst disk surface while rotating

(Figure 1.13), giving a thin layer of pollutant solution covering the photocatalyst surface which is rapidly degraded.

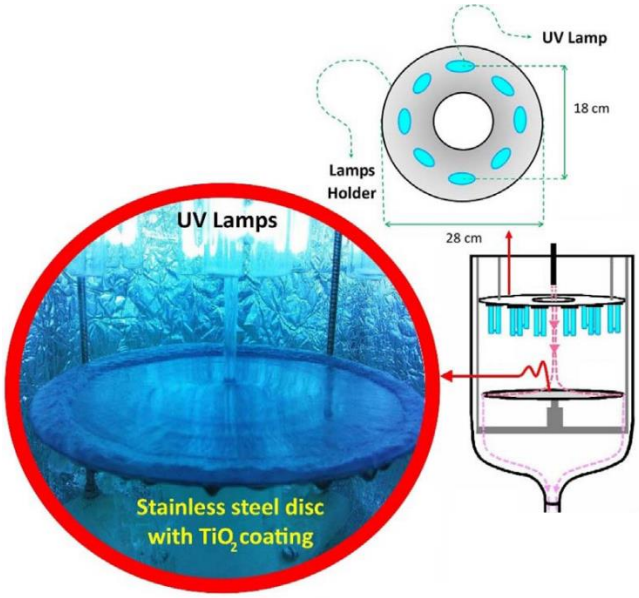

Figure 1.13. Jet impinging of a pollutant solution onto a TiO_2 coated disk surface in the set up developed by Jafarikojour et al. Image adapted from reference 85.

To make use of such a technique the photocatalyst must be adhered strongly to the disk surface to be successfully retained. While jet impinging of the pollutant is quite an extreme measure, this work demonstrates the importance of robustness of the immobilisation and stability of the materials to producing effective photocatalyst systems, where high force methods may be needed to give high degradation rates.

Membrane type reactors, where the photocatalytic material is immobilised on a porous support through which contaminated water is passed, have been studied due to the large quantity of prior work surrounding the preparation and characterisation of membrane filters[86,87]. Forcing a pollutant solution through such a material typically gives short contact times between the photocatalyst and pollutant molecules, resulting in poor performance in a single pass. Research in this area typically has used multiple stage or recirculating systems to achieve good degradation efficiencies. Yu *et al.*[88] used recirculation over a membrane of C_3N_4-TiO_2 on a polymer support to degrade a model anti-biotic under UV/visible irradiation as shown in Figure 1.14.

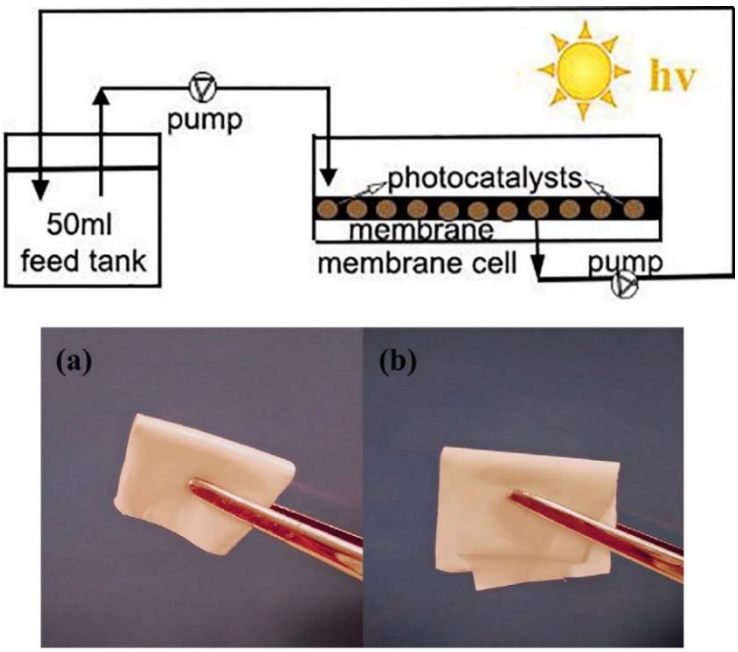

Figure 1.14. Schematic of the recirculation membrane photoreactor system used by Yu et al, and the flexibility of the polymeric membrane used. Image adapted from reference 88.

While the membrane was found to be robust under the prolonged mechanical stresses in the reactor, some instability under irradiation was noted by the authors. A loss in tensile strength of the membrane was concluded to be due to hydroxyl radical attack or photolysis of the organic support material. While Yu *et al.* postulated that membranes do not require very high mechanical strengths to be viable, a question that should be posed is the safety of the polymer degradation products in the downstream water. A more robust carbon fibre cloth supported C_3N_4 photocatalyst was reported by Shen *et al.*[89] recently. Multiple stage treatment was used to increase the degradation of rhodamine B, going from around 18% degradation in a single photocatalytic/filtration stage, to 92% after passing through seven membrane systems fitted in series as shown in Figure 1.15.

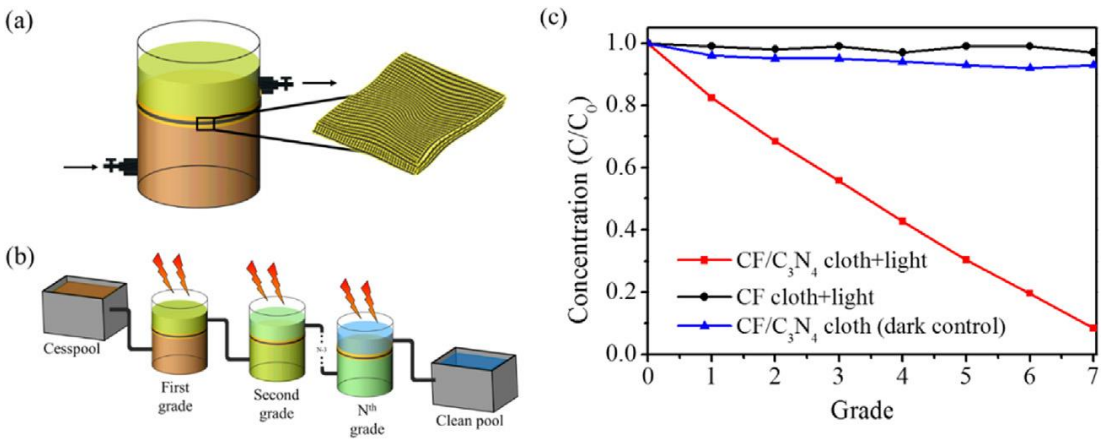

Figure 1.15. Photocatalytic membrane system devised by Shen et al. showing (a) a single grade system where pollutant is pumped through the membrane, (b) the connection of several grade systems in series and (c) the improvement in Rhodamine B removal after multiple grades. Image adapted from reference 89.

This system appears to be stable, with several repeat measurements being undertaken with no loss in activity, and no observed change in the structure or morphology noted by the authors.

It is noteworthy that flow systems such as those described above are relatively complex pieces of equipment, which may not be viable in some areas of the planet where the skills and funds needed for maintenance are not available. In such areas point of use purification of drinking water sources would be a logical starting point[11], which has been noted as an area where photocatalysis could give a degree of treatment where other techniques are not possible[90]. Therefore, low tech reactor designs in these areas may be preferable. A simple TiO_2 coated carbon foam based microreactor has been developed by Zhu *et al*[91]. In the operation of this microreactor the foam acts as a sponge to soak up pollutant solutions, which can be photocatalytically purified before simply squeezing the foam to release the decontaminated water as shown in Figure 1.16.

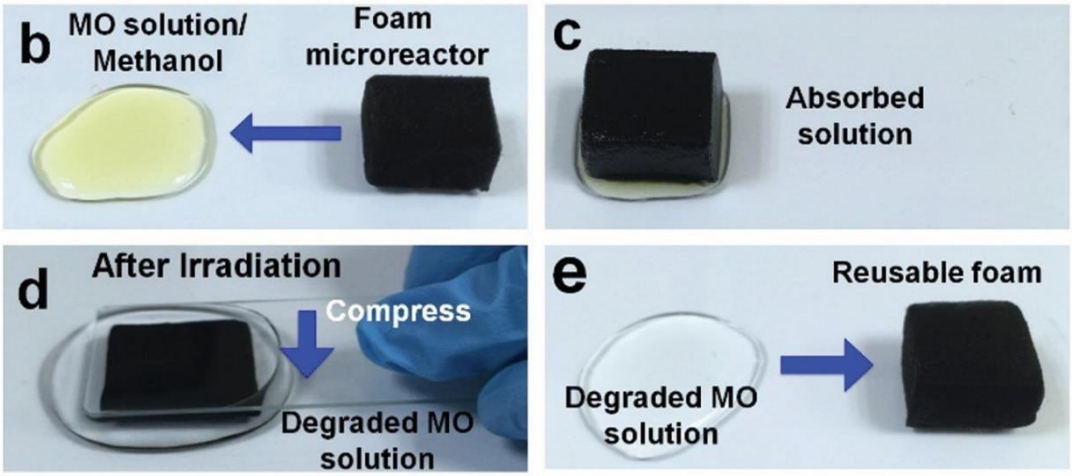

Figure 1.16. Uptake of MO solution by soaking of the foam microreactor developed by Zhu et al.*[91] *and subsequent regeneration of the foam leaving the purified solution. Image adapted from reference 91.

They note that no mechanical mixing is required in this set up due to channelling of the pollutant solution by the foam to the TiO_2 surface. As such, this type of microreactor could well be particularly effective in an environment with little or no access to electricity, where a powered agitation or flow system may not be viable. Similarly, Mei *et al.*[92] recently demonstrated the use of an unpowered flow reactor system using a carbon cloth framework as shown in Figure 1.17.

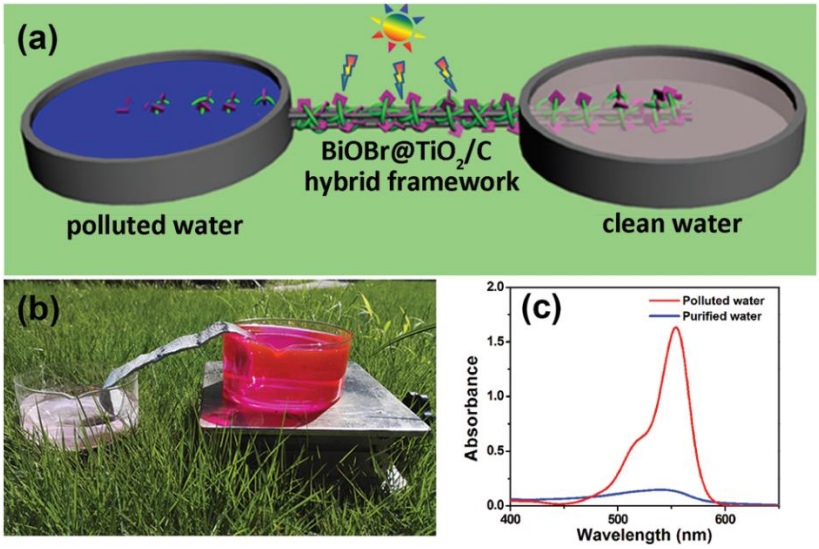

Figure 1.17. (a) Schematic image of the un-powered flow reactor used by Mei et al*[92]*. (b) Photograph of the system in operation under solar irradiation and (c) the removal of rhodamine B using the system. Image adapted from reference 92.

Using capillary force, the authors were able to drive the flow of a pollutant solution over the photocatalyst surface while under solar irradiation, producing a flow system without any external electrical input. Such innovative systems fit the niche of photocatalysis in remote "off grid" communities perfectly.

While a huge number of reactor designs and optimisation studies upon these reactors are being published continually, the work of Mei *et al* described above is somewhat in the minority in that it makes use of a more complex material than the industry standards. A great many reports are also being generated on new materials with reportedly higher efficiencies than the standard P25 TiO_2 photocatalysts, yet most are not designed with any particular application or reactor system in mind. This is a common disconnect in the field of photocatalytic water treatment, where application is not considered during the material development stage, and few make any effort to produce working reactors with novel materials. There is therefore a clear potential for collaborative efforts to develop new materials with immobilisation and reactor use in mind, and thereby take steps toward a useable system.

Are Current Testing Methods Applicable?

Simply by examining the information contained in Tables 2-4 in this review it becomes clear that there is a huge array of different testing conditions used in the literature. Light sources used to power photocatalytic reactions often differ in terms of their emission wavelengths and intensities, and there is no clear consensus on which pollutants should be used to test photocatalysts against. Thus, even after thorough testing of a new material it can be very difficult or impossible to compare to the results of others in a meaningful way. As the field moves towards application of materials developed in the laboratory, it is worth examining some issues that have arisen in testing conditions used.

While there is typically a high quality of control experiments run using materials from within a single piece of research, one further control method which should be applied is to compare all prepared materials to an industrial standard such as P25[93], even if the prepared material is not a TiO_2 based photocatalyst[94]. The percentage improvement

over this standard then becomes the metric which can be used to compare various materials. This can then be compared to others who have carried out the same test, and thus account to some extent for differences in set up and light source. Often comparisons are made to a synthesised control material (i.e. TiO_2 synthesised in parallel in the laboratory)[95], which is worthwhile but does not allow for comparison between laboratories. Running a control using P25 or a similar material gives extra value to a piece of work as it allows a degree of comparison between studies by different authors. However, this test is applied inconsistently in the literature, and therefore becomes difficult to use to date. It also breaks down somewhat when the goal of a piece of research is to impart visible light sensitisation upon a UV-absorbing material, as the light source for such a test will be fundamentally incompatible with most industrial standards which are typically UV-absorbers. In these cases, the improvement of the sensitised material over, for instance, P25 will be misleadingly high. It has been suggested that nitrogen-doped TiO_2 control could be used as a standard for visible light performance[96], however the use of this material is even more infrequent than that of the normal P25 standard. Thus, the use of such control experiments should always be encouraged, as the quality of comparison which can be made through them relies upon their widespread use. If a consensus can be reached on the material and conditions used for UV, UV-visible and visible active photocatalysts, then comparison of performance could be improved significantly.

A large variety of different model pollutants has been used to determine activity in photocatalytic systems. Pollutants such as agricultural molecules, drugs, explosives or industrial waste products have been studied, but by far the most common class of molecules used in testing are dyes[97]. While the textile industry is indeed reckoned to be the cause of much of the worlds contaminated water[98], questions must be raised about the validity of the use of dyes in ascertaining performance. For truly applicable systems to be developed, thorough reliable testing methods should be encouraged, which dyes may not satisfy. While it is often overlooked, a process known as self-sensitisation or dye-sensitisation by dye model pollutants can give entirely misleading photocatalytic performance results for a new material[99]. A schematic representation of this effect is given in Figure 1.18.

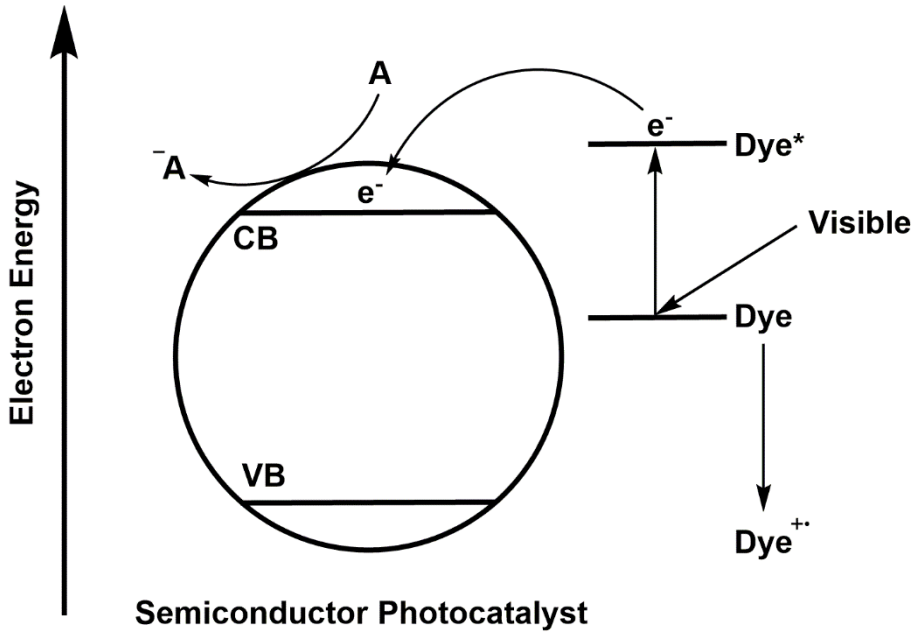

Figure 1.18. Mechanism of self-sensitisation by a dye molecule on the surface of a semiconductor photocatalyst

In this mechanism, excitation of the model pollutant facilitates ROS generation, bypassing the semiconductors used. Therefore, activity is not dependent upon the excitation of the photocatalyst material at all and is simply determined by the properties of the dye. For this mechanism to hold, the excited state energy must be able to transfer photogenerated charges to the semiconductor, meaning that this transfer must be energetically downhill. As the absorption is dependent upon the dye model pollutant and the photocatalyst used, the optical properties of the dye and its surface adsorption become important in determining activity[33], and thus the activity becomes specific to that dye pollutant under the irradiation conditions used. Some dye/semiconductor combinations will demonstrate photocatalytic activity where changing the dye to a different model pollutant, or even a different dye, can show lower or no activity. This is not necessarily a problem if activity is clearly claimed solely for the dye pollutant in question, however issues arise when general performance is assumed based on a dye decolourisation test alone, or when comparisons between different dyes are attempted.

It is possible to overcome this sensitisation effect by either applying a light source which has no overlap with the dye absorption, or simply studying the removal of a

colourless pollutant such as simple aromatic molecules. A selection of recent examples of photocatalysts tested where self-sensitisation is discussed are given in Table 1.5.

Table 1.5 – Self-sensitisation comparisons in the recent literature

Photocatalytic Material	Light Source	Model Pollutants	Degradation Measure
Bi_3O_4Br-Bi_2O_3[121]	350 W Xe Lamp (>400 nm)	Methyl Orange	0.03703 min^{-1}
		Phenol	0.28826 $hour^{-1}$
WO_3-Vanadium Phosphate[122]	180 W UV/visible Irradiation Chamber	Rhodamine B	100 % removal in 10 minutes
		Phenol	60% removal in 10 minutes
$SrTiO_3$-Ag-AgCl[123]	300 W Xe Lamp (>420 nm)	Various dyes	93-96% removal in 30-70 minutes
		Bisphenol A	83% removal in 4 hours
		Phenol	70% removal in 4 hours

ZnO-reduced graphene oxide[124]	300 W Xe Lamp	Rhodamine B	0.291 min^{-1}
		Phenol	$5.56x10^{-2}$ min^{-1}
Boron nitride-TiO_2[125]	Xe lamp producing 350 W m^{-2}	Rhodamine B	99 % removal in 6 hours
		Phenol	83 % removal in 30 hours
Boron nitride-BiOI[126]	350 W Xe lamp (>420 nm)	Methylene Blue & Rhodamine B	~90% removal in 100 minutes
		4-chlorophenol	~75% removal in 150 minutes
BiOBr-WO_3[127]	300 W Xe lamp (>400 nm)	Methyl Orange	61.9 % removal in 3 hours
		Rhodamine B	100 % removal in 20 minutes
		4-chlorophenol	71 % removal in 6 hours

This self-sensitisation effect has led to examples of visible inactive materials demonstrating activity under visible light[100], however publications are continually forthcoming where this effect is not addressed sufficiently. Indeed, the effect of self-sensitisation can be significant enough to be the cause of all apparent photocatalytic activity. Recently Cates *et al.*[101] surveyed several reported upconverting lanthanide based phosphors under visible light, and determined that these examples could not give the reported improvements in activity based on their upconverting properties. They conclude that such examples are likely down to self-sensitisation as shown in Figure 1.19, and thus much of the field of upconverting photocatalyst for water purification are likely unreliable for this reason.

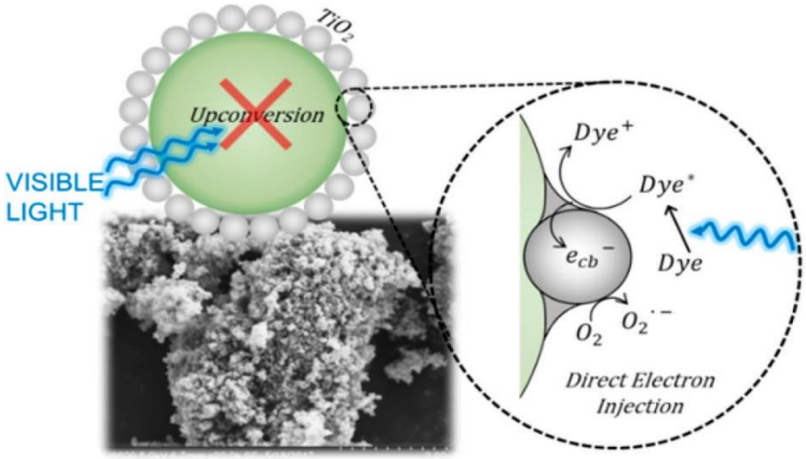

Figure 1.19. Schematic representation of the lack of activity derived from upconversion in upconverting nanocomposites. Image adapted from reference 101.

The study of Cates *et al.* is thorough, but it is clear that this problem goes beyond upconverting photocatalysts, and questions must be raised going forward about the true activity of reported photocatalysts.

A further reason that tests upon dyes may be unreliable is the measurement of decolourisation rather than degradation. Many studies exist where degradation is claimed, however the evidence provided for this relies upon a simple loss of colour of the solution. It is possible that complete degradation does indeed occur in these cases; recent work by Hao *et al.*[102] observed that the mineralisation of methyl orange closely matched the decolourisation in their system, however it is also possible that

decolourisation is not being matched. A simple change in the chromophore may well be occurring, leaving most of the molecule intact, but appearing as if complete degradation has occurred. Indeed, examples such as that of Jiang *et al.*[103] and Zhang *et al.*[104] demonstrate that dyes such as Rhodamine B can undergo slight modifications such as de-ethylation under photocatalytic conditions, causing a shift of the absorption peak as shown in Figure 1.20.

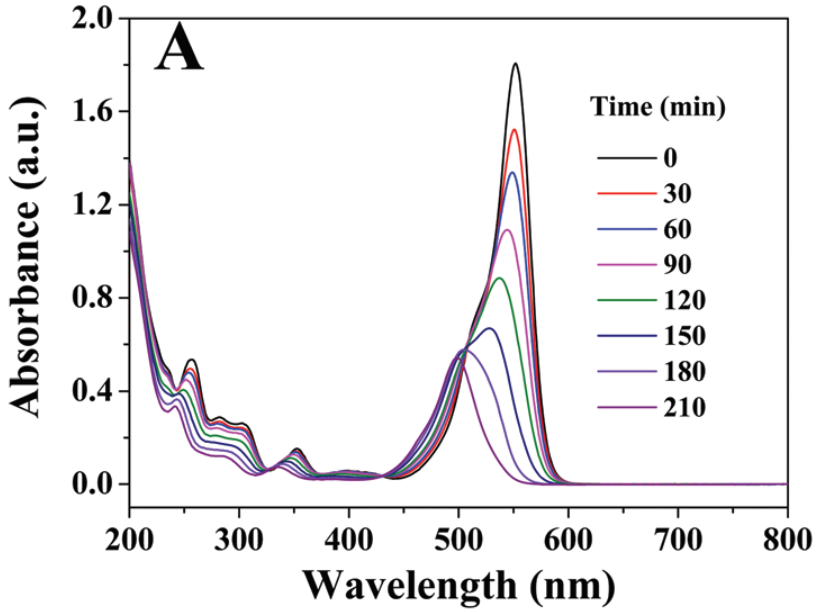

Figure 1.20. Spectral changes of Rhodamine B under photocatalytic conditions showing blue shift of peak. Image adapted from reference 103.

In these examples, there is a clear difference in rate of decolourisation and degradation, but in other cases it may not be clear if the initial product formed is colourless. While studying the degradation of methyl orange, Deng *et al.*[105] recently found that the rate of mineralisation was significantly slower than decolourisation using their BiOBr photocatalyst, and that changes to their reaction conditions which were beneficial for decolourisation were in fact decreasing the mineralisation performance. Incomplete degradation giving decolourisation or shifts in absorption maxima of dyes may not even involve significant structural changes. Methylene blue for example is known to be able to undergo a two-electron reduction to give the colourless leuco-methylene blue[106] as shown in Figure 1.21, which is a possible reaction pathway in photocatalytic systems[107].

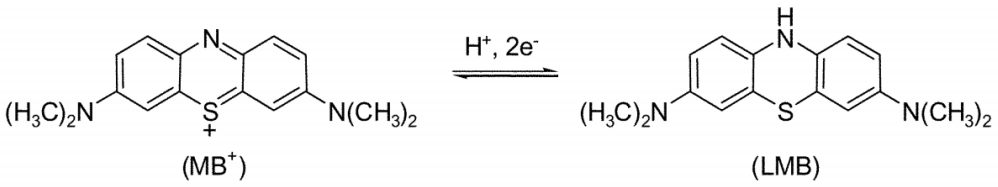

Figure 1.21. Redox process of converting methylene blue (MB^+) to leuco-methylene blue (LMB). Image adapted from reference 106.

If the aim of a photocatalytic study is to degrade methylene blue, care should be taken to confirm that the loss of MB observed is destruction of the molecule, rather than this reduction process, which may be significantly faster.

Combinations of self-sensitisation and decolourisation processes such as this may be complicated even further by electron transfer from dyes to other species in water such as dissolved oxygen. Mitoraj *et al.*[108] noted that methylene blue can decolourise in several different ways in the presence of $InVO_4/BiVO_4$ composites depending on the wavelength of light used, including electron transfer to oxygen. If, as is typical, a broad emission light source such as a Xe lamp is used, these processes may be occurring simultaneously, and the true photocatalytic degradation derived from the photocatalyst itself is almost impossible to ascertain.

Thus, while literature examples of photocatalysts tested against dyes are, and continue to be, the most common to date, claims based on a test against a single dye molecule should be treated with caution. Care should be taken to ensure clarity of the claims being made in any published work; if the aim is to decolourise a specific dye, and this is made plain to the reader, these factors are not an issue. There is however a trend to conflate decolourisation with non-specific performance and total mineralisation, which should be avoided.

The question then remains: what can be done to overcome these inconsistencies and thus improve the applicability of photocatalysts?

While dye models are particularly prone to inconsistencies, molecules of other classes are not immune from giving misleading results, and as such testing against as wide and diverse a set of pollutants as possible is key. Good examples in the literature

address this by focusing upon a subset of organic pollutants such as drug molecules[109], explosives[110] or agricultural chemicals[111] and study the degradation of numerous examples. In doing so, these studies provide a baseline of activity against the molecule classes tested, which gives a much more thorough and reliable proof of activity. As compounds of the same class are often used concurrently in a mixture, they have often been found to occur together in water sources[112]. Evidence of activity against multiple compounds of the same class is therefore invaluable in demonstrating that a photocatalytic material or reactor could be applicable against real water samples. The European Union Water Framework Directive and United States of American Environmental Protection Agency both have released lists[113,114] of compounds that are identified as problematic, giving a host of different molecules which there is a clear avenue of inquiry for photocatalytic treatment. In addition, there exist numerous surveys of water contaminants present in different areas of the world[115–119], which identify numerous organic contaminants which would be logical test subjects. Thus, there exists many compounds which can be used for testing which have clear real-world applications. While there is still a need for the development of new photocatalytic materials and reactor systems, there is a gap which has been relatively overlooked in applying new materials to the degradation of these relevant compounds.

1.5 Chapter 1 Conclusion

To summarise, water purification is a critical problem, which is likely to grow in coming years. Photocatalytic purification using semiconductors has emerged as a method to remove contamination from water, and much work has been undertaken to develop newer high efficiency materials for this purpose. While increasing efficiencies has been the focus of much work to date, new materials which can be simply applied have been reported, but little attention has been brought to them, which this review aims to remedy. It is observed that there has been something of a disconnect between the materials development and efforts to produce workable systems. Despite the multitude of new materials reported, reactor designs mostly focus upon standard materials, and as such a clear opportunity exists in the field for those working upon novel materials to work with those aiming to improve reactor designs. Such collaborative efforts are invaluable to inform both partners of the considerations and

limitations of each other's systems, and thereby inform future developments. While new materials taking steps to produce better photocatalysts have been consistently published, testing methods are somewhat inconsistent by comparison. Much of the reported work uses un-realistic or misleading test systems, and in the recent published work reports have arisen questioning some of these results which are highlighted and discussed in this review. Thus, it is the conclusion of this review that if water purification photocatalysis is to become a ubiquitous treatment method in the real world then greater focus should be put upon applicability, consistent and thorough testing, and consideration of the target users' needs.

1.6 Chapter 1 References

1 World Health Organisation, *Progress on Drinking Water, Sanitation and Hygiene*, 2017.
2 The United Nations, *Water Scarcity*, 2013.
3 The United Nations, *The United Nations World Water Development Report 2015: Water for a sustainable world*, 2015.
4 The United Nations, *The United Nations World Water Development Report 2016: Water and Jobs*, 2016.
5 J. R. Mihelcic, Z. J. Ren, P. K. Cornejo, A. Fisher, A. J. Simon, S. W. Snyder, Q. Zhang, D. Rosso, T. M. Huggins, W. Cooper, J. Moeller, B. Rose, B. L. Schottel and J. Turgeon, *Environ. Sci. Technol.*, 2017, **51**, 7749–7758.
6 United Kingdom House of Lords, *European Union Committee - Thirty-Third Report, An Indispensable Resource: EU Freshwater Policy, Chapter 2*, 2012.
7 *https://sustainabledevelopment.un.org/*, 2018.
8 The United Nations, *The United Nations World Water Development Report 2017: Wastewater: The Untapped Resource*, 2017.
9 L. Hossain, S. K. Sarker and M. S. Khan, *Environ. Dev.*, 2018, 1–11.
10 Y. Valcárcel, A. Valdehíta, E. Becerra, M. López de Alda, A. Gil, M. Gorga, M. Petrovic, D. Barceló and J. M. Navas, *Chemosphere*, 2018, **201**, 388–398.
11 J. Mac Mahon and L. W. Gill, *Dev. Eng.*, 2018, **3**, 47–59.
12 E. Rahmanian, R. Malekfar and M. Pumera, *Chem. - A Eur. J.*, 2018, **24**, 18–31.
13 J. Low, J. Yu, M. Jaroniec, S. Wageh and A. A. Al-Ghamdi, *Adv. Mater.*, 2017, **29**, 1601694.
14 X. Liu, J. Iocozzia, Y. Wang, X. Cui, Y. Chen, S. Zhao, Z. Li and Z. Lin, *Energy Environ. Sci.*, 2017, **10**, 402–434.
15 M. R. Hoffmann, S. T. Martin, W. Choi and D. W. Bahnemann, *Chem. Rev.*, 1995, **95**, 69–96.
16 X. Wang, L. Bai, H. Liu, X. Yu, Y. Yin and C. Gao, *Adv. Funct. Mater.*, 2018, **28**, 1704208.
17 C. Song, L. Wang, F. Gao and Q. Lu, *Chem. - A Eur. J.*, 2016, **22**, 6368–6373.
18 Y. Wang, Q. Wang, X. Zhan, F. Wang, M. Safdar and J. He, *Nanoscale*, 2013, **5**, 8326–39.
19 D. C. Hurum, A. G. Agrios, K. A. Gray, T. Rajh and M. C. Thurnauer, *J. Phys. Chem. B*, 2003, **107**, 4545–4549.
20 Y. Sang, H. Liu and A. Umar, *ChemCatChem*, 2015, **7**, 559–573.
21 Y. Nosaka and A. Y. Nosaka, *Chem. Rev.*, 2017, **117**, 11302–11336.
22 P. Chen, F. Wang, Z.-F. Chen, Q. Zhang, Y. Su, L. Shen, K. Yao, Y. Liu, Z. Cai, W. Lv and G. Liu, *Appl. Catal. B Environ.*, 2017, **204**, 250–259.
23 P. Karaolia, I. Michael-Kordatou, E. Hapeshi, C. Drosou, Y. Bertakis, D. Christofilos, G. S. Armatas, L. Sygellou, T. Schwartz, N. P. Xekoukoulotakis and D. Fatta-Kassinos, *Appl. Catal. B Environ.*, 2018, **224**, 810–824.
24 W. Y. Teoh, J. A. Scott and R. Amal, *J. Phys. Chem. Lett.*, 2012, **3**, 629–639.
25 R. Abe, H. Takami, N. Murakami and B. Ohtani, *J. Am. Chem. Soc.*, 2008, **130**, 7780–7781.

26 S. Nagarajan, N. C. Skillen, F. Fina, G. Zhang, C. Randorn, L. A. Lawton, J. T. S. Irvine and P. K. J. Robertson, *J. Photochem. Photobiol. A Chem.*, 2017, **334**, 13–19.

27 M. R. D. Khaki, M. S. Shafeeyan, A. A. A. Raman and W. M. A. W. Daud, *J. Environ. Manage.*, 2017, **198**, 78–94.

28 J. Schneider, M. Matsuoka, M. Takeuchi, J. Zhang, Y. Horiuchi, M. Anpo and D. W. Bahnemann, *Chem. Rev.*, 2014, **114**, 9919–9986.

29 W. Kim, T. Tachikawa, G. H. Moon, T. Majima and W. Choi, *Angew. Chemie - Int. Ed.*, 2014, **53**, 14036–14041.

30 S. Foteinis, J. M. Monteagudo, A. Durán and E. Chatzisymeon, *Sci. Total Environ.*, 2018, **612**, 605–612.

31 M. Ge, C. Cao, J. Huang, S. Li, Z. Chen, K.-Q. Zhang, S. S. Al-deyab and Y. Lai, *J. Mater. Chem. A*, 2016, **4**, 6772–6801.

32 N. Wu, *Nanoscale*, 2018, **10**, 2679–2696.

33 X. Li, H. Lin, X. Chen, H. Niu, J. Liu, T. Zhang and F. Qu, *Phys. Chem. Chem. Phys.*, 2016, **18**, 9176–9185.

34 C. Ratanatawanate, A. Bui, K. Vu and K. J. Balkus, *J. Phys. Chem. C*, 2011, **115**, 6175–6180.

35 A. Gondikas, F. von der Kammer, R. Kaegi, O. Borovinskaya, E. Neubauer, J. Navratilova, A. Praetorius, G. Cornelis and T. Hofmann, *Environ. Sci. Nano*, 2018, **5**, 313–326.

36 M. Shekofteh-Gohari and A. Habibi-Yangjeh, *RSC Adv.*, 2016, **6**, 2402–2413.

37 J. Ni, J. Xue, L. Xie, J. Shen, G. He and H. Chen, *Phys. Chem. Chem. Phys.*, 2017, **20**, 414–421.

38 Q. Sun, Y. Hong, Q. Liu and L. Dong, *Appl. Surf. Sci.*, 2018, **430**, 399–406.

39 C. Zhao, C. Shao, X. Li, X. Li, R. Tao, X. Zhou and Y. Liu, *J. Alloys Compd.*, 2018, **747**, 916–925.

40 K. N. Kim, H.-R. Jung and W.-J. Lee, *J. Photochem. Photobiol. A Chem.*, 2016, **321**, 257–265.

41 X. Wang, A. Wang and J. Ma, *J. Hazard. Mater.*, 2017, **336**, 81–92.

42 E. Casbeer, V. K. Sharma and X. Z. Li, *Sep. Purif. Technol.*, 2012, **87**, 1–14.

43 H. W. P. Carvalho, P. Hammer, S. H. Pulcinelli, C. V. Santilli and E. F. Molina, *Mater. Sci. Eng. B Solid-State Mater. Adv. Technol.*, 2014, **181**, 64–69.

44 Z. Shi, Y. Xiang, X. Zhang and S. Yao, *Photochem. Photobiol.*, 2011, **87**, 626–631.

45 H. Yao, M. Fan, Y. Wang, G. Luo and W. Fei, *J. Mater. Chem. A*, 2015, **3**, 17511–17524.

46 J. Xiao, Q. Han, Y. Xie, J. Yang, Q. Su, Y. Chen and H. Cao, *Environ. Sci. Technol.*, 2017, **51**, 13380–13387.

47 J. Fu, J. Yu, C. Jiang and B. Cheng, *Adv. Energy Mater.*, 2018, **8**, 1–31.

48 J. Herney-Ramirez, M. A. Vicente and L. M. Madeira, *Appl. Catal. B Environ.*, 2010, **98**, 10–26.

49 O. S. N. Sum, J. Feng, X. Hub and P. L. Yue, *Top. Catal.*, 2005, **33**, 233–242.

50 X. S. Nguyen, G. Zhang and X. Yang, *ACS Appl. Mater. Interfaces*, 2017, **9**, 8900–8909.

51 S. Giannakis, S. Liu, A. Carratalà, S. Rtimi, M. Talebi Amiri, M. Bensimon and C. Pulgarin, *J. Hazard. Mater.*, 2017, **339**, 223–231.

52 F. Yu, M. Zhou, L. Zhou and R. Peng, *Environ. Sci. Technol. Lett.*, 2014, **1**, 320–324.

53 A. Fernández, G. Lassaletta, V. M. Jiménez, A. Justo, A. R. González-Elipe, J.-M. Herrmann, H. Tahiri and Y. Ait-Ichou, *Appl. Catal. B Environ.*, 1995, **7**, 49–63.

54 A. Di Mauro, M. Cantarella, G. Nicotra, G. Pellegrino, A. Gulino, M. V. Brundo, V. Privitera and G. Impellizzeri, *Sci. Rep.*, 2017, **7**, 40895.

55 J.-P. Niemelä, G. Marin and M. Karppinen, *Semicond. Sci. Technol.*, 2017, **32**, 093005.

56 X. Meng, *J. Mater. Chem. A*, 2017, **5**, 18326–18378.

57 S. Yaparatne, C. P. Tripp and A. Amirbahman, *J. Hazard. Mater.*, 2018, **346**, 208–217.

58 Y. Chen and D. D. Dionysiou, *Appl. Catal. B Environ.*, 2006, **62**, 255–264.

59 D. P. Debecker and P. H. Mutin, *Chem. Soc. Rev.*, 2012, **41**, 3624.

60 W.-Q. Wu, B.-X. Lei, H.-S. Rao, Y.-F. Xu, Y.-F. Wang, C.-Y. Su and D.-B. Kuang, *Sci. Rep.*, 2013, **3**, 1352.

61 G. W. An, M. A. Mahadik, W. S. Chae, H. G. Kim, M. Cho and J. S. Jang, *Appl. Surf. Sci.*, 2018, **440**, 688–699.

62 M. Abdullah and S. K. Kamarudin, *Renew. Sustain. Energy Rev.*, 2017, **76**, 212–225.

63 H. Wang, Y. Liang, L. Liu, J. Hu and W. Cui, *J. Hazard. Mater.*, 2018, **344**, 369–380.
64 J. C. Cardoso, G. G. Bessegato and M. V. Boldrin Zanoni, *Water Res.*, 2016, **98**, 39–46.
65 V. Augugliaro, G. Camera-Roda, V. Loddo, G. Palmisano, L. Palmisano, J. Soria and S. Yurdakal, *J. Phys. Chem. Lett.*, 2015, **6**, 1968–1981.
66 P. Mazierski, A. Malankowska, M. Kobylański, M. Diak, M. Kozak, M. J. Winiarski, T. Klimczuk, W. Lisowski, G. Nowaczyk and A. Zaleska-Medynska, *ACS Catal.*, 2017, **7**, 2753–2764.
67 D. Jeon, N. Kim, S. Bae, Y. Han and J. Ryu, *ACS Appl. Mater. Interfaces*, 2018, **10**, 8036–8044.
68 T. Wang, Y. Wei, X. Chang, C. Li, A. Li, S. Liu, J. Zhang and J. Gong, *Appl. Catal. B Environ.*, 2018, **226**, 31–37.
69 Y. Sun, R. Chen, J. Oh, B. Yoo and H. Lee, *RSC Adv.*, 2017, **7**, 2880–2883.
70 X. J. Yuan, J. H. Yi, H. J. Wang, H. Yu, S. Q. Zhang and F. Peng, *Mater. Chem. Phys.*, 2017, **196**, 237–244.
71 J. Cai, J. Huang and Y. Lai, *J. Mater. Chem. A*, 2017, **5**, 16412–16421.
72 Z. Wang, F. Tang, H. Fan, L. Wang and Z. Jin, *Langmuir*, 2017, **33**, 5938–5946.
73 C. Wang, Y. Wu, J. Lu, J. Zhao, J. Cui, X. Wu, Y. Yan and P. Huo, *ACS Appl. Mater. Interfaces*, 2017, **9**, 23687–23697.
74 S. Liu, Q. Hu, J. Qiu, F. Wang, W. Lin, F. Zhu, C. Wei, N. Zhou and G. Ouyang, *Environ. Sci. Technol.*, 2017, **51**, 5137–5145.
75 A. Ranjbari and N. Mokhtarani, *Appl. Catal. B Environ.*, 2018, **220**, 211–221.
76 S. Ghasimi, S. Prescher, Z. J. Wang, K. Landfester, J. Yuan and K. A. I. Zhang, *Angew. Chemie Int. Ed.*, 2015, **54**, 14549–14553.
77 S. Ghosh, N. A. Kouamé, L. Ramos, S. Remita, A. Dazzi, A. Deniset-Besseau, P. Beaunier, F. Goubard, P.-H. Aubert and H. Remita, *Nat. Mater.*, 2015, **14**, 505–511.
78 L. Ling, H. Tugaoen, J. Brame, S. Sinha, C. Li, J. Schoepf, K. Hristovski, J. H. Kim, C. Shang and P. Westerhoff, *Environ. Sci. Technol.*, 2017, **51**, 13319–13326.
79 H. O'Neal Tugaoen, S. Garcia-Segura, K. Hristovski and P. Westerhoff, *Sci. Total Environ.*, 2018, **613**–**614**, 1331–1338.
80 N. Wang, X. Zhang, Y. Wang, W. Yu and H. L. W. Chan, *Lab Chip*, 2014, **14**, 1074–1082.
81 P. Zhao, N. Qin, J. Z. Wen and C. L. Ren, *Appl. Catal. B Environ.*, 2017, **209**, 468–475.
82 A. Manassero, M. L. Satuf and O. M. Alfano, *Chem. Eng. J.*, 2017, **326**, 29–36.
83 M. Kete, O. Pliekhova, L. Matoh and U. L. Štangar, *Environ. Sci. Pollut. Res.*, 2017, 1–13.
84 B. İkizler and S. M. Peker, *Thin Solid Films*, 2016, **605**, 232–242.
85 M. Jafarikojour, B. Dabir, M. Sohrabi and S. J. Royaee, *Chem. Eng. Process. Process Intensif.*, 2017, **121**, 215–223.
86 A. W. Mohammad, Y. H. Teow, W. L. Ang, Y. T. Chung, D. L. Oatley-Radcliffe and N. Hilal, *Desalination*, 2015, **356**, 226–254.
87 M. Paul and S. D. Jons, *Polymer (Guildf).*, 2016, **103**, 417–456.
88 S. Yu, Y. Wang, F. Sun, R. Wang and Y. Zhou, *Chem. Eng. J.*, 2018, **337**, 183–192.
89 X. Shen, T. Zhang, P. Xu, L. Zhang, J. Liu and Z. Chen, *Appl. Catal. B Environ.*, 2017, **219**, 425–431.
90 P. Westerhoff, P. Alvarez, Q. Li, J. Gardea-Torresdey and J. Zimmerman, *Environ. Sci. Nano*, 2016, **3**, 1241–1253.
91 L. Zhu, C. Fu Tan, M. Gao and G. W. Ho, *Adv. Mater.*, 2015, **27**, 7713–7719.
92 Y. Mei, Y. Su, Z. Li, S. Bai, M. Yuan, L. Li, Z. Yan, J. Wu and L.-W. Zhu, *Dalt. Trans.*, 2017, **46**, 347–354.
93 F. Dufour, S. Pigeot-Remy, O. Durupthy, S. Cassaignon, V. Ruaux, S. Torelli, L. Mariey, F. Maugé and C. Chanéac, *Appl. Catal. B Environ.*, 2015, **174**–**175**, 350–360.
94 Y. H. Ding, X. L. Zhang, N. Zhang, J. Y. Zhang, R. Zhang, Y. F. Liu and Y. Z. Fang, *Dalt. Trans.*, 2017, **47**, 684–692.
95 W. Gu, F. Lu, C. Wang, S. Kuga, L. Wu, Y. Huang and M. Wu, *ACS Appl. Mater. Interfaces*, 2017, **9**, 28674–28684.
96 Y. Bi, H. Hu, S. Ouyang, G. Lu, J. Cao and J. Ye, *Chem. Commun.*, 2012, **48**, 3748–3750.
97 K. He, G. Chen, G. Zeng, A. Chen, Z. Huang, J. Shi, T. Huang, M. Peng and L. Hu, *Appl. Catal. B Environ.*, 2018, **228**, 19–28.

98 D. Rawat, V. Mishra and R. S. Sharma, *Chemosphere*, 2016, **155**, 591–605.
99 G. Odling and N. Robertson, *ChemPhysChem*, 2016, **17**, 2872–2880.
100 L. Zhang, C. G. Niu, G. X. Xie, X. J. Wen, X. G. Zhang and G. M. Zeng, *ACS Sustain. Chem. Eng.*, 2017, **5**, 4619–4629.
101 S. P. Sahu, S. L. Cates, H.-I. Kim, J.-H. Kim and E. L. Cates, *Environ. Sci. Technol.*, 2018, **52**, 2973–2980.
102 L. Hao, H. Huang, Y. Guo and Y. Zhang, *ACS Sustain. Chem. Eng.*, 2018, **6**, 1848–1862.
103 Z. Jiang, W. Wei, D. Mao, C. Chen, Y. Shi, X. Lv and J. Xie, *Nanoscale*, 2015, **7**, 784–797.
104 Y. Zhang, Z. Zhao, J. Chen, L. Cheng, J. Chang, W. Sheng, C. Hu and S. Cao, *Appl. Catal. B Environ.*, 2015, **165**, 715–722.
105 W. Deng, H. Zhao, F. Pan, X. Feng, B. Jung, A. Abdel-Wahab, B. Batchelor and Y. Li, *Environ. Sci. Technol.*, 2017, **51**, 13372–13379.
106 S. Lee and A. Mills, *Chem. Commun.*, 2003, 2366.
107 A. Mills and J. Wang, *J. Photochem. Photobiol. A Chem.*, 1999, **127**, 123–134.
108 D. Mitoraj, U. Lamdab, W. Kangwansupamonkon, M. Pacia, W. Macyk, N. Wetchakun and R. Beranek, *J. Photochem. Photobiol. A Chem.*, 2018.
109 F. Chen, Q. Yang, F. Yao, S. Wang, J. Sun, H. An, K. Yi, Y. Wang, Y. Zhou, L. Wang, X. Li, D. Wang and G. Zeng, *J. Catal.*, 2017, **352**, 160–170.
110 J. Huang, B. Jin, H. Liu, X. Li, Q. Zhang, S. Chu, R. Peng and S. Chu, 2018, 11424–11434.
111 N. Vela, M. Calín, M. J. Yáñez-Gascón, I. Garrido, G. Pérez-Lucas, J. Fenoll and S. Navarro, *J. Photochem. Photobiol. A Chem.*, 2018, **353**, 271–278.
112 D. Tian, H. Mao, H. Lv, Y. Zheng, C. Peng and S. Hou, *Chemosphere*, 2018, **192**, 362–371.
113 *Priority Substances and Certain Other Pollutants according to Annex II of Directive 2008/105/EC, European Commission Water Framework Directive*, 2016.
114 United States Environmental Protection Agency, *National Primary Drinking Water Regulations*, 2018.
115 X. C. Hu, D. Q. Andrews, A. B. Lindstrom, T. A. Bruton, L. A. Schaider, P. Grandjean, R. Lohmann, C. C. Carignan, A. Blum, S. A. Balan, C. P. Higgins and E. M. Sunderland, *Environ. Sci. Technol. Lett.*, 2016, **3**, 344–350.
116 C. M. G. Carpenter and D. E. Helbling, *Environ. Sci. Technol.*, 2018, **52**, 6187–6196.
117 U. J. Kim and K. Kannan, *Environ. Sci. Technol.*, 2018, **52**, 5625–5633.
118 C. Xu, L. Chen, L. You, Z. Xu, L.-F. Ren, K. Yew-Hoong Gin, Y. He and W. Kai, *Environ. Sci. Process. Impacts J. Name*, 2016, **18**, 1–3.
119 T. G. Schwanz, M. Llorca, M. Farré and D. Barceló, *Sci. Total Environ.*, 2016, **539**, 143–152.
120 Y. Shen, X. Yu, W. Lin, Y. Zhu and Y. Zhang, *Appl. Surf. Sci.*, 2017, **399**, 67–76.
121 J. guo Guo, Y. Liu, Y. juan Hao, Y. lei Li, X. jing Wang, R. hong Liu and F. tang Li, *Appl. Catal. B Environ.*, 2018, **224**, 841–853.
122 G. C. Behera, N. Biswal and K. Parida, *Catal. Today*, 2017, **284**, 84–91.
123 S.-F. Yang, C.-G. Niu, D.-W. Huang, H. Zhang, C. Liang and G.-M. Zeng, *Environ. Sci. Nano*, 2017, **4**, 585–595.
124 F. Wang, Y. Zhou, X. Pan, B. Lu, J. Huang and Z. Ye, *Phys. Chem. Chem. Phys.*, 2018, **20**, 6959–6969.
125 D. Liu, M. Zhang, W. Xie, L. Sun, Y. Chen and W. Lei, *Appl. Catal. B Environ.*, 2017, **207**, 72–78.
126 D. Liu, Z. Jiang, C. Zhu, K. Qian, Z. Wu and J. Xie, *Dalt. Trans.*, 2016, **45**, 2505–2516.
127 J. Zhang, L. Zhang, X. Shen, P. Xu and J. Liu, *CrystEngComm*, 2016, **18**, 3856–3865.

Chapter 2 Experimental

2.1 Overview

A great many techniques have been used to prepared, characterise and test the materials developed as part of this body of work. Generally, TiO_2 has been immobilised, and then modified post-deposition to form a composite immobilised photocatalyst. A brief description of the immobilisation technique used to coat TiO_2 onto each substrate is given, and a general description of the sequential ionic layer adsorption reaction (SILAR) method used in much of the enclosed work is discussed. Characterisation methods used to study the materials properties are not discussed, as the techniques used are well-established, and have been used in a way typical for the characterisation of solids. However, relevant equations and the instrumentation used to produce the characterisation data is given. The focus of this section will instead be the immobilisation and modification methods, photocatalytic testing set ups and metrics used to quantify photocatalytic activity that have been applied in this work.

2.2 TiO_2 Immobilisation Techniques & Corresponding Reactors

Three reactor systems have been used to measure photocatalytic activity, with three corresponding methods by which TiO_2 has been immobilised on different substrates. Once immobilised, these coated systems were typically post-modified in different ways to improve activity, which will be covered in a later section.

2.2.1 Glass Plate System

Coating layers of photocatalytic material on flat glass plates is an oft-used method by which an immobilisation of an active material can be achieved[1,2]. In this work one method which was applied is the doctor blading of TiO_2 onto glass plates using a procedure known as doctor blading, in much the same way which is well-established in the dye-sensitised and perovskite solar cell field[3]. In brief, a viscous slurry of TiO_2 is cast between two spacers by passing a squeegee with an appropriate amount of slurry over the top, depositing the slurry between the spacers. The spacers can then be removed leaving the TiO_2 slurry which is then dried and fired at high temperature to

give the TiO_2 film adhered to the glass plate. The general process is shown schematically in Figure 2.1.

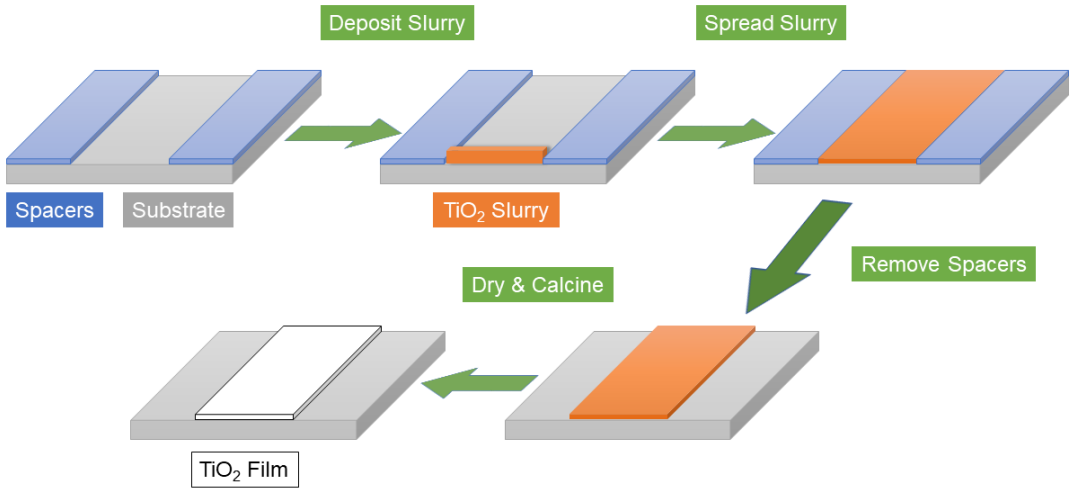

Figure 2.1. Doctor blading method to deposit TiO_2 films onto a substrate surface.

Flat plates coated in this way with TiO_2 were immersed in a pollutant solution in a standard UV-vis quartz cuvette and irradiated from the side as shown in Figure 2.2.

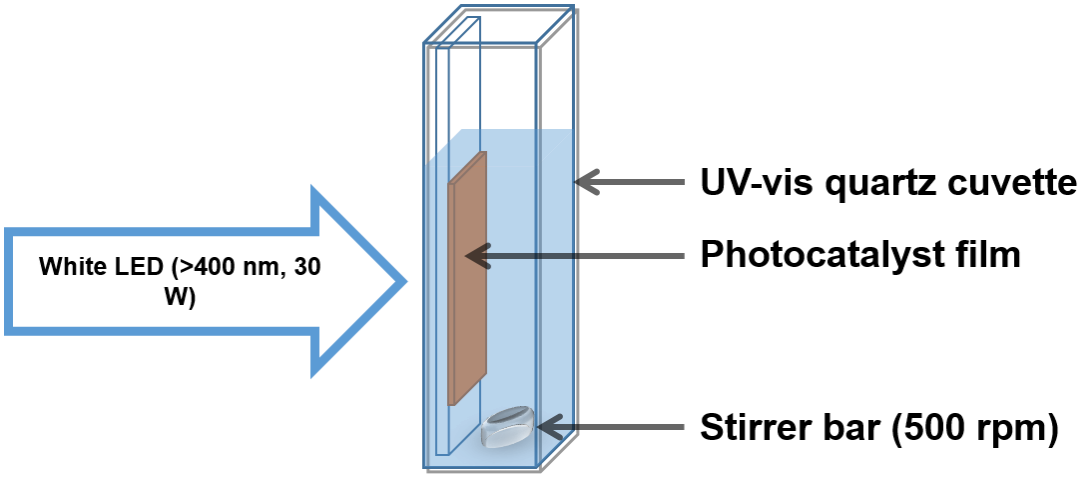

Figure 2.2. Set up used to test photocatalysts immobilised on glass plates

The films applied in this way were irradiated from the back side using a small white LED light fitted with a 400 nm long-pass filter. In this way this set up was used to test materials activity against pollutants under visible only irradiation.

2.2.2 Glass Bead Systems

To improve the versatility of the photocatalyst towards non-regular containers, photocatalyst materials were deposited on glass beads. To deposit TiO_2 onto the bead surface a dip-coating method was applied using a TiO_2 suspension. In brief, glass beads were immersed in the suspension and the excess suspension removed before drying and annealing. This process was typically carried out multiple times to build up the quantity of TiO_2 on the bead surface. The general process is described in Figure 2.3.

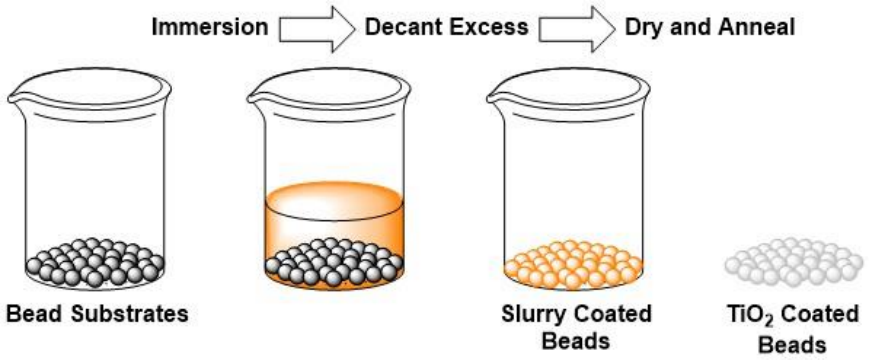

Figure 2.3. Bead coating process used to prepare TiO_2 coated glass beads

Initially a water based suspension containing surfactants to reduce aggregation of the TiO_2 nanoparticles was used according to the procedure reported by Chiou *et al*.[4] These beads were loaded into a column type reactor with a particular pollutant and irradiated from the side using a 400 W halogen lamp as shown in Figure 2.4.

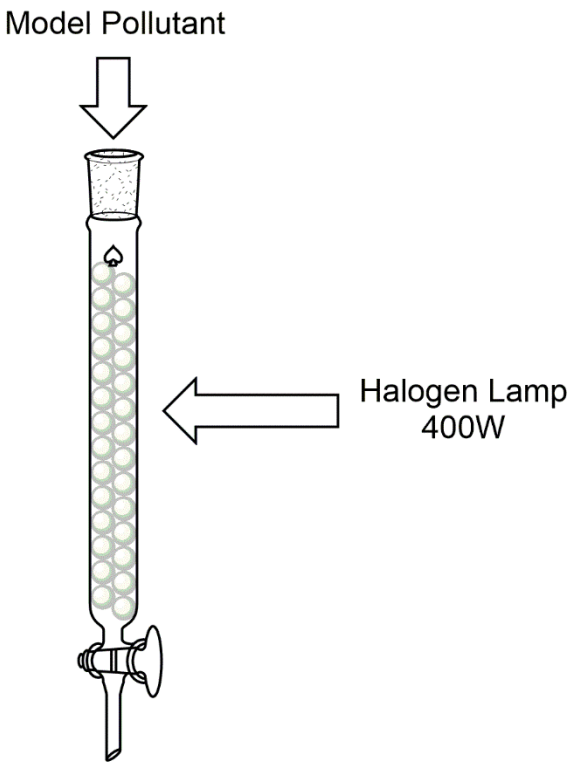

Figure 2.4. Column type reactor used in the testing of glass bead photocatalysts

The halogen lamp used produced a broad spectrum of light from ~300 nm into the IR. Tungsten lamps such as the one used in this work have been used as approximations to the solar spectrum, albeit with the use of filters[5]. This method was therefore used to test using a mixture of UV and visible light, as an approximation to solar irradiation.

Improvements were made to the coating process by switching to a P25 enriched TiO_2 sol system, a concept which was first described by Balasubramabian *et al.*[6], giving a much more robust TiO_2 layer. Using this updated coating procedure, a new reactor/lamp set up was designed using a bed of beads surrounding central stirrer as shown in Figure 2.5.

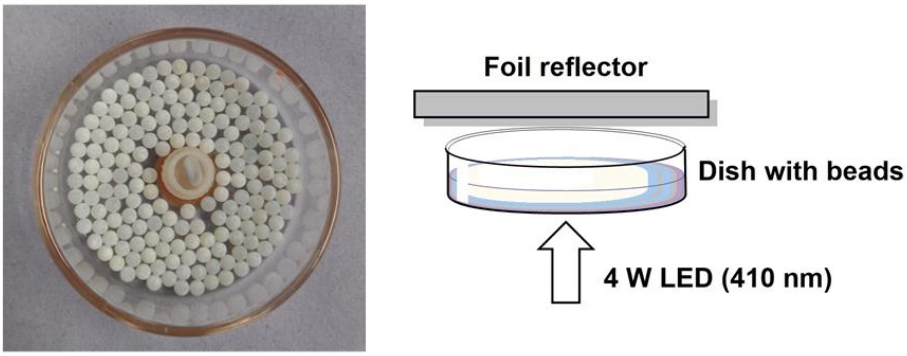

Figure 2.5. Left) View of dish reactor from above. Right) Schematic showing irradiation direction and reflector.

This set up was used in conjunction with a 410 nm LED array consisting of two banks of five LEDs producing 2 W of radiant flux each. Thus, the LEDs have irradiance on the UV-visible border and were used to test materials absorbing in this region.

2.3 Modification Using SILAR

Much of the work contained within this thesis focuses on the use of SILAR modification of the basic TiO_2 coatings to produce modified TiO_2 with a view to improving its activity. SILAR arose in the mid-1980s as a method of depositing thin sulfide or oxide films[7,8]. What differentiates SILAR from a regular chemical bath deposition is the use of alternating cation and anion baths, giving a great deal of control over the deposition conditions, in principal allowing layer by layer growth of the material on the substrate. A schematic representation of a typical SILAR process is given in Figure 2.6.

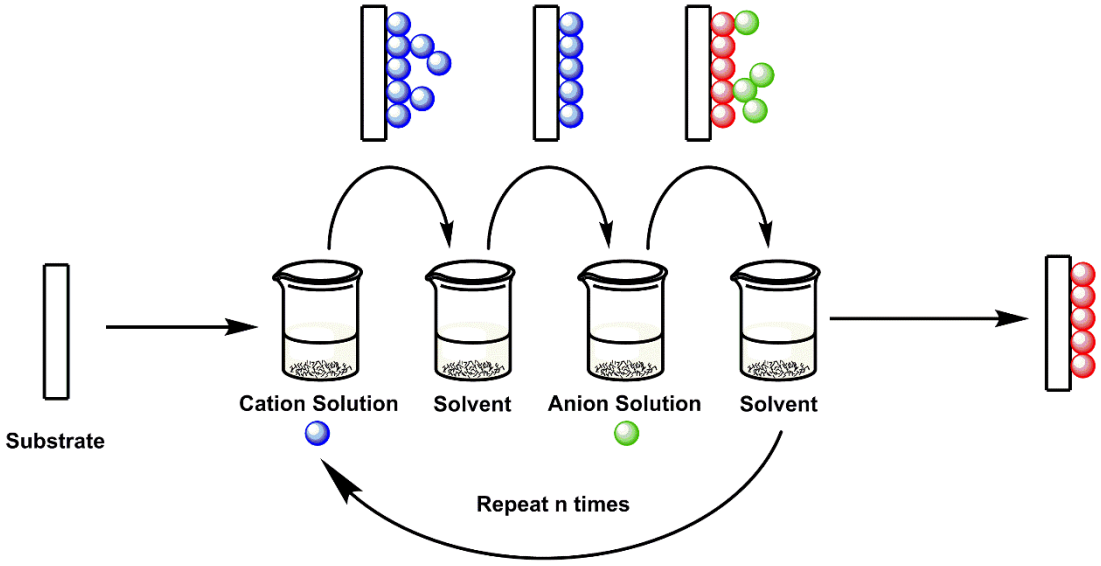

Figure 2.6. Schematic of the SILAR process, Blue spheres = cations, green spheres = anions, red spheres = reacted material.

While this process can be simply applied to flat substrates (as shown in Figure 2.6) by moving the substrate between solutions, the same technique can be applied by keeping the substrate stationary and sequentially passing solutions over the substrate surface, which has been used to modify coated bead samples in a column type system. A general description of this process is given in Figure 2.7.

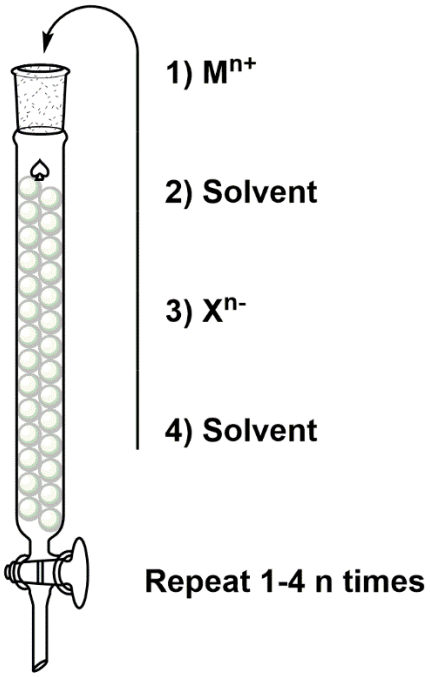

Figure 2.7. SILAR on a bead system, where beads are kept stationary and solutions are passed in sequence through the column

SILAR has many advantages in the preparation or modification of films despite its simplicity:

- The lack of a vacuum or high purity metal target precursors which are typically used in a sputtering or vapor deposition reduces the set-up complexity and therefore costs significantly for SILAR over vacuum techniques.
- Dopants are easily introduced by simply including a small amount of the dopant in the cation or anion bath solutions.
- Deposition temperature are generally low, allowing a variety of different substrates (glass, plastics, metals).
- Easily automatable, which aids in scalability.

These features have allowed SILAR to garner considerable interest in the field of solar cells[9–11]. However, for the purposes of photocatalysis, SILAR is relatively unexplored.

2.4 Test Metrics

To assess photocatalytic efficiencies, two methods have been used; kinetic analysis using the observed first order rate constant and the final overall degradation percentage.

2.4.1 Langmuir-Hinshelwood Kinetic Model

The most commonly applied kinetic model to the degradation of organic pollutants via semiconductor photocatalysis is the Langmuir-Hinshelwood model[12–14]. This is a general model for an adsorbed species on a catalyst surface, but has been shown to be effective in modeling photocatalytic degradation reactions. The model assumes fast adsorption of reactants followed by a single slow surface reaction, which can be described as shown:

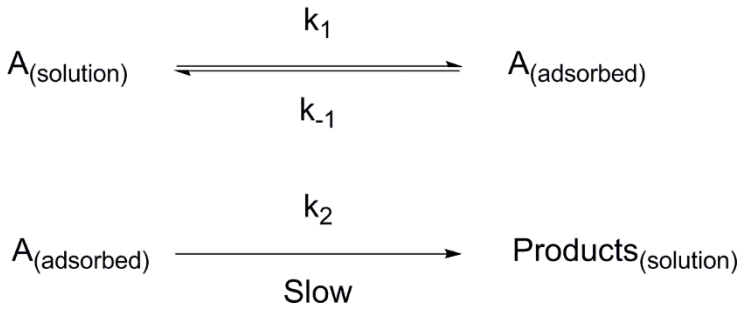

Hence the reaction rate can be described by as shown:

$$-r_A = k_{LH}\theta_A$$

Where r_A is the rate of degradation, k_{LH} is the Langmuir-Hinshelwood rate constant and θ_A is the fractional coverage of A on the catalyst surface, which can be described as shown:

$$\theta_A = \frac{\frac{k_1}{k_{-1}}C_A}{1 + \frac{k_1}{k_{-1}}C_A}$$

Where k_1/k_{-1} is the adsorption equilibrium constant (K_{ads}) and C_A is the concentration of A. Therefore, the rate equation can be expressed as:

$$-r_A = k_{LH} \frac{K_{ads} C_A}{1 + K_{ads} C_A}$$

This expression can be further simplified as in a typical photodegradation reaction the polluting species A is in a very low concentration, such that $K_{ads}C_A << 1$, and k_{LH} and K_{ads} are normally combined into a single apparent rate constant k_{app}, and the equation becomes a classic 1st order rate equation:

$$-r_A = \frac{dC_A}{dt} = k_{app} C_A$$

This may be integrated to give:

$$-\ln \frac{C_A}{C_{A0}} = k_{app} t$$

Where C_{A0} is the initial concentration of the pollutant. From this stage it is trivial to extract k_{app} for the process.

It should be noted that while this relationship is commonly used as above for determination of photocatalytic rate determination, that the intensity of light plays an inherent role in photocatalytic processes. According to Chen *et al.*[15], for a constantly irradiated photocatalytic system, the Langmuir-Hinshelwood mechanism can be modified with a term for light intensity as shown:

$$-\ln \frac{C_A}{C_{A0}} = I^m k_{app} t$$

Where I^m is the reaction order of the light intensity and all other terms are as defined above. Work by Ollis *et al.*[16] has shown that at low light intensities (<80 W m^{-2}) this order is near 1, and rates increase linearly with light intensity, however at higher intensity the order m drops to 0 as electron-hole recombination processes dominate due to exciton saturation. However, the unmodified Langmuir-Hinshelwood equations

are used predominantly in the literature as light intensities are typically high enough that the intensity term can be ignored. Throughout this work the intensity of light is high, and therefore not considered and the normal Langmuir-Hinshelwood expression used to compare the effectiveness of the prepared photocatalysts.

2.4.2 Degradation Efficiency

A simpler metric often used is the final overall degradation efficiency percentage. Degradation efficiency (DE) is calculated according to the following equation:

$$DE = \left(1 - \frac{C}{C_0}\right) \times 100$$

Where C is the concentration of the pollutant after irradiation and C_0 is the initial concentration. DE is therefore the amount of model pollutant destroyed expressed as a percentage. Such a test is used particularly where a testing method is destructive, such that multiple time points cannot be measured.

2.4.3 Mechanism Determination Experiments

Scavenging for certain reactive oxygen species key in the photocatalytic degradation of organic pollutants is an oft-used method to probe the photocatalytic mechanism[17]. Introduction of a relatively large quantity of an interfering molecule which is known to interact with a certain reactive species can be used to soak up these species, effectively removing them from the reaction with the model pollutant in question. In this work, three scavenging species have been applied; methanol, *tert*-butanol and degassing using N_2. Addition of methanol is a known electron donor, and as such has been used to scavenge for photogenerated holes[18]. *tert*-butanol as a molecule which is resistant to oxidation has been applied as a selective scavenger for the highly oxidising hydroxyl radical[19]. Degassing with N_2 is a common technique used to force O_2 from a sample, and therefore is used to shut down electron transfer to O_2 to form superoxide[20].

2.4.4 Chemical Oxygen Demand

An example where degradation efficiency must be used is in the determination of chemical oxygen demand (COD). It is typical to use UV-visible spectrophotometry to

determine photocatalytic efficiencies. In most cases this is sufficient to assess activity as a blank UV absorption spectrum of a pollutant solution is indicative of near complete degradation, where most of the large pi systems responsible for absorption in the UV have been destroyed. However small degradation fragments such as methanol that have no absorption can remain. To overcome this limitation, COD titration is used. COD operates on the principle that using a sufficiently powerful oxidising agent such as acidified dichromate solution, any organic material can be converted to CO_2 according to the following equation:

$$C_nH_aO_bN_c + dCr_2O_7^{2-} + (8d + c)H^+ \rightarrow nCO_2 + \frac{a+8d-3c}{2}H_2O + cNH_4^+ + 2dCr^{3+}$$

COD is therefore used as a useful indicator of overall total degradation. It is often found that that COD measurements lag behind the degradation measured by absorption spectroscopy[21-23] due to the destruction of the chromophore being usually several oxidation steps removed from full mineralisation[24].

2.4.5 Bactericidal Activity Determination

In addition to testing against organic molecules, the removal of viable bacterial content can be investigated. *Escherichia coli (E. coli)* is used as a marker for bacterial content in contaminated of water,[25] and is the most commonly studied model bacterial pollutant. The process of determination of bactericidal activity involves the growth of *e.coli* colonies on nutrient agar plates from contaminated water samples. Often after an appropriate serial dilution, the number of *e.coli* colonies can be determined simply by counting the distinct colonies grown on the plate, giving the number of colony forming units (CFU) in the sample. A reduction in the number of CFU can be ascribed to photocatalytic damage to the *e.coli* sufficient enough to prevent growth into a colony. An example photograph of an agar plate with *e.coli* colonies grown on the surface is given in Figure 2.8.

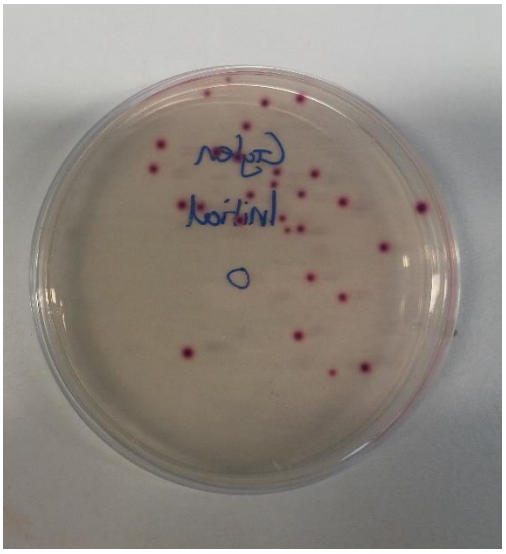

Figure 2.8. Example agar plate with e.coli colonies grown on the surface

In this work, an agar specific to *e.coli* has been used and as such colonies form as dark red spots on the agar surface as can be seen in Figure 2.8. The disinfection kinetic metric used is according to the Chick-Watson model[26], which takes the same form as the 1st order degradation of organic pollutants as per the Langmuir-Hinshelwood model. The equation is below:

$$log\frac{N}{N_0} = -kt$$

Where N/N_0 is the fraction of the original CFU present at a particular time, k is the disinfection kinetic constant, and t is the irradiation time. When large sample volumes are not available, the overall final disinfection percentage can also be calculated in a way analogous to degradation efficiency of organic pollutants, substituting the concentration values for CFU.

2.5 Electrochemical & Optical Relationships

Beyond the rate equations used to determine photocatalytic efficiency, two others have been used in the characterisation of the prepared materials; the Mott-Schottky equation, and the Tauc plot and Kubelka Munk equation. These two concepts are discussed briefly below.

2.5.1 Diffuse Reflectance: The Kubelka Munk Equation & Tauc Plot

Diffuse reflectance is a technique used to obtain optical band gap values from solid samples[27], where transmission absorption experiments are not viable. The Kubelka-Munk function quantifies the absorption (K) and scattering (S) of the sample as shown:

$$F(R_\infty) = \frac{(1 - R_\infty)^2}{2R_\infty} = \frac{K}{S}$$

Where $F(R_\infty)$ is the Kubelka-Munk function and R_∞ is the reflectivity of the sample (i.e. the outgoing flux divided by the ingoing flux) as a percentage. Measuring the reflectivity of the sample at various wavelengths can therefore be used to obtain the Kubelka-Munk quantity as a function of wavelength.

This quantity can be applied in a Tauc plot to obtain the band gap[28] as shown:

$$(F(R_\infty)h\nu)^{\frac{1}{n}} = A(h\nu - E_g)$$

Where h is Planck's constant, ν is frequency of incident light, A represents the tailing of the onset of the absorption determined by the transmission of the sample, and E_g is the band gap. The band gap can therefore be obtained plotting $(F(R_\infty)h\nu)^{\frac{1}{n}}$ against energy. n in this case denotes whether the transition is direct or indirect, with n = 0.5 for direct transitions and n = 2 for indirect transitions. Extrapolation of the linear portion of the onset to the x-axis (i.e. where $(F(R_\infty)h\nu)^{\frac{1}{n}} = 0$) therefore gives the band gap E_g.

2.5.2 Electrochemical Impedance Spectroscopy: Mott-Schottky Analysis

Mott-Schottky analysis uses the electrochemical depletion layer that exists at the surface of a semiconductor material in contact with an electrolyte solution to gauge band energies for n- or p-type materials[29]. In brief, Mott-Schottky analysis measures the capacitance caused by band bending at the semiconductor-electrolyte interface by treating the space-charge region as a parallel plate capacitor[30]. This can be used to

calculate the flat band potential (i.e. the potential where no band bending occurs) according to the following equation:

$$\frac{1}{C^2} = \frac{2}{e\varepsilon\varepsilon_o N_d}(E - E_{fb} - \frac{k_b}{T})$$

Where C is the capacitance of the space-charge region, ε is the dielectric constant of the material, ε_o is the permittivity of a vacuum, N_d describes the charge carrier density, E describes the applied potential, E_{fb} is the flat band potential and k_b/T describes thermal energy, which is considered to be small enough to be safely ignored. Thus, upon sweeping across a potential range, $1/C^2$ will rise when a depletion layer forms, and therefore the flat band potential can be obtained by extrapolating a plot of $1/C^2$ against potential to the x-axis. For n-type semiconductors (such as TiO_2), the flat band is estimated to be around 0.1 eV below the conduction band, and as such can be used to gauge the conduction band energy[31].

2.6 Instrumentation

X-ray diffraction studies were performed using a Bruker D2 phaser or a STOE STADI P diffractometer operated in capillary Debye–Scherrer mode, diffraction traces from both instruments were collected using monochromated CuKα radiation. UV-vis diffuse reflectance, transmission and solution measurements were made using a JASCO V-670 spectrophotometer with an integrating sphere attachment or transmission attachment as appropriate. SEM images were collected using a Carl Zeiss SIGMA HD VP Field Emission SEM, operated in secondary electron or InLens mode with a 10 keV accelerating voltage. SEM-EDS measurements were made on the same instrument, using an Oxford AZtec ED X-ray analysis set up with accelerating voltages ranging from 10 keV to 20 keV. ICP-MS analysis was then performed on an Agilent 7500ce ICP-MS system. Inductively coupled plasma optical emission spectroscopy analysis was carried out on a PerkinElmer Optima 5300 DV ICP-OES. Solutions for ICP-OES and ICP-MS analysis were obtained by dissolving the materials in concentrated nitric acid before dilution to give a 3 vol% HNO_3 solution. Photoluminescence measurements were carried out using a Horiba Jobin Yvon Fluoromax-3. A fibre optic attachment was used arranged such that the excitation

source was angled at 45° to the sample and the detector fibre optic at 90°. TEM images were captured with a FEI Titan Themis electron microscope, a JEOL 2100F FEG TEM, or a JEM-2011 TEM. Element maps were collected using either the FEI Titan Themis electron microscope or JEOL 2100F FEG TEM operated in STEM mode. X-ray photoelectron spectroscopy measurements were carried out using an Scienta 300 XPS spectrometer or a Kratos Analytical AXIS Nova instrument, both of which were operating using monochromated 1486.6 eV Al Kα irradiation. The C 1s peak due to adventitious carbon was used as a calibration peak by alignment to 284.8 eV. Mott–Schottky analyses were performed using an Metrohm Autolab PGSTAT30 with FRA software to control a standard three electrode setup. A Ag/AgCl reference electrode and Pt wire counter electrode were used, with the film constituting the working electrode, the electrolyte used in all cases was 0.05M Na_2SO_4.

2.7 References

1 I.-K. Ding, J. Melas-Kyriazi, N.-L. Cevey-Ha, K. G. Chittibabu, S. M. Zakeeruddin, M. Grätzel and M. D. McGehee, *Org. Electron.*, 2010, **11**, 1217–1222.

2 G. Peng, L. Xing, J. Barrio, M. Volokh and M. Shalom, *Angew. Chemie Int. Ed.*, 2018, **57**, 1186–1192.

3 S. Tang, Y. Deng, X. Zheng, Y. Bai, Y. Fang, Q. Dong, H. Wei and J. Huang, *Adv. Energy Mater.*, 2017, **7**, 1700302.

4 C.-S. Chiou, J.-L. Shie, C.-Y. Chang, C.-C. Liu and C.-T. Chang, *J. Hazard. Mater.*, 2006, **137**, 1123–1129.

5 J. A. McMillan and E. M. Peterson, *Sol. Energy*, 1979, **22**, 467–469.

6 G. Balasubramanian, D. D. Dionysiou, M. T. Suidan, V. Subramanian, I. Baudin and J.-M. Laîné, *J. Mater. Sci.*, 2003, **38**, 823–831.

7 T. P. Niesen and M. R. De Guire, in *Solid State Ionics*, 2002, vol. 151, pp. 61–68.

8 V. P. Tolstoi, *Russ. Chem. Rev.*, 1993, **62**, 237–242.

9 Y. Jin-nouchi, S. Naya and H. Tada, *J. Phys. Chem. C*, 2010, **114**, 16837–16842.

10 N. Guijarro, T. Lana-Villarreal, T. Lutz, S. A. Haque and R. Gómez, *J. Phys. Chem. Lett.*, 2012, **3**, 3367–3372.

11 S. S. Mali, R. S. Devan, Y.-R. Ma, C. A. Betty, P. N. Bhosale, R. P. Panmand, B. B. Kale, S. R. Jadkar, P. S. Patil, J.-H. Kim and C. K. Hong, *Electrochim. Acta*, 2013, **90**, 666–672.

12 A. V. Emeline, V. K. Ryabchuk and N. Serpone, *J. Phys. Chem. B*, 2005, **109**, 18515–18521.

13 A. Mills, J. Wang and D. F. Ollis, *J. Phys. Chem. B*, 2006, **110**, 14386–14390.

14 D. F. Ollis, *J. Phys. Chem. B*, 2005, **109**, 2439–2444.

15 H.-W. Chen, Y. Ku and A. Irawan, *Chemosphere*, 2007, **69**, 184-190

16 D. Ollis, E. Pelizzetti and N. Serpone, *Environ. Sci. Technol.*, 1991, **25**, 1523-1529

17 Y. Nosaka and A. Y. Nosaka, *Chem. Rev.*, 2017, **117**, 11302–11336.

18 M. Shen and M. A. Henderson, *J. Phys. Chem. Lett.*, 2011, **2**, 2707–2710.

19 J. Kim, C. W. Lee and W. Choi, *Environ. Sci. Technol.*, 2010, **44**, 6849–6854.

20 Y. Jin, D. Jiang, D. Li and M. Chen, *Catal. Sci. Technol.*, 2017, **7**, 2308–2317.

21 S. Sakthivel, B. Neppolian, M. V. Shankar, B. Arabindoo, M. Palanichamy and V. Murugesan, *Sol. Energy Mater. Sol. Cells*, 2003, **77**, 65–82.

22 I. A. Alaton and I. A. Balcioglu, *J. Photochem. Photobiol. A Chem.*, 2001, **141**, 247–254.

23 M. Y. Ghaly, J. Y. Farah and A. M. Fathy, *Desalination*, 2007, **217**, 74–84.

24 M. Czaplicka, *J. Hazard. Mater.*, 2006, **134**, 45–59.
25 O. CARP, *Prog. Solid State Chem.*, 2004, **32**, 33–177.
26 J. Marugán, R. van Grieken, C. Sordo and C. Cruz, *Appl. Catal. B Environ.*, 2008, **82**, 27–36.
27 A. A. Kokhanovsky, *J. Phys. D. Appl. Phys.*, 2007, **40**, 2210–2216.
28 A. H. Slavney, T. Hu, A. M. Lindenberg and H. I. Karunadasa, *J. Am. Chem. Soc.*, 2016, **138**, 2138–2141.
29 M. Grätzel, *Nature*, 2001, **414**, 338–344.
30 T. Kirchartz, W. Gong, S. a. Hawks, T. Agostinelli, R. C. I. MacKenzie, Y. Yang and J. Nelson, *J. Phys. Chem. C*, 2012, **116**, 7672–7680.
31 H. Huang, H. Huang, D. Li, D. Li, Q. Lin, Q. Lin, Y. Shao, Y. Shao, W. Chen, W. Chen, Y. Hu, Y. Hu, Y. Chen, Y. Chen, X. Fu and X. Fu, *J. Phys. Chem. C*, 2009, **113**, 14264–14269.

Chapter 3 Wide Band Gap Composites

3.1 Overview

Contained within this chapter is a report of two composites including their preparation, characterisation and application for photocatalysis against a variety of pollutants. The materials described within this section are UV or high energy visible absorbers, and thus their combination with TiO_2 mainly aims to address improvements to charge separation, with some slight sensitisation to visible light. The two materials chosen for this purpose are bismuth titanate ($Bi_4Ti_3O_{12}$, BTO) and Lanthanum vanadate ($LaVO_4$, LVO), which have been formed on TiO_2 using SILAR.

3.2 Bismuth Titanate – TiO_2 Composites I: Materials Development & Initial Photocatalytic Testing

3.2.1 Introduction

The use of TiO_2 as a photocatalyst is limited due to low activity under visible light and recombination of photo-generated charges, which have been found to be orders of magnitude faster than the desired surface reactions[1,2]. Most of the photo-excited holes and electrons in pure TiO_2 recombine before being able to generate any useful reactive species. One method by which TiO_2 can be given both visible light activity and a mechanism to allow charges to separate is to form a heterojunction with another, narrower band gap semiconductor[3]. The narrower band gap allows excitation by visible light, and the interface between the two materials allows charges to be separated in space and therefore recombination is hindered. Bismuth based semiconductors have been suggested as potential materials for this purpose due to the low cost and low toxicity of bismuth. Of interest are the Aurivillius structured bismuth containing semiconductors such as $BiVO_4$[4], Bi_2MoO_6[5], Bi_2WO_6[6] and $Bi_4Ti_3O_{12}$[7]. These materials are characterised by their layered structure with perovskite layers of $(A_{n-1}B_nO_{3n+1})^{2-}$ sandwiched between layers of bismuth oxide $(Bi_2O_2)^{2+}$[8]. An example of this BTO with this structure is shown in Figure 3.1.

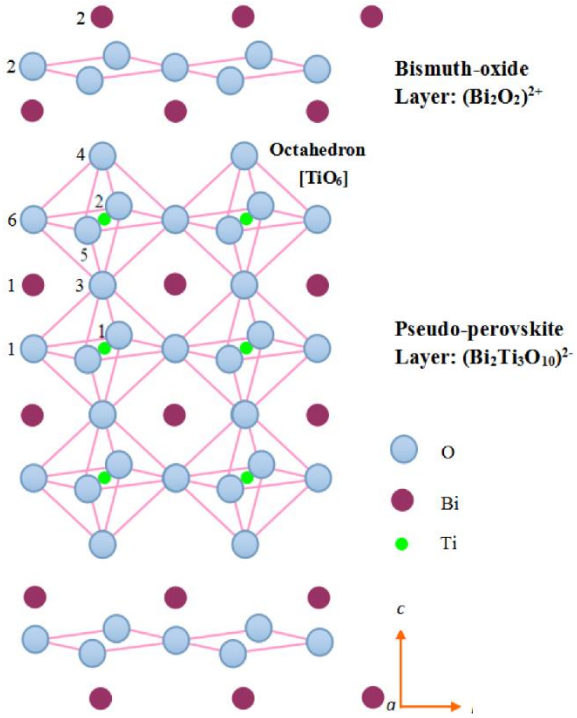

Figure 3.1. Aurivillius structure of BTO adapted from the work of Chen et al.[9]

Such materials have been proven to have interesting luminescent, dielectric and ion conductive properties[10], but have rarely been combined with TiO_2 for photocatalytic purposes to date.

In this section the formation of a composite photocatalyst comprised of the Aurivillius semiconductor BTO and TiO_2 is described. Using TiO_2 immobilised on glass bead substrates as a basis, SILAR has been used as a method to introduce a BiOBr precursor. Upon heating, it has been discovered that this BiOBr precursor is converted to BTO along with the concurrent loss of Br. Recently, Zhang *et al.* demonstrated a similar modification by epitaxial growth of BTO on the anatase TiO_2 [001] surface[11]. This was achieved by hydrothermal modification of anatase with exposed [001] facets with $Bi(NO_3)_3$. However, to date this conversion from BiOBr to BTO has not been reported, and represents something of an anomaly in preparation of more complex semiconductors by SILAR. Typically, SILAR is restricted to simple binary chalcogenides[12,13], and would not be thought of as a potential method to prepare a titanate semiconductor due to the insolubility of the titanate anion.

In addition to a thorough investigation of the conversion from $BiOBr/TiO_2$ to $BTO\text{-}TiO_2$, the electronic structure of the heterojunction formed has been investigated by valence band XPS and diffuse reflectance measurements, and a plausible band structure proposed. The immobilised composites have then been applied to the photocatalytic degradation of a variety of different organic pollutants as well as bactericidal testing, and the applicability of the system investigated by stability tests and identification of the key reactive species.

3.2.2 Results & Discussion

3.2.2.1 Photocatalyst Preparation

The general fabrication process for the coated bead samples is given in Figure 3.2.

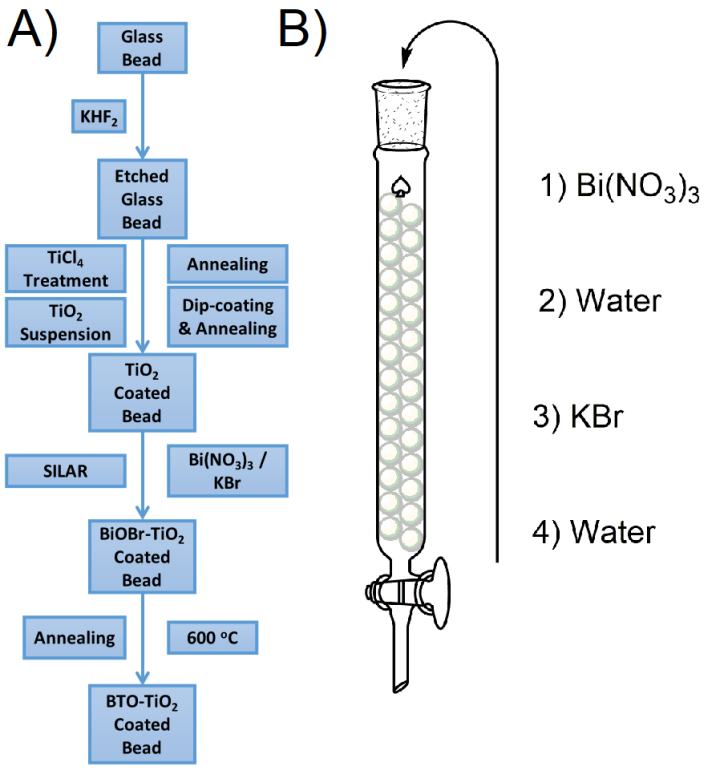

Figure 3.2. A) Process of producing the $BTO\text{-}TiO_2$ coated glass beads. B) SILAR processing method used to deposit the $BiOBr$ precursor onto the TiO_2 surface

The beads are first etched to provide a roughened surface to which TiO_2 particles are well adhered. A sample SEM image of the bead surface post-etching is given in Figure 3.3.

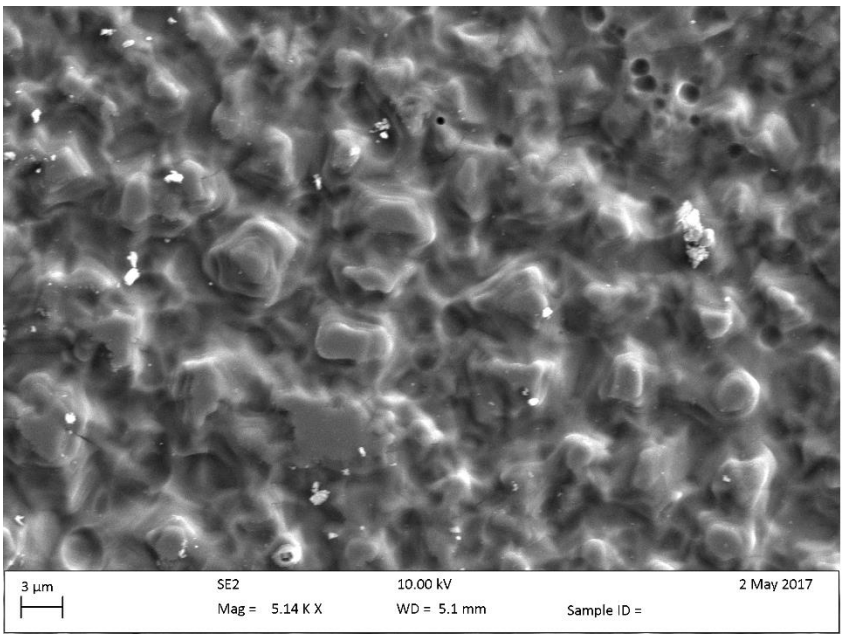

Figure 3.3. SEM image of the bead surface post-etching

Once roughened, a TiO_2 coating is applied by firstly treatment with a solution of $TiCl_4$, and then immersion in a water based suspension of P25 as reported by Arabatzis *et al.*[14] and described earlier in the experimental section. BiOBr SILAR is then carried out by packing the TiO_2 coated beads into a column and sequentially passing solutions of $Bi(NO_3)_3$ and KBr through as shown in Figure 3.2b. This SILAR process was repeated between 3 and 9 times to give different amounts of the BiOBr precursor, which after a final annealing step gave BTO-TiO_2 coated beads. The samples will henceforth be named NxBTO, where N is the number of SILAR cycles used upon the beads. While the beads were used exclusively for the photocatalytic testing, much of the analysis requires a flat surface to be carried out, therefore the same process was applied to microscope slides for some of the analytical measurements.

3.2.2.2 Materials Characterisation

3.2.2.2.1 X-ray Diffraction

X-ray diffraction (XRD) traces of the pristine TiO_2 and BTO-TiO_2 samples are given in Figure 3.4a.

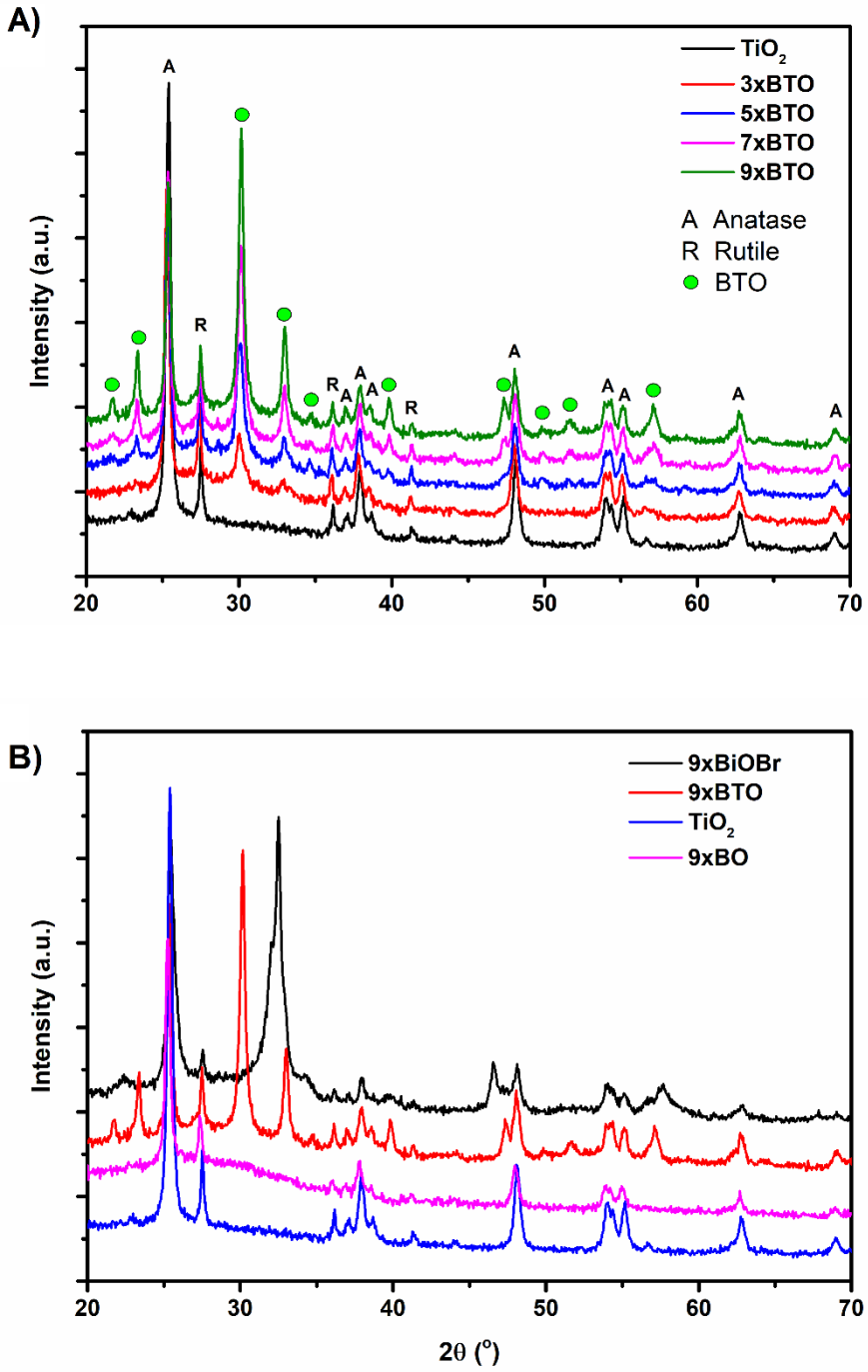

Figure 3.4. A) XRD trace changes on different levels of BTO modification. B) Comparison of precursor and different similar materials to BTO

Due to P25 being the source of TiO_2 used, a mixture of anatase and rutile phase TiO_2 was found in the pristine TiO_2 sample. Upon SILAR modification and annealing, a variety of new peaks appeared, which can be assigned to the orthorhombic aurivillius

structure of BTO (JCPDS card #35-795). These peaks were found to increase in intensity as the number of SILAR cycles increased, corresponding to the formation of larger amounts of BTO. Two major peaks were observed at 2θ values of 30.2 and 33.0 corresponding to the [171] and [200] planes of BTO respectively[15]. Other bismuth titanate phases such as $Bi_2Ti_2O_7$ and $Bi_{12}TiO_{20}$ have been previously reported, however peaks for these phases[16,17] were not observed, indicating a single pure phase of $Bi_4Ti_3O_{12}$. Further smaller peaks were also observed and assigned as shown in Figure 3.4a. For comparison, XRD traces of a BiOBr-TiO_2 sample (9xBiOBr) before annealing and a Bi_2O_3 sample (9xBO) prepared by a previously reported SILAR method[18] were measured as shown in Figure 3.4b. The prepared BTO-TiO_2 was found to share no peaks with the BiOBr and Bi_2O_3 comparison materials, indicating that the preparation method used to generate BTO is indeed forming a distinct phase. The intensity of the major TiO_2 peaks were found to decrease on increased number of SILAR cycles, indicating the conversion of some TiO_2 into BTO. Interestingly, certain TiO_2 peaks were observed to decrease more than others. A summary of the peak areas obtained from the XRD traces is given in Table 3.1.

Table 3.1 – Peak area changes on BTO modification of P25

Sample	Peak Areas (a.u.)			
	Anatase [101]	Rutile [110]	Rutile [101]	Rutile [200]
P25	1836	176	53	415
3xBTO	1260	199	62	352
5xBTO	1036	171	81	316
7xBTO	1065	161	75	346
9xBTO	940	124	47	355

The intensity of the [101] anatase peak at a 2θ value of ~25.4^o was around one half the area for the 9xBTO sample compared with the pristine TiO_2. Conversely, the area of

the main [110] rutile peak at ~27.5^{o} and the smaller [101] peak at ~ 36.1^{o} were found to be largely unaffected. A very small decrease was noted for the anatase [200] peak at 48.1^{o}. All other observed peaks were found to be unaffected by the formation of BTO. Therefore, it can be concluded that BTO is being formed mostly from the [101] plane of anatase TiO_2. It is known that the [101] surface is the most thermodynamically stable facet of anatase, with many studies having been undertaken to investigate reactivity on this facet[19]. It is possible that BTO has formed with the consumption of titanium from anatase surfaces of this facet predominantly due to preferred deposition of the BiOBr precursor on this facet. These findings contrast with the conclusions of Zhang et al, who used a hydrothermal modification of Bi onto anatase with exposed [001] facets[11]. In their study, it was concluded that BTO would not form on the anatase [101] facet, and would preferentially form on their exposed [001] facet due to lattice matching. Zhang et al were however unsuccessful in using their hydrothermal method to deposit BTO on P25, which they concluded was due to the mis-match of BTO with the exposed anatase [101] facet in P25. In this work, it has been demonstrated that it is indeed possible to grow BTO from this facet when going via a SILAR BiOBr/thermal annealing route. In addition, the crystallinity of the BTO material formed in this route is significantly higher than that demonstrated by Zhang et al, a factor which has been demonstrated to be very significant in photocatalysis[20,21].

3.2.2.2.2 Electron Microscopies

Both scanning electron microscope (SEM) images of the intact TiO_2 bead surface, and transmission electron microscope (TEM) images of the nanomaterials removed from the surface were used to investigate the morphological features of the material.

Under investigation using SEM imaging, a porous network of particles could be observed with particle sizes of around 20-30 nm for the pristine TiO_2 sample (Figure 3.5a). Upon modification with BTO, the particles appear to increase in size somewhat to ~50-100 nm, and the gaps between the particles widen significantly (Figure 3.5b).

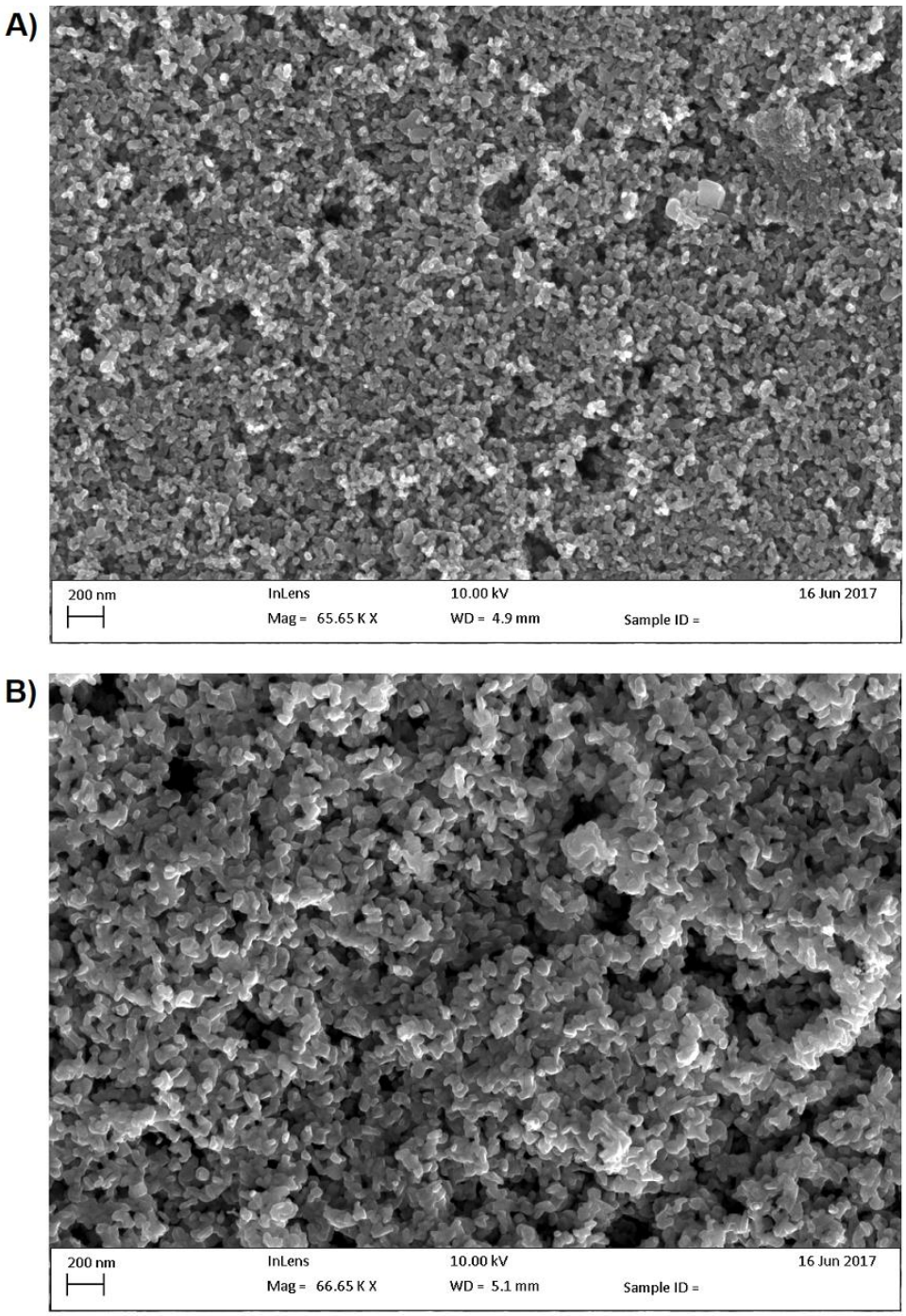

Figure 3.5. A) SEM image of the unmodified P25. B) SEM image of the 7xBTO bead surface.

No obvious interface between the BTO and TiO_2 materials was observed however at this magnification. Energy dispersive X-ray spectroscopy (EDX) was used to identify the elements present in the coatings (Figure 3.6).

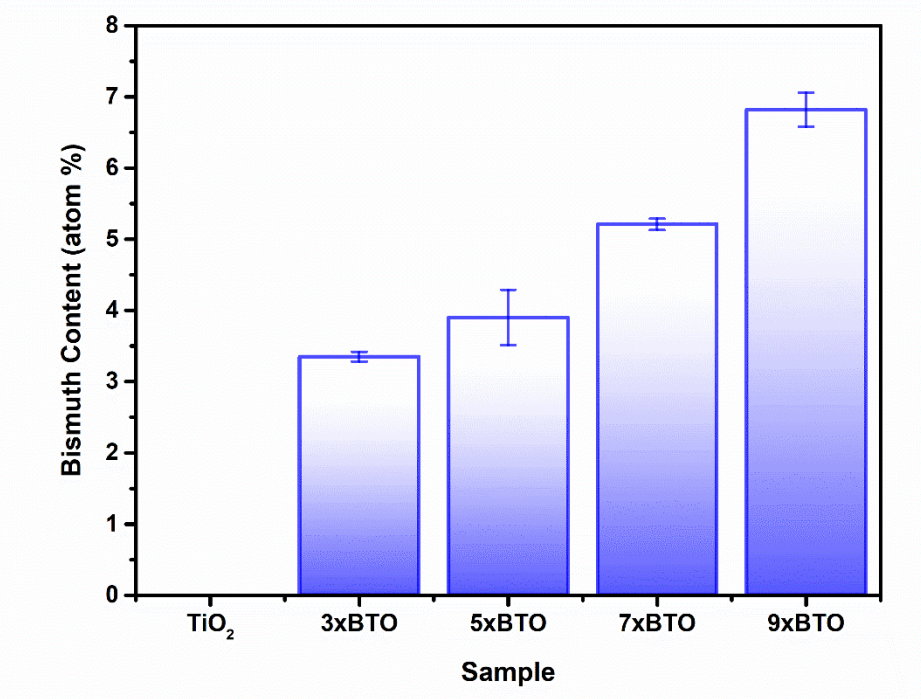

Figure 3.6. EDX analysis of the Bi content of the BTO modified P25 samples

A clear increase in Bi concentration was found as the number of SILAR cycles was increased, corresponding to larger amounts of BTO in the structure. No indication was found of any Br, indicating the complete conversion of BiOBr to BTO by annealing.

Transmission electron microscope (TEM) elemental mapping was used to characterise the distribution of bismuth in the composite (Figure 3.7).

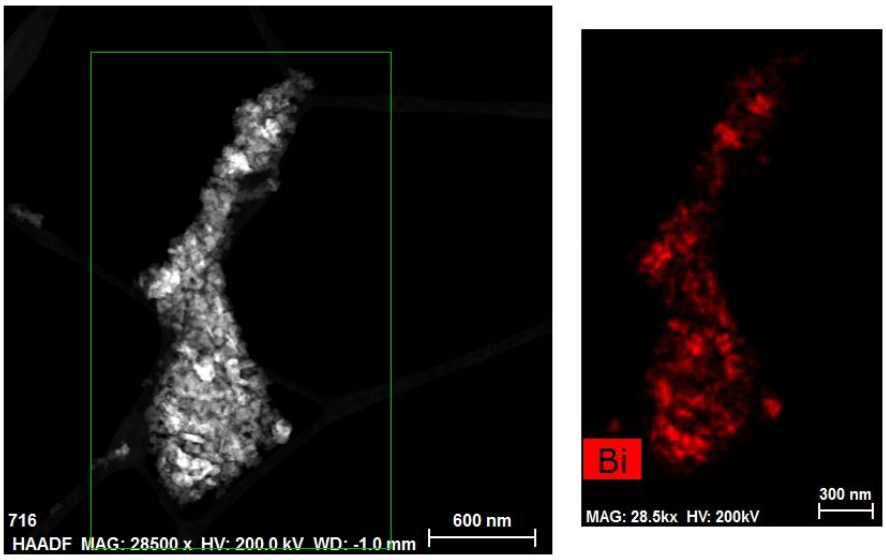

Figure 3.7. TEM HAADF Image (left) and corresponding Bi elemental map (right)

The Bi content in the material was found to be inhomogeneous, with some particles appearing completely converted to BTO, while others contained little bismuth. The origin of this was investigated by examination of the BiOBr-TiO_2 precursor (Figure 3.8).

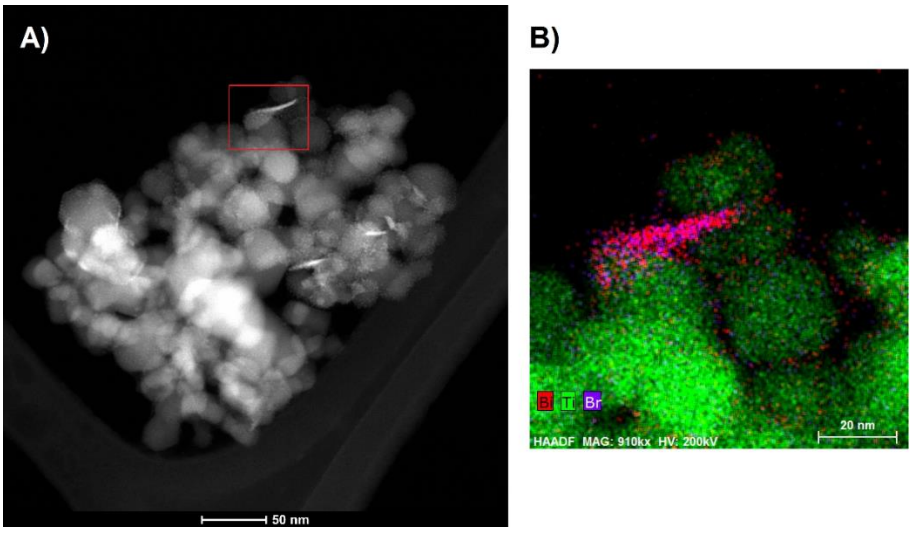

Figure 3.8. A) TEM HAADF image of the BiOBr precursor on P25 and B) Corresponding elemental map of Bi, Ti and Br

BiOBr was observed to have been deposited as nanoflakes on the TiO_2 surface, a typical morphology for bismuth oxyhalides[22,23]. However, many particles were devoid

of BiOBr material, and it is therefore likely that the areas of high Bi concentration after annealing correspond to areas in which the BiOBr nanoflake precursor had grown.

3.2.2.2.3 ICP-MS Analysis

To overcome the inherent sampling depth and sample size issues in electron microscopy EDX analysis, ICP-MS analysis was carried out to prove the conversion of BiOBr to BTO on heating. An acidic leach solution was prepared from the films and the Br content in the leach was then quantified by inductively coupled plasma mass spectrometry (ICP-MS) (Figure 3.9).

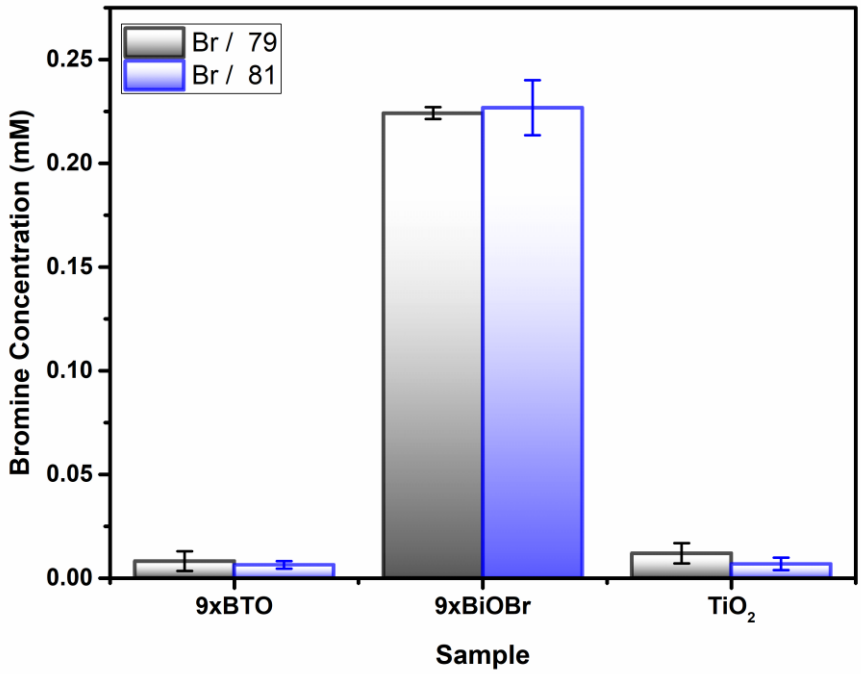

Figure 3.9. ICP-MS analysis of Br in the 9xBTO, 9xBiOBr precursor and P25 TiO_2 samples

Before annealing in the 9xBiOBr sample, large quantities of Br were found, whereas after annealing the Br has completely left the structure. Small quantities of Br appear to remain; however, these were also found to be present in the blank, indicating that they do not originate from the sample. This result is in keeping with the SEM-EDS, indicating the complete conversion of BiOBr to BTO on heating.

3.2.2.2.4 X-ray Photoelectron Spectroscopy

X-ray photoelectron spectroscopy (XPS) analysis was used to characterise the various chemical states of the elements present in the composite (Figure 3.10).

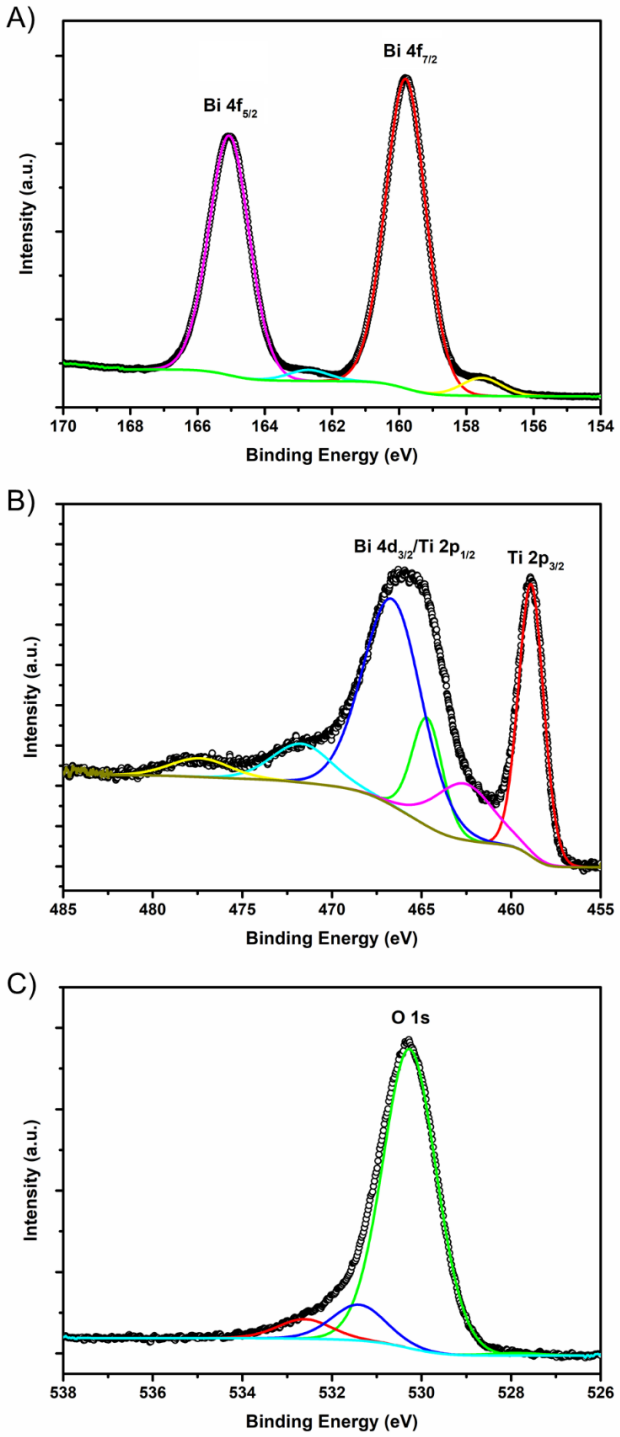

Figure 3.10. XPS scans of the A) Bi 4f, B) Ti 2p and C) O1s regions of the 7xBTO sample

7xBTO displays clear peaks at binding energies typical for Bi^{3+} 4f electrons at 159.8 and 165.1 eV, corresponding to the s=7/2 and 5/2 spin states respectively in good agreement with previous reports for BTO[24]. The Ti^{4+} region (Figure 10b) of the composite is somewhat complicated by overlapping of the Bi 4d and Ti 2p peaks resulting in a broad band between ~460-470 eV, but is in keeping with previous reports for Ti 2p states in BTO[25]. O1s region scans (Figure 10c) show a single asymmetric peak at 530.3 eV, with a slight shoulder toward higher energy which can be assigned to the presence of surface adsorbed oxygen containing species and surface terminal oxygen atoms[26]. In accordance with the SEM-EDX and ICP-MS results, no peaks due to Br were observed in the survey scan (Figure 3.11).

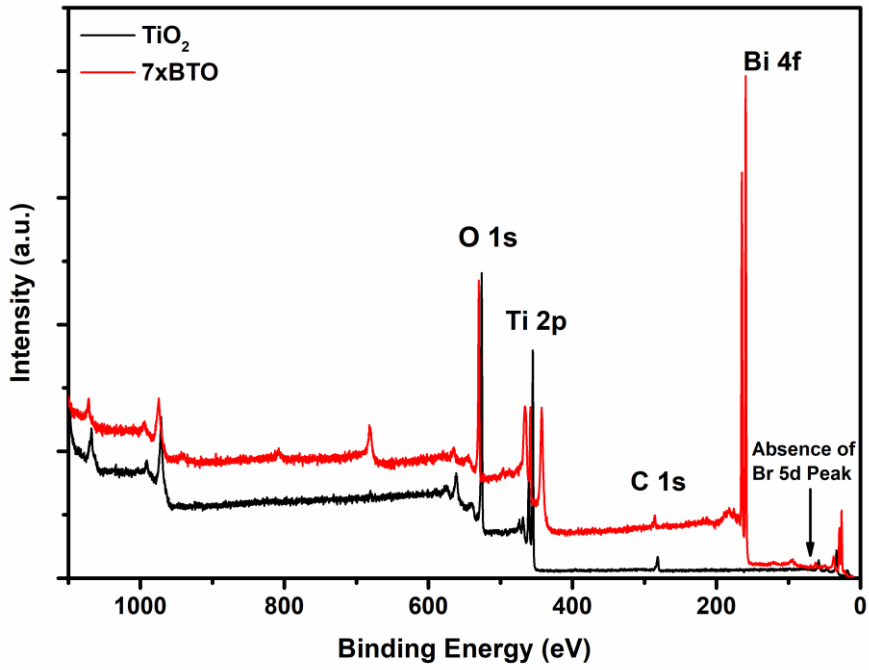

Figure 3.11. Survey scan of the TiO_2 and 7xBTO samples showing the absence of Br post heating

3.2.2.3 Optical Characterisation

3.2.2.3.1 Diffuse Reflectance Spectroscopy

To investigate the light absorbing properties of the materials, UV-visible diffuse reflectance spectra were measured and converted into the corresponding Tauc plots (Figure 3.12).

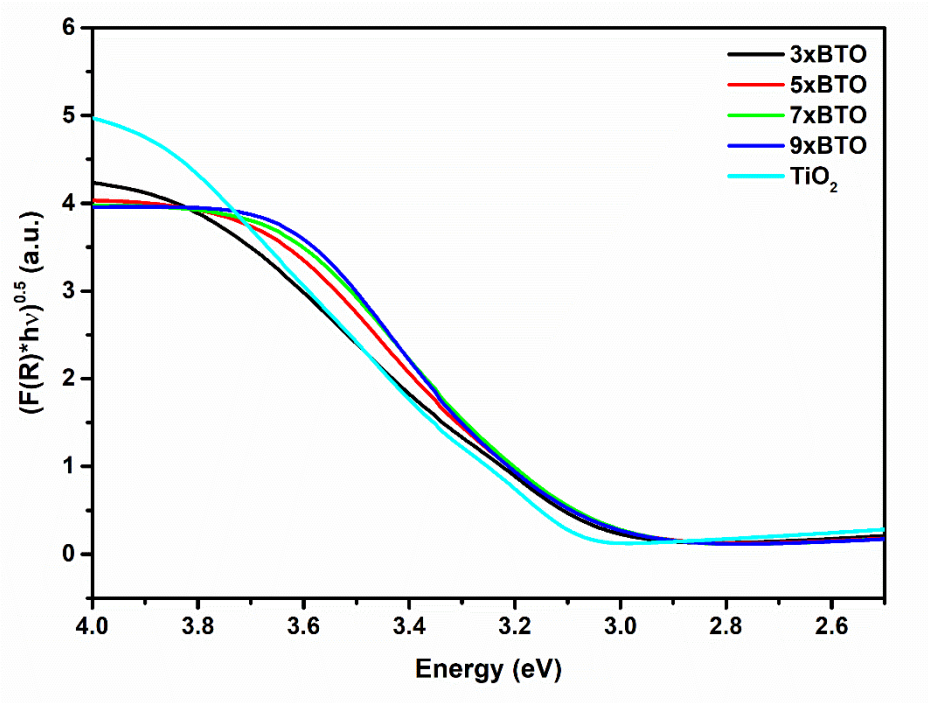

Figure 3.12. Tauc plots of the P25 and modified P25 samples

Modest shifts into the visible were noted for the BTO modified samples, the band gaps obtained by extrapolation of the linear portion of the Tauc plots are summarised in Table 3.2.

Table 3.2 – Band gaps obtained from diffuse reflectance measurements

Sample	Band Gap (eV)
TiO_2	A:3.12(7), R: 3.04(7)
3xBTO	2.98(3)
5xBTO	2.97(6)
7xBTO	2.95(8)
9xBTO	2.98(2)

Two values were clearly obtainable for the pristine P25 TiO_2 sample, due to the presence of both anatase and rutile, with nominal band gaps of 3.1 eV and 3 eV

respectively. The BTO modified samples all exhibited approximately the same band gap of around 2.96-2.98 eV, within the range of values reported previously for the $Bi_4Ti_3O_{12}$ phase of BTO[27]. While this value does not constitute a great deal of visible light harvesting (2.96 eV = 419 nm), it is important to note that upon lowering the band gap, there is less driving force to produce reactive species for water purification. Fundamentally low band gap materials give high light harvesting, but may be poor photocatalysts for water purification due to the low energy of photoexcited charges, leading to an inability to form the highly reactive oxygen species needed for full mineralisation[28].

3.2.2.3.2 Photoluminescence Spectroscopy

Photoluminescence (PL) measurements are a common method used to investigate the degree of charge separation in heterojunctions[29,30]. Upon excitation of the TiO_2 at 325 nm, the PL spectra of the prepared materials were measured (Figure 3.13).

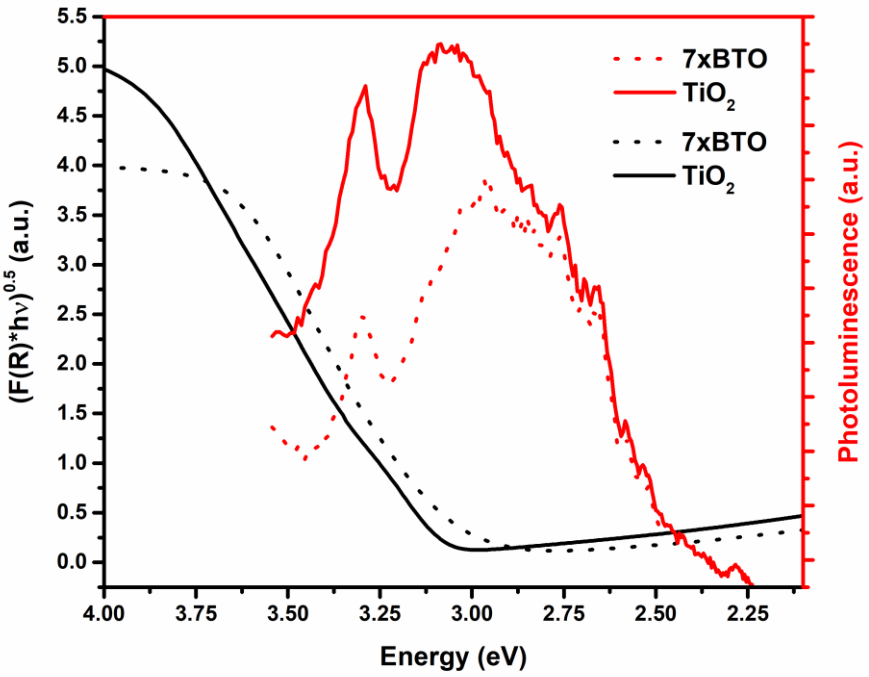

Figure 3.13. Photoluminesence spectra and diffuse reflectance comparison for TiO_2 and 7xBTO

Broad PL signals were observed from 355 nm to 550 nm for all the samples, with the BTO-TiO_2 heterojunctions generally exhibiting lower PL intensity over this range.

This can be indicative of lower charge recombination. However, it is important to note that lowered PL intensity in the range that BTO absorbs may in fact be due simply to re-adsorption of emitted photons by BTO, and not separation of charges. This has often been overlooked in previous reports[31], and should be considered. Therefore, in this work the Tauc plot of 7xBTO has been overlayed with its PL spectrum. A general decrease in PL intensity across the entire emission is observed, however it should be noted that emission above ~2.98 eV should not be relied upon due to the effect of re-absorption. Nevertheless, the PL intensity below the BTO band gap energy is also lowered, and as such there is some separation of charges occurring across the BTO-TiO_2 interface.

3.2.2.4 Photocatalytic Activity

3.2.2.4.1 Degradation of Organic Pollutants

Photocatalytic water purification tests were run the column reactor described in Figure 3.14.

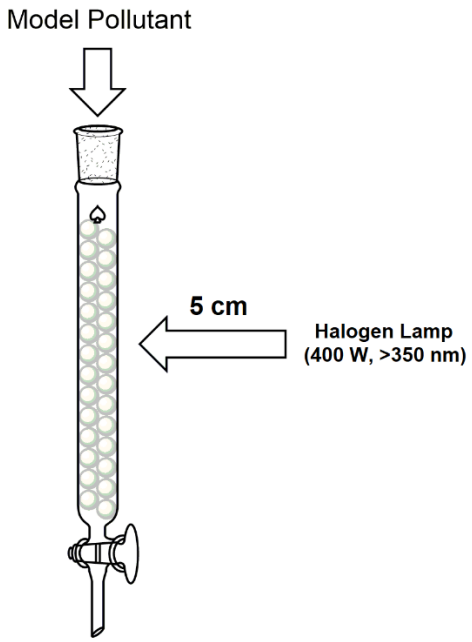

Figure 3.14. Reactor used to test the photocatalytic bead samples.

To avoid any photosensitisation which may occur when using a dye molecule as a model pollutant, the destruction of colourless 4-chlorophenol (4CP) was chosen as a

metric for photocatalysis. Before irradiation, dark adsorption experiments were carried out and no adsorption was observed (Figure 3.15).

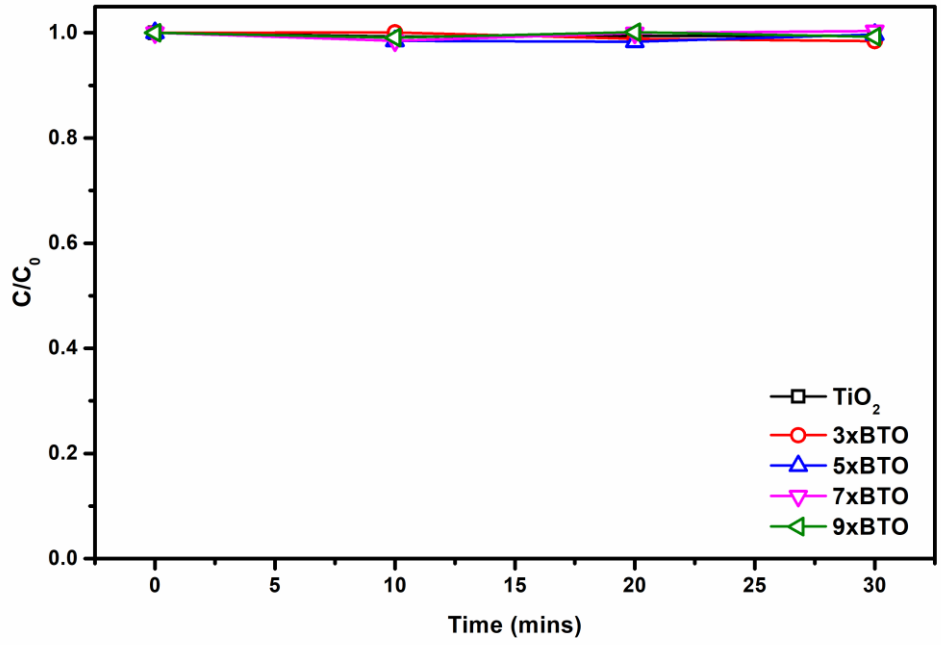

Figure 3.15. Dark adsorption of 4CP by pristine TiO_2 and the BTO modified samples

The 4CP/photocatalyst apparatus was then tested under irradiation with a 400W halogen lamp. Higher DE was observed for the BTO modified materials than the pristine TiO_2 sample, with the greatest activity exhibited by the sample derived from 7 SILAR cycles, achieving ~75% DE during the 3 hours of illuminaton (Figure 3.16).

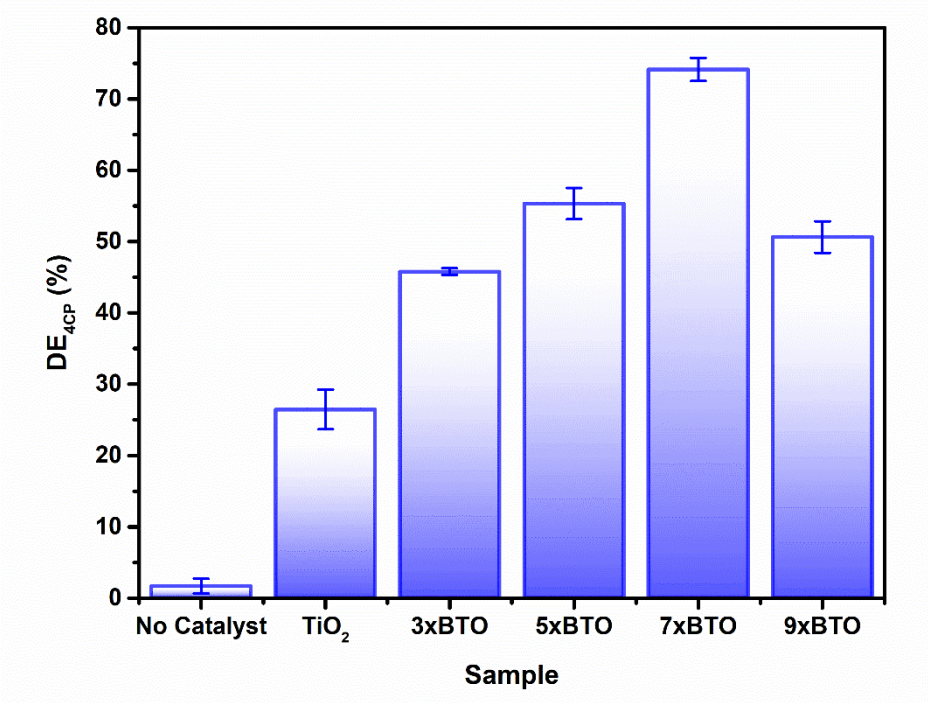

Figure 3.16. Testing of the prepared photocatalytic bead materials against 4CP

While direct comparisons with the photocatalytic results of others are difficult, it should be noted that a previous investigation by Zhang et al on the photocatalytic activity of BTO-P25 composites yielded no activity at all[11]. It was concluded that this was due to an inability for BTO to form on the anatase [101] facet under hydrothermal conditions. Using the SILAR/thermal annealing route described here however it appears that it is possible for BTO for form on this facet and give good photocatalytic activity.

As the composite with the best activity, 7xBTO was chosen for further studies. An important property for the viability of a photocatalyst system is the ability to re-use the photocatalyst materials. To test this, the photocatalytic degradation of 4CP was measured by successive photocatalytic tests, with a fresh solution of 4CP on each run (Figure 3.17).

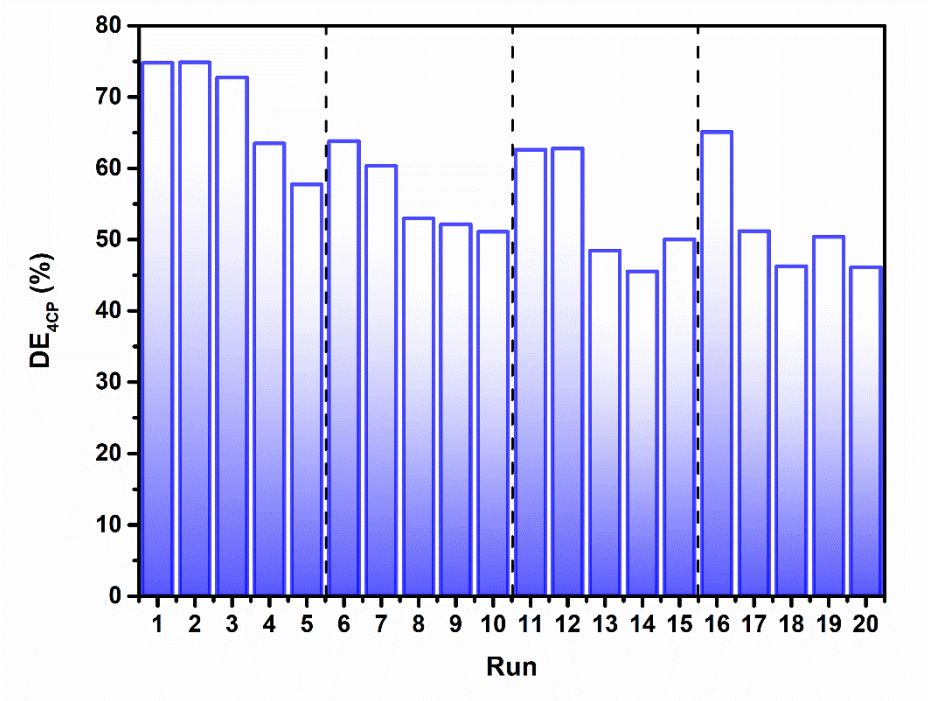

Figure 3.17. Recycling test of 7xBTO against 4CP. Dashed lines denote regeneration cycles.

Slight losses of activity were observed after the first run but remained stable on subsequent runs. It was found that the activity could be returned to the original level by using a calcination process to regenerate the photocatalyst beads. This could be due to inhibition of the photocatalyst surface by degradation products, which can be removed by calcination. Regeneration of the photocatalyst by this method was found to be effective in extending the photocatalyst activity up to at least 60 hours.

To investigate the effect of interfering contaminants and to move toward a more realistic system, the activity of 7xBTO was tested upon 4-nitrophenol (4-NP) in synthetic wastewater (Figure 3.18).

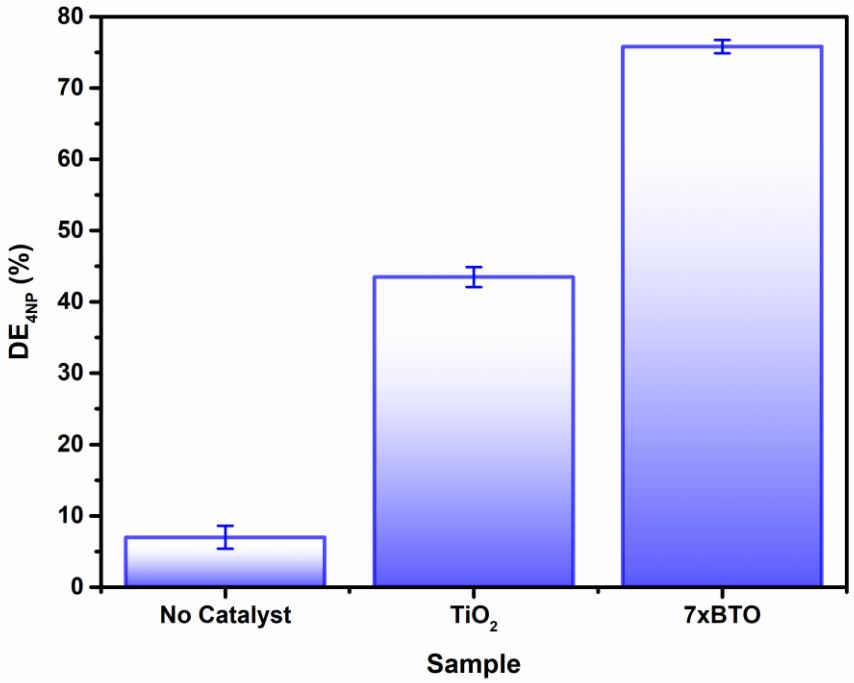

Figure 3.18. Degradation of 4-NP in a synthetic wastewater medium.

It was found that using synthetic wastewater as a medium had no effect on the photocatalytic activity of 7xBTO, displaying similar degradation efficiency (~75%) as in a deionised water medium. The ability of photocatalysts to handle relatively highly contaminated water and retain good degradation activity in this way is key in moving away from somewhat artificial tests against single model contaminants in de-ionised water, and as such is an important assessment of a photocatalytic materials applicability.

To gain an insight into the degree of complete mineralisation, as opposed to initial degradation, chemical oxygen demand (COD) measurements were made on samples of synthetic wastewater before and after photocatalytic treatment (Figure 3.19).

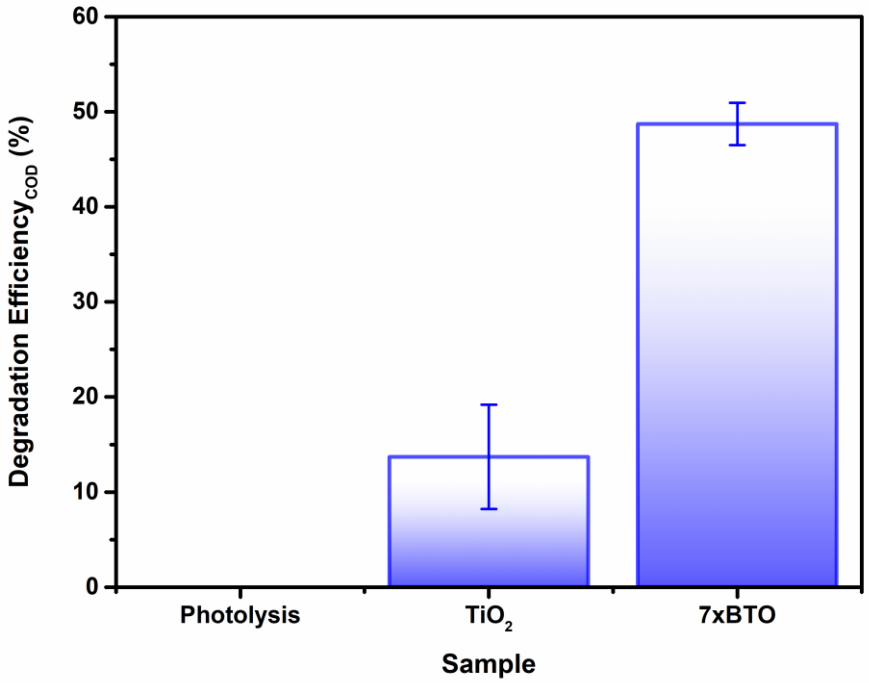

Figure 3.19. Degradation of synthetic wastewater determined using chemical oxygen demand titration

While 7xBTO displayed a clear improvement over the TiO_2 control, it was noted that the COD removal was significantly lower than the degradation tests on 4CP/4NP measured by absorption spectroscopy, only achieving 50% DE rather than 75%. This can be ascribed to the aforementioned difference between apparent destruction of a chromophore and total mineralisation.

3.2.2.4.2 Bactericidal Testing

To investigate the bactericidal activity of the prepared photocatalyst beads, the destruction of *E. coli* was measured. After 90 minutes, almost complete removal of viable colony forming units (CFU) was observed for the 7xBTO sample, while in the unmodified TiO_2 sample around 40 times the number of CFU remained (Figure 3.20).

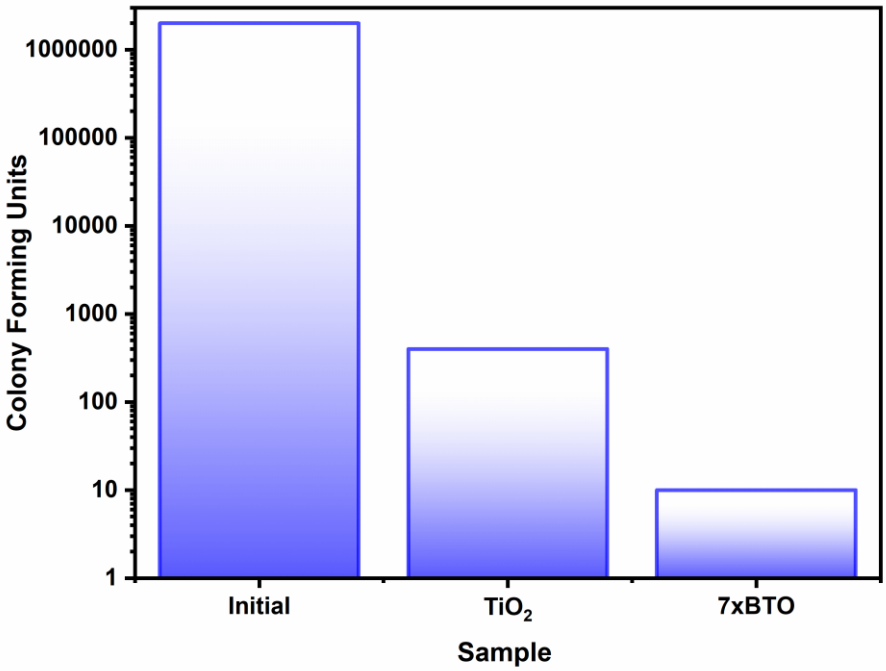

Figure 3.1. Bactericidal activity of the 7xBTO and pristine TiO_2 samples

It has been proposed that photocatalytic bactericidal activity works by oxidative damage to the cell wall[32,33] and modifications to bacterial DNA[34] by reactive oxygen species reducing the ability of bacteria to form viable colonies. Rapid destruction of E. coli is an encouraging sign of bactericidal activity; however, it should be noted that as a gram-negative bacteria *E. coli* is more susceptible to destruction using advanced oxidation processes than gram-positive bacteria[35]. Previous work has demonstrated that under the same conditions gram-negative bacteria take significantly longer to be de-activated than gram-positive[36]. The BTO-TiO_2 system affects rapid deactivation of *E. coli*, but assuming such efficient bactericidal action against other micro-organisms should be warned against.

3.2.2.4.3 Mechanistic Studies

To probe the mechanism of photocatalytic activity a series of scavenging tests were carried out on 4-chlorophenol. Upon addition of methanol, *tert*-butanol and degassing using N_2, drops of activity against 4CP were noted (Figure 3.21).

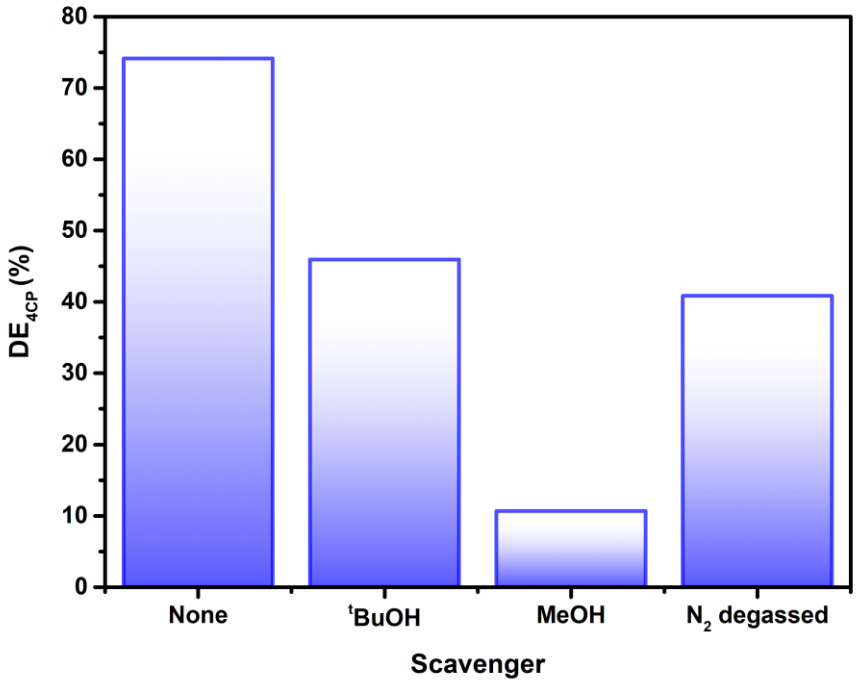

Figure 3.21. Reactive species identification using scavenging tests against 4-CP

It was found that *tert*-butanol reduced the photoactivity to around 40%, while the addition of methanol almost completely stopped the photocatalytic reaction. This would suggest that the mechanism involves both hole driven production of hydroxyl radicals and direct oxidation of the model pollutants by holes. Degassing with nitrogen to remove dissolved oxygen from the solution also reduced the photoactivity to around 45%, indicating that electron transfer from the composite to oxygen is key in the degradation mechanism. Hydrogen peroxide and hydroxyl radicals[37] may be formed via the superoxide ion resulting from electron transfer to oxygen. It is likely that without oxygen in the solution a combination of loss of these reactive species and increased recombination results in a reduced degradation efficiency.

Hydroxyl radicals, due to their high oxidising power and fast reaction rates approaching the diffusion limit[28,38] are key in the mineralisation of organic pollutants and the destruction of bacteria. A common strategy to prove the production of hydroxyl radicals is to monitor the hydroxylation of sodium terephthalate to the fluorescent 3-hydroxy sodium terephthalate[39]. After 2 hours of irradiation of a solution of sodium

terephthalate with TiO_2 and 7xBTO samples a photoluminescence peak at 425 nm typical of 3-hydroxy sodium terephthalate was observed (Figure 3.22).

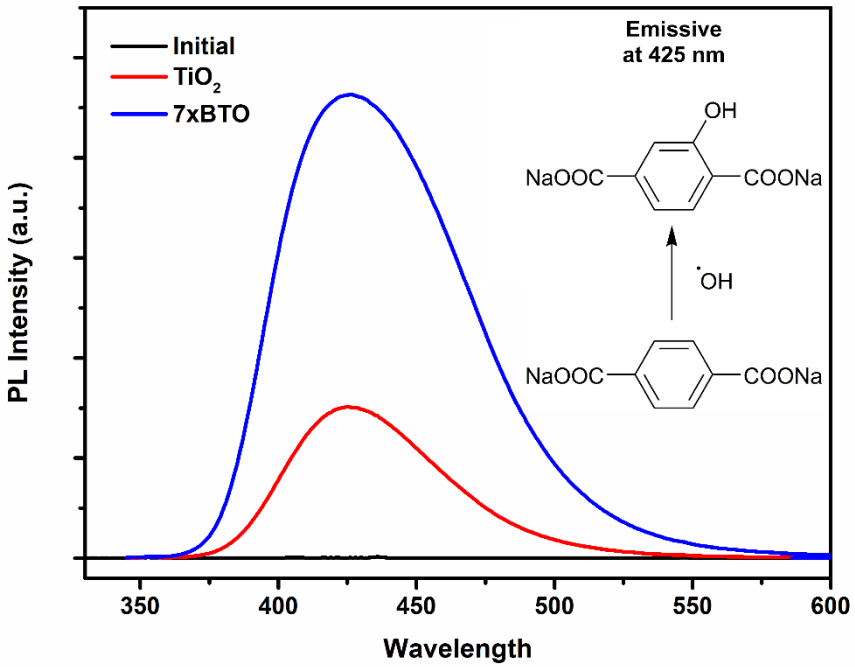

Figure 3.22. Hydroxylation of Na_2-terephthalate by photogenerated hydroxyl radicals

While both TiO_2 and 7xBTO produced hydroxyl radicals, the yield of the hydroxylated product was found to be ~3 times higher on 7xBTO compared to TiO_2. This finding is in accord with the scavenging tests, indicating that hydroxyl radicals are involved in the photocatalytic degradation mechanism.

According to values calculated in the literature, the BTO and TiO_2 valence bands lie at 2.92 eV[25] and 2.86 eV[40] on the hydrogen scale respectively. Using these values, and the band gaps determined by diffuse reflectance measurements, it is possible to propose a band alignment diagram, and a plausible mechanism (Figure 3.23).

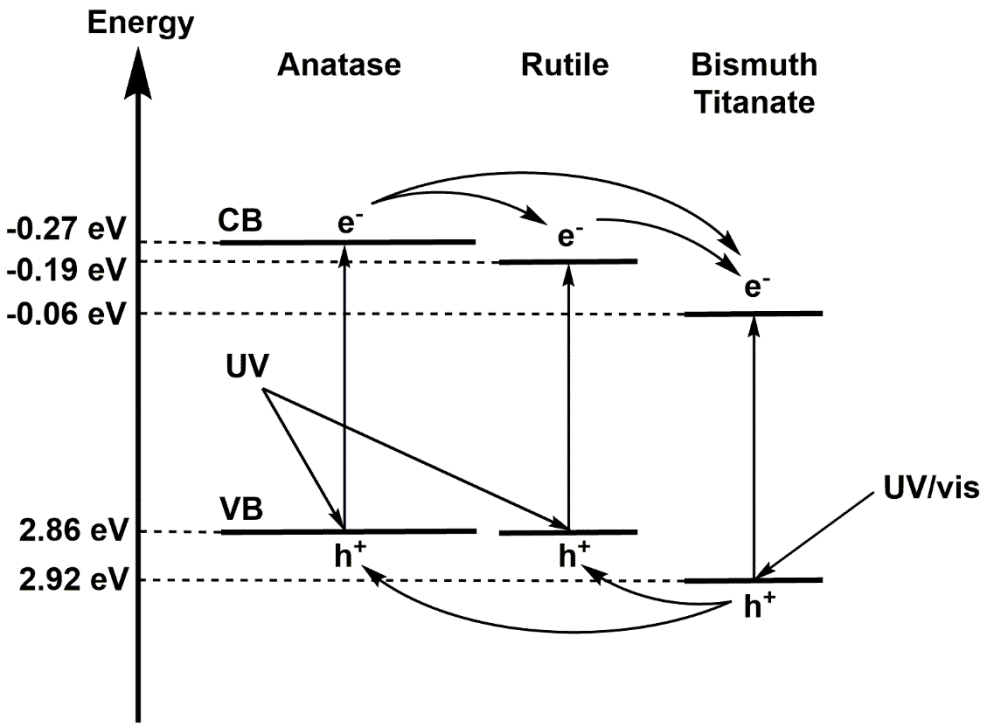

Figure 3.23. Band alignment diagram of the BTO-TiO_2 interface showing charge separation under UV/vis irradiation. Energy scale = hydrogen scale.

Accordingly, a driving force of 160 mV exists for holes to migrate from BTO to TiO_2, allowing transfer of photogenerated holes and subsequent direct oxidation of pollutants, or formation of surface hydroxyl radicals (~1.6 V vs NHE). Photogenerated electrons on the anatase portion of P25 TiO_2 also have a driving force to transfer to BTO/rutile TiO_2, however once there they lie slightly below the potential required for electron transfer to oxygen. While in as a gas at standard temperature and pressure O_2 is known to be reduced to superoxide at -0.33 V, it has been estimated that O_2 reduction goes ahead at around -0.16 V[28], slightly higher than the calculated BTO CB energy. Thus, it is unlikely that BTO allows formation of superoxide, and any superoxide formed may arise from the electrons in the P25 conduction bands. It is possible that the mechanism on BTO goes via the reduction of oxygen to give the hydroperoxyl radical (-0.05 V vs NHE) or the two-electron reduction to give hydrogen peroxide (+0.685 V vs NHE). Given that removal of oxygen from a test solution somewhat abated the photocatalytic efficiency, it can be concluded that BTO is acting in one of these ways, however from this test alone it is not clear.

3.3 Bismuth Titanate – TiO_2 Composites II: Improving Robustness & Further Photocatalytic Testing

3.3.1 Introduction

In this section is described the application of a photocatalyst bead system with improved robustness, stability and activity against a wider array of possible pollutants, with a view to creating a more easily applicable system. A large component of impurities that may be present in drinking water sources are organic in nature, which can arise from a wide variety of sources such as leeching from agriculture[41,42], medical wastes[43,44], and domestic[45] or industrial[46,47] effluents. Thus, it is important that any photocatalytic remediation strategy is effective against such a wide range of different pollutants. In this section is described a method by which TiO_2 is robustly coated onto the surface of glass beads using a P25 enriched Ti sol. This process produces a film of P25 particles with a degree of surface roughness derived from the sol, which binds strongly to the glass surface. To this is applied the same BiOBr SILAR and thermal decomposition process as described earlier, imparting the same improvement to photocatalytic activity.

In testing this activity, model pollutants used in testing were chosen based on key examples from important molecule classes, such as pesticides, drugs and explosives. Pentachlorophenol, nonylphenol, trinitrotoluene, nitrotriazolone, paracetamol and tetracycline were chosen, giving a diverse sample of targets with different structural features to test against. The structures of the pollutants are given in Figure 3.24.

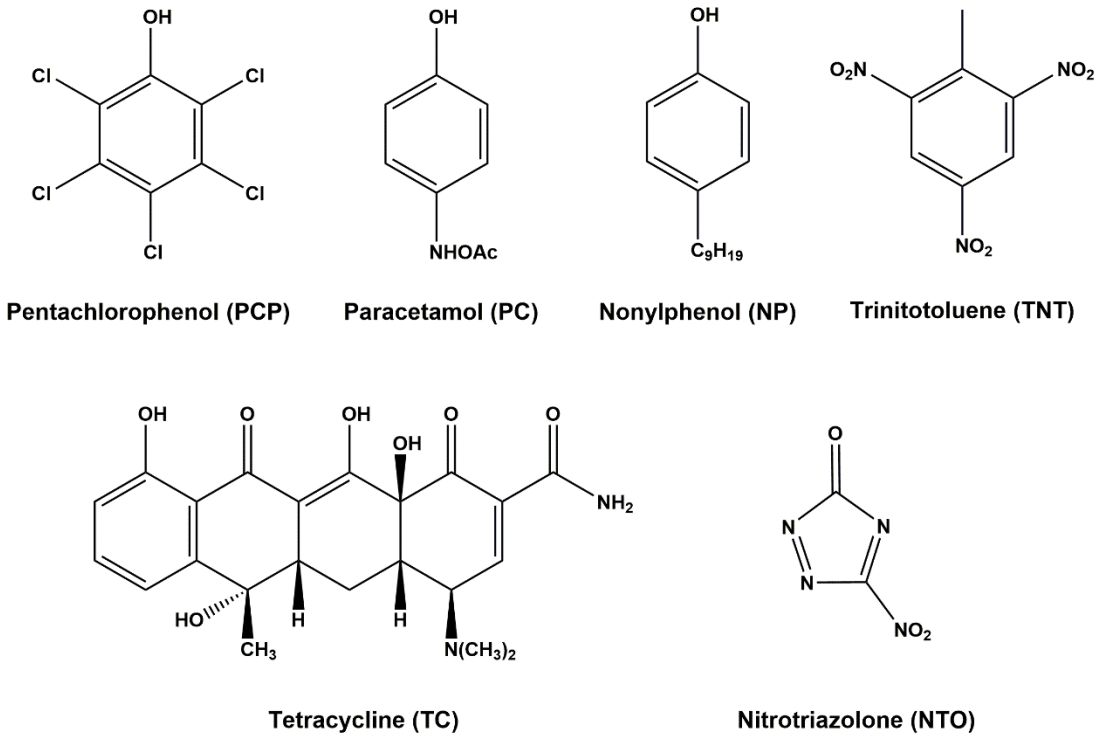

Figure 3.24. Molecular structures of the model pollutants studied using the BTO-TiO_2 sol derived system

Pentachlorophenol (PCP) was used as a model pesticide pollutant, having been noted as a having renal, carcinogenic and neurological effects[48], its removal has been designated a priority by the European Union Water Framework Directive (EUWFD) [49]. Nonylphenol (NP) is another phenolic pollutant priority substance of the EUWFD used in this study, being an endocrine disruptor[50] commonly used in the manufacture of consumer products such as nonylphenol ethoxylates, which are typically used in surfactants[51]. Leeching of explosives into drinking water sources from the mining industry and military operations has been noted to cause significant contamination of drinking water sources[52,53]. Typically containing nitro groups, these molecules are resistant to standard oxidation processes due to the electron withdrawing nature of these substituents[54]. As such, two widely used explosives, trinitrotoluene (TNT) and nitrotriazolone (NTO), were chosen for study, with TNT being a known poison with hematological effects[55] and NTO exposure being suggested to cause reductions in sperm production in mammalian model studies[56]. The presence of pharmaceutical molecules in drinking water has been noted as an area of increasing concern in recent

years[57]. The popular analgesic drug paracetamol (PC) has been found at relatively high concentrations of 6 ppb in treated water samples[58], and while its toxicity is not high, low continuous doses have been suggested to be a target for removal as a precautionary measure[59]. Tetracycline (TC) is a common anti-biotic compound often studied in photocatalytic degradation tests[60], removal of low levels of which from water is key in avoiding the spread of anti-biotic resistant bacteria[61]. Thus, this section aims to prove the applicability of the prepared system against a wide variety of molecules with distinct structural features that have been identified as potential hazard compounds.

3.3.2 Results & Discussion

3.3.2.1 Photocatalyst Preparation

The general process of producing the photocatalytic bead system is as given earlier in Figure 3.2a. Coating using a suspension of P25 in a sol of $Ti(OBu)_4$ rather than the typical suspension in water or alcohols[62,63] was found to give a well attached coverage of titania on the bead surface, with only relatively severe impacts able to remove the material from the bead surface. Indeed, compared to the previously described water-based suspension, this method was found to be significantly better in terms of robustness of the resulting coating. To this coating, modification with BiOBr using SILAR was applied in the same manner as before (Figure 3.2b). In this section, SILAR was carried out 7 times to build up a greater amount of BiOBr on the bead surface, before drying and annealing. Due to the heating in the annealing stage, decomposition of the BiOBr takes place as noted previously, consuming the nearby titania to form bismuth titanate in the process.

3.3.2.2 Materials Characterisation

3.3.2.2.1 X-ray Diffraction

X-ray diffraction (XRD) studies on the prepared pristine TiO_2 coatings and 7xBTO sample showed little difference between the two materials (Figure 3.25a). No new peaks were observed on SILAR processing which could be indexed, although an indistinct bump in the baseline can be observed between ~25° and ~35° when the traces were stacked together (Figure 3.25b).

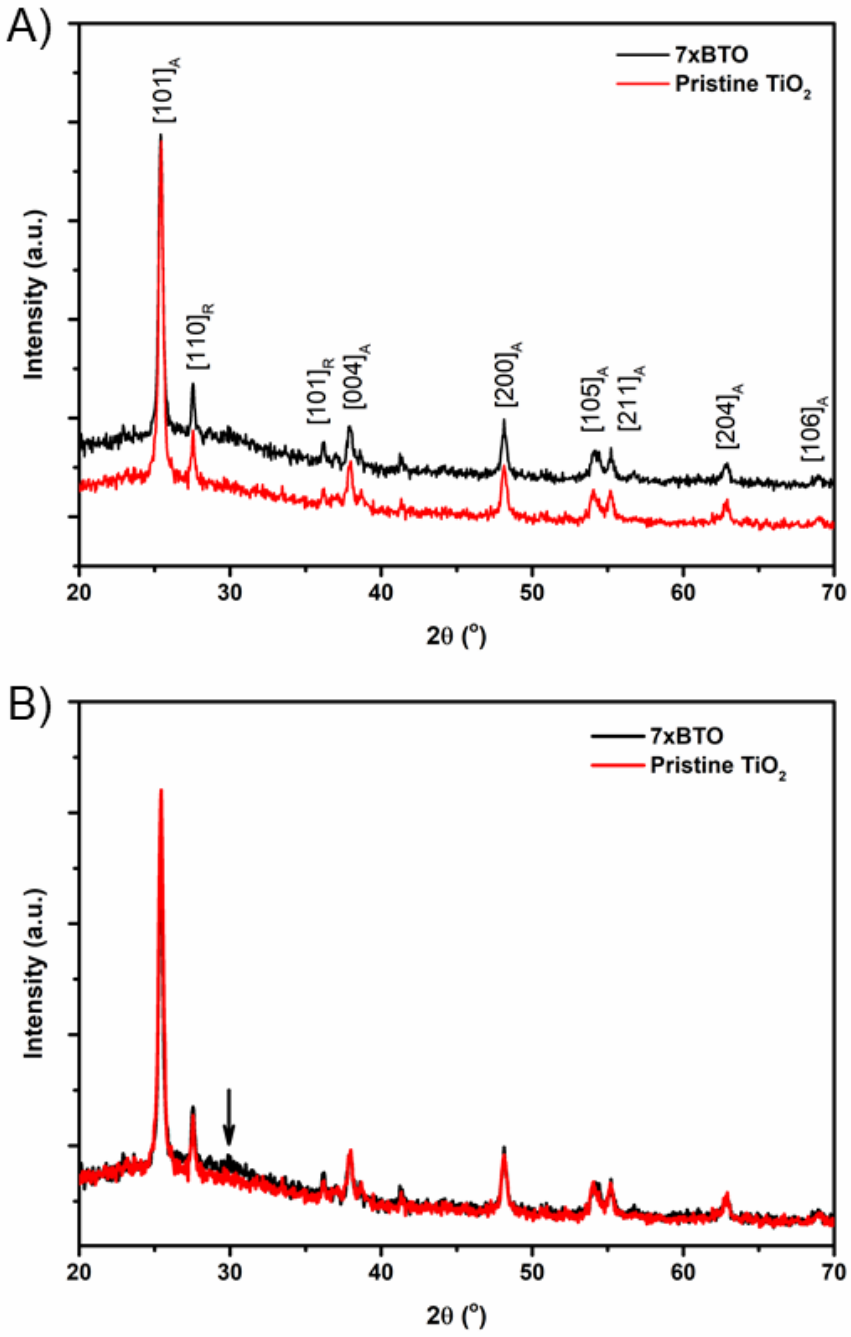

Figure 3.25. A) XRD traces of the pristine TiO_2 film surface and the BTO modified material. B) Stacked traces showing possible BTO "peak"

The peaks which were observed can be indexed clearly to the anatase and rutile peaks expected in P25 (JCPDS card numbers: 21-1272 & 76-1940). The lack of peaks corresponding to BTO could be due to a low concentration of BTO in the sample, or due to small particle sizes resulting in amorphous characteristics. Often in samples

prepared by SILAR the crystal domain sizes can be small initially[12] where the material has had little chance to grow into a crystal large enough to be observed in the XRD.

3.3.2.2.2 Electron Microscopies

Further investigations into the particle size were conducted by scanning electron microscopy. Prior to thermal decomposition of the BiOBr precursor, large nanoplates of BiOBr could be observed covering the whole surface of the film (Figure 3.26), a typical morphology with which bismuth oxyhalides have been found to form[22,64].

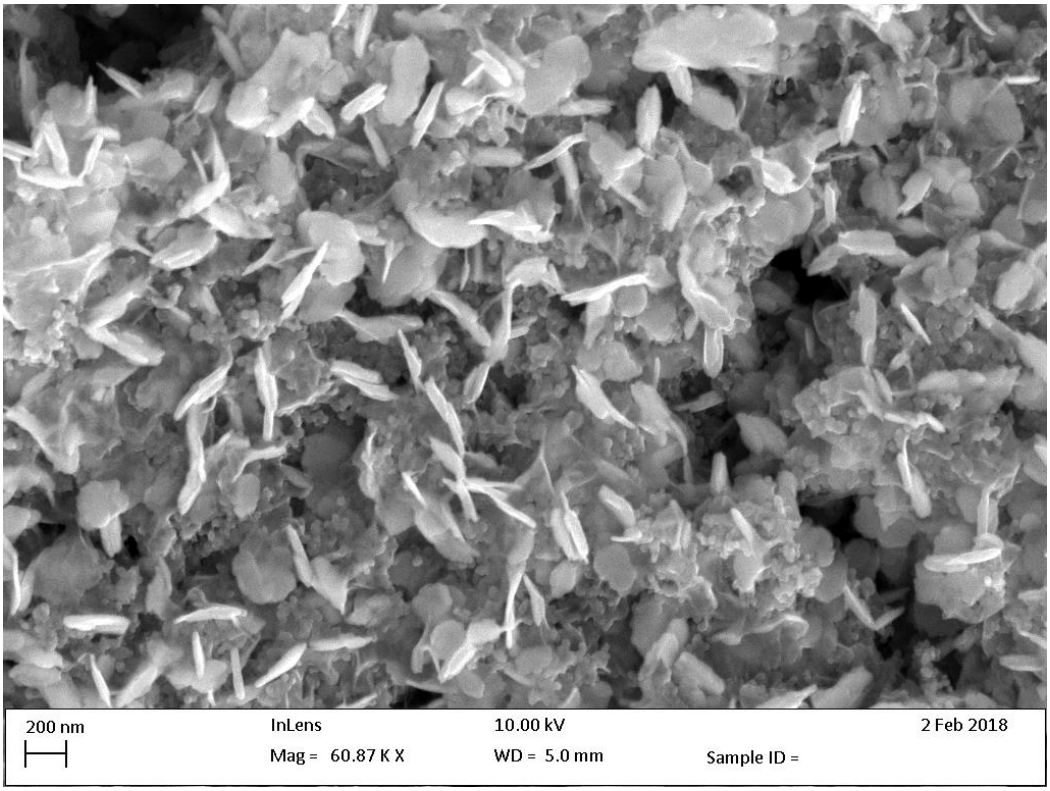

Figure 3.26. SEM image of the BiOBr-TiO_2 precursor showing BiOBr nanoplates

After annealing however these nanoplates disappear, indicating decomposition of the BiOBr. Both pristine (Figure 3.27a) and 7xBTO modified materials (Figure 3.27b) display a porous network of interconnected particles.

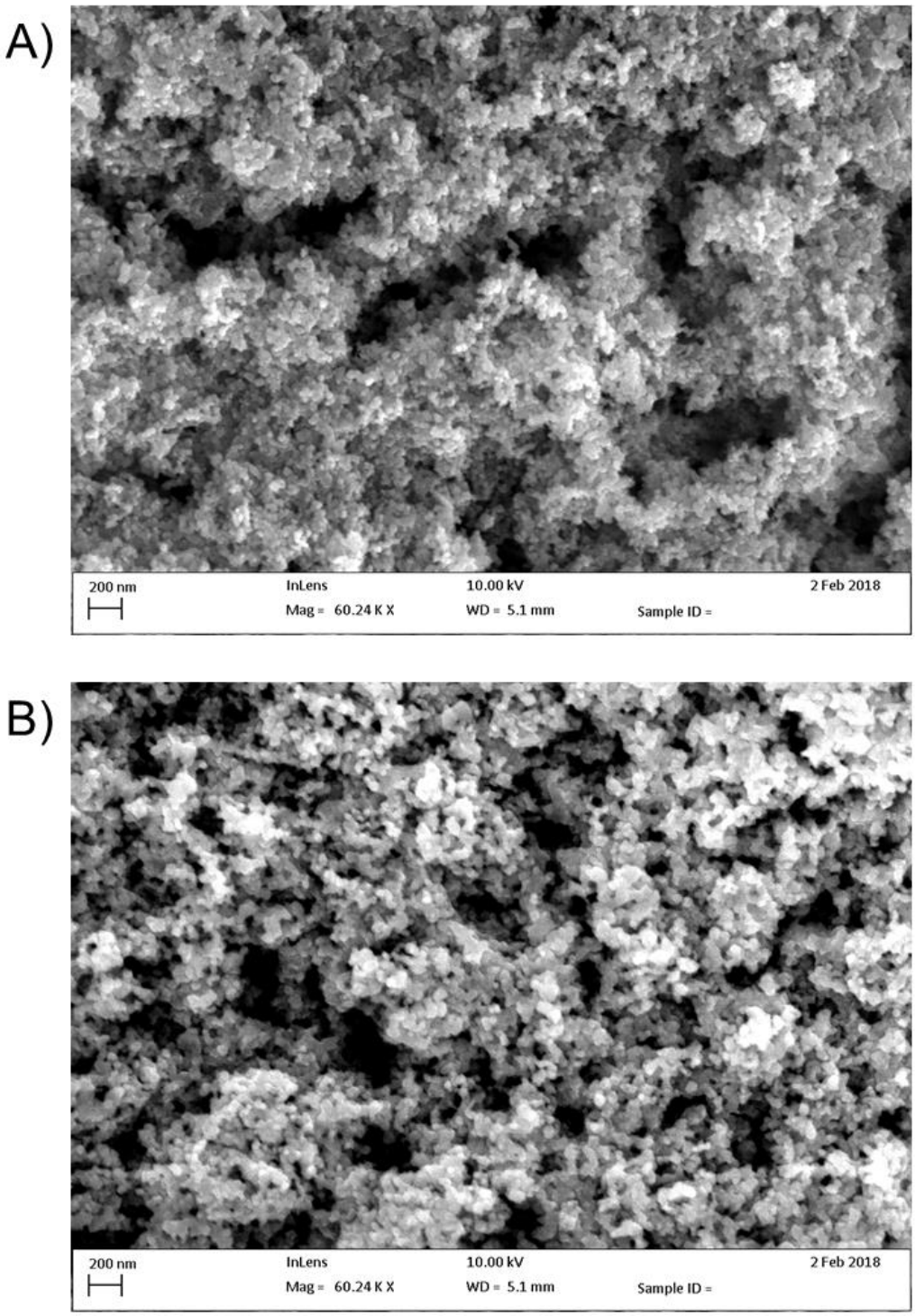

Figure 3.27. SEM images of A) the pristine TiO_2 surface and B) the BTO modified TiO_2 surface

Similarly, to when a water based P25 coating suspension was used, a particle size increase was noted upon modification of the TiO_2 surface, likely due to the higher

temperatures used to decompose the BiOBr precursor. Energy dispersive x-ray spectroscopy (EDX) analysis of the material revealed the presence of ~5 atomic % Bi present in the material (Figure 3.28).

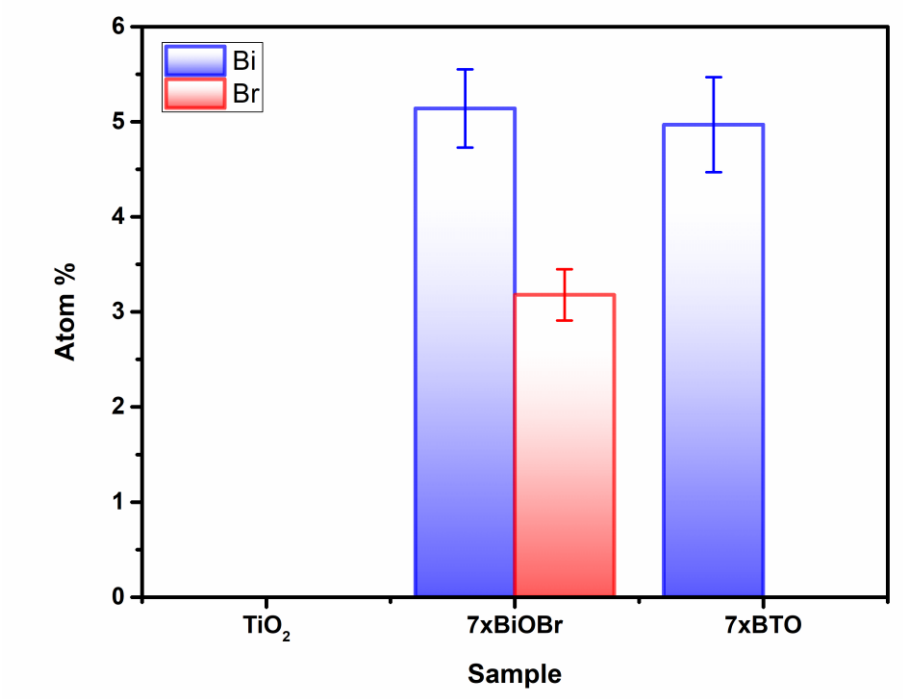

Figure 3.28. EDX analysis of the Bi and Br content of the prepared films before and after decomposition of the BiOBr precursor

No loss of bismuth was apparent before and after annealing however no peaks were observed for Br after annealing, indicating the complete decomposition of the BiOBr precursor in forming BTO. The levels of Bi and Br in the original BiOBr material were found to not be 1:1, as would be expected for pure BiOBr. However, many different stoichiometries of BiOBr exist, such as $Bi_{24}O_{31}Br_{10}$, $Bi_4O_5Br_2$, Bi_3O_4Br and Bi_5O_7Br[65,66], which have different Bi:Br ratios. It may also be possible to form a mixture of BiOBr materials in a single sample, which could be the origin of the non-stoichiometry observed in the EDX analysis. Transmission electron microscope (TEM) images revealed the effect of a sol based P25 coating suspension versus coating from a water based P25 suspension. Covering the surface of the particles in the pristine TiO_2 sample were very small clusters, giving the particles a certain amount of surface roughness (Figure 3.29a). These clusters were not observed in the absence of the

$Ti(OBu)_4$ sol (Figure 3.29b), and can be concluded to arise from decomposition of the sol under raised temperatures.

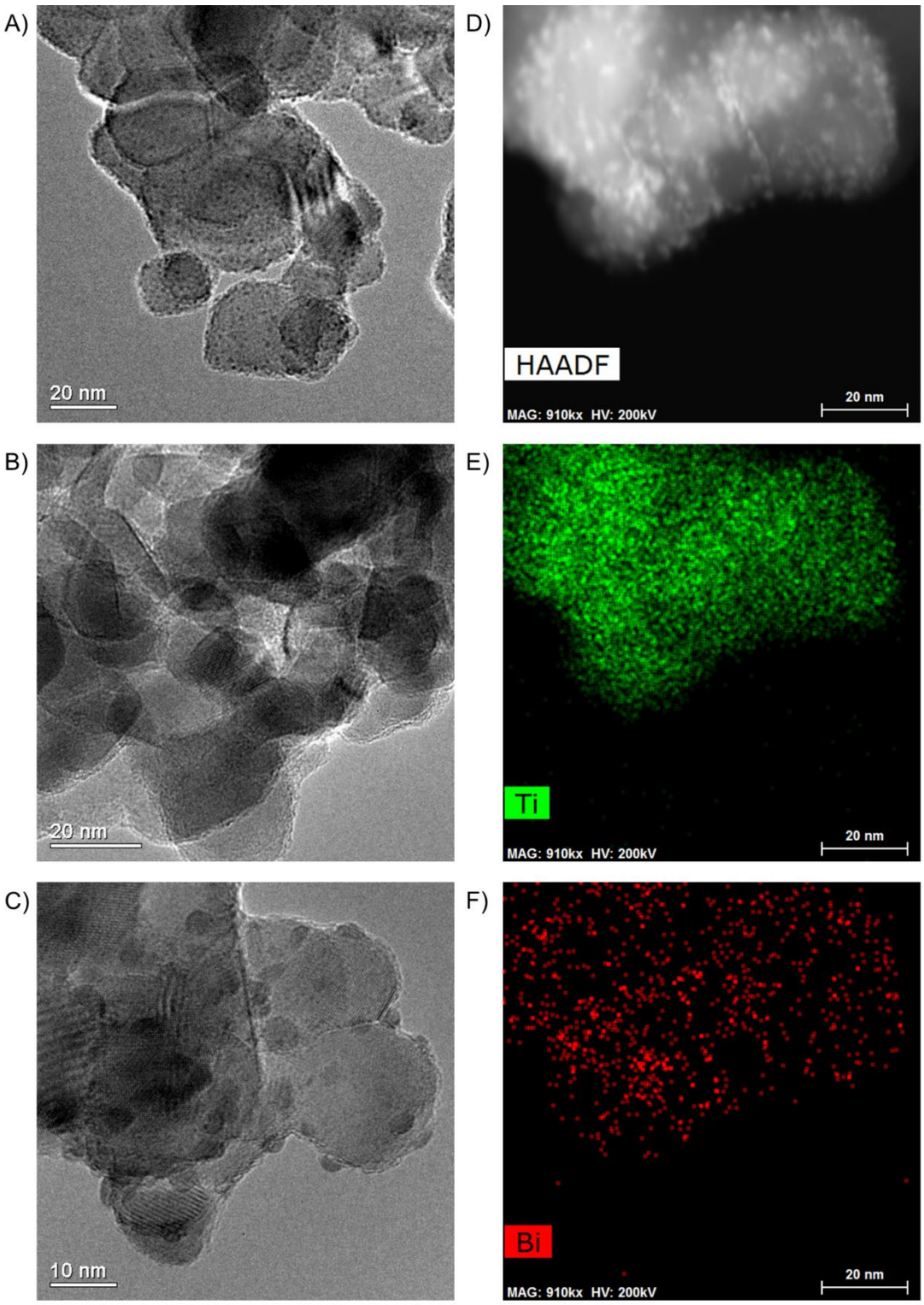

Figure 3.29. TEM images of A) the P25/TiO_2 sol derived material. B) P25 and C) The BTO modified P25/TiO_2 sol. C) HAADF image of the BTO modified TiO_2 and corresponding elemental maps for E) Ti and F) Bi

After SILAR processing and annealing, these particles were found to have grown to particles around 5 nm (Figure 3.29c), which could again be due to the increased annealing temperature used to decompose the BiOBr precursor, or growth of the BTO material on these high surface energy particles. The particles grown in this way were observed to be highly dependent on the beam conditions, aggregating when the TEM beam was kept in place for extended periods of time. TEM high angle annular dark field (HAADF) and the corresponding elemental mapping revealed the distribution of Bi on the titania particle surface (Figure 3.29c-f). While some Bi was found across much of the particles, higher concentrations were observed in areas coinciding with the small particles, suggesting that the growth of these particles is in part driven by growth of BTO on these secondary particles.

3.3.2.3 Photocatalytic Activity

3.3.2.3.1 Degradation of Organic Pollutants

In testing of the photocatalyst coated beads, the dish type batch reactor was used, irradiated with a 410 nm LED array from below. The reactor and a setup schematic and a photograph of the dish are given in Figure 3.30.

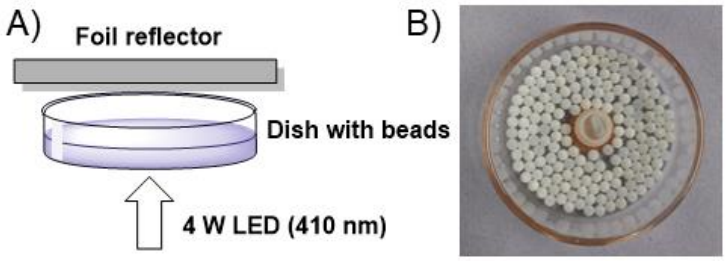

Figure 3.30. A) Schematic of the reactor setup used. B) Photograph of the dish with BTO-TiO_2 beads

Prior to irradiation, each bead set up was allowed to stir in the dark to measure any dark adsorption (Figure 3.31).

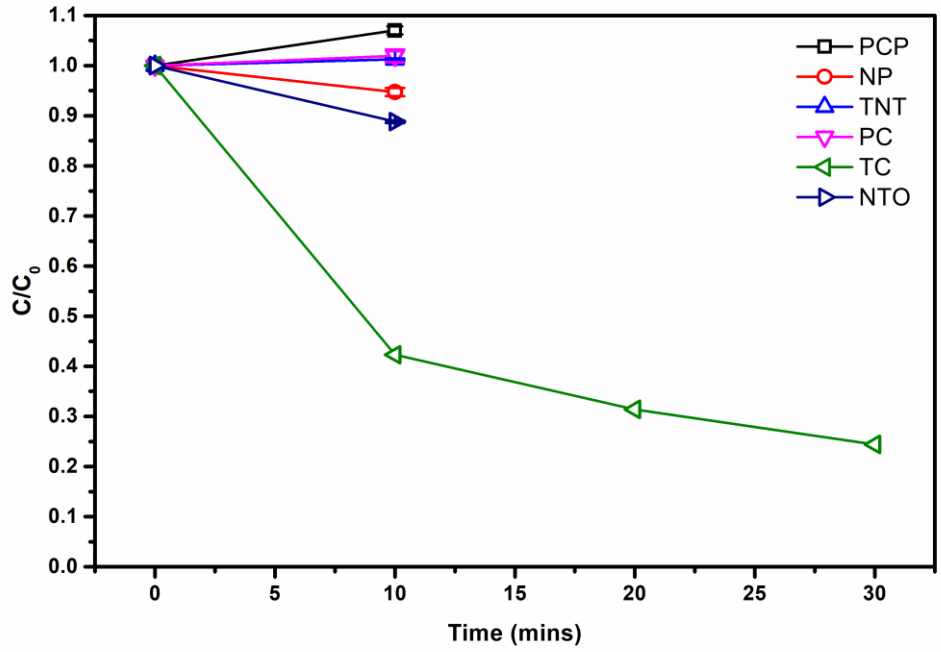

Figure 3.31. Dark adsorption test of the 7xBTO materials against the chosen pollutants

Minimal adsorption was observed for all of the pollutants other than TC, which showed strong adsorption over 30 minutes. Such adsorption has been previously reported and shown to be beneficial in the overall degradation process[67].

Photocatalytic beads were then irradiated, and the activity determined by their first order rate constants. A sample first order rate plot is given in Figure 3.32.

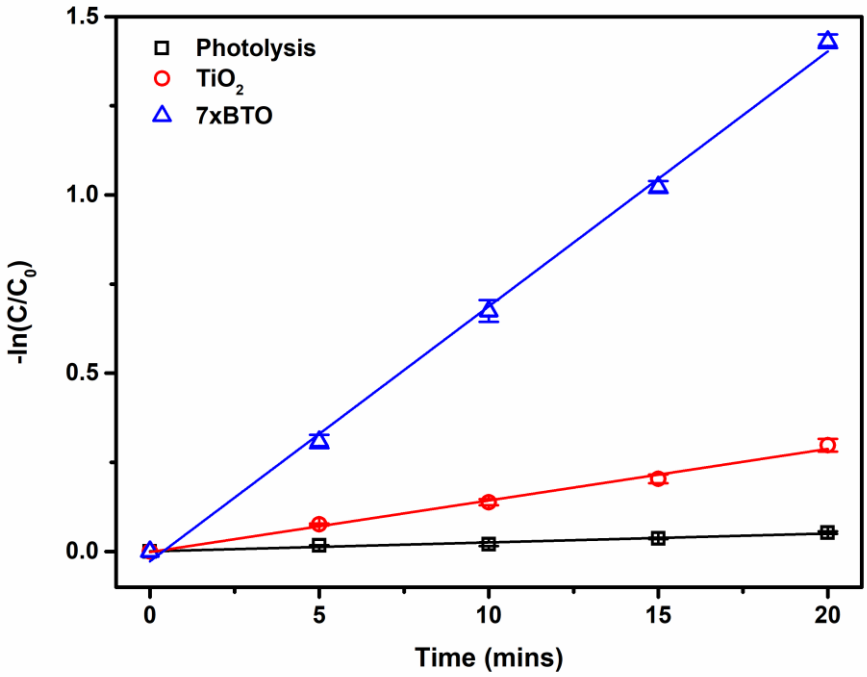

Figure 3.32. Example first order rate plot for the degradation of TNT

Other first order rate plots were calculated in the same way. Each species was observed to degrade at somewhat different rates, with different improvements over the TiO_2 and photolysis controls. In every case however, the BTO-modified photocatalyst performed substantially better than unmodified TiO_2. First order rate constants for the 7xBTO samples and controls are given in Figure 3.33.

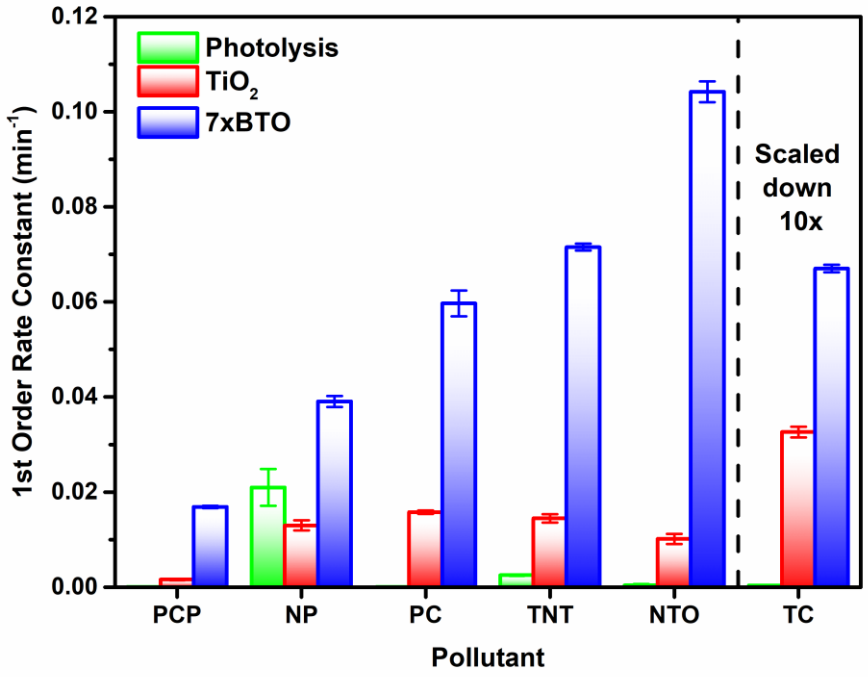

Figure 3.33. First order rate constants of the 7xBTO, pristine TiO_2 and photolysis control against the chosen pollutants

Highest activity was noted for the degradation of TC, achieving ~94% removal in 4 minutes of irradiation, a first order rate constant of 0.67 min^{-1}, note should be taken of the scaling necessary in Figure 3.33 to bring the bar into a similar range to the others due to this high efficiency. It is possible that some sensitization of the semiconductor was occurring due to this surface adsorption of TC, as the LED used has some overlap with the absorption spectra of TC. During the test it is possible that this increased activity, and relatively high activity on plain TiO_2, is in part due to excitation and subsequent electron or hole transfer from TC to the semiconductor photocatalyst in the same way that sensitisation with a dye works. While this can be advantageous as it typically increases photocatalytic rates, care should be taken when suggesting photocatalytic activity based on such a test alone. Aside from TC, the other molecules studied showed varying degrees of activity, with rate constants ranging from 0.017 min^{-1} for PCP to 0.10 min^{-1} for NTO. Interestingly, there seemed little link between structural features and degradation rate. PCP, PC and NP may be grouped together as phenolic pollutants; however, it can be noted that PCP degrades much slower than PC and NP. A likely caused for this could be the highly electron deficient nature of the

aromatic ring system due to the presence of five chlorine substituents. Often for phenolic pollutants a key step is the hole driven oxidation of the phenol ring, followed by hydroxylation of the resulting radical[68]. Previous studies on pentachlorophenol have suggested that the presence of multiple electron withdrawing groups will make such molecules resistant to oxidation in this way[69]. Aside from the phenolic type pollutants, TNT and NTO can be grouped as nitro group containing compounds. While greater in similarity in terms of their degradation rate than the phenolic pollutants, it was noted that NTO was destroyed somewhat quicker than TNT. This difference can be ascribed once again to the effects of self-sensitisation of NTO on the photocatalyst surface. NTO has an absorption tail into the emission wavelength region of the LED light source and hence a similar sensitization mechanism as described for TC can be assumed.

This study highlights the significant differences in photocatalytic degradation rates that can be demonstrated even when studying relatively similar molecules, suggesting that there may be many previously reported photocatalyst materials which may behave very differently against targets other than those for which they have been reported. While some thorough studies covering large groups of similar compounds exist[70,71], it is much more common to test on a single model pollutant, and as such there are many studies to date which may not completely reflect potential of the material in question. While there is clearly a place for short studies using a single pollutant to demonstrate interesting activity, if claims are to be made about the promise or otherwise of a material, demonstration of activity against a broader pollutant scope is key.

3.3.2.3.2 Mechanistic Studies

Quantification of the degradation was achieved according to degradation efficiency (DE) achieved by the photocatalyst upon the pollutant solutions spiked with methanol and *tert*-butanol and degassed with N_2 to gain insight into the photocatalytic mechanism. The results of the scavenging tests are shown in Figure 3.34.

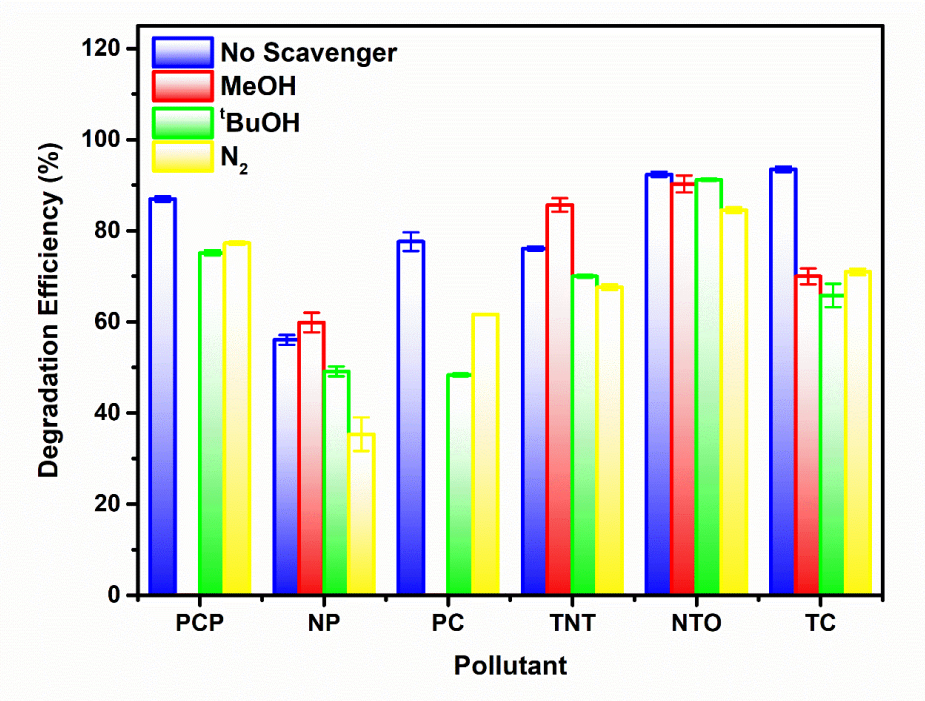

Figure 3.34. Scavenging testing of 7xBTO against the chosen pollutants

Both PCP and PC showed significant losses in activity on introduction of methanol, supporting the previously reported degradation pathway of oxidation via surface holes. However, the other phenolic pollutant NP showed no loss in activity when spiked with methanol, instead a slight increase in DE was noted indicating that this mechanism does not hold for NP. Instead the greatest loss of efficiency was observed upon degassing the solution with N_2, shutting down the possibility of formation of the superoxide ion by electron transfer from the semiconductor valence band to O_2. The increase in DE upon addition of methanol supports the main reactive species involved in the degradation of NP is generated via electron transfer reactions to O_2. As addition of methanol is scavenging for holes the chance that photoexcited electrons in the conduction band will simply recombine is reduced, leaving them free to form greater quantities of superoxide. It has been shown that combining NP with other organic molecules can, in fact, increase degradation rates as the akyl chains of nonyl phenol assist in bringing non-polar molecules in close proximity to the photocatalyst surface[72]. Scavenging tests on TC showed a decrease in the DE for every scavenger introduced. Thus, no single reactive species can be concluded to be essential for the degradation

of TC, the decomposition of which likely goes by a combination of different mechanisms. Given the size and relative complexity of the TC molecule compared to the other pollutants tested, it is unsurprising that TC may have multiple different degradation routes. The nitro group containing TNT and NTO pollutants demonstrated only very slight losses in activity on introduction of any of the scavenger molecules. It was noted that upon introduction of scavengers to the degradation of TNT and NTO that a new asymmetrical peak at around 197 nm appeared as shown in Figure 3.35.

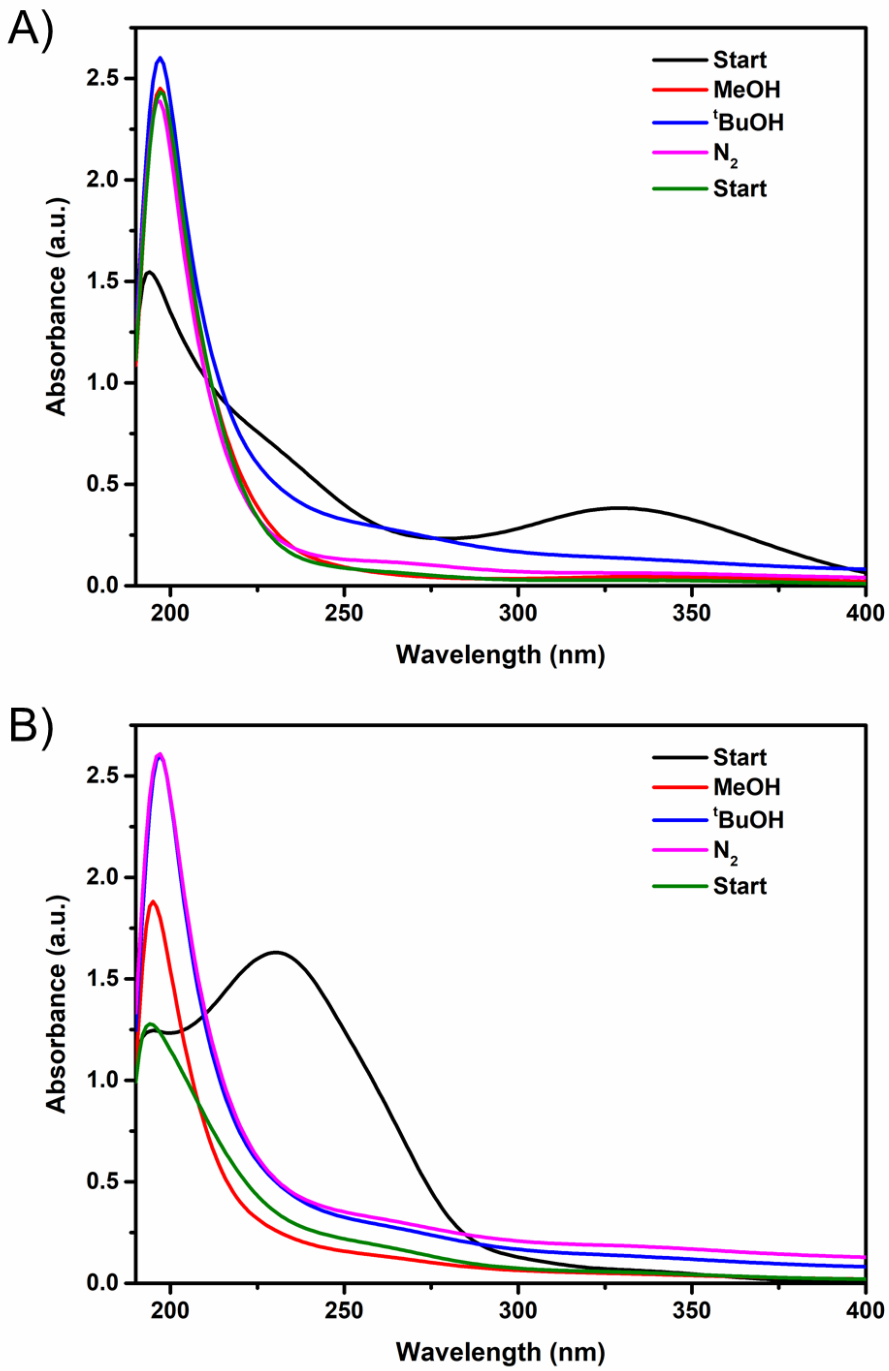

Figure 3.35. Spectral changes of A) NTO and B) TNT upon photodegradation using 7xBTO in the presence of various scavengers.

It is known that nitrate (NO_3^-) has an absorption peak in this wavelength region[73], which is known to be sometimes formed when nitro containing compounds are photocatalytically degraded[74]. It has been shown that nitrate can affect photocatalytic

reactions by scavenging for hydroxyl radicals[75], explaining why when other scavengers for such species are introduced that the nitrate concentration is able to rise. Hence, while no loss in the destruction of TNT and NTO was noted upon addition of any of the scavengers, it is clear that these species do play a role in the degradation.

3.3.2.3.3 Recyclability Tests

Recycling tests were carried out by introducing fresh pollutant solution and testing in the same way as before and quantified according to their DE, the results of which are given in Figure 3.36.

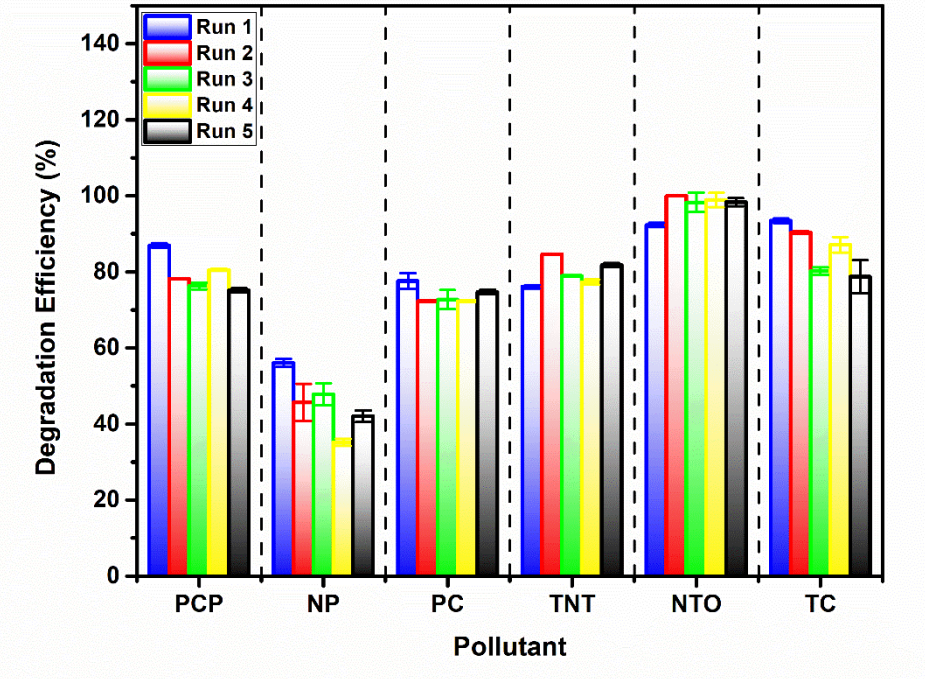

Figure 3.36. Recycling tests of 7xBTO against the chosen pollutants

No losses in activity were noted for the photocatalyst against all pollutants other than nonyl-phenol, where the DE decreased from ~56% to around 35% at its lowest. Losses such as this can be due to incomplete destruction of the pollutant, leaving degradation products on the semiconductor surface and hindering the degradation of fresh pollutant. Interestingly, there appeared to be a small increase in activity for NTO after recycling, going from ~93% to ~99% DE. This could be due to the same self-sensitisation effect noted earlier, where some of the NTO molecules are retained from

the previous run and are able to sensitise the 7xBTO material to the LED light source, increasing the DE.

The good recyclability demonstrated in this work is a key feature of the photocatalyst bead system, where the photocatalytic material is both stable under irradiation and adhered well enough to the substrate to be repeatedly immersed in water samples with no loss of activity. Coupling such recyclability with the immobilization of the photocatalyst material indicates the potential of a system such as this for real world application.

3.4 Lanthanum Vanadate – TiO_2 Composites

3.4.1 Introduction

To overcome fast charge recombination by providing charge separation across an interface, the choice of material for combination with TiO_2 is key, as the band energies must align correctly for charges to separate across the interface efficiently. Many successful composites in this area have a staggered band arrangement, where conduction and valence bands of one material lie slightly above those of the other, known as a type-II junction. Many different oxides and sulfides have been shown to form a Type-II junction with TiO_2[3], and these often demonstrate improvements in a variety of different photocatalytic reactions due to improved charge separation[76,77].

A potential candidate material for formation of a type-II junction with TiO_2 is lanthanum vanadate ($LaVO_4$). Thoroughly explored as a phosphor matrix material[78,79], it has been somewhat overlooked in the field of photocatalysis. A few examples exist of $LaVO_4$ being combined with TiO_2, with some focusing upon the application of the heterojunction in gas phase photocatalytic degradation reactions[80–83].The work of Fang *et al.*[80] and Huang *et al.*[83] have demonstrated that $LaVO_4$ forms with a monoclinic structure on the surface of TiO_2, with a relatively narrow band gap of around 2.1 eV, which in both cases proved effective for the gas phase degradation of benzene. Conversely, in this work, a method has been developed by which an amorphous phase of $LaVO_4$ may be formed on TiO_2 in a conformal layer arrangement. Using a pre-immobilised TiO_2 substrate on glass beads, a SILAR method has been applied to deposit a thin conformal layer of $LaVO_4$ onto the TiO_2 surface. To date, this is the first example of $LaVO_4$ being prepared by SILAR and represents a new easily controllable method by which thin layers of $LaVO_4$ can be prepared for a variety of different applications. It is demonstrated that $LaVO_4$ prepared in this manner has a significantly wider band gap of 3.5 eV, but that the conduction and valence band both are arranged in the same staggered type-II arrangement as previous reports. This new composite has been found to be effective for the photocatalytic degradation of 4-chlorophenol in water, and a mechanism for this activity based upon the type-II band arrangement of the two materials is proposed.

3.4.2 Results & Discussion

3.4.2.1 Photocatalyst Preparation

TiO_2 was coated onto soda lime glass beads according to our previously reported method using the previously discussed water based TiO_2 suspension. To the TiO_2 coated beads, $LaVO_4$ was deposited by SILAR. A schematic describing the entire process is given in Figure 3.37.

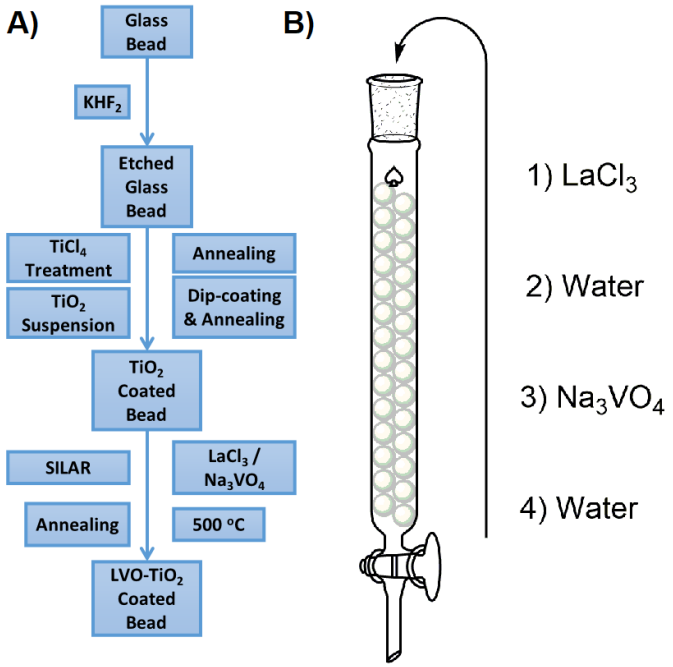

Figure 3.37. A) General process of producing the LVO-TiO_2 composites. B) SILAR deposition of LVO onto the TiO_2 coated glass beads

In brief, aqueous solutions of $LaCl_3$ and Na_3VO_4 were sequentially introduced to a column packed with TiO_2 coated beads, washing with water between each solution. This process was repeated between 2 and 8 times, to build up varying levels of $LaVO_4$ onto the TiO_2 surface, and as such the samples were denoted NxLVO, where N is the number of SILAR cycles. The process was also repeated on flat microscope glass slides and conducting FTO glass to facilitate some analyses.

3.4.2.2 Materials Characterisation

3.4.2.2.1 Phase & Morphology

X-ray diffraction (XRD) was used to analyse the crystal structures of the prepared materials (Figure 3.38).

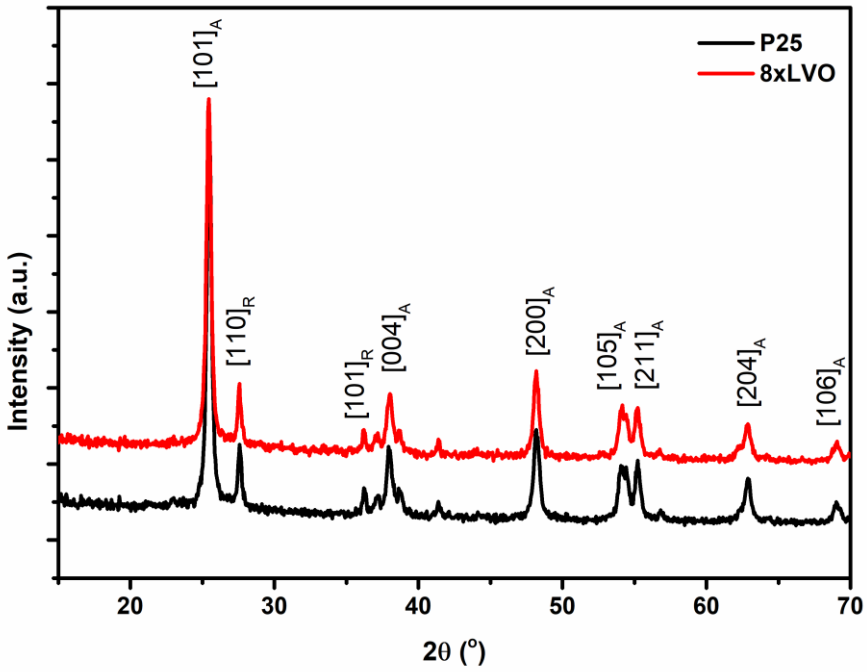

Figure 3.38. XRD traces of the unmodified TiO_2 and LVO modified TiO_2

No new peaks were observed after SILAR deposition of $LaVO_4$, with the remaining peaks being indexed to the anatase and rutile forms of TiO_2. This has been noted previously by Fang et al in their preparation of $LaVO_4$-TiO_2 composites[80], and was determined to be due to low concentration and small particle sizes of $LaVO_4$ produced in their work. To overcome these barriers, a sample of $LaVO_4$ using the same precursors was prepared by simple precipitation and annealing, which was found to give diffraction peaks mainly corresponding to the tetragonal form of $LaVO_4$ (Figure 3.39).

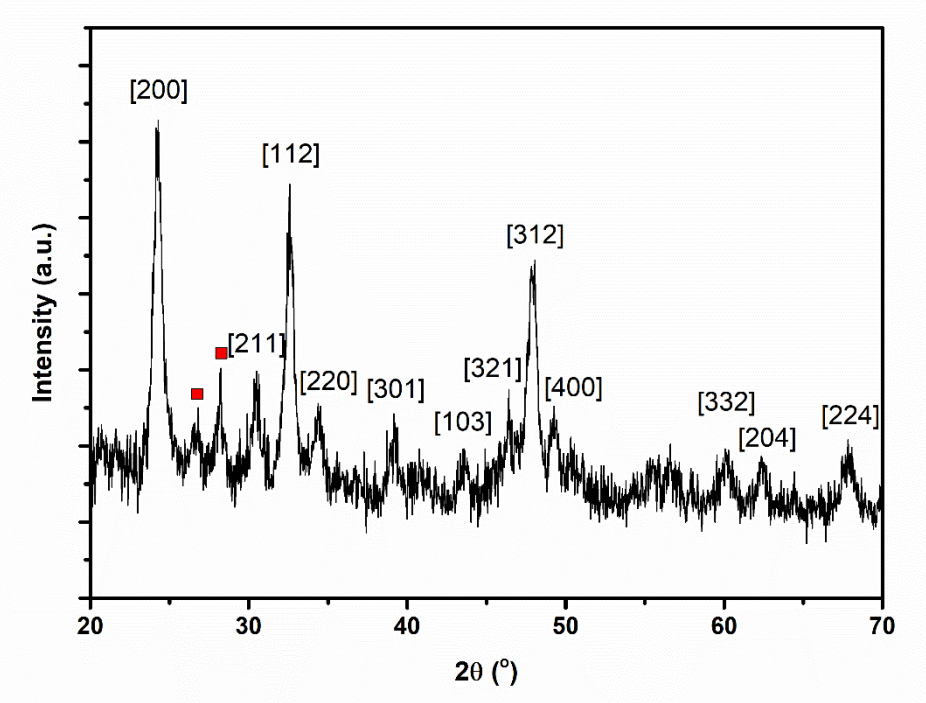

Figure 3.39. XRD trace of the precipitated LVO material with peak assignments. Red squares indicate peaks from the monoclinic phase of LVO.

A few lower intensity peaks were identified in this trace as possibly being present due to small amounts of the monoclinic phase, indicating that his precipitation had given a mix of phases (red squares in Figure 3.39), but with the tetragonal form as the main product. As SILAR can be considered as a controlled precipitation reaction on the TiO_2 surface, the $LaVO_4$ produced by this process might be expected in the tetragonal form, however in this case it is found to be amorphous likely due to size restrictions originating from the small TiO_2 substrate particle sizes.

SEM images of the P25 films modified with $LaVO_4$ showed little to no observable difference in morphology upon repeated SILAR cycles (Figure 3.40).

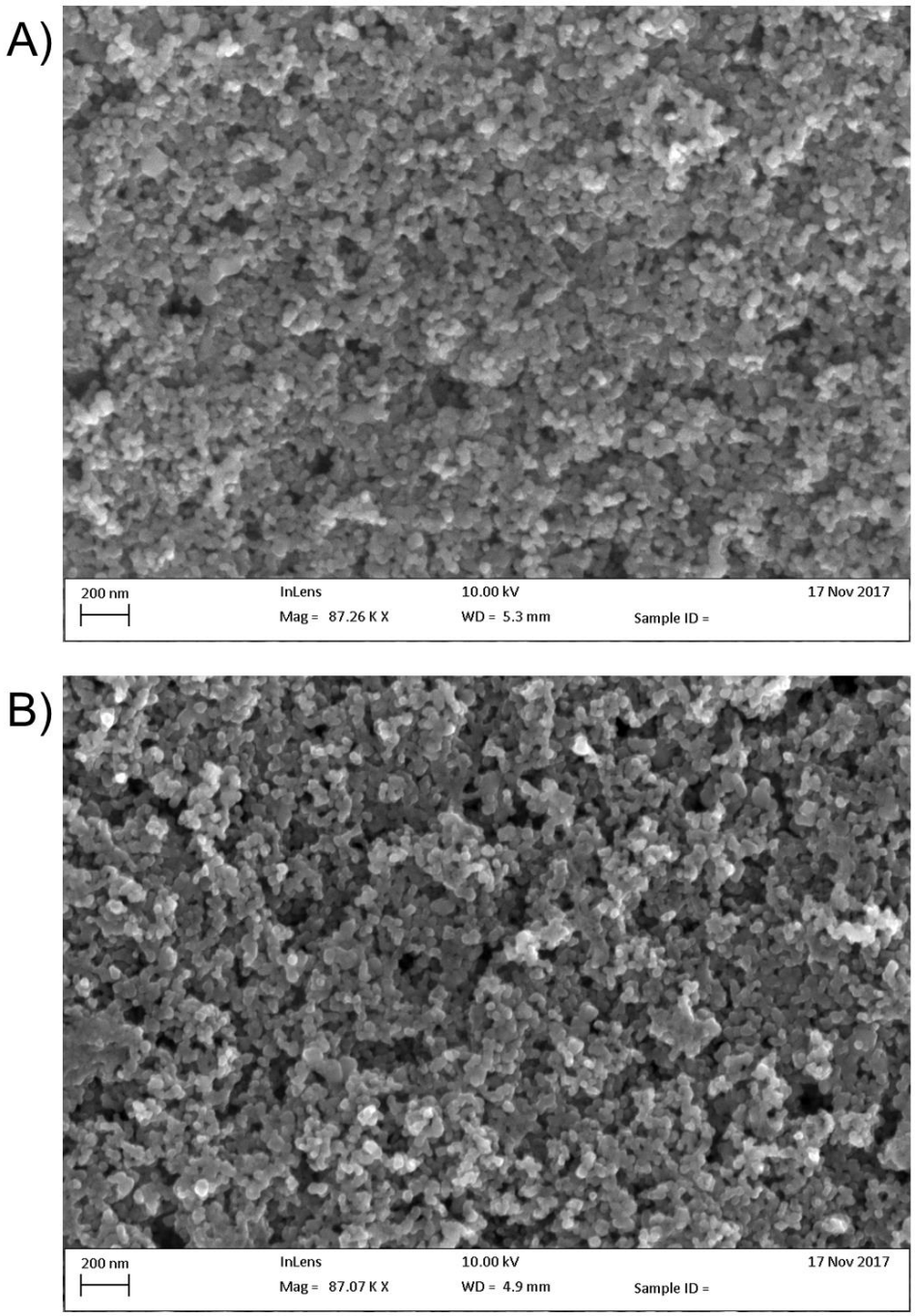

Figure 3.40. SEM images of A) the pristine TiO_2 film surface and B) the 8xLVO sample surface

This would suggest that the growth of $LaVO_4$ on the TiO_2 surface forms a conformal layer, and as such the particles appear approximately the same in terms of morphology.

Transmission electron microscope (TEM) images agreed with the conclusion of the SEM studies, with little morphological difference being apparent upon SILAR

processing. However, close inspection of the images revealed signs of a thin surface coverage of a secondary material (Figure 3.41).

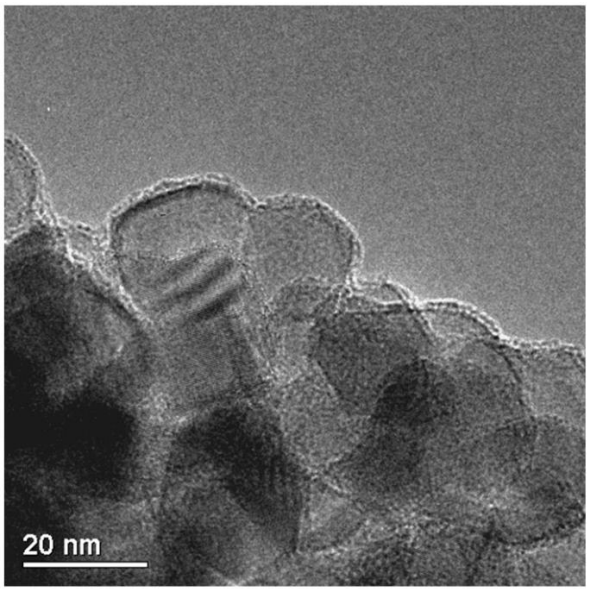

Figure 3.41. TEM image of the 8xLVO material

Scanning transmission electron microscope high angle annular dark field (STEM HAADF) images revealed some very small aggregates formed on the surface (Figure 3.42).

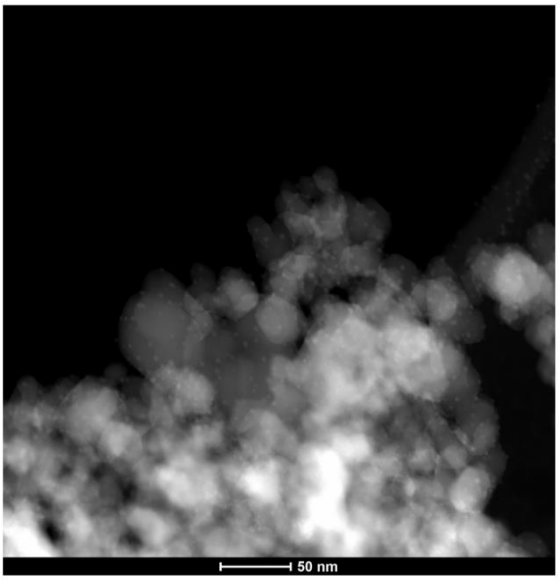

Figure 3.42. STEM-HAADF image of the 8xLVO material

Appearing as small light dots in the HAADF image, these aggregates, which are likely to be LVO, are of around 2-5 nm and as such would not have peaks in the XRD, which agrees with the lack of LVO crystal reflections observed.

3.4.2.2.2 Elemental Analysis

Elemental analysis using energy dispersive x-ray spectroscopy (EDX) analysis was used to quantify the levels of La and V being deposited by the SILAR process (Figure 3.43).

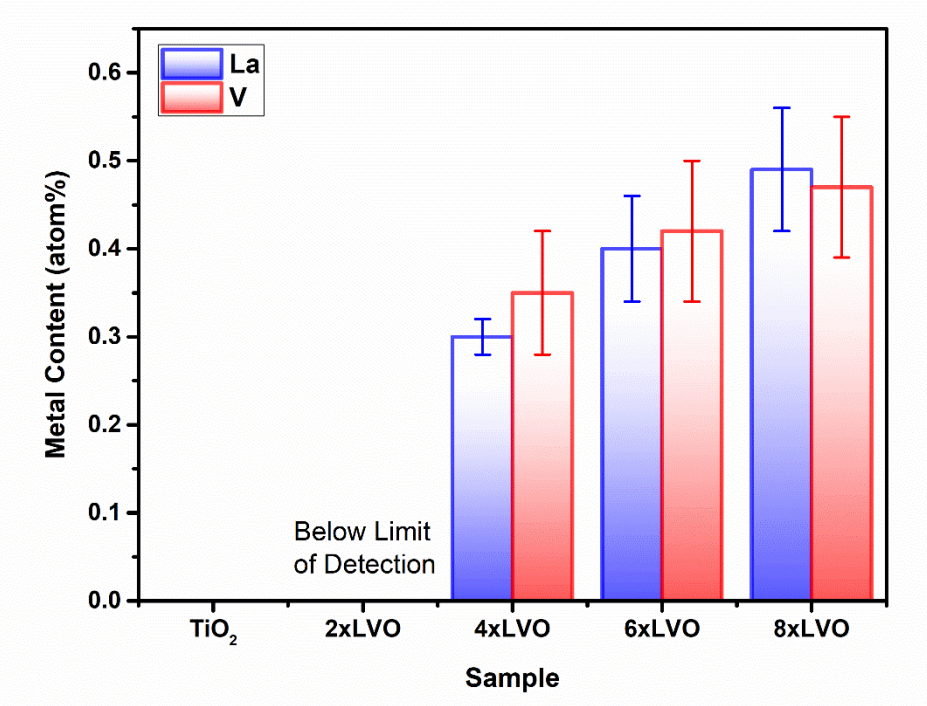

Figure 3.43. EDX analysis of the La and V content of the LVO modified TiO_2 materials

Small numbers of SILAR cycles were found to introduce very low amounts of La and V, which were below the detection limit of the instrument used in this study. However, repeated SILAR cycles were found to deposit higher levels of both La and V onto the TiO_2 substrate, in a ratio within experimental error of 1:1, indicating the formation of pure $LaVO_4$. In a similar manner, TEM EDX element mapping experiments revealed a full surface coverage of LVO present across the whole of the observed sample (Figure 3.44).

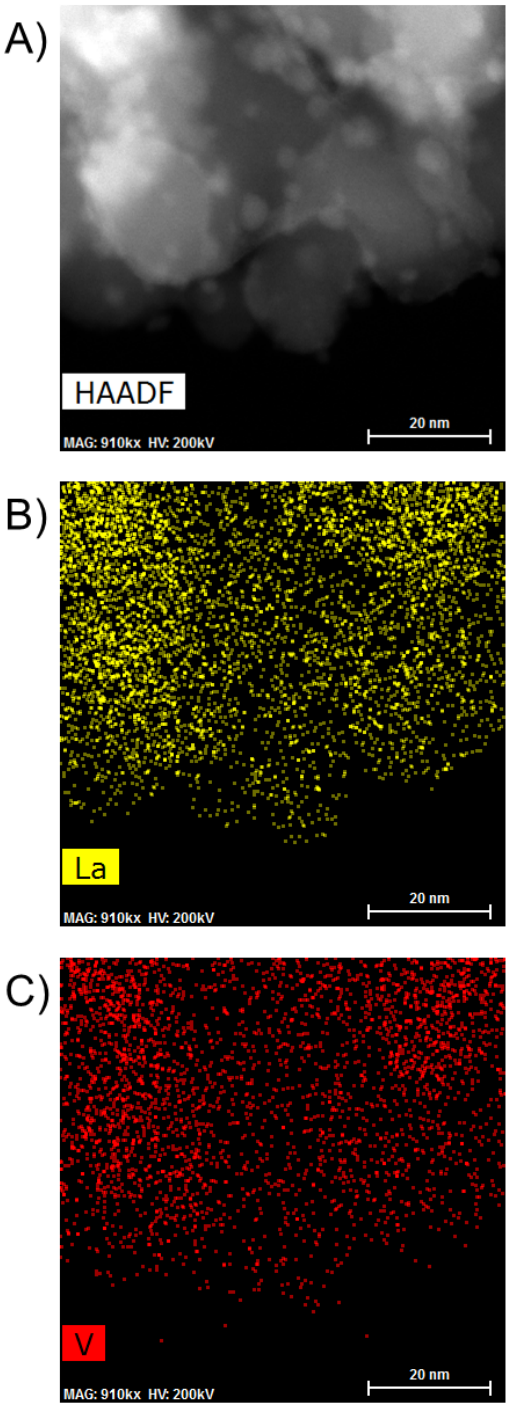

Figure 3.44. A) STEM-HAADF image of 8xLVO with corresponding elemental maps for B) La and C) V

No distinct areas of high concentration were noted, indicating that the LVO material forms across the surface of the whole P25 particle surface. The formation of LVO can

therefore be determined to give a combination of 2-5 nm particles contained within a continuous layer of LVO on the P25 surface.

To further establish the formation of $LaVO_4$, x-ray photoelectron spectroscopy (XPS) was used to identify the chemical environments of the constituent elements in the 8xLVO and unmodified TiO_2 samples (Figure 3.45).

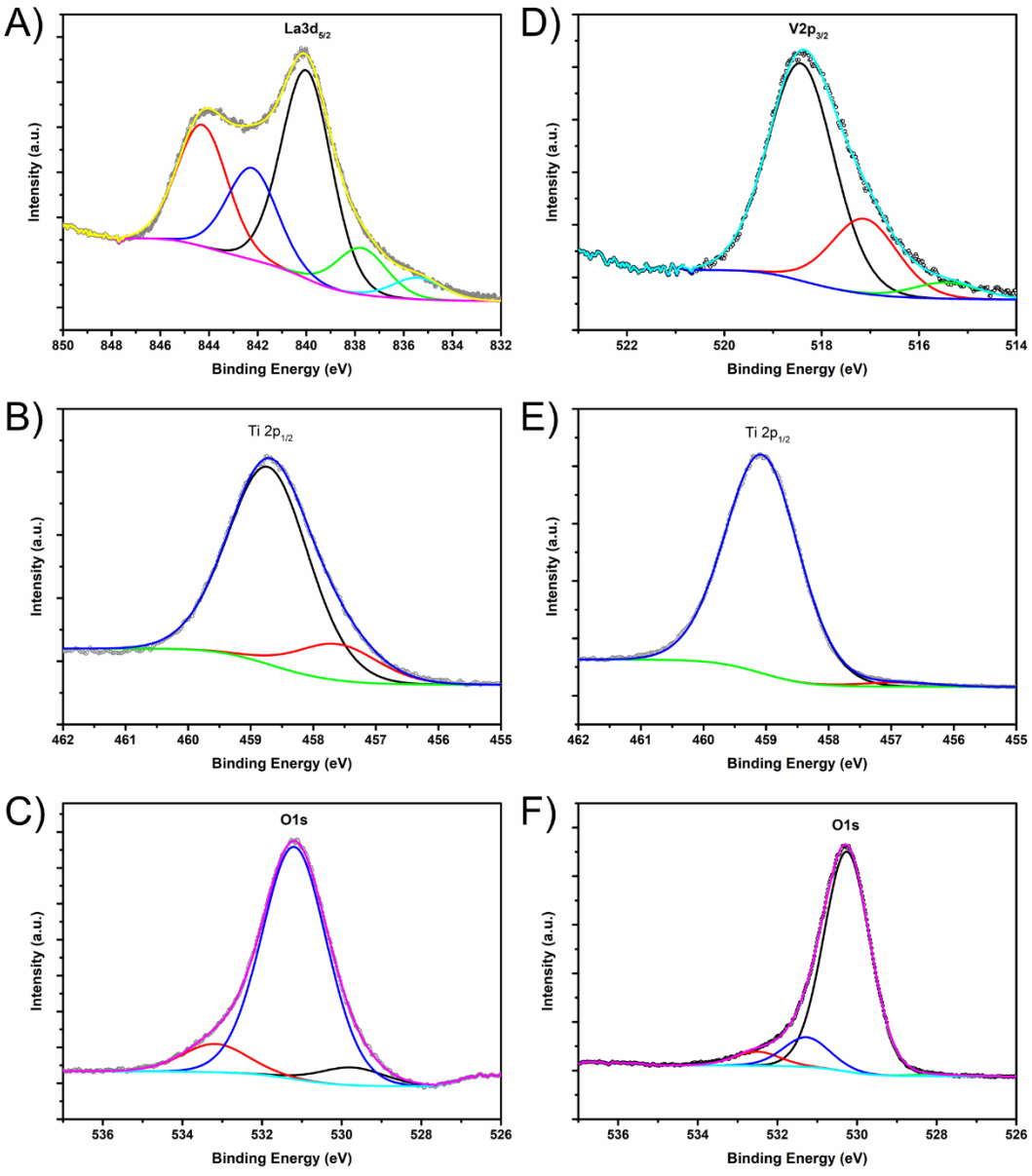

Figure 3.45. XPS scans of the 8xLVO A) La 3d region B) Ti 2p region C) O1s region D) V2p region and pristine TiO_2 E) Ti 2p region and F) O1s region

Peaks due to the La $3d_{5/2}$ were identified at binding energies of 840 eV and 844 eV, agreeing well with previous reports for La in LVO[84]. The peak at 518 eV may be assigned to vanadium in LVO[85]. The peak at 530 eV may be assigned to oxygen, with shoulders which may either be due to a slight difference in the binding energy of LVO based O atoms compared with TiO_2 based O atoms, or surface bound water molecules[86]. A peak at 459 eV was observed, which may be simply assigned to a emission of electrons from a Ti 2p orbital, a slight shoulder was noted when modification with LVO was applied, indicating a second chemical environment, likely due to Ti in close proximity with surface LVO.

To further confirm the presence of LVO on the TiO_2 surface, and to overcome any surface sensitivity of the XPS and TEM/SEM-EDX measurements, the La and V contents were examined by dissolving the LVO material in strongly acidic conditions and studying the resulting solution using ICP-OES (Figure 3.46).

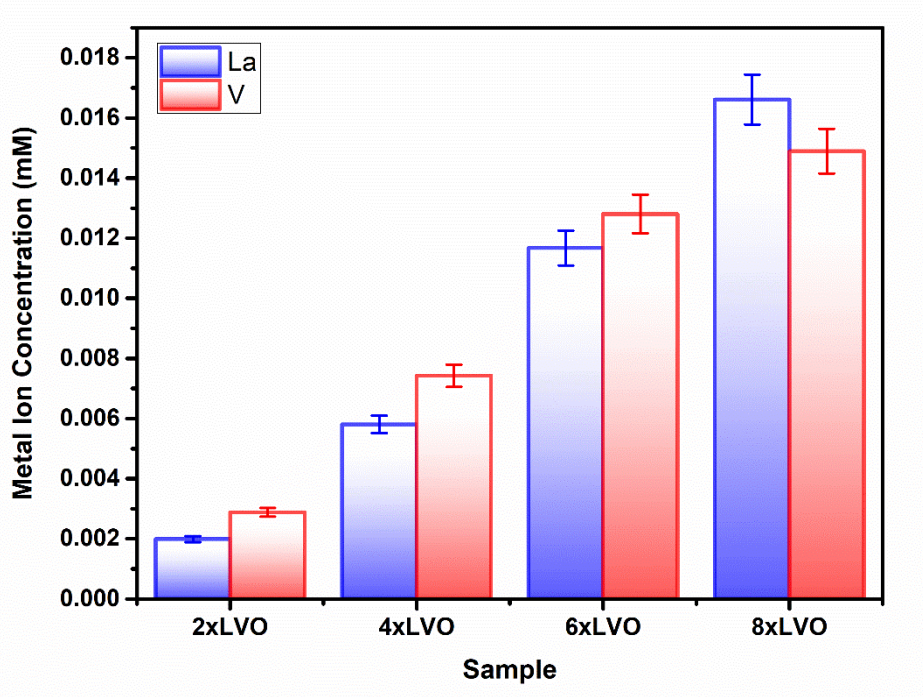

Figure 3.46. ICP-OES analysis of the La and V content in an acidic leach solution of the LVO modified samples

La and V were observed to be present in approximately a 1:1 ratio, confirming the formation of pure LVO by SILAR. Increased numbers of SILAR cycles were found to

give higher concentrations of La and V in the leached solution, but the ratio remained to be ~1:1.

3.4.2.2.3 Band Alignment Determination

Key in photocatalytic activity of a composite is the alignment of valence and conduction bands of the two constituent materials. In this regard, diffuse reflectance and electrochemical impedance measurements were used to construct a band alignment diagram.

Absorption profiles of LVO, TiO_2 and the LVO-TiO_2 composite materials were measured using diffuse reflectance spectroscopy (Figure 3.47).

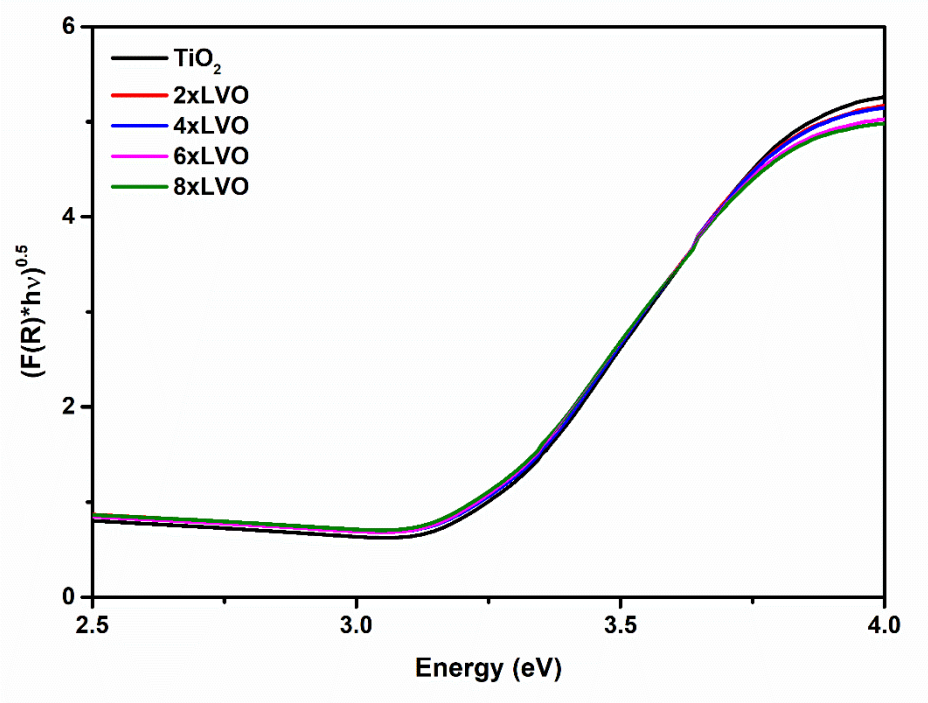

Figure 3.47. Diffuse reflectance derived Tauc plots of the TiO_2 and LVO modified films

Band gaps were estimated by extrapolation of the Tauc plot according to the Tauc equation. No shift of the TiO_2-LVO composites was noted on SILAR cycling, indicating that the band gap of the deposited LVO material is masked by the onset of the TiO_2 absorption. In keeping with this observation, the band gap of the pure tetragonal LVO material, prepared by precipitation, was found to be 3.4 eV (Figure

3.48), consistent with previous reports for tetragonal LVO[86] rather than the narrower value of 2.2 eV for the monoclinic phase[87].

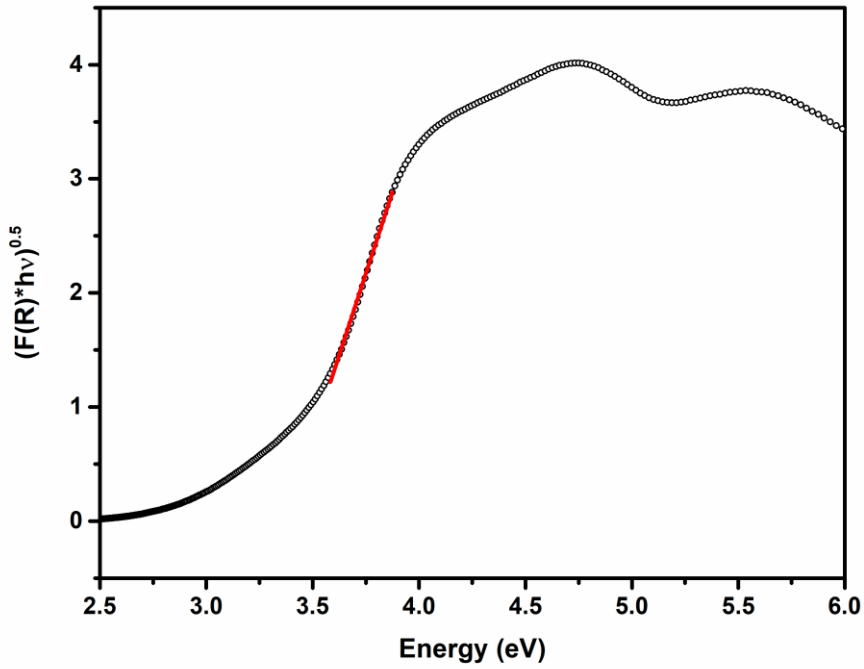

Figure 3.48. Tauc plot derived from diffuse reflectance data for the pure precipitated LVO material

To gauge the flat band energy of LVO relative to TiO_2, Mott-Schottky analysis was carried out in 0.5 M Na_2SO_3 at the frequency of 10 KHz in the dark (Figure 3.49).

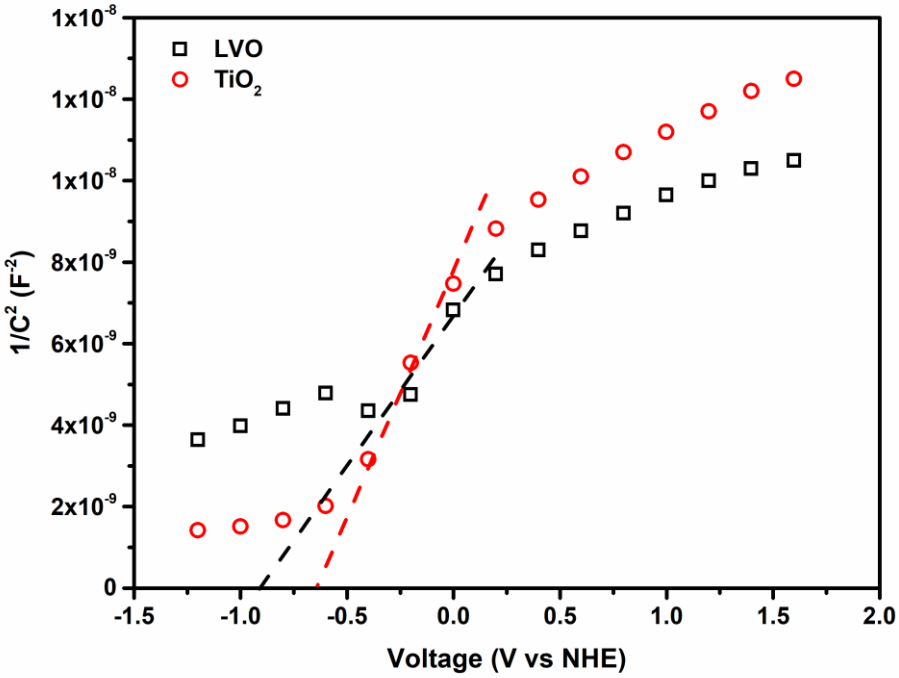

Figure 3.49. Mott-schottky analysis of the pristine TiO_2 and LVO materials

Both materials displayed plots consistent with the materials in question being of n-type conductivity[88,89], with a positive slope in the linear region of the plot. Therefore, the difference in conduction band energies between LVO and TiO_2 in the prepared composites is the same as the shift in flat bands, with the conduction band of LVO lying 0.27 eV cathodically shifted from TiO_2.

Using both band gaps obtained by diffuse reflectance measurements and conduction band shifts obtained using Mott-Schottky analysis, a theoretical band alignment diagram may be constructed (Figure 3.50).

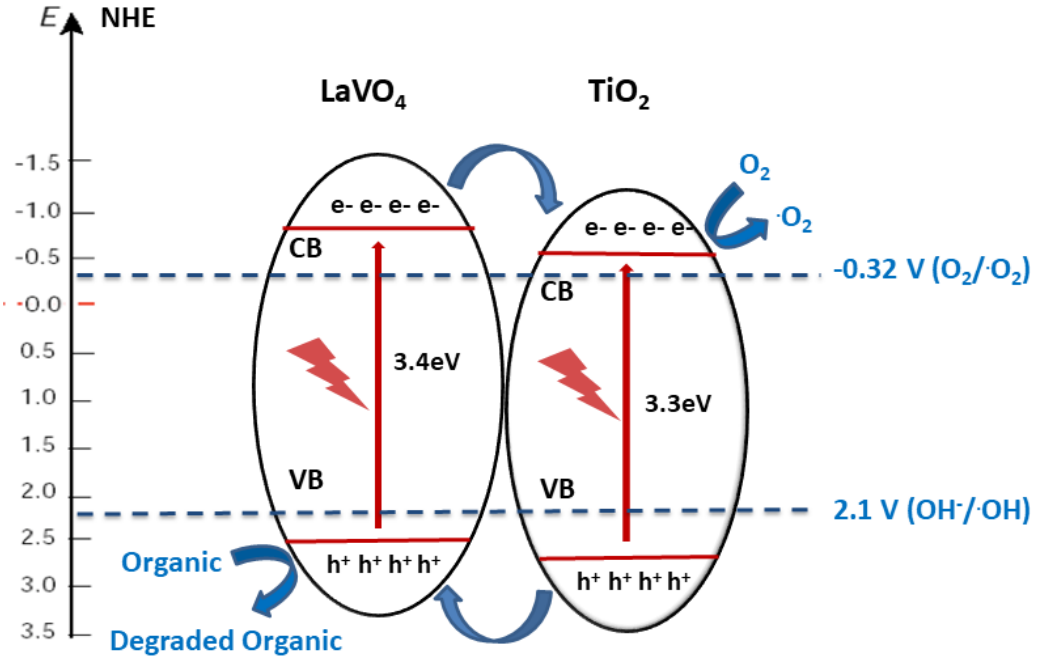

Figure 3.50. Band energy alignment diagram of the LVO-TiO_2 interface showing charge separation and potential ROS generation

Where the difference in the conduction band energies are determined by Mott-Schottky analysis and the valence bands are calculated based on the band gaps determined by diffuse reflectance spectroscopy. The prepared composites demonstrate a type-II heterojunction structure, allowing photoexcited electrons and holes to separate from LVO to TiO_2 conduction bands, and from TiO_2 to LVO valence bands respectively. As per the annotated radical formation redox processes in Figure 3.50, it is clear that the prepared materials have the potential to form key radical species used in the degradation of organic pollutants.

Photoluminescence (PL) spectroscopy was used to probe the degree of charge separation in the composites (Figure 3.51).

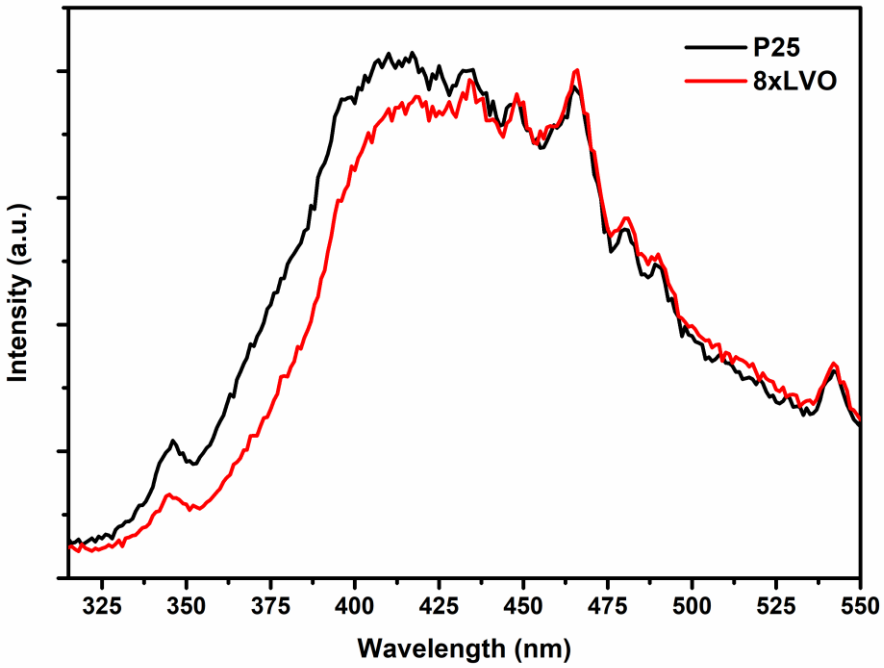

Figure 3.51. Photoluminescence spectra of the pristine TiO_2 and 8xLVO samples excited at 300 nm

It is well established that a reduction in PL intensity from a semiconductor composite indicates a reduction of charge recombination[90]. This can be ascribed to increased charge separation across the interface between the two materials, typically leading to increased photocatalytic activity[91]. When excited at 300 nm, the unmodified P25 produced a broad emission from 350 to 550 nm. When modified with LVO however this emission was reduced somewhat between 325 and 425 nm, indicating transfer of photoexcited electrons and holes between the two materials, reducing the likelihood of recombination. As previously noted, some of this reduction could be due to re-adsorption of emitted photons, however as the band gap of the composite material was found to not differ significantly from the TiO_2 and considering the pure LVO band gap of around 3.4 eV it is unlikely that this is the case. The reduction of emission from the composite therefore can be ascribed to separation of photogenerated charges across the LVO-TiO_2 interface.

3.4.2.3 Photocatalytic Activity

Testing of the photocatalytic bead system was carried out by packing the coated beads into a jacketed condenser type reactor. To the column was added a pollutant solution

and the whole apparatus irradiated with a 400W halogen lamp for 180 minutes. Performance of the photocatalysts was determined according to the degradation efficiency (DE) Initial optimization of the number of SILAR cycles used in the preparation of the photocatalytic beads was studied using the degradation of the model pollutant 4-chlorophenol (4CP) (Figure 3.52).

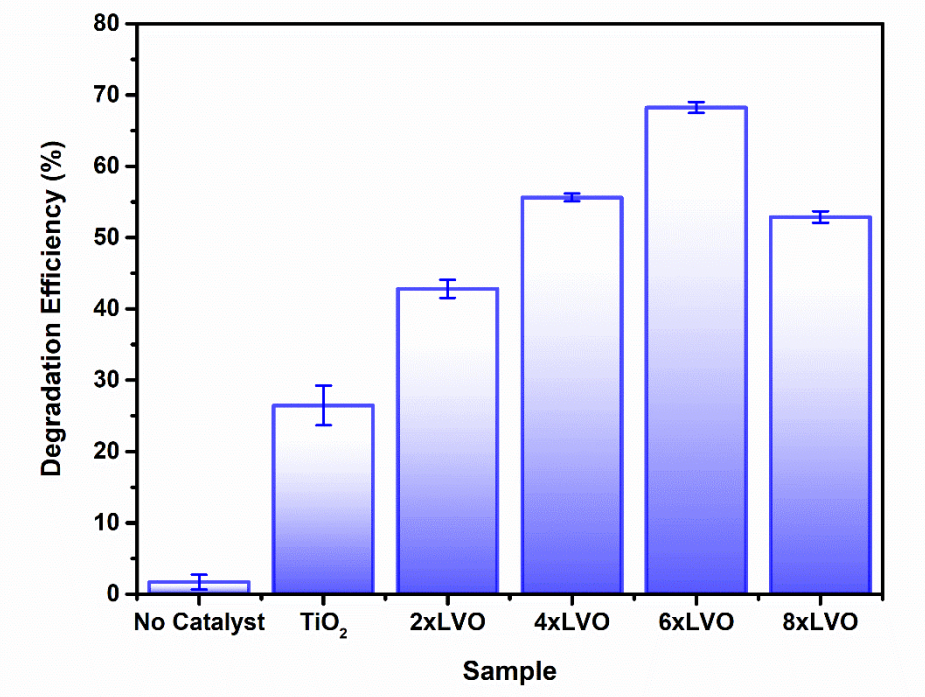

Figure 3.52. Degradation efficiency of the prepared materials against 4CP

An increase in the degradation efficiency was observed between the samples 2xLVO to 6xLVO, however upon addition of a further 2 SILAR cycles to give 8xLVO a reduction in activity was noted. Thus, the optimal number of SILAR cycles was determined to be 6. As the SILAR processing of LVO on TiO_2 gives as a conformal layer covering the TiO_2 surface, an optimal coverage of LVO has clearly been reached by the 6^{th} SILAR cycle, and further processing causes inhibition of the TiO_2 surface and subsequent formation of reactive species.

To probe the photocatalytic mechanism, scavenging tests were applied to the degradation of 4CP by introduction of methanol, *tert*-butanol and degassing with N_2 (Figure 3.53).

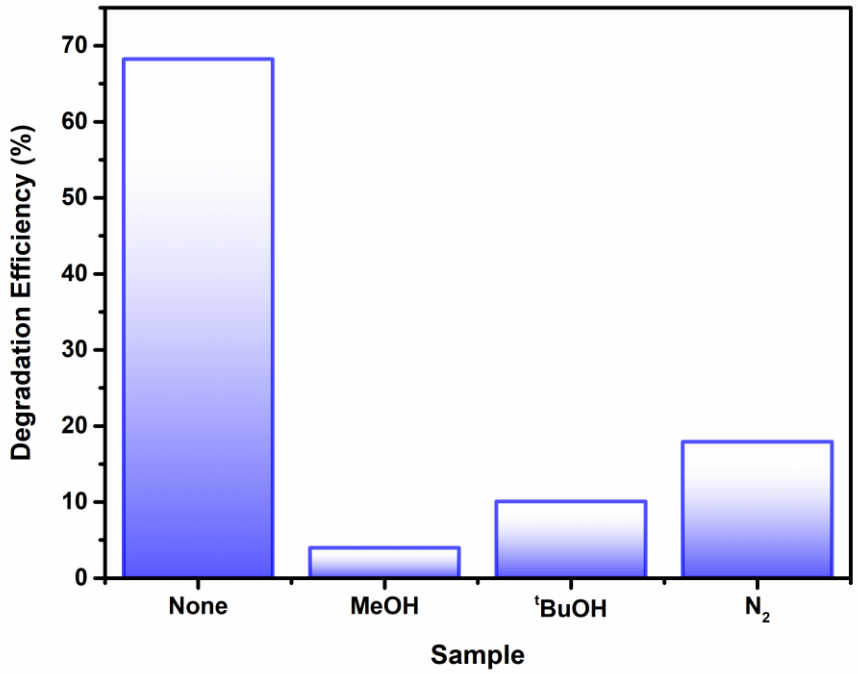

Figure 3.53. Scavenging tests of 6xLVO against 4CP

Introduction of all scavengers resulted in large drops in activity when compared to the baseline sample, indicating that each reactive species is involved to some extent in the photocatalytic degradation mechanism. A widely studied route for photocatalytic destruction on TiO_2 surfaces is the hole driven formation of hydroxyl radicals from hydroxide or water[92], supporting the similar losses of activity noted when holes and hydroxyl radicals are scavenged from the reaction. Removal of O_2 from the photocatalytic system also results in a large loss of activity, indicating that the formation of the superoxide radical is key in the degradation of 4CP. However, it is possible that by removing the main way in which electrons are trapped at the surface that recombination is favoured, reducing the number of reactive holes and/or hydroxyl radicals. In this way it is clear that each reactive species has a role in the overall degradation mechanism.

3.5 Chapter 3 Conclusions

Composites of two materials, bismuth titanate and lanthanum vanadate, and TiO_2 have been prepared, characterised and tested. These materials have been immobilised on glass beads as a support and applied to a variety of different photocatalytic tests to evaluate activity and applicability.

A sequential ionic layer adsorption reaction method and thermal annealing has been investigated as a new way to produce bismuth titanate on titanium dioxide surfaces. This route is previously unknown in the literature and demonstrates that SILAR may be used to generate more than simple binary chalcogenides. The TiO_2-BTO system has been found to be effective on molecular organic targets, providing high degradation and a degree of mineralisation, as well as photocatalytic bactericidal properties.

The SILAR BTO modified TiO_2 system has been applied against a variety of different pollutants including drugs, pesticides, industrial intermediates and explosives using an inexpensive 410 nm LED light source. An investigation into the mechanism of photocatalytic degradation of the prepared photocatalyst beads against each target molecule is presented, concluding that even when comparing pollutants with similar structural features distinct differences in mechanism can be noted. Each pollutant tested in this study showed little to no loss of photocatalyst activity after five recycles, indicating the good stability of the material, and the strong adhesion to the glass bead substrate. This work demonstrates the viability of our immobilized and enhanced TiO_2-based system to a wide range of pollutants, however also draws attention to the major differences in photocatalytic rates which can be demonstrated against different target molecules.

SILAR has also been applied as a method by which $LaVO_4$ may be deposited in a controlled manner as a conformal layer onto the surface of P25 TiO_2 particles. This $LaVO_4$ layer has been shown to be amorphous in nature due to its small scale, however synthesis of larger scale particles has shown that this method preferentially forms the tetragonal form of $LaVO_4$, in contrast to other previously reported methods for $LaVO_4$ deposition. The electronic structure of this composite material of $LaVO_4$ and TiO_2 has

been determined by diffuse reflectance and Mott-Schottky analyses to be of a type-II heterojunction, with both conduction and valence bands of $LaVO_4$ lying cathodically shifted from those of TiO_2. This heterojunction structure thermodynamically allows charge separation and has been shown to give improved activity for the photocatalytic degradation of a model pollutant 4-chlorophenol.

Thus, composites of wide band gap semiconductors and TiO_2 immobilised on glass bead substrates are demonstrated to be a promising method of removing a variety of different pollutants from water. High driving force for degradation arises from widely separated valence and conduction band energies but relies upon the use of relatively high energy irradiation. Further work focused upon using narrower band gap materials which have greater response under visible light.

3.6 Chapter 3 Specific Experimental

3.6.1 Sample Preparation

3.6.1.1 Glass Bead Etching & Pre-treatment

Soda-lime glass beads were added into a solution of potassium bifluoride (10 mg ml^{-1}) and left to etch for 3 days, with occasional agitation. The beads were then rinsed thoroughly with water, then sonicated in water for 15 minutes, followed by rinsing with ethanol and sonication in ethanol for a further 15 minutes. The beads were then recovered and dried at 100 ^oC for 30 minutes before use. The beads were then treated with $TiCl_4$ (40 mM) at 70 ^oC for 30 minutes and then annealed at 500 ^oC for 30 minutes.

3.6.1.2 TiO_2 Suspension Preparation

The water-based suspension was prepared as follows. P25 TiO_2 powder (2.5 g) was added slowly to water (14 ml) with stirring. Acetyl acetone (0.5 ml) was then added with stirring. Finally, Triton X-100 (5 drops) was added, the resulting suspension was then stirred vigorously overnight before use. The suspension was continually stirred when not in use. This suspension was used to prepare the initial BTO-TiO_2 beads and LVO-TiO_2 beads.

The TiO_2 sol-based suspension was prepared as follows. The suspension used for coating the etched beads was prepared as follows. A $Ti(OBu)_4$ sol was first prepared

by adding $Ti(OBu)_4$ (1 ml) to a mixture of n-butanol (20 ml) and HCl (0.23 ml, 37%) slowly under vigorous stirring. To this sol was added P25 TiO_2 (0.667 g) and the resulting suspension stirred overnight before use.

3.6.1.3 Bead Coating Procedure

The etched and treated glass beads were then coated with the suspension by immersion of an appropriate amount of the beads in the prepared suspension for 5 minutes. The excess suspension was then drained by initially decanting and then using a syringe to remove the last few drops. The beads were then spread on a glass dish and heated to 150 ^oC while constantly swirling the dish to ensure an even coating until the beads were dry and not clumped together. The beads were then annealed at 500 ^oC for 1 hour. This process was repeated three times to build up a larger amount of TiO_2 on the bead surface. To simplify some of the analytical methods used to characterise the materials, where a flat surface is required, standard microscope slides were coated with the TiO_2 suspension by dip-coating. The slides were wiped clean on one side, and allowed to dry at 150 ^oC until dry. The coated slides then annealed at 500 ^oC for 1 hour. This process was repeated three times as before.

3.6.1.4 SILAR Processing

The TiO_2 coated glass beads were firstly packed into a standard chromatography column. Two solutions were then prepared, solution A consisting of $Bi(NO_3)_3$ in water (1 mM), and solution B consisting of KBr (1 mM) in water. Solution A was added to the column in enough volume such that the beads were fully immersed and left to stand for 300 seconds. Solution A was then drained, and de-ionised water was then added and allowed to stand for 300 seconds. The water was then drained, and solution B added and allowed to stand for 300 seconds. After draining, water was finally added and allowed to stand for another 300 seconds. This process is termed as one SILAR cycle and was repeated multiple times times to give a greater loading of bismuth onto the bead surface. To convert the SILAR deposited BiOBr made using this method, the coated glass substrates were then annealed at 600 ^oC in air, for 1 hour. Modification of the coated microscope glass was achieved in similar fashion. TiO_2 coated glass slide substrates were dipped for 300 seconds into a beaker containing solution A, then

washed with de-ionised water for 300 seconds, then dipped into solution B for 300 seconds, before finally washing with water for a further 300 seconds. As before, this was repeated multiple times, before finally drying and annealing at 600 ^{o}C for 1 hour in air.

LVO was produced using the same method, but replacing $Bi(NO_3)_3$ with $LaCl_3$ (50 mM) and KBr with Na_3VO_4 (50 mM), and annealing at 500 ^{o}C rather than 600 ^{o}C. Pure powder samples of LVO were produced for some analyses using these same solutions by slow addition under stirring, before centrifugation to isolate the solid material. This material was then dried and annealed at 500 ^{o}C.

3.6.2 Photocatalytic Testing

BTO-TiO_2 formed from the water-based suspension and LVO-TiO_2 were tested as follows.

The coated glass bead samples (Approx. 11.5 g) were packed into a jacketed column. 5 ml of a solution of 4-chlorophenol (156 µmolar) was then added such that the beads were immersed in the solution. The assembly was then irradiated with an unfiltered halogen lamp (400 W, >350 nm) from the side from 5 cm away for 3 hours, keeping the temperature approximately constant at room temperature using a flowing water jacket. The change in absorption of the solution was measured on a JASCO V-670 UV-Vis spectrophotometer at 223 nm.

Testing of the TiO_2 sol derived BTO-TiO_2 beads was carried out as follows.

Photocatalytic testing was carried out in a simple glass dish fitted with a plastic cup to hold a stirrer bar. A quantity of photocatalyst coated beads sufficient to form a monolayer (8g), were added to the dish and a pollutant solution (5 ml) was then added. The pollutants chosen were pentachlorophenol, nonylphenol, tetracycline hydrochloride, paracetamol, trinitrotoluene or nitrotriazolone of 20 ppm concentration. To improve the solubility of pentachlorophenol and nonylphenol, they were dissolved in 50 mM KOH solution. Absorption maxima of these solutions were determined using a Jasco J670 UV-vis spectrophotometer. The photocatalytic beads were stirred in

contact with a pollutant solution in the dark until no change in the absorption maximum was noted. A foil cover slip was then placed over the top of the dish and the entire apparatus irradiated with two LED arrays of 10 LEDs (410 nm peak wavelength, 2 W irradiative power, Intelligent LED solutions). At certain time points samples were withdrawn and the absorption measured using the same spectrophotometer as before to calculate the degradation.

Synthetic wastewater was prepared in deionised water according to the OECD standard for synthetic wastewater (Peptone 160 mg l^{-1}, meat extract 110 mg l^{-1}, urea 30 mg l^{-1}, NaCl 7 mg l^{-1}, $CaCl_2.2H_2O$ 4 mg l^{-1}, $MgSO_4.7H_2O$ 2 mg l^{-1}, K_2HPO_4 28 mg l^{-1}). To this solution was introduced 4-nitrophenol (20 mg l^{-1}), before measuring the photocatalytic removal of the 4-nitrophenol in the same way as used in previous tests. Degradation of 4-nitrophenol was measured using the same UV-vis spectrophotometer as before, using the peak at 350 nm for 4-nitrophenol. Chemical oxygen demand titrations of the synthetic wastewater were carried out before and after photocatalytic degradation as follows. To a sample of wastewater (5 ml) was added concentrated H_2SO_4 (20 ml) and potassium dichromate (4 mM, 25 ml). The resulting solution was swirled and allowed to stand for 15 minutes before adding a couple of drops of ferroin indicator and titrating against freshly prepared ammonium iron sulfate solution (40 mM). A blank deionised water sample was also run in the same fashion.

3.6.2.1 Photocatalytic Scavenging Tests

Photocatalytic scavenging tests were carried out in the same way as the regular photocatalytic testing, using the same concentration of 4-chlorophenol solution, with the addition of tertiary butanol (50 mM), methanol (50 mM) or with the 4-chlorophenol solution being degassed by bubbling with N_2 for 30 minutes prior to the test.

3.6.2.2 Photocatalytic Recycling Tests

Recycle tests were carried out by rinsing the beads with water and leaving them to dry overnight before addition of fresh pollutant solution and determining the degradation efficiency at the same final time point that was used for the pollutant in question.

Regeneration, where used, of the BTO-TiO_2 photocatalyst was achieved by heating at 600 ^oC in air for 1 hour.

3.6.2.3 Bactericidal Testing

Bactericidal testing was carried out in a similar method to the photocatalytic testing. Coated beads (Approx. 11.5 g) were packed into a jacketed column and de-ionised water spiked with *Escherichia coli* (*E. coli)* (5 ml, $2x10^6$ CFU) added such that the beads were immersed. The assembly was then irradiated with an unfiltered halogen lamp (400 W, >350 nm) from the side from 5 cm away for 90 minutes. The standard E. coli ATCC 23716 (American Type Culture Collection, Rockville, MD, USA) strain was used. The freeze-dried cultures were rehydrated and reactivated according to the manufacturer's instructions. Viable E. coli bacteria were measured using a serial dilution pour plate agar technique. Serial dilutions of the reaction solution were performed in sterile aqueous solution and 200 μL of each dilution (including neat sample) were pipetted and spread onto Brilliance E. coli/Coliform Agar (Oxoid) plates, a selective culture medium. The plates were incubated at 37 ◦C for 20–24 h before viable counts were determined.

3.7 Chapter 1 References

1 M. R. Hoffmann, S. T. Martin, W. Choi and D. W. Bahnemann, *Chem. Rev.*, 1995, **95**, 69–96.
2 S. G. Kumar and L. G. Devi, *J. Phys. Chem. A*, 2011, **115**, 13211–13241.
3 Y. Wang, Q. Wang, X. Zhan, F. Wang, M. Safdar and J. He, *Nanoscale*, 2013, **5**, 8326–39.
4 G. Xi and J. Ye, *Chem. Commun.*, 2010, **46**, 1893.
5 Y. Hao, X. Dong, S. Zhai, X. Wang, H. Ma and X. Zhang, *Chem. Commun.*, 2016, **52**, 6525–6528.
6 Y. Jia, S. Zhan, S. Ma and Q. Zhou, *ACS Appl. Mater. Interfaces*, 2016, **8**, 6841–6851.
7 T. Cao, Y. Li, C. Wang, Z. Zhang, M. Zhang, C. Shao and Y. Liu, *J. Mater. Chem.*, 2011, **21**, 6922.
8 K. R. Kendall, C. Navas, J. K. Thomas and H.-C. zur Loye, *Chem. Mater.*, 1996, **8**, 642–649.
9 Y. Chen, J. Xu, S. Xie, Z. Tan, R. Nie, Z. Guan, Q. Wang and J. Zhu, *Materials (Basel).*, 2018, **11**, 821.
10 J. Cai, J. Huang and Y. Lai, *J. Mater. Chem. A*, 2017, **5**, 16412–16421.
11 J. Zhang, L. Huang, P. Liu, Y. Wang, X. Jiang, E. Zhang, H. Wang, Z. Kong, J. Xi and Z. Ji, *J. Alloys Compd.*, 2016, **654**, 71–78.
12 T. P. Niesen and M. R. De Guire, in *Solid State Ionics*, 2002, vol. 151, pp. 61–68.
13 V. P. Tolstoi, *Russ. Chem. Rev.*, 1993, **62**, 237–242.
14 I. M. Arabatzis, S. Antonaraki, T. Stergiopoulos, A. Hiskia, E. Papaconstantinou, M. . Bernard and P. Falaras, *J. Photochem. Photobiol. A Chem.*, 2002, **149**, 237–245.
15 W. F. Yao, H. Wang, X. H. Xu, S. X. Shang, Y. Hou, Y. Zhang and M. Wang, *Mater. Lett.*, 2003, **57**, 1899–1902.
16 S. Burrows, K. McAughey, R. Edwards and S. Dixon, *RSC Adv.*, 2012, **2**, 3678.
17 W. Guo, S. Zhang, Y. Guo, L. Ma, F. Su, Y. Guo and A. Geng, *RSC Adv.*, 2013, **3**, 4008.

18 M. Ge, C. Cao, S. Li, S. Zhang, S. Deng, J. Huang, Q. Li, K. Zhang, S. S. Al-Deyab and Y. Lai, *Nanoscale*, 2015, **7**, 11552–11560.

19 T. R. Gordon, M. Cargnello, T. Paik, F. Mangolini, R. T. Weber, P. Fornasiero and C. B. Murray, *J. Am. Chem. Soc.*, 2012, **134**, 6751–6761.

20 W. Zhou, F. Sun, K. Pan, G. Tian, B. Jiang, Z. Ren, C. Tian and H. Fu, *Adv. Funct. Mater.*, 2011, **21**, 1922–1930.

21 G. Tian, H. Fu, L. Jing, B. Xin and K. Pan, *J. Phys. Chem. C*, 2008, **112**, 3083–3089.

22 Y. Mei, Y. Su, Z. Li, S. Bai, M. Yuan, L. Li, Z. Yan, J. Wu and L.-W. Zhu, *Dalt. Trans.*, 2017, **46**, 347–354.

23 W. Li, P. Li, Y. Liu, B. Zhang, H. Zhang, W. Geng and Q. Zhang, *ChemCatChem*, 2015, **7**, 4163–4172.

24 J. Hou, R. Cao, Z. Wang, S. Jiao and H. Zhu, *J. Mater. Chem.*, 2011, **21**, 7296.

25 D. Hou, X. Hu, P. Hu, W. Zhang, M. Zhang and Y. Huang, *Nanoscale*, 2013, **5**, 9764.

26 Č. Jovalekić, M. Pavlović, P. Osmokrović and L. Atanasoska, *Appl. Phys. Lett.*, 1998, **72**, 1051–1053.

27 R. C. Oliveira, L. S. Cavalcante, J. C. Sczancoski, E. C. Aguiar, J. W. M. Espinosa, J. A. Varela, P. S. Pizani and E. Longo, *J. Alloys Compd.*, 2009, **478**, 661–670.

28 Y. Nosaka and A. Y. Nosaka, *Chem. Rev.*, 2017, **117**, 11302–11336.

29 Y. Wang, S. Li, H. Shi and K. Yu, *Nanoscale*, 2012, **4**, 7817.

30 V. Etacheri, M. K. Seery, S. J. Hinder and S. C. Pillai, *Chem. Mater.*, 2010, **22**, 3843–3853.

31 R. Bajaj, M. Sharma and D. Bahadur, *Dalt. Trans.*, 2013, **42**, 6736.

32 M. Pelaez, N. T. Nolan, S. C. Pillai, M. K. Seery, P. Falaras, A. G. Kontos, P. S. M. Dunlop, J. W. J. Hamilton, J. A. Byrne, K. O'Shea, M. H. Entezari and D. D. Dionysiou, *Appl. Catal. B Environ.*, 2012, **125**, 331–349.

33 X. Zeng, Z. Wang, N. Meng, D. T. McCarthy, A. Deletic, J. Pan and X. Zhang, *Appl. Catal. B Environ.*, 2017, **202**, 33–41.

34 K. S. Yao, D. Y. Wang, J. J. Yan, L. Y. Yang and W. S. Chen, *Surf. Coatings Technol.*, 2007, **201**, 6882–6885.

35 J. Bogdan, J. Zarzyńska and J. Pławińska-Czarnak, *Nanoscale Res. Lett.*, 2015, **10**, 309.

36 D. Venieri, E. Chatzisymeon, E. Politi, S. S. Sofianos, A. Katsaounis and D. Mantzavinos, *J. Water Health*, 2013, **11**, 21–29.

37 M. Hayyan, M. A. Hashim and I. M. AlNashef, *Chem. Rev.*, 2016, **116**, 3029–3085.

38 M. Mrowetz, W. Balcerski, A. J. Colussi and M. R. Hoffmann, *J. Phys. Chem. B*, 2004, **108**, 17269–17273.

39 K. Ishibashi, A. Fujishima, T. Watanabe and K. Hashimoto, *Electrochem. commun.*, 2000, **2**, 207–210.

40 X. Zhang, L. Zhang, T. Xie and D. Wang, *J. Phys. Chem. C*, 2009, **113**, 7371–7378.

41 I. C. Yadav, N. L. Devi, J. H. Syed, Z. Cheng, J. Li, G. Zhang and K. C. Jones, *Sci. Total Environ.*, 2015, **511**, 123–137.

42 M. A. Rodrigo, N. Oturan and M. A. Oturan, *Chem. Rev.*, 2014, **114**, 8720–8745.

43 D. Kanakaraju, B. D. Glass and M. Oelgemöller, *J. Environ. Manage.*, 2018, **219**, 189–207.

44 Y. Yang, Y. S. Ok, K. H. Kim, E. E. Kwon and Y. F. Tsang, *Sci. Total Environ.*, 2017, **596**–**597**, 303–320.

45 J. Altmann, F. Zietzschmann, E.-L. Geiling, A. S. Ruhl, A. Sperlich and M. Jekel, *Chemosphere*, 2015, **125**, 198–204.

46 Z. Hasan and S. H. Jhung, *J. Hazard. Mater.*, 2015, **283**, 329–339.

47 X. C. Hu, D. Q. Andrews, A. B. Lindstrom, T. A. Bruton, L. A. Schaider, P. Grandjean, R. Lohmann, C. C. Carignan, A. Blum, S. A. Balan, C. P. Higgins and E. M. Sunderland, *Environ. Sci. Technol. Lett.*, 2016, **3**, 344–350.

48 *Toxicological Profile for Pentachlorophenol (Update), Agency for Toxic Substances and Disease Registry (ATSDR), Public Health Service, U.S. Department of Health and Human Services, Atlanta, GA.*, 1999.

49 *Priority Substances and Certain Other Pollutants according to Annex II of Directive 2008/105/EC, European Commission Water Framework Directive*, 2016.

50 A. Soares, B. Guieysse, B. Jefferson, E. Cartmell and J. N. Lester, *Environ. Int.*, 2008, **34**, 1033–1049.

51 *Nonylphenol (NP) and Nonylphenol Ethoxylates (NPEs) Action Plan [RIN 2070-ZA09], United States Environmental Protection Agency*, 2010.
52 D. T. F. Kuo, M. Simini and H. E. Allen, *Sci. Total Environ.*, 2017, **599**–**600**, 2135–2141.
53 H. A. Yu, J. Lee, S. W. Lewis and D. S. Silvester, *Anal. Chem.*, 2017, **89**, 4729–4736.
54 R. Podlipná, B. Pospíšilová and T. Vaněk, *Ecotoxicol. Environ. Saf.*, 2015, **112**, 54–59.
55 *Public Health Statement, 2,4,6-Trinitrotoluene, Agency for Toxic Substances and Disease Registry (ATSDR), Public Health Service, U.S. Department of Health and Human Services*, 1995.
56 M. S. Johnson, W. S. Eck and E. M. Lent, *Propellants, Explos. Pyrotech.*, 2017, **42**, 9–16.
57 J. Rivera-Utrilla, M. Sánchez-Polo, M. Á. Ferro-García, G. Prados-Joya and R. Ocampo-Pérez, *Chemosphere*, 2013, **93**, 1268–1287.
58 T. A. Ternes, *Water Res.*, 1998, **32**, 3245–3260.
59 R. Andreozzi, V. Caprio, R. Marotta and D. Vogna, *Water Res.*, 2003, **37**, 993–1004.
60 F. Chen, Q. Yang, J. Sun, F. Yao, S. Wang, Y. Wang, X. Wang, X. Li, C. Niu, D. Wang and G. Zeng, *ACS Appl. Mater. Interfaces*, 2016, **8**, 32887–32900.
61 C. Reyes, J. Fernández, J. Freer, M. A. Mondaca, C. Zaror, S. Malato and H. D. Mansilla, *J. Photochem. Photobiol. A Chem.*, 2006, **184**, 141–146.
62 E. Portjanskaja, M. Krichevskaya, S. Preis and J. Kallas, *Environ. Chem. Lett.*, 2004, **2**, 123–127.
63 C.-S. Chiou, J.-L. Shie, C.-Y. Chang, C.-C. Liu and C.-T. Chang, *J. Hazard. Mater.*, 2006, **137**, 1123–1129.
64 S. Luo, J. Chen, Z. Huang, C. Liu and M. Fang, *ChemCatChem*, 2016, **8**, 3780–3789.
65 Y.-R. Jiang, S.-Y. Chou, J.-L. Chang, S.-T. Huang, H.-P. Lin and C.-C. Chen, *RSC Adv.*, 2015, **5**, 30851–30860.
66 J. Shang, W. Hao, X. Lv, T. Wang, X. Wang, Y. Du, S. Dou, T. Xie, D. Wang and J. Wang, *ACS Catal.*, 2014, **4**, 954–961.
67 L. Zhao, J. Deng, P. Sun, J. Liu, Y. Ji, N. Nakada, Z. Qiao, H. Tanaka and Y. Yang, *Sci. Total Environ.*, 2018, **627**, 1253–1263.
68 G. Mills and M. R. Hoffmann, *Environ. Sci. Technol.*, 1993, **27**, 1681–1689.
69 A. P. Davis and C. p. Huang, *Water Res.*, 1990, **24**, 543–550.
70 Y. He, N. B. Sutton, H. H. H. Rijnaarts and A. A. M. Langenhoff, *Appl. Catal. B Environ.*, 2016, **182**, 132–141.
71 M. Cruz, C. Gomez, C. J. Duran-Valle, L. M. Pastrana-Martínez, J. L. Faria, A. M. T. Silva, M. Faraldos and A. Bahamonde, *Appl. Surf. Sci.*, 2017, **416**, 1013–1021.
72 K. Inumaru, M. Murashima, T. Kasahara and S. Yamanaka, *Appl. Catal. B Environ.*, 2004, **52**, 275–280.
73 J. Mack and J. R. Bolton, *J. Photochem. Photobiol. A Chem.*, 1999, **128**, 1–13.
74 G. K. C. Low, S. R. McEvoy and R. W. Matthews, *Environ. Sci. Technol.*, 1991, **25**, 460–467.
75 J. Farner Budarz, A. Turolla, A. F. Piasecki, J.-Y. Bottero, M. Antonelli and M. R. Wiesner, *Langmuir*, 2017, **33**, 2770–2779.
76 S. Yu, J. Liu, Y. Zhou, R. D. Webster and X. Yan, *ACS Sustain. Chem. Eng.*, 2017, **5**, 1347–1357.
77 Y. Huo, X. Yang, J. Zhu and H. Li, *Appl. Catal. B Environ.*, 2011, **106**, 69–75.
78 J. W. Stouwdam, M. Raudsepp and F. C. J. M. van Veggel, *Langmuir*, 2005, **21**, 7003–7008.
79 Q. Wang, Z. Zhang, Y. Zheng, W. Cai and Y. Yu, *CrystEngComm*, 2012, **14**, 4786.
80 J. Fang, D. Li, Y. Shao and J. Hu, *J. Mater. Chem. A*, 2016, **4**, 14213–14221.
81 X. Zou, X. Li, Q. Zhao and S. Liu, *J. Colloid Interface Sci.*, 2012, **383**, 13–18.
82 R. Yuan, T. Chen, E. Fei, J. Lin, Z. Ding, J. Long, Z. Zhang, X. Fu, P. Liu, L. Wu and X. Wang, *ACS Catal.*, 2011, **1**, 200–206.
83 H. Huang, D. Li, Q. Lin, W. Zhang, Y. Shao, Y. Chen, M. Sun and X. Fu, *Environ. Sci. Technol.*, 2009, **43**, 4164–4168.
84 C.-Y. Liu, S.-Y. Tsai, C.-T. Ni and K.-Z. Fung, *J. Electron. Mater.*, 2017, **46**, 2301–2308.
85 P. Parhi and V. Manivannan, *Solid State Sci.*, 2008, **10**, 1012–1019.
86 Y. He, J. Cai, L. Zhang, X. Wang, H. Lin, B. Teng, L. Zhao, W. Weng, H. Wan and M. Fan, *Ind. Eng. Chem. Res.*, 2014, **53**, 5905–5915.
87 Y. He, Y. Wang, L. Zhao, X. Wu and Y. Wu, *J. Mol. Catal. A Chem.*, 2011, **337**, 61–67.

88 K. Sayama, A. Nomura, T. Arai, T. Sugita, R. Abe, T. Oi, Y. Iwasaki, Y. Abe and H. Sugihara, *J. Phys. Chem. B*, 2006, **3**, 11352–11360.
89 G. Wang, Y. Ling, X. Lu, F. Qian, Y. Tong, J. Z. Zhang, V. Lordi, C. Rocha Leao and Y. Li, *J. Phys. Chem. C*, 2013, **117**, 10957–10964.
90 H. Xu, J. Yi, X. She, Q. Liu, L. Song, S. Chen, Y. Yang, Y. Song, R. Vajtai, J. Lou, H. Li, S. Yuan, J. Wu and P. M. Ajayan, *Appl. Catal. B Environ.*, 2018, **220**, 379–385.
91 Y. Wang, W. Yang, X. Chen, J. Wang and Y. Zhu, *Appl. Catal. B Environ.*, 2018, **220**, 337–347.
92 C. Turchi and D. Ollis, *J. Catal.*, 1990, **122**, 178–192.

Chapter 4 Narrowing the Band Gap

4.1 Overview

Contained within this chapter is a report of two separate materials which aim to improve upon the visible light response of the photocatalytic system by using narrower band gap materials in conjunction with TiO_2. These studies aim to combine this improvement in visible absorption with the good charge separation in the same way as the BTO and LVO materials described previously. $BiVO_4$ with a band gap of around 2.5 eV and BiOI with a band gap of around 2.2 eV were chosen for deposition on TiO_2 immobilised on glass plates using SILAR.

4.2 $BiVO_4$-TiO_2 Composites

4.2.1 Introduction

A promising method of providing both visible light harvesting and hindered charge recombination is formation of heterojunctions with narrow band gap inorganic semiconductors such as other metal oxides[1–3] and metal sulphides[4]. Bismuth vanadate ($BiVO_4$) is a cheap, low toxicity replacement for cadmium compounds in the pigment industry and has been investigated as a promising visible-active photocatalyst in its own right[5,6]. Sensitisation of TiO_2 using $BiVO_4$ has been reported to produce photocatalysts with good visible light activity[7,8] by both increasing the absorption into the visible and suppressing charge recombination by providing an interface across which charges are separated.

Herein is described the formation of immobilised thin film $BiVO_4$-TiO_2 photocatalysts via a SILAR method. Commercially available TiO_2 pastes most commonly used in the fabrication of dye-sensitised solar cells have been used to fabricate films with high surface areas as a base to which SILAR is applied. While SILAR has been applied as a sensitisation technique in solar cells[9,10] for the purposes of generating visible-active photocatalysts it is relatively unexplored, and to date has not been used to generate $BiVO_4$. We also describe a new control experiment to examine charge separation in composite nanoparticle films by making comparisons between SILAR modified TiO_2 and ZrO_2 films. As ZrO_2 has a much wider band gap than TiO_2[11] it is both inactive to

visible light and disallows charge separation across the $BiVO_4$-ZrO_2 interface. By applying a commercially available ZrO_2 precursor paste designed to be compatible with the TiO_2 used we ensure that the nanoparticle formation and film properties closely resemble that of the TiO_2-$BiVO_4$ film, making the ZrO_2-$BiVO_4$ control a meaningful comparison in all but charge separation.

4.2.2 Results & Discussion

4.2.2.1 Photocatalyst Preparation

Base TiO_2 and ZrO_2 films were prepared using commercial pastes sold by Dyesol and Solaronix respectively, using a doctor blading and annealing method as described in the experimental section. To these films, SILAR deposition of Bi and V precursors is applied, the process of which is detailed in Figure 4.1.

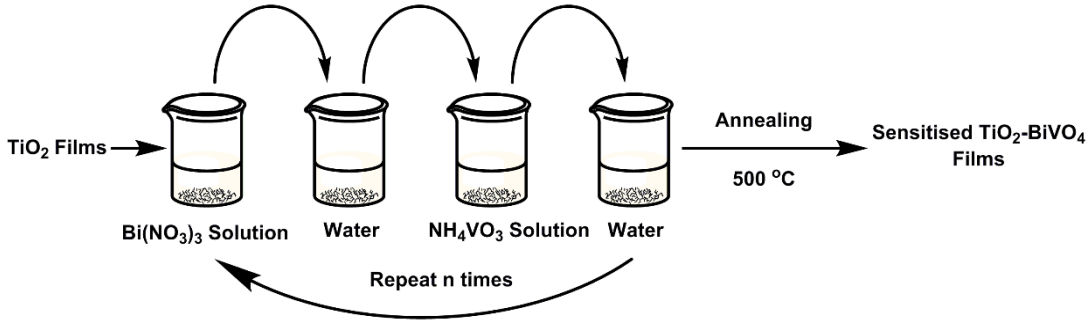

Figure 4.1. SILAR deposition of $BiVO_4$

Mesoporous TiO_2 and ZrO_2 films were chosen as a starting point due to their high surface area, a distinct advantage in catalysis. Upon SILAR cycling, the films became increasingly yellow in colour, corresponding to an increase in the amount of $BiVO_4$ on the surface. Samples will henceforth be named as SILARxN where N = the number of cycles, the SILAR modified ZrO_2 film is termed SILARxN-Z.

4.2.2.2 Structure and Morphology

An XRD trace of the SILARx6 modified sample is shown in Figure 4.2.

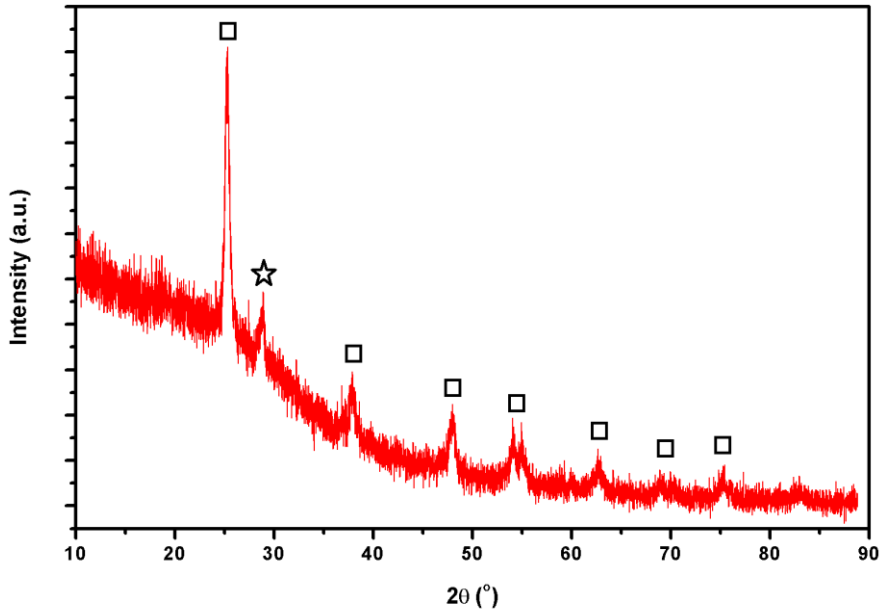

Figure 4.2. XRD trace of the 6xSILAR sample, (~) anatase TiO_2, (☆) monoclinic-scheelite $BiVO_4$ 121 peak.

Due to the low concentration of $BiVO_4$ present even after 6 SILAR cycles the only peak observed is due to diffraction from the [121] plane (JCPDS card #14-0688), the most intense peak in the monoclinic-scheelite polymorph of $BiVO_4$. A sample of $BiVO_4$ formed by the standard co-precipitation method using the same solutions and heat treatment yielded a pure powder sample of monoclinic-scheelite type $BiVO_4$ (Figure 4.3), and hence it can be assumed that the SILAR modification of TiO_2 is indeed producing monoclinic-scheelite $BiVO_4$ on the TiO_2 surface.

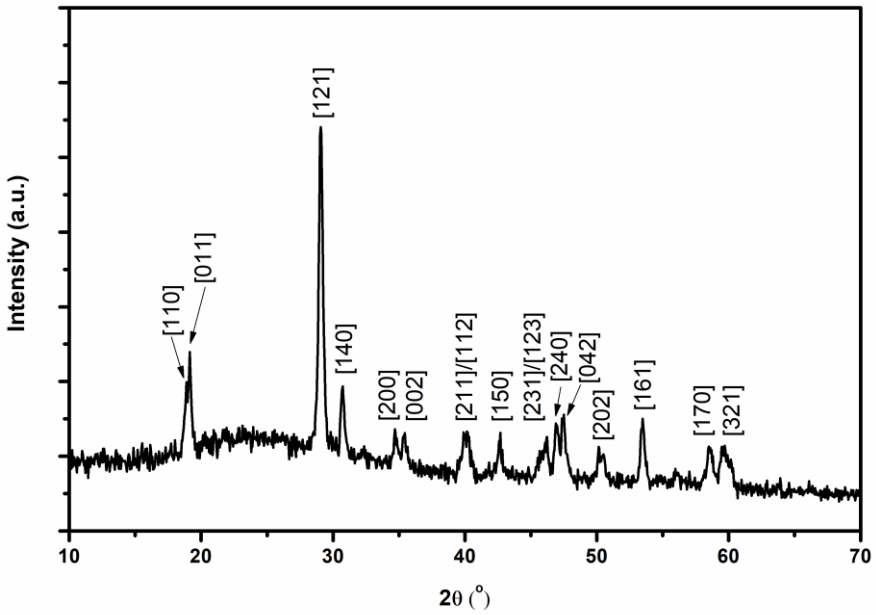

Figure 4.3. XRD of the precipitated $BiVO_4$ material

The monoclinic-scheelite structure of $BiVO_4$ has previously been noted to be superior in terms of visible photocatalytic activity to the alternative tetragonal forms owing to lower band gap allowing greater visible light harvesting[12,13]. Similarly, when examining a SILARx6-Z control sample (Figure 4.4), the $BiVO_4$ was found to be very weak, complicated further by the similar diffraction angles of monoclinic and tetragonal ZrO_2[14].

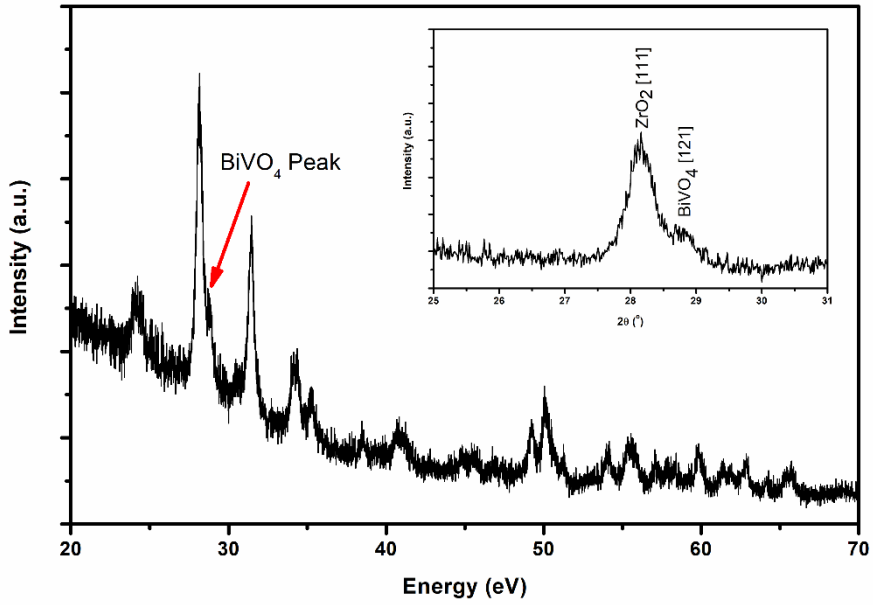

Figure 4.4. XRD trace of the 6xSILAR-Z sample. Inset) Zoom of the region surrounding the ZrO_2 [111] peak

However, the same peak that can be assigned to the 121 plane appears upon close examination of the fine area around 30° (Inset Figure 4.4). Hence it is assumed that the same $BiVO_4$ polymorph is found in both SILARx6 and SILARx6-Z samples indicating that the SILARxN-Z samples provide a good control system to compare with SILARxN.

Scanning electron microscopy (SEM) images of the films' surface show a porous network of sintered TiO_2 particles. When comparing a SILAR modified film with a pristine film no observable change in porosity or surface morphology was found (Figure 4.5), indicating that SILAR is not obstructing the pore structure at all.

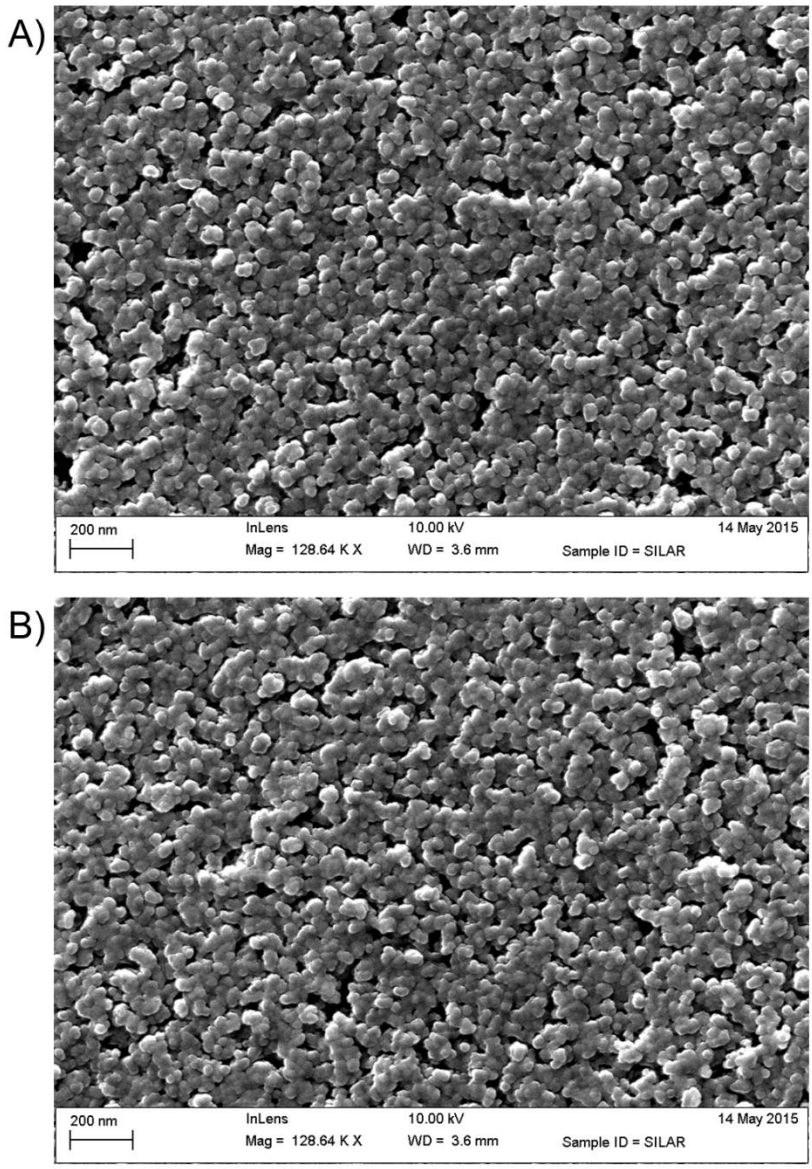

Figure 4.5. SEM images of A) the pristine TiO_2 film surface and B) 5xSILAR film surface.

To observe the $BiVO_4$ particles higher magnification TEM images were taken (Figure 4.6).

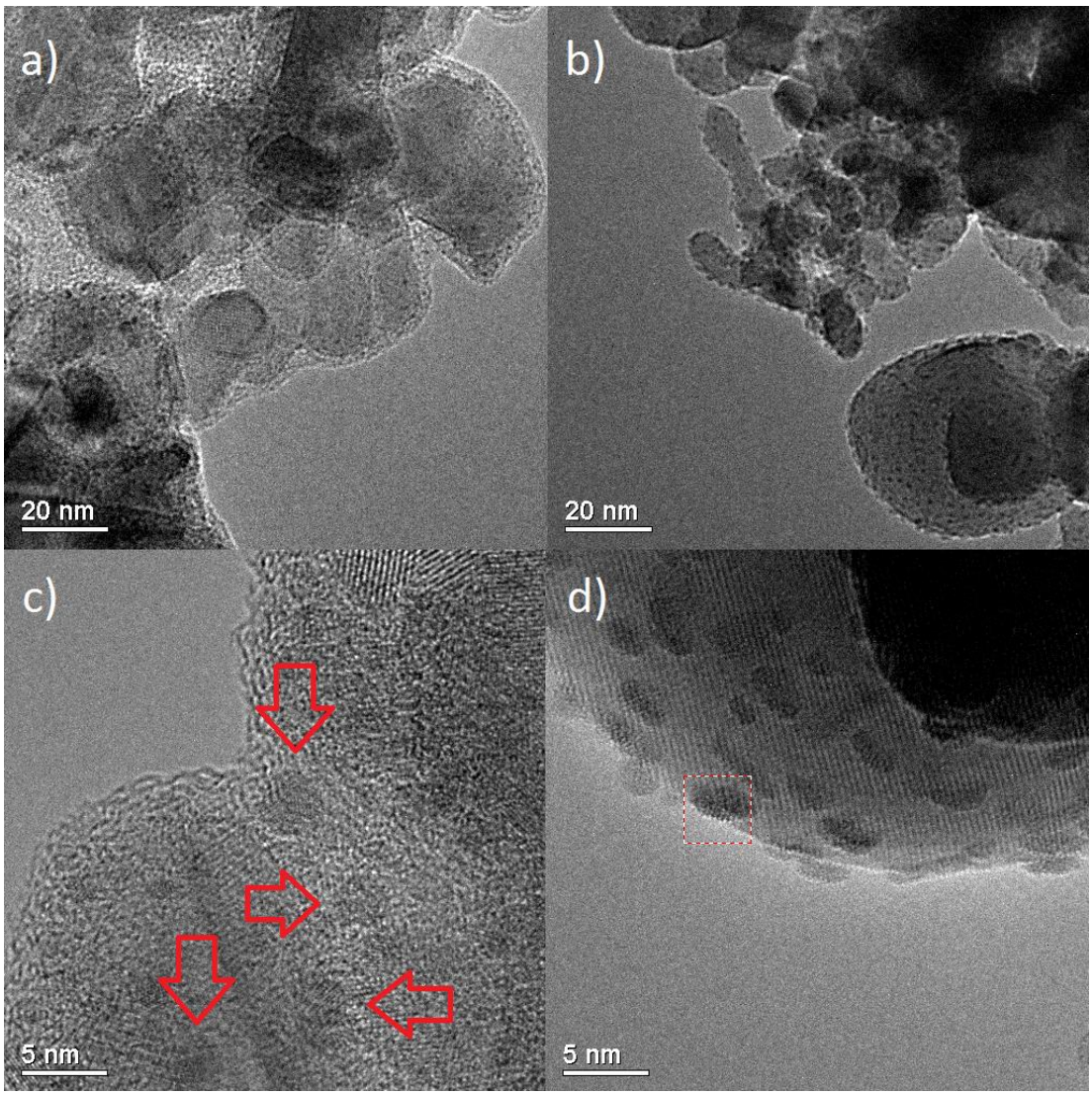

Figure 4.6. TEM images of a) & c) SILARx5 and b) & d) SILARx5-Z

TEM images of SILARx5 and SILARx5-Z revealed large particles of TiO_2 and ZrO_2 of similar sizes decorated with small nanoparticles of $BiVO_4$ (Figure 4.6 a & b). From high resolution TEM images (Figure 4.6 c & d) the particles were found to be irregularly shaped with an estimated size of around 5 nm across. The nanoparticle features were observed to be approximately the same in both SILARx5 and SILARx5-Z samples, and therefore differences between the two therefore cannot be ascribed to particle size effects, further establishing the SILARxN-Z system as a meaningful control.

4.2.2.3 Optical Properties

Incremental increases in the yellow colour intensity was observed upon increasing SILAR cycles, corresponding to the growth of the blue-absorbing $BiVO_4$ on the TiO_2 surface. A shoulder peak corresponding to growth of $BiVO_4$ was observed in the Kubelka-Munk and corresponding Tauc plots of the SILAR modified material (Figure 4.7).

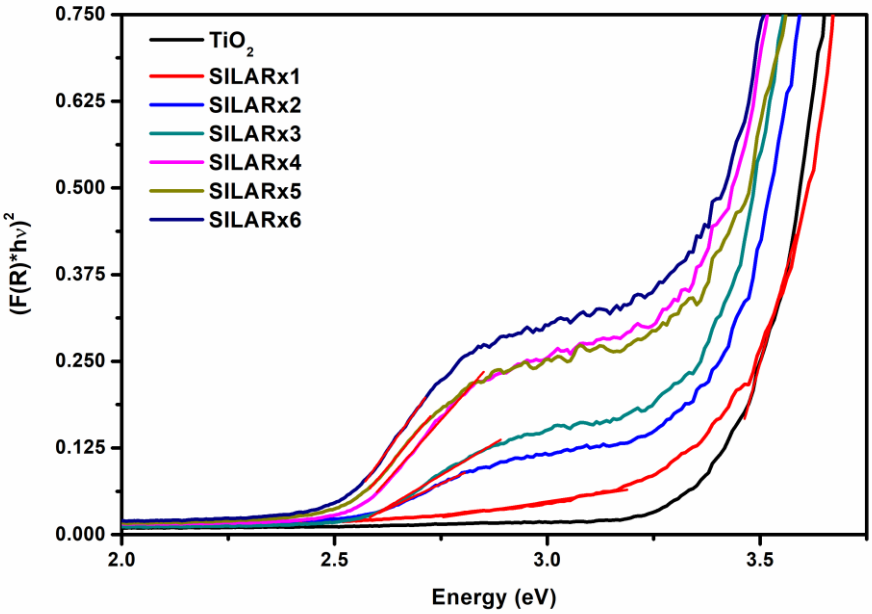

Figure 4.7. Tauc plot of the prepared materials, showing the shoulder caused by $BiVO_4$ modification

The band gaps (Eg) of the plain and SILAR modified were determined for each sample from the x-intercept of the Tauc plot according to the Tauc equation and are summarised in Table 4.1.

Table 4.1 – TiO_2-$BiVO_4$ Band Gaps

Sample	Band Gap (eV)
TiO_2	3.387
SILARx1	2.482
SILARx2	2.496
SILARx3	2.515
SILARx4	2.510
SILARx5	2.492
SILARx6	2.482

Band gaps were found to be approximately constant across the SILAR modified samples at around 2.5 eV, in accord with the literature[15]. As the number of SILAR cycles increased absorption in the blue region also increased while the bandgap remains largely unchanged, suggesting an increased number of the same sized nanoparticles.

4.2.2.4 Elemental Analysis

The bulk composition of the $BiVO_4$ present in the films was determined by dissolving the $BiVO_4$ and performing inductively coupled plasma optical emission spectroscopy (ICP-OES) (Figure 4.8).

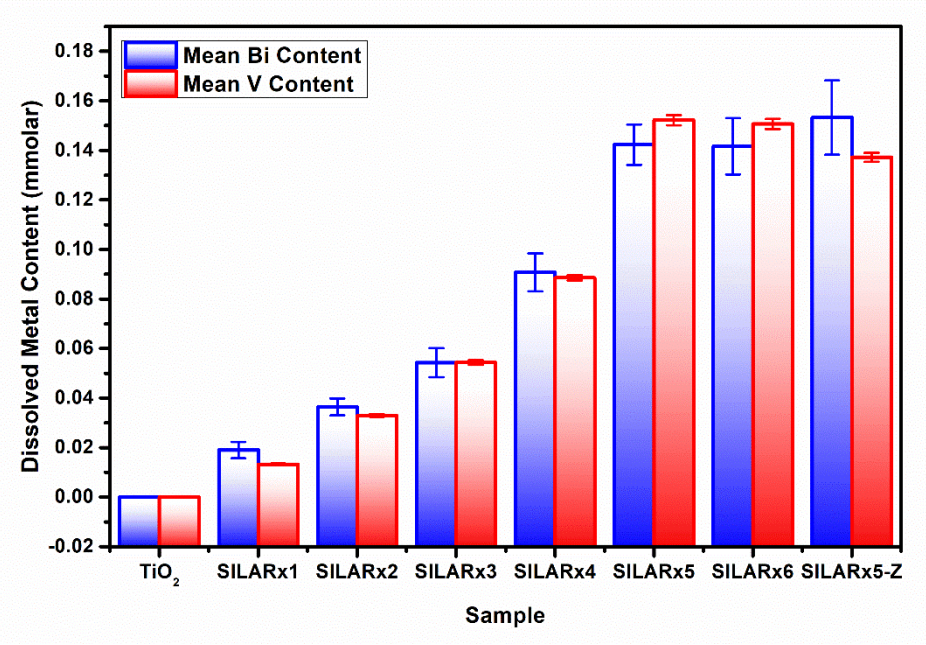

Figure 4.8. Metal content of the acidic leech solution obtained from various samples

Increased levels of Bi and V are observed for increased SILAR cycles. Importantly, the levels of Bi and V in SILARx5 and SILARx5-Z are very similar, again verifying the ZrO_2 system as a good control. Additionally, ICP-OES gives further credence to the material analysed being pure $BiVO_4$, as the Bi:V ratio across all samples is within approximately 1:1.

To investigate the chemical speciation of the film surface x-ray photoelectron spectroscopy (XPS) measurements were made. Survey scans (Figure 4.9) identified the presences of Ti, O, Bi and V.

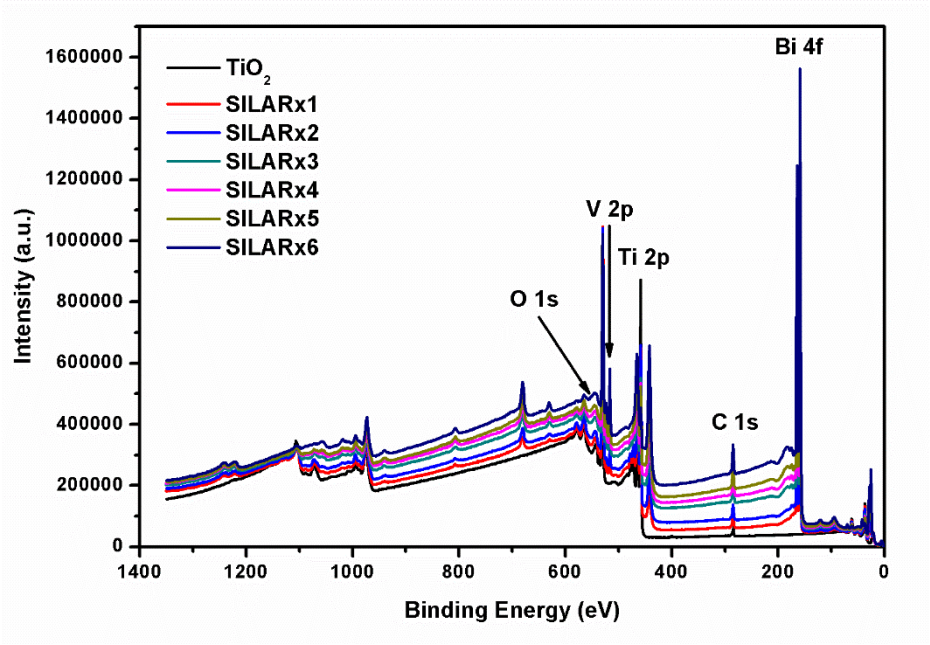

Figure 4.9. XPS survey scans of the $BiVO_4$ modified materials and pristine TiO_2

Carbon was also detected, most likely due to adventitious carbon introduced in the processing or measurement and was used as a reference around the peak at 284.8 eV. High-resolutions XPS scans of the Ti, O, Bi and V peaks were measured, showing an increase in the Bi and V content as the number of SILAR cycles increased (Figure 4.10).

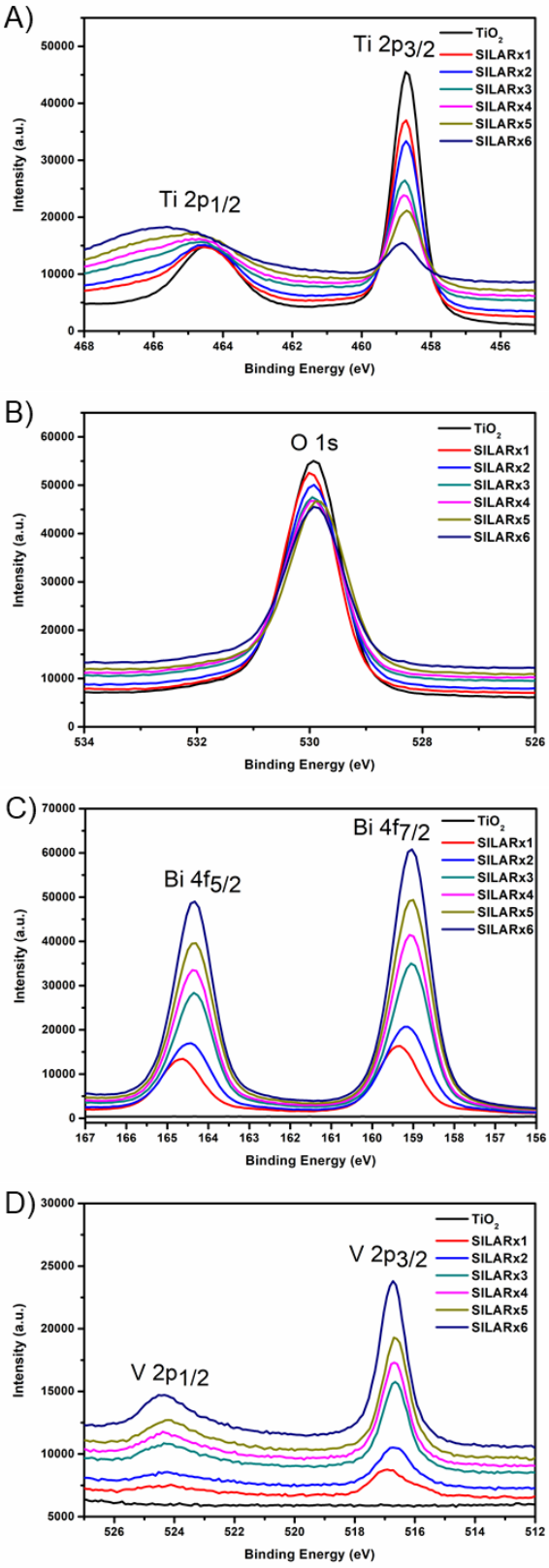

Figure 4.10. XPS scans of the A) Ti 2p B) O1s C) Bi 4f and D) V 2p regions

The values obtained for Bi and V are largely consistent with the reported values for Bi^{3+} and V^{5+} in $BiVO_4$[16–19], indicating that no change in oxidation state had occurred during the SILAR processing. Small shifts in the Bi and V peaks to higher binding energy in TiO_2-$BiVO_4$ composites compared to the reported values for pure $BiVO_4$ have been previously observed and rationalised as being due to electron transfer between $BiVO_4$ and TiO_2[8].

4.2.2.5 Band Alignment and Charge Separation

To gain insight into the band structure of the prepared composites valence band XPS measurements were carried out (Figure 4.11).

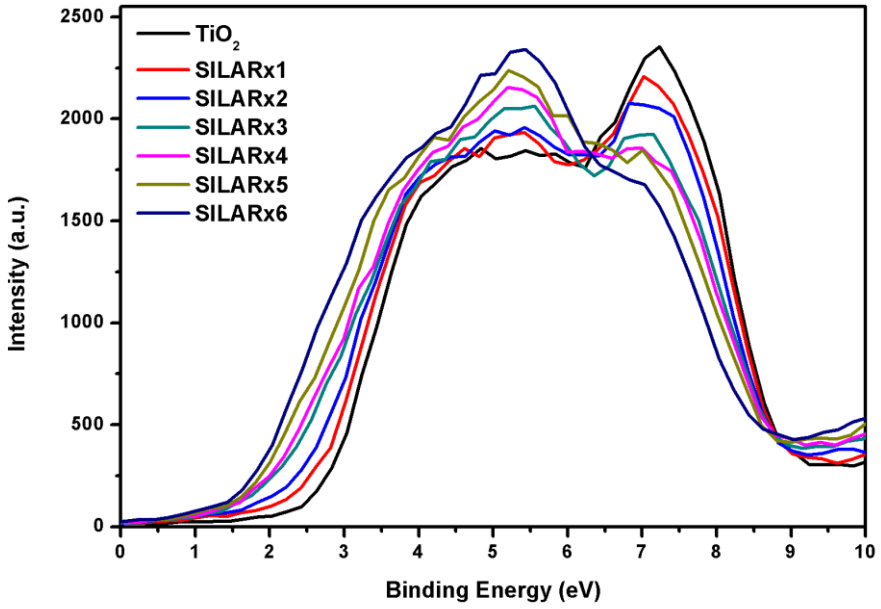

Figure 2. Valence band XPS scans for the SILAR modified and pristine TiO_2 films

The onset of the valence band was observed to decrease after SILAR processing. From the x-intercepts of the valence band plots the valence band maximum (E_{vb}) was determined (Table 4.2).

Table 4.2 - Valence band maxima

Sample	Valence Band Maxima (eV)
TiO_2	2.660 ± 0.189
SILARx1	1.858 ± 0.113
SILARx2	1.854 ± 0.078
SILARx3	1.803 ± 0.014
SILARx4	1.818 ± 0.032
SILARx5	1.690 ± 0.021
SILARx6	1.568 ± 0.049

The decrease in E_{vb} can be assigned to photoelectrons emitted from the $BiVO_4$ valence band. Hence there is a ~1 eV driving force for holes to migrate from the TiO_2 to the $BiVO_4$, providing a route for charge separation.

To investigate the conduction band energies of the prepared materials, Mott-Scottky analysis was carried out. The linear portion of the M-S plots (Figure 4.12) can be extrapolated to the x-intercept to obtain a value for the E_{fb} according to the M-S equation.

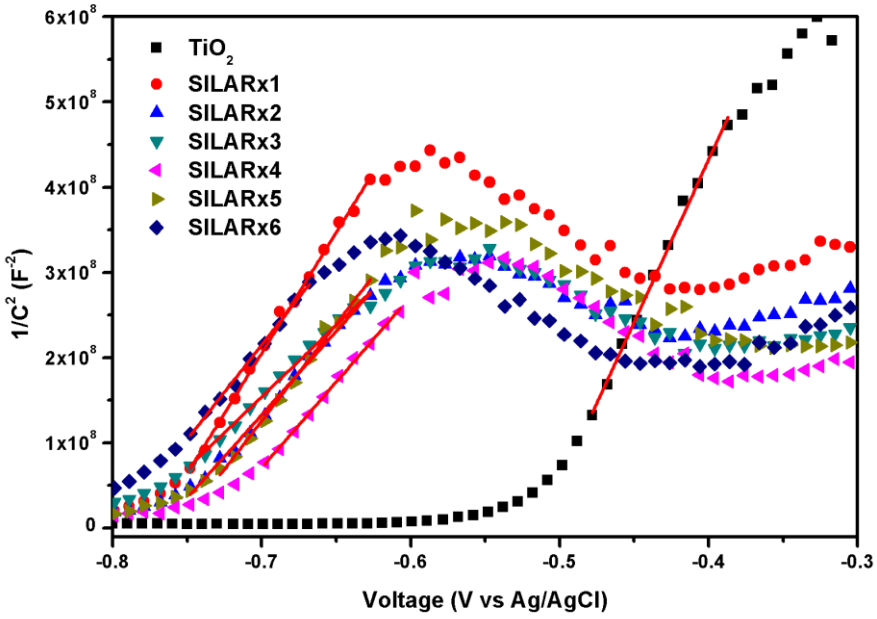

Figure 4.12. Mott-Schottky scans of the $BiVO_4$-TiO_2 and TiO_2 films

The flat band potentials are summarised in table 4.3.

Table 4.3 - Flat band potentials

Sample	E_{fb} (V vs Ag/AgCl)
TiO_2	-0.507 ± 0.012
SILARx1	-0.771 ± 0.008
SILARx2	-0.771 ± 0.025
SILARx3	-0.797 ± 0.012
SILARx4	-0.746 ± 0.016
SILARx5	-0.753 ± 0.008
SILARx6	-0.792 ± 0.039

Both $BiVO_4$-TiO_2 and TiO_2 exhibited Mott-Schottky plots typical for n-type materials, with a positive gradient in the linear region of the plot, indicating that the majority charge carriers are electrons. The flat band potentials of the TiO_2-$BiVO_4$

heterojunctions are all within experimental error of one another, and are in keeping with the reported values for $BiVO_4$ under similar experimental conditions[18,20,21]. Each shows a ~265 mV cathodic shift from the TiO_2, indicating that the SILAR deposited $BiVO_4$ is shifting the flat band upwards in energy by ~265 mV. This indicates that there is a thermodynamic driving force for electron injection, and hence charge separation, across the $BiVO_4$-TiO_2 interface.

Photoluminescence (PL) spectroscopy is useful in exploring the extent of charge separation across the $BiVO_4$-TiO_2 interface[7,21]. Emission from $BiVO_4$ has been assigned to recombination of high energy electrons and holes in V3d and O2p orbitals respectively[22,23]. Upon selective excitation of $BiVO_4$ with visible light (400 nm), several bands in the 460-500 nm range were observed in the emission spectrum of both SILARx5 and SILARx5-Z films (Figure 4.13).

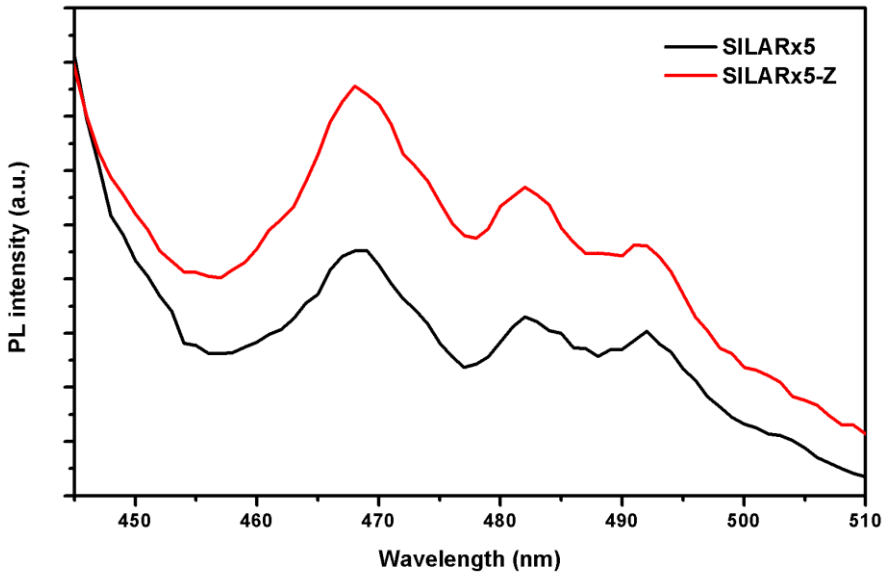

Figure 4.13. Photoluminescence spectra of $BiVO_4$ on TiO_2 and ZrO_2

The reduction in photoluminescence from SILARx5-Z to SILARx5 can be rationalised by the energy level matching of $BiVO_4$ with TiO_2 and ZrO_2. As demonstrated the VB and CB edges of $BiVO_4$ lie cathodically shifted from that of TiO_2. This is not the case in the much wider band gap material ZrO_2, where the CB and VB edges lie between

those of ZrO_2 and hence charge separation cannot occur between ZrO_2 and $BiVO_4$ and charge recombination prevails (Figure 4.14).

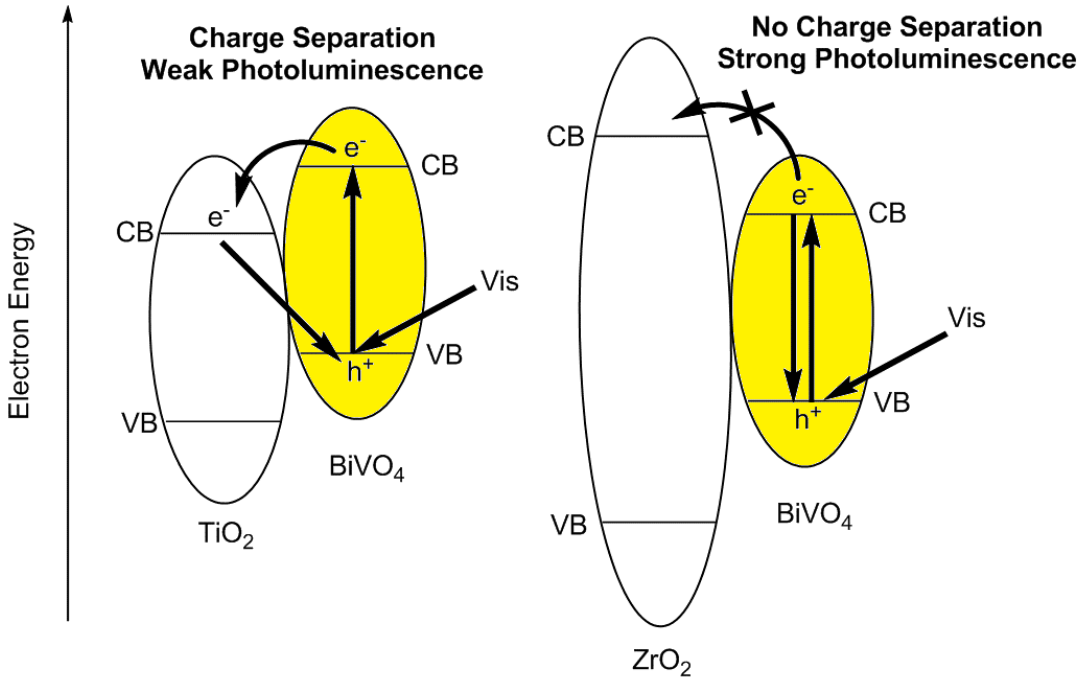

Figure 4.14. Charge separation on $BiVO_4$-TiO_2 and $BiVO_4$-ZrO_2 under visible irradiation

In the case of TiO_2 and $BiVO_4$ the interface allows charge separation and therefore the photoluminescence is lowered.

The valence band XPS, Mott-Schottky and photoluminescence analyses have shown that the VB and CB edges of the composites lie cathodically shifted from the plain TiO_2, indicating a band structure known as a type II heterojunction, where electrons move from the conduction band of $BiVO_4$ to the conduction band of TiO_2, and holes vice versa. This structure is in agreement with that described recently by Hu *et al.*[24], Xie *et al.*[25], and Sun *et al.*[7] for $BiVO_4$-TiO_2 heterojunctions.

4.2.2.6 Photocatalysis

4.2.2.6.1 Model Pollutant Degradation

The photocatalytic activity of the composites was assessed using the model organic rhodamine 6G (Rh6G). Glass substrates with the prepared films were used in the

cuvette type reactor described in the experimental section and allowed to reach an adsorption/desorption equilibrium for 30 minutes (Figure 4.15).

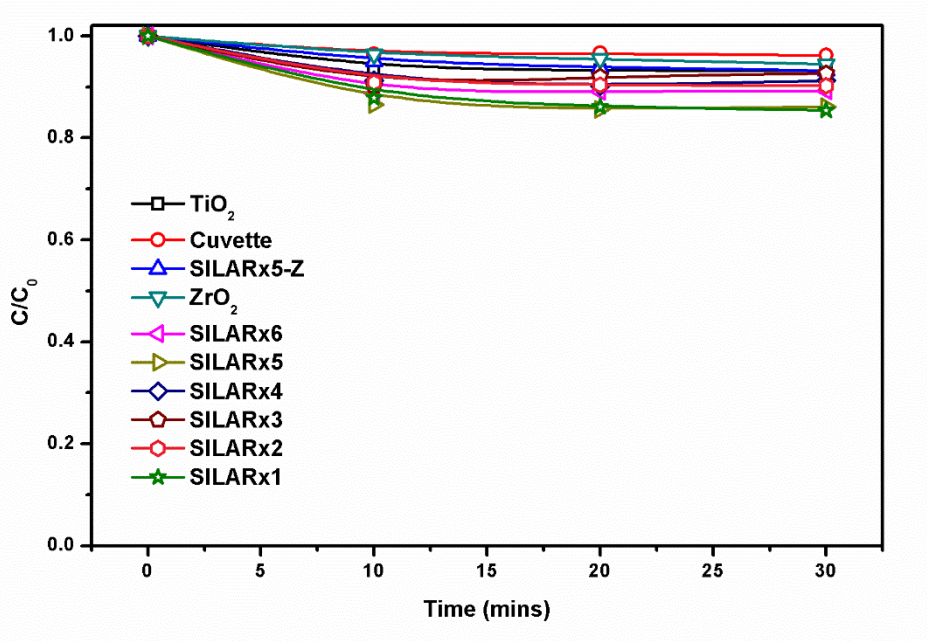

Figure 4.15. Dark adsorption of Rh6G by the $BiVO_4$-TiO_2 samples and various control samples

During this time all films exhibited a small amount of dye adsorption (~10%). The samples were then illuminated from the side using a white LED fitted with a 400 nm long-pass filter to ensure visible only irradiation. The resulting first order rate plots are given in Figure 4.16.

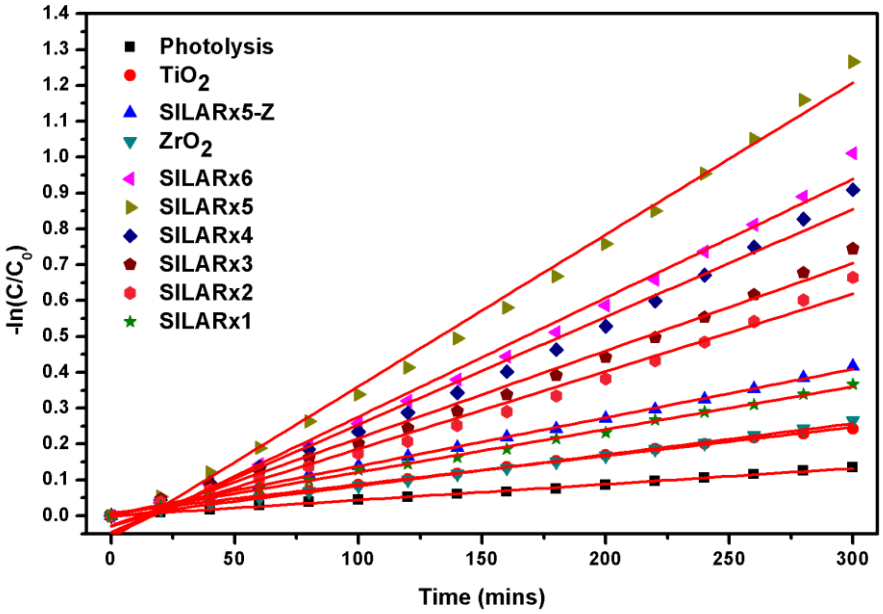

Figure 4.16. First order rate plots of the films on the degradation of Rh6G

All the SILAR modified photocatalysts exhibited improved activity over the TiO_2 and ZrO_2 control, demonstrating the improvement of the SILAR modification. The rate constants of the photocatalysts films are summarised in table 4.3.

Table 4.3 – Degradation rate constants of the prepared films

Sample	Pseudo 1st order rate constants ($x10^{-3}$ min^{-1})
Photolysis	0.442
TiO_2	0.800
SILARx5-Z	1.351
ZrO_2	0.868
SILARx1	1.192
SILARx2	2.161
SILARx3	2.438
SILARx4	3.001
SILARx5	4.231
SILARx6	3.314

It was found that the photodegradation improved in order of the number of SILAR cycles up to a maximum for SILARx5 before decreasing for SILARx6. This optimum number of SILAR cycles is reached despite SILARx6 having marginally better light harvesting than SILARx5. This could be due to there being an optimum coverage of $BiVO_4$ nanoparticles on the TiO_2 surface. A marked improvement is also observed when comparing the photocatalytic activity of the optimum number of SILAR cycles on TiO_2 (SILARx5) to the same number of cycles on ZrO_2 (SILARx5-Z). This highlights the heterojunction effect in the $BiVO_4$-TiO_2 film. The composite performs better than the sum of the individual materials, a difference which can be ascribed to charge separation across the interface.

4.2.2.6.2 Photocatalytic Mechanism Investigation

To eradicate the effects of self-sensitisation, control photocatalytic reactions were run using the colourless organic model pollutants phenol, 4-chlorophenol and catechol.

However, no degradation of these organics was observed suggesting that the mechanism of action of the composites does not involve excitation of the $BiVO_4$. This suggests that electron transfer from the Rh6G dye to the semiconductor conduction band is the dominant mechanism in the production of the highly reactive oxygen species that are known for degradation of organic contaminants. Hence the improvement in photocatalytic activity when comparing SILAR modified films is only due to improved charge separation and not visible light sensitisation by the $BiVO_4$ nanoparticles. The mechanism of photocatalytic degradation therefore can be concluded to be as shown (Figure 4.17).

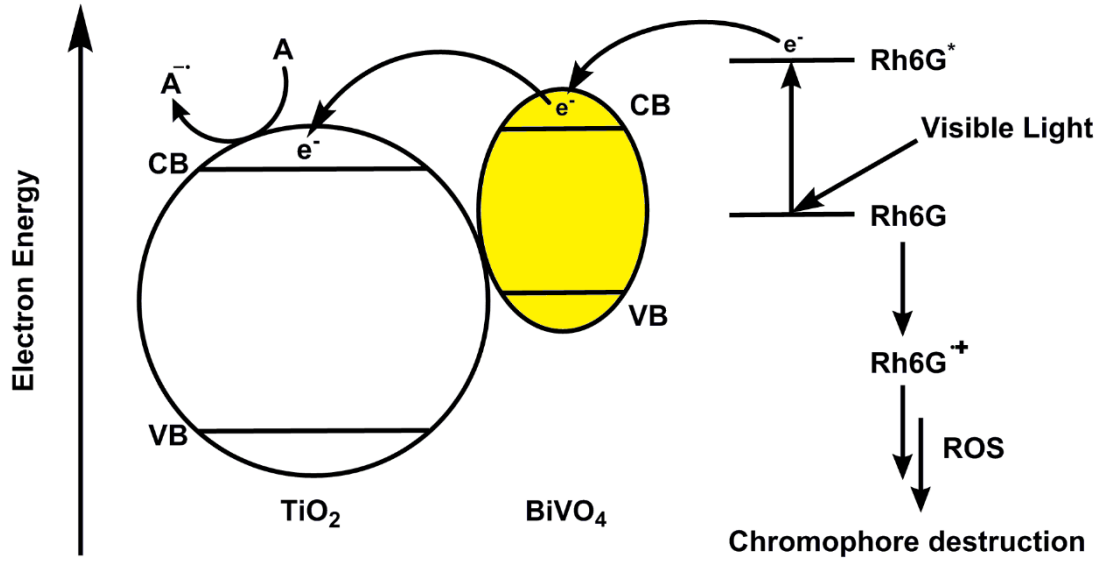

Figure 4.17. Self-sensitisation mechanism of degradation of Rh6G on $BiVO_4$-TiO_2

To further prove this self-sensitisation mechanism, the ability of Rh6G to charge inject into the conduction bands of $BiVO_4$, TiO_2 and ZrO_2 was studied using a series of photoluminescence experiments. The emission of Rh6G molecules adsorbed onto the surface of the semiconductors was measured upon excitation with 525 nm light (Figure 4.18).

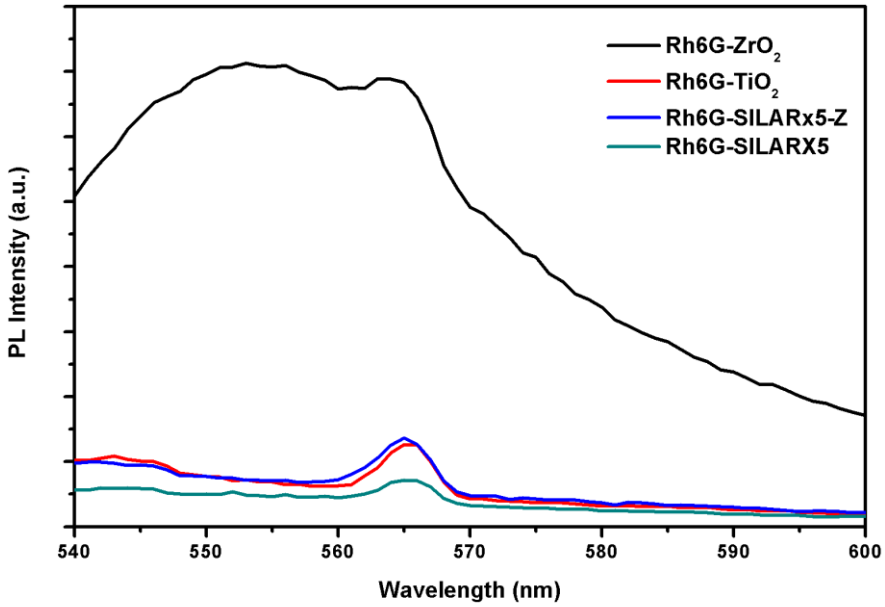

Figure 4.18. Photoluminescence spectra of Rh6G adosorbed onto different substrates

Adsorbed Rh6G on ZrO_2 displays a broad emissive peak around 555 nm, however when adsorbed upon TiO_2, $BiVO_4$-ZrO_2 or $BiVO_4$-ZrO_2 the signal became effectively quenched, indicating that efficient charge separation is occurring which prevents emission (Figure 4.19).

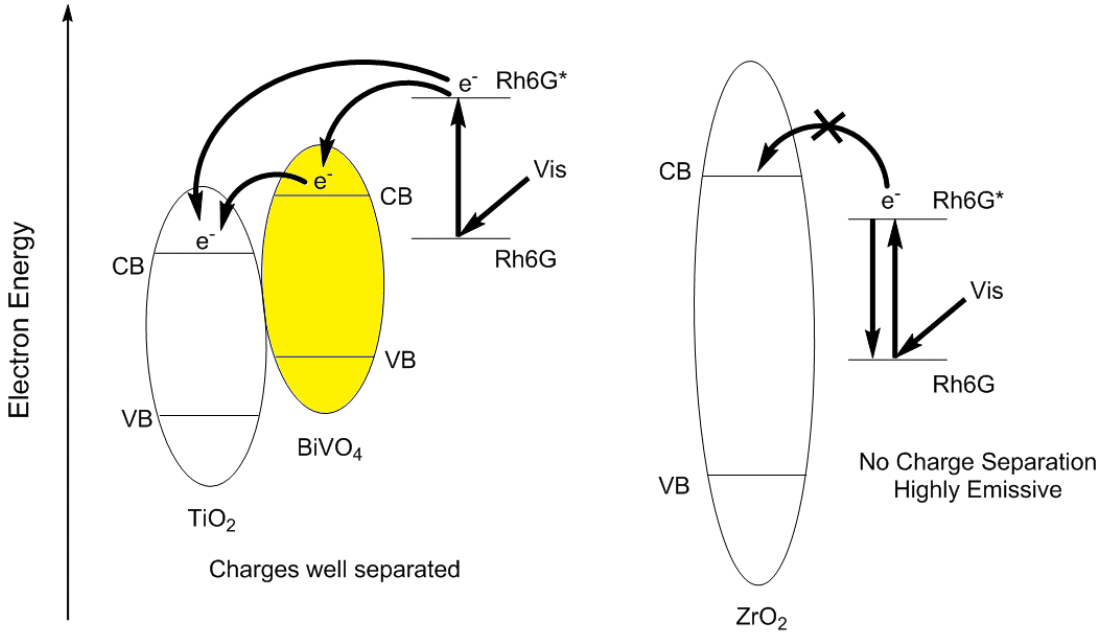

Figure 4.19. Mechanism of charge injection from Rh6G onto various semiconductors

Rh6G is concluded to be able to easily inject excited electrons into the conduction band of TiO_2 and/or $BiVO_4$, therefore demonstrating that the mechanism of photocatalytic action of the composites will be reinforced by self-sensitisation of Rh6G.

4.2.2.6.3 Literature Comparisons

The photocatalytic films prepared in this work display pseudo 1st order rate constants typically on the lower end of what has been reported in the literature (Table 4.4).

Table 4.4 – Previously reported $BiVO_4$-TiO_2 photocatalysts

Analyte	Catalyst Loading & Form	Light Source	k_{app} or % Degradation	Reference
Rhodamine 6G	0.77 ± 0.07 mg film in 2.5 ml	30W White LED (>400 nm)	0.004 min^{-1}	This Work
Rhodamine B	20 mg powder in 50 ml	6x18W Ne Lamp (400-800 nm)	0.026 min^{-1}	Zalfani et al[8]
4-nonylphenol	60 mg powder in 20 ml	300W Xe Lamp (>422 nm)	0.051 min^{-1}	Li et al[26]
Phenol	100 mg powder in 100 ml	150W Xe Lamp (>420 nm)	0.005 min^{-1}	Xie et al[25]
Toluene (gaseous)	20 mg wafer in 160 ml reactor	500W Xe Lamp (>400 nm)	0.006 min^{-1}	Sun et al[27]
Benzene (gaseous)	1.35 g powder in 1.2 ml reactor	500W Xe Lamp (450-900 nm)	92% in 8 hours	Hu et al[24]

However, it is important to remember the factors which contribute to photocatalytic activity. Firstly, the catalyst loading, which in this work is significantly lower than what is commonly used by others. Secondly the energy and intensity of light used, which can vary significantly from one piece of work to another and in this work was markedly lower than literature comparisons. Thirdly the form of which the catalyst takes, such as a stirred slurry or an immobilised film or wafer, which can dramatically affect mass transfer to the surface. While the degradation of colourless organics has previously been found to be possible using the $BiVO_4$-TiO_2 system in the work detailed in Table 4, it has not been observed in this work despite a band structure that should allow it to occur. It has been established that the activity of the SILAR prepared films under the conditions presented is dominated by self-sensitisation, and it could be that degradation of colourless organics is simply very slow, whereas under similar

conditions to those used by others in Table 4 some activity may have been measurable. It is noteworthy that while the films reported here do give lower activities, having the catalyst pre-immobilised is highly advantageous in moving from laboratory interest to real-world applications.

4.2.2.7 Recyclability Testing

Recyclability testing of SILARx5 showed no loss of activity after five repeat tests of Rh6G photodegradation (Figure 4.20).

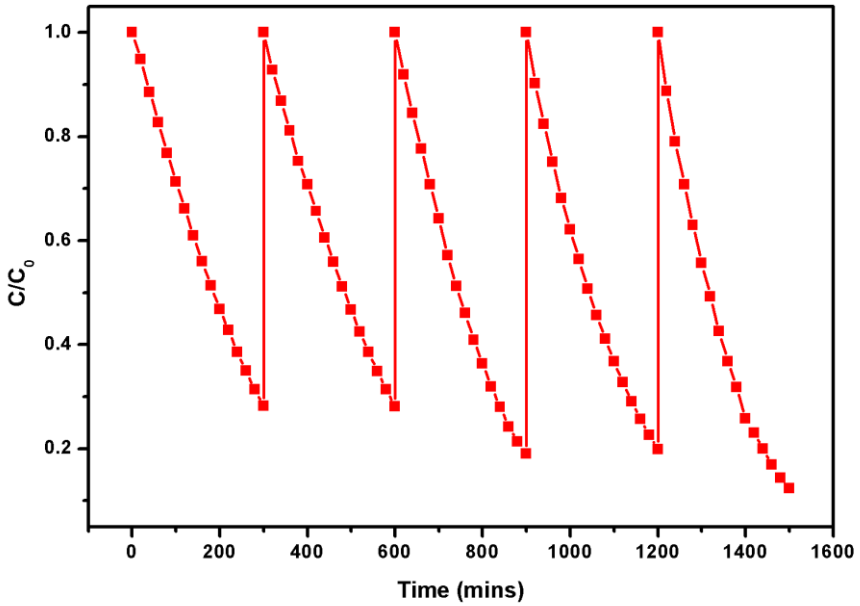

Figure 4.20. Recyclability testing of Rh6G using 5xSILAR

In fact, small increases in activity were noted on repeated cycles. This could be due to adsorbed Rh6G molecules retained post washing increasing the self-sensitisation effect.

4.3 BiOI-TiO_2 Composites

4.3.1 Introduction

Bearing the drawbacks of the $BiVO_4$ modification in mind, further improvements to visible light absorption and charge separation were both investigated through the combination of TiO_2 with the narrow band gap material bismuth oxyiodide (BiOI). TiO_2 is an n-type semiconductor due to the presence of oxygen vacancies in the

lattice[28]. Therefore, a heterojunction between a semiconductor of p-type character and TiO_2 forms a p-n junction which has an internal electric field promoting charge separation by driving charges away from one another across the junction[29,30]. By applying a narrow band gap p-type semiconductor we can take advantage this effect and provide visible light sensitisation to give highly efficient visible active photocatalysts. BiOI is a well-known p-type material with a band gap of approximately 2 eV that can be used as a visible photocatalyst in its own right[31,32], which has been shown to form p-n junctions with n-type materials such as TiO_2[33,34], and as such improve the photoactivity of the material.

In this section is described the sensitisation of an immobilised film of nanoporous TiO_2 with nanoplates of the narrow band gap p-type material bismuth oxyiodide using a SILAR technique. While BiOI SILAR for photovoltaic applications has been previously studied[35–37], to date there are no examples of BiOI-TiO_2 heterojunctions formed by SILAR for photocatalytic applications to date. In addition to a full physical and chemical characterisation of the SILAR prepared BiOI-TiO_2 films, we provide experimental evidence for the band structure of the heterojunctions and use this to rationalise the observed photocatalytic properties.

4.3.2 Results & Discussion

4.3.2.1 Photocatalyst Preparation

Nanoporous TiO_2 films were formed using commercially available TiO_2 pastes commonly used in the fabrication of dye-sensitised or perovskite solar cells. Upon firing, these pastes give a film of high surface area consisting of an interconnected network of TiO_2 particles to which BiOI SILAR was applied. The typical procedure for BiOI SILAR is given in Figure 4.21a. During the SILAR processing, the films turned from white to an orange/red colour (Figure 4.21b), indicating the deposition of BiOI on the surface.

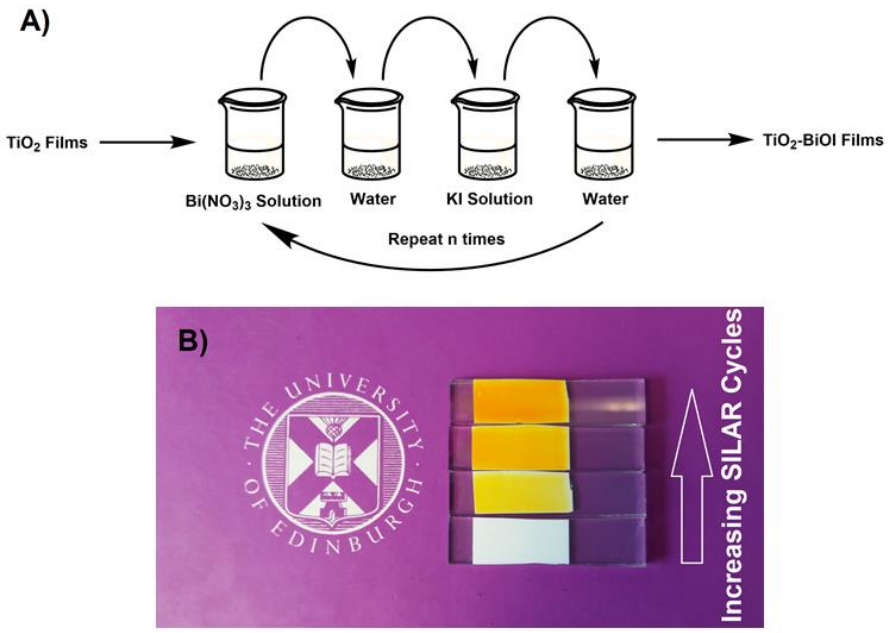

Figure 4.21. A) SILAR process for deposition of BiOI onto TiO_2 B) Photograph of the films modified using SILAR

Samples will henceforth be named as BiOIxN where N = the number of cycles. SILAR was repeated 3, 5 or 7 times to give increasing amounts of BiOI on the TiO_2 surface, giving an increasingly intensely orange coloured film.

4.3.2.2 Structure & Morphology

4.3.2.2.1 X-ray Diffraction

XRD traces of the prepared BiOI-TiO_2 composites are given in Figure 4.22.

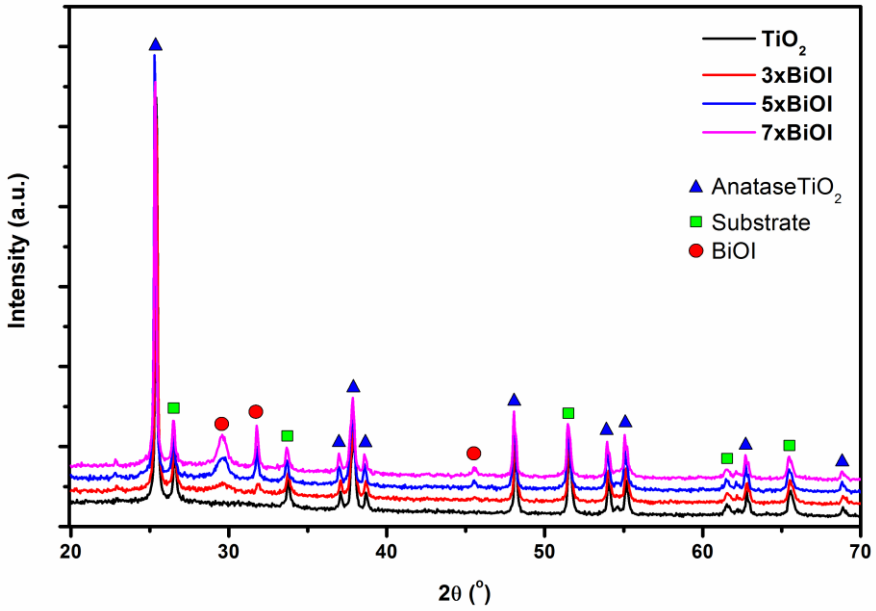

Figure 4.22. XRD traces of the plain TiO_2 and BiOI SILAR modified films

Three new peaks of high crystallinity were observed at 2θ values of 29.7°, 33.7° and 45.6°. These can be indexed to the [012], [110] and [020] planes of tetragonal BiOI (JCPDS Card #73-2062). Peaks found at 2θ denoted by blue triangles in Figure 4.22 were found to be consistent with the anatase phase of TiO_2 (JCPDS Card # 21-1272). Crystallinity has previously been noted to be important in photo-active materials due to raising the diffusion length of excited electrons and holes, leading to improved charge separation in the heterojunction[38,39]. Increased numbers of SILAR cycles were found to increase the intensity of these peaks, indicating the deposition of larger amounts of BiOI.

4.3.2.2.2 Electron Microscopies

SEM images of the surface of the prepared films revealed a network of TiO_2 particles of around 150-250 nm with roughly cubic or rod-like morphologies (Figure 4.23).

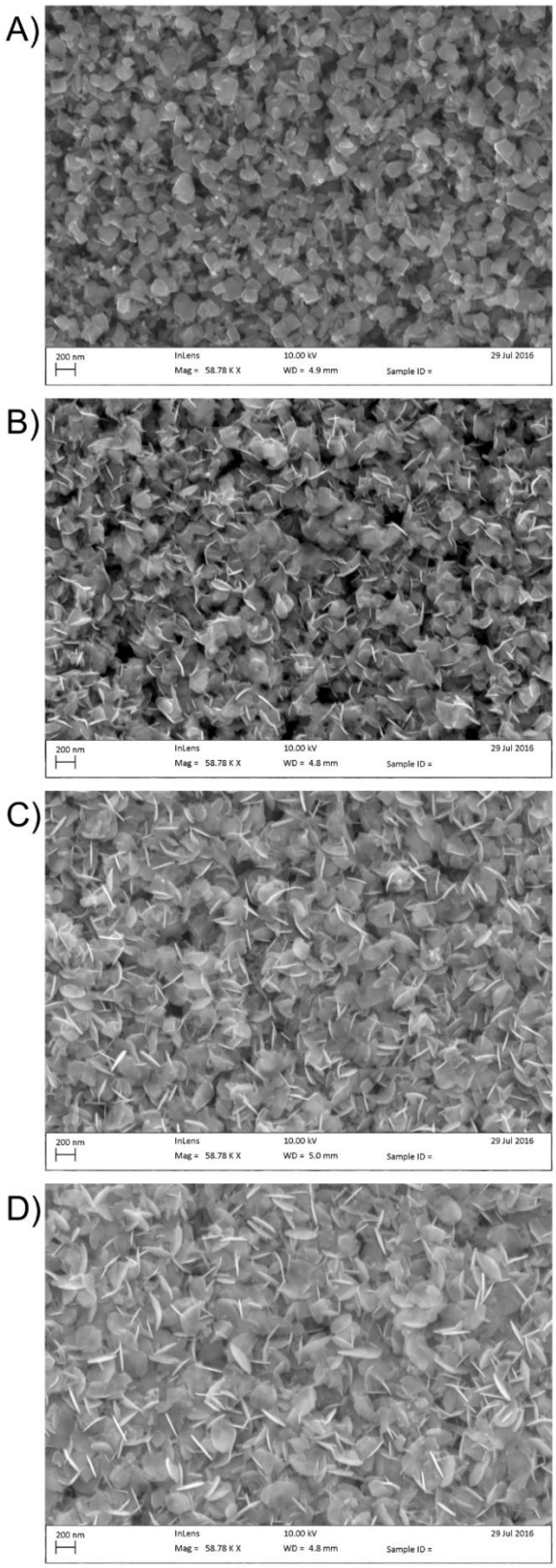

Figure 4.23. SEM images of A) the pristine TiO_2 film. B) 3xBiOI C) 5xBiOI and D) 7xBiOI

Upon SILAR cycling BiOI is observed to grow out from the TiO_2 surface with a plate-like morphology, with the plates becoming larger and more prevalent as the number of SILAR cycles is increased. To gain an insight into the film's homogeneity below the top layer, cross-sectional SEM images were recorded (Figure 4.24).

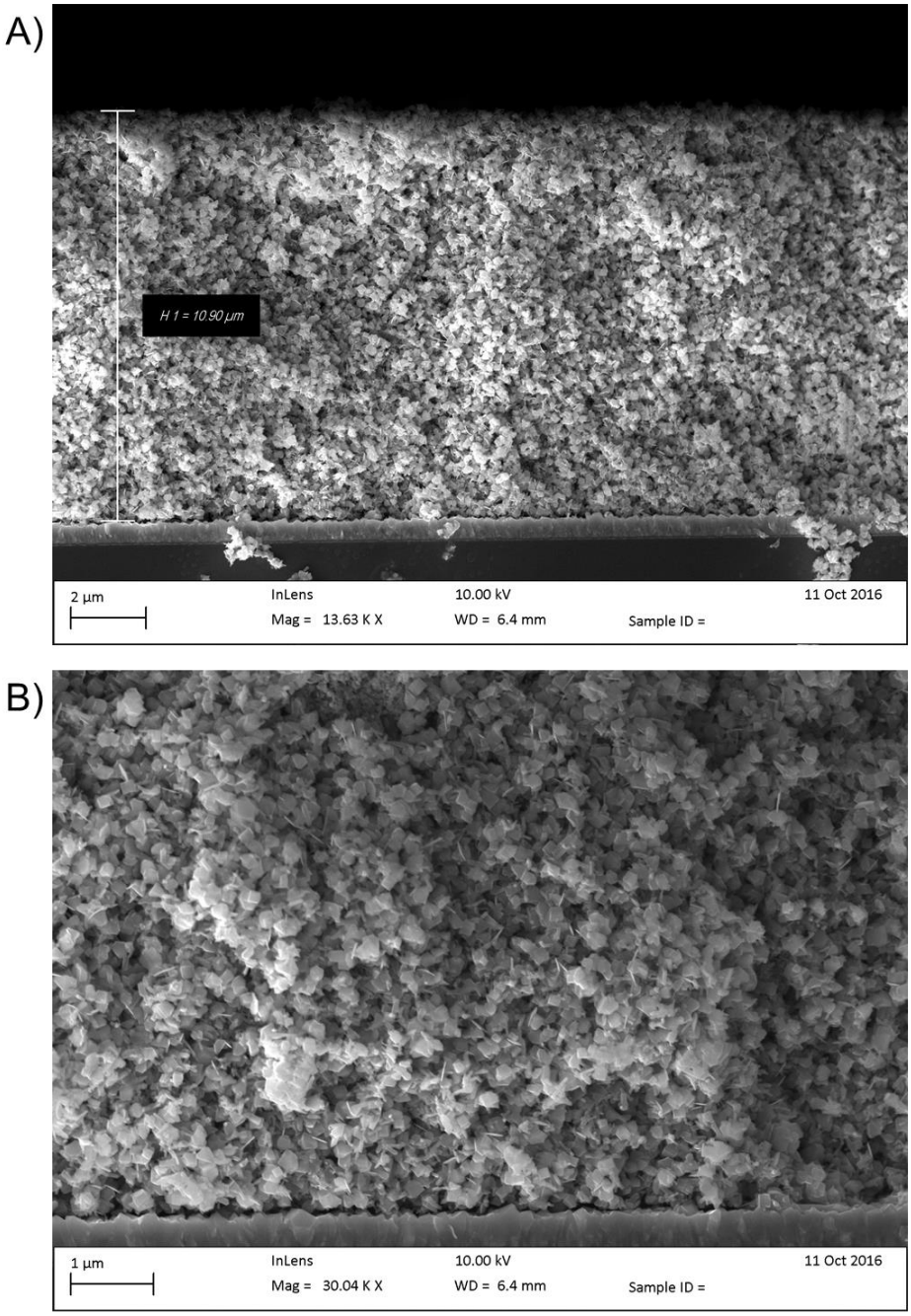

Figure 4.24. Cross-sectional SEM of 7xBiOI showing A) the whole film and B) BiOI nanoplates growth into the deepest point of the film adjacent to the substrate)

The films were all found to be approximately 10 µm thick, with BiOI nanoplates found across the whole cross-section down to the substrate. Transmission electron microscopy (TEM) images of BiOIx5 revealed good contact between the BiOI nanoplates and the TiO_2 particles (Figure 4.25).

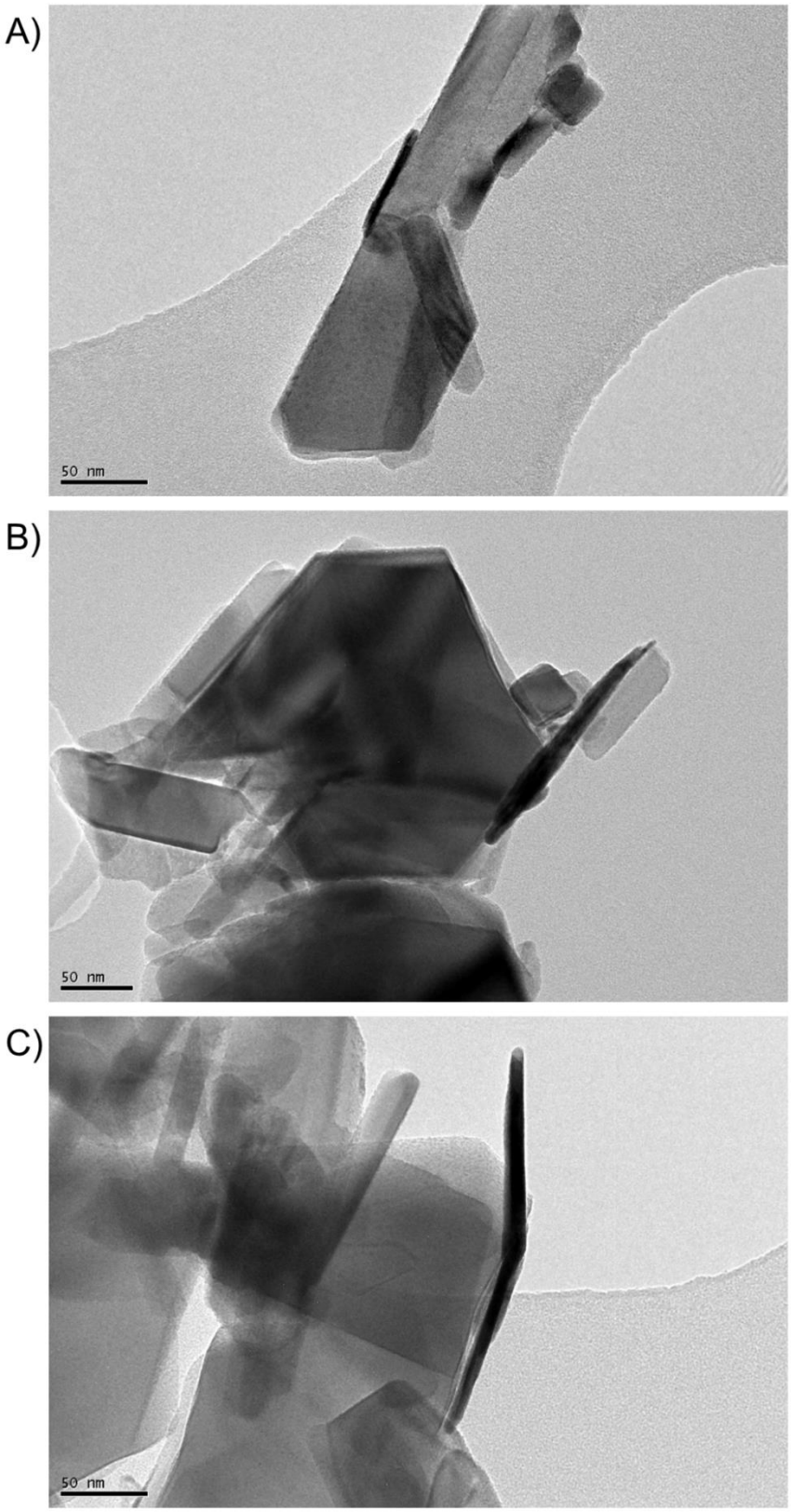

Figure 4.25. TEM images of BiOI nanplates on TiO_2

Most of the plates were found to be of the order of ~100 nm in length, and around 10-20 nm in width, although shorter plates were also present. Lattice fringes were also recorded from the TEM images (Figure 4.26).

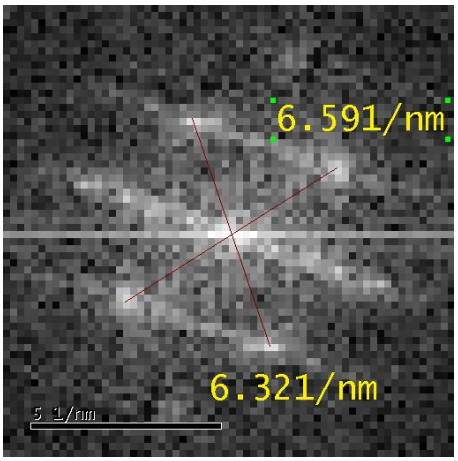

Figure 4.26. FFT lattice spacings of a BiOI nanoplate

d-spacings of 0.303 and 0.316 nm were measured for the plates, corresponding to the [102] and [312] planes of BiOI respectively[40,41].

4.3.2.3 Elemental Analyses

4.3.2.3.1 X-ray Photoelectron Spectroscopy

The presence of the elements Bi, I, O and Ti were identified in the x-ray photoelectron spectroscopy (XPS) survey scans (Figure 4.27).

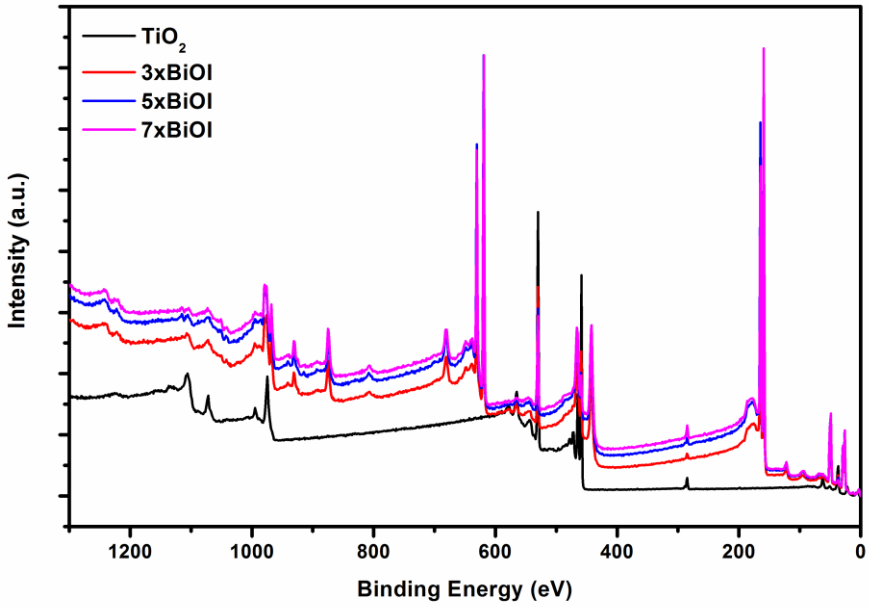

Figure 4.27. XPS survey scans of the TiO_2 and BiOI modified TiO_2 films

High resolution XPS scans of were then used to inspect the Bi, Ti, O and I regions (Figure 4.28).

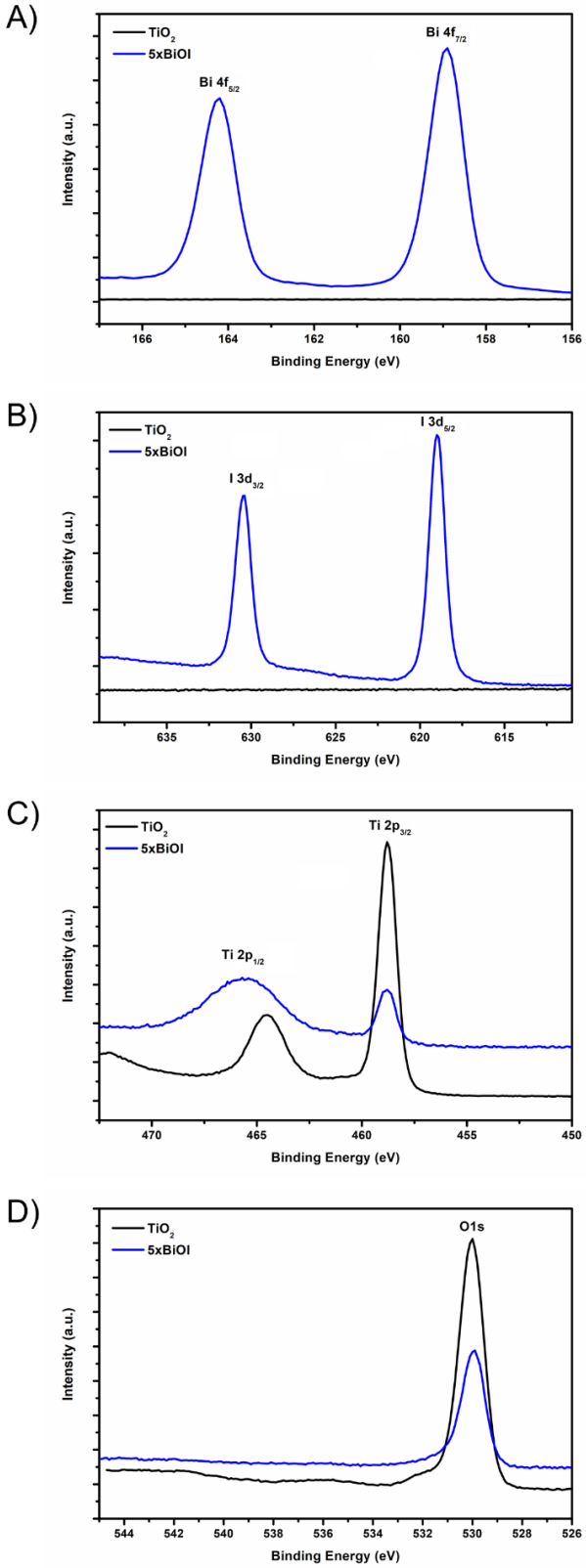

Figure 4.28. XPS scans of the A) Bi 4f B) I 3d C) Ti 2p and D) O 1s regions

The 5xBiOI Bi4f region (Figure 4.28a) showed two peaks at 164.2 eV and 158.9 eV binding energy, corresponding to the $4f_{5/2}$ and $4f_{7/2}$ states of Bi^{3+}. Similarly, the I 3d HR-XPS scans (Figure 4.28b) revealed two peaks at 619.0 eV and 630.4 eV corresponding to the $3d_{1/2}$ and $3d_{3/2}$ peaks of I^-.

4.3.2.3.2 TEM Elemental Mapping

TEM elemental maps (Figure 4.29) showed that high concentrations of Bi and I were only found in the nanoplates identified in the TEM analysis.

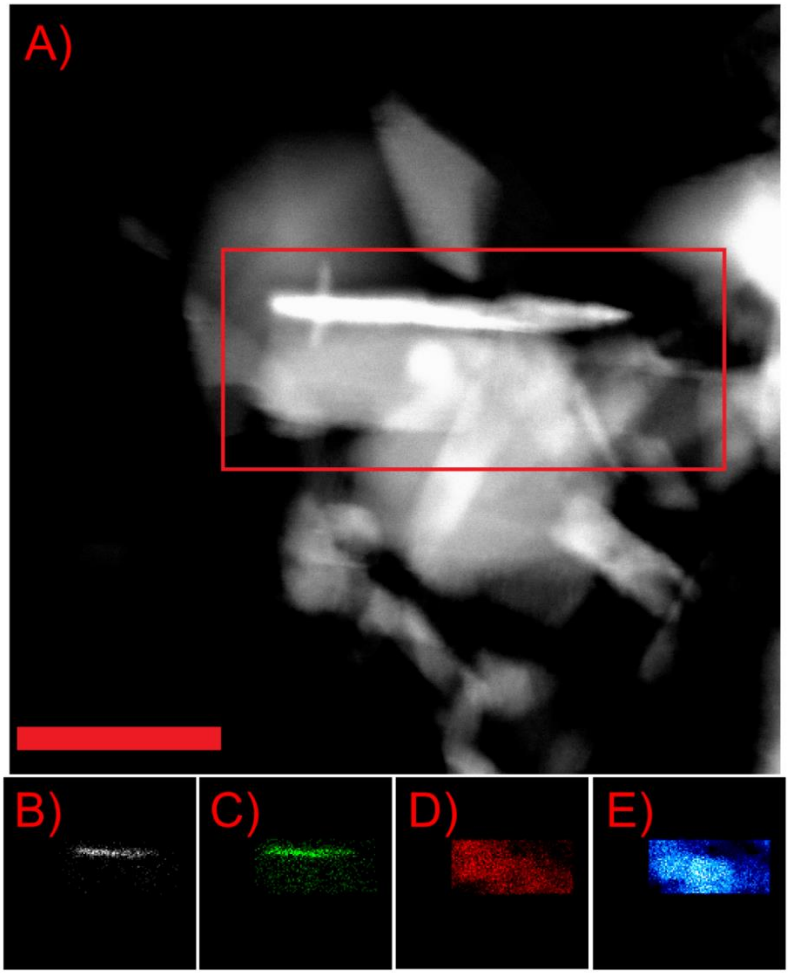

Figure 4.29. A) STEM HAADF image of a BiOI nanoplate and corresponding B) Bi C) I D) Ti and E) O elemental maps. Red bar in A) corresponds to 100 nm.

Thus, it can be confirmed that these structures are indeed the BiOI formed by SILAR.

4.3.2.4 Electronic & Optical Characterisation

4.3.2.4.1 Diffuse Reflectance Spectroscopy

BiOI is well known to have an indirect band gap[42–44], and as such the band gap can be obtained from the Tauc plot (Figure 4.30) according to the indirect band gap Tauc equation.

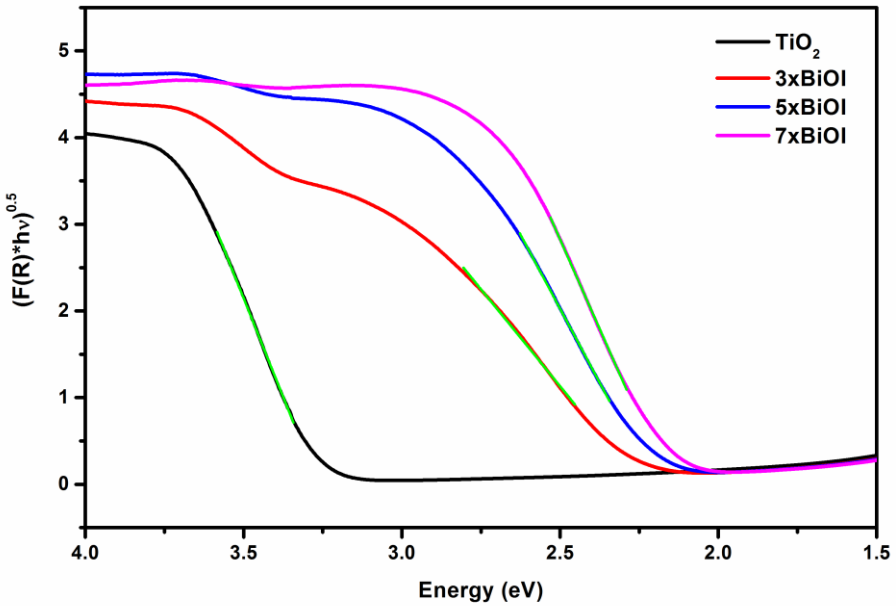

Figure 4.30. Tauc plots of the pristine TiO_2 and BiOI modified films. Green lines indicate regions used to determine band gaps.

Extrapolation of the Tauc plot to the x-axis therefore gives the band gaps for the prepared materials, which have been summarised in Table 4.5.

Table 4.5 – TiO_2-BiOI band gaps and valence band maxima

Sample	Valence Band Maxima (eV)	Band Gap (eV)
TiO_2	2.7 ± 0.1	3.26 ± 0.01
3xBiOI	1.0 ± 0.2	2.25 ± 0.01
5xBiOI	1.0 ± 0.0(4)	2.19 ± 0.01
7xBiOI	1.1 ± 0.1	2.14 ± 0.02

The band gaps of the composites were found to be decrease very slightly as the number of SILAR cycles was increased, while the absorption in the visible is improved on repeated SILAR cycling.

4.3.2.4.2 Valence Band XPS

To gain insight into the composite's electronic structure, valence band XPS measurements were also made (Figure 4.31) and the results are summarised in Table 4.5.

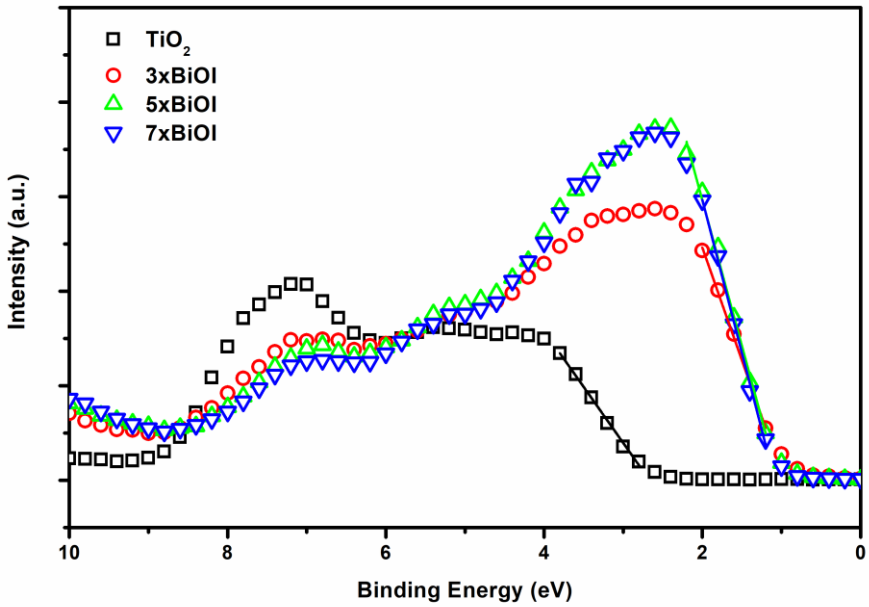

Figure 4.31. Valence band XPS scans of the TiO_2 and BiOI modified TiO_2 films.

A large positive shift of ~1.7 eV was noted for the samples modified by SILAR, indicating a raising of the valence band with respect to TiO_2.

4.3.2.5 Band Alignment & Potential Mechanism

Starting from the TiO_2 band gap of 3.2 eV it is possible to construct a band alignment diagram for the composites using the valence band maxima and band gaps determined by diffuse reflectance according to the equation below.

$$E_{cb} = E_{vb} + E_g$$

Where E_{cb} is the conduction band minimum, E_{vb} is the valence band maximum and E_g is the band gap determined from the diffuse reflectance measurement. As found by the valence band XPS measurements, the BiOI valence band lies 1.7 eV above that of TiO_2, and hence the conduction band minimum lies at a value of (1.7 + E_g) above the TiO_2 valence band. Applying this method gives the conduction band of BiOI around 0.7 eV above that of TiO_2 as shown in Figure 4.32.

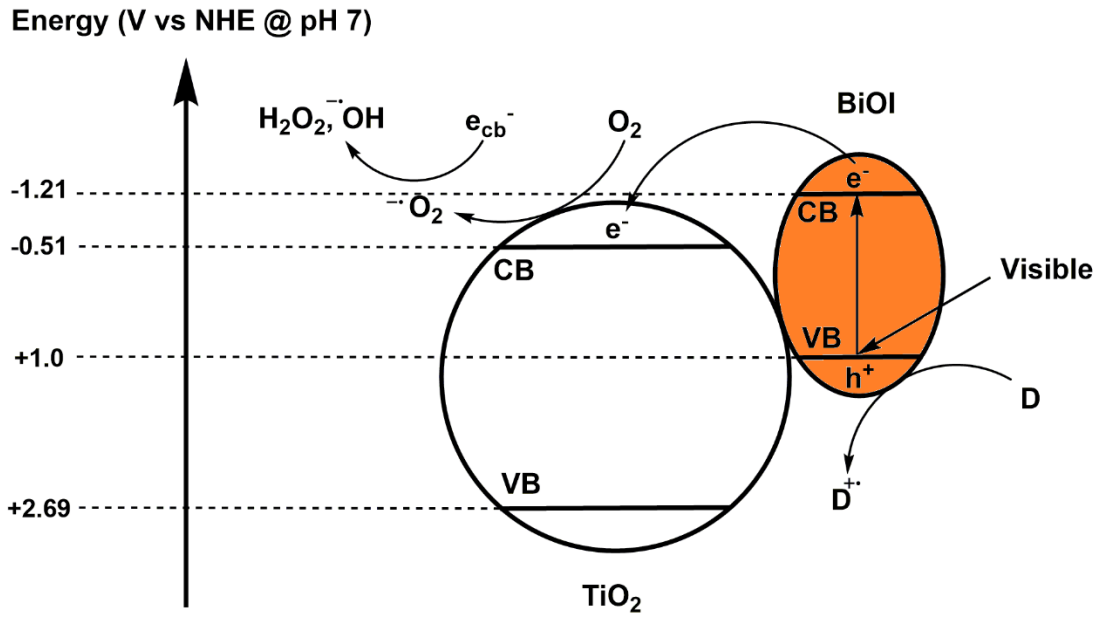

Figure 4.32. Type 2 band alignment and mechanism of action of BiOI-TiO_2 under visible light irradiation

Therefore, electrons excited by visible light incident upon BiOI have a 0.7 eV driving force to separate from their corresponding holes by transport across the TiO_2-BiOI interface. In a similar fashion, any UV-generated holes in TiO_2 would have a 1.7 eV driving force to migrate to BiOI. This arrangement of the bands is in agreement with the previously suggested alignment formed by equilibration of the Fermi levels of BiOI and TiO_2 when the p-n heterojunction is formed[34,45]. This heterojunction has been recently shown by scavenging experiments carried out by Luo *et al.*[46] to degrade organic species via the formation of the superoxide and hydroxyl radicals under visible light. It is likely however that holes in the valence band of BiOI in this heterojunction are not oxidising enough to directly produce hydroxyl radicals, and therefore must be scavenged by organic electron donors. The hydroxyl radicals formed as noted by Luo

et al. must therefore originated from the multi-electron reduction pathway starting from the reduction of oxygen to superoxide.

The formation of a p-n junction is advantageous in driving photoexcited electrons and holes away from one another at the interface between two materials, improving charge separation and therefore photocatalytic activity. As such we have established that the energetics of the BiOI-TiO_2 heterojunction allows both the absorption of visible light, and a mechanism for charge separation across the interface.

4.3.2.6 Photoluminescence

The photoluminescence spectra of the prepared materials excited at 300 nm are given in Figure 4.33.

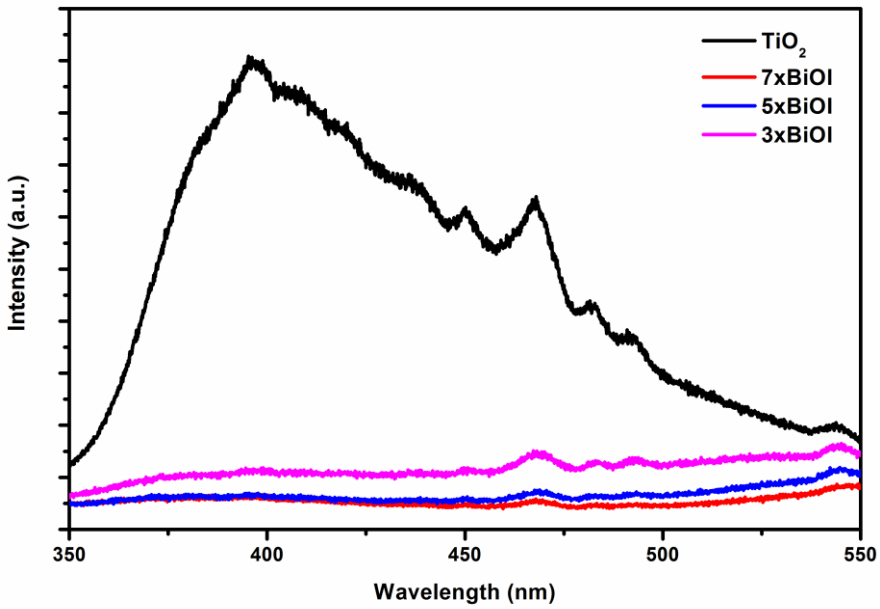

Figure 4.33. Photoluminescence spectra of the TiO_2 and BiOI modified TiO_2 films excited at 300 nm.

A large broad peak in the region of 350-550 nm was observed for unaltered TiO_2, where in the SILAR modified samples the peak became almost entirely quenched. This is likely in part due to re-absorption of emitted photons by BiOI and cannot be taken as conclusive proof of charge separation, however it is noteworthy that there is still a

significant decrease in emission intensity at longer wavelengths where the absorption of the BiOI is not high.

4.3.2.7 Photocatalytic Testing

4.3.2.7.1 Degradation of Organic Pollutants

Initial photocatalytic screening was carried out by following the photobleaching of the dye Rhodamine B (RhB). Using the cuvette reactor system as described in the experimental section, the films were placed in the RhB solution and allowed to reach an adsorption-desorption equilibrium (Figure 4.34).

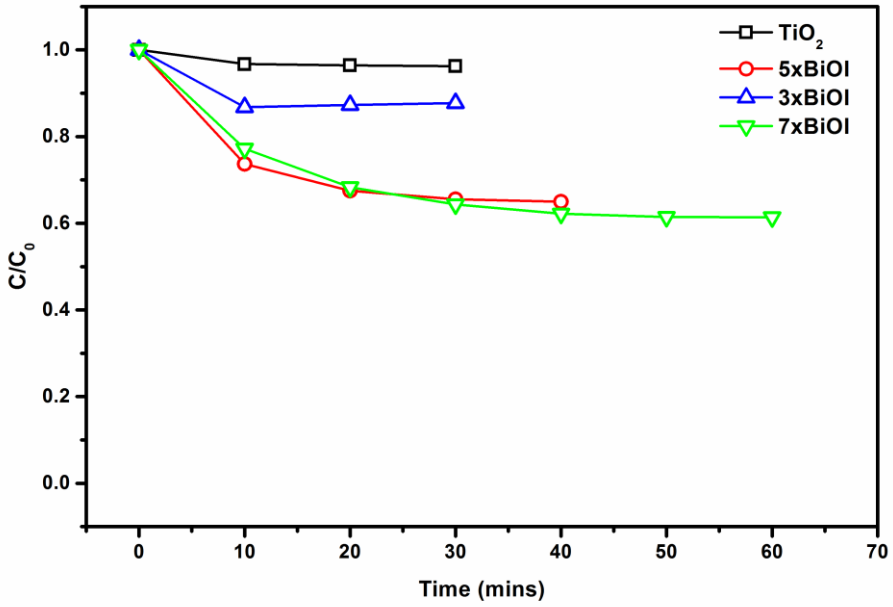

Figure 4.34. Dark adsorption of RhB on TiO_2 and BiOI modified TiO_2

The films were there irradiated using a white LED giving the pseudo 1st order rate plots as shown in Figure 4.35.

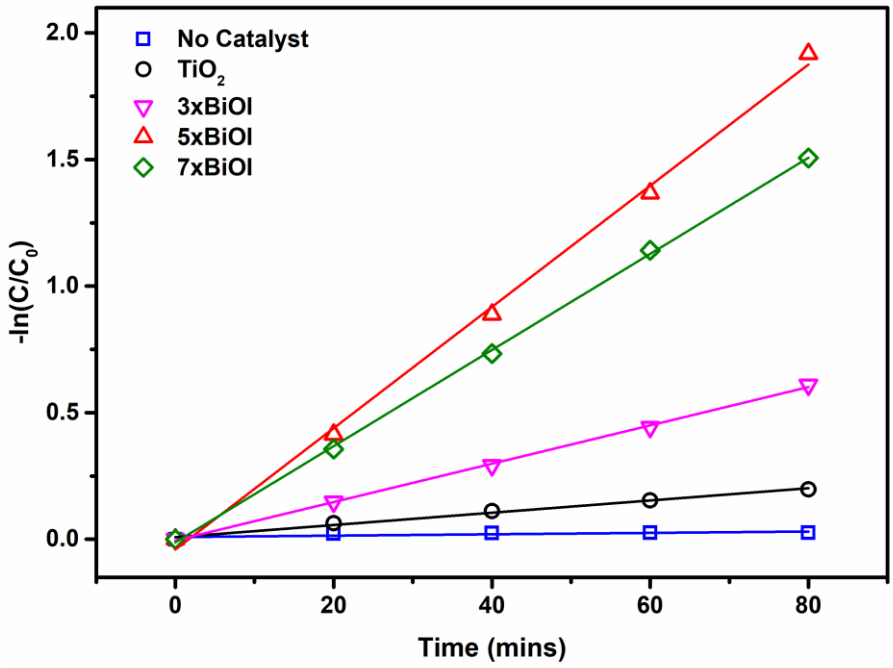

Figure 4.35. Pseudo first order rate plots of TiO_2 and the BiOI modified TiO_2 films against RhB

According to this equation, the 1st order rate constants for the photocatalytic decomposition of RhB are given in table 4.6.

Table 4.6 – TiO_2-BiOI Photocatalytic Degradation Studies

Sample	1st order rate constant (10^{-3} min^{-1})	
	RhB	4CP
No catalyst	0.27	-
TiO_2	2.42	0.09 ± 0.14
3xBiOI	7.57	-
5xBiOI	23.9	3.47 ± 0.05
7xBiOI	19.0	-

It was observed that the composite photocatalytic rates increased as the number of SILAR cycles increased up to 5xBiOI, at which point no further increase was observed

and in fact a small decrease was found. This could be due to the BiOI nanoplates becoming too large for charges to effectively inject into the TiO_2 conduction band, or the number of plates could perhaps be hindering the surface of the TiO_2 from the solution. In view of removing the effects of self-sensitisation, the best photocatalyst film (5xBiOI) was selected from this initial screening for further testing upon the photobleaching of the UV only absorbing organic pollutant 4-chlorophenol (4-CP) (Figure 4.36).

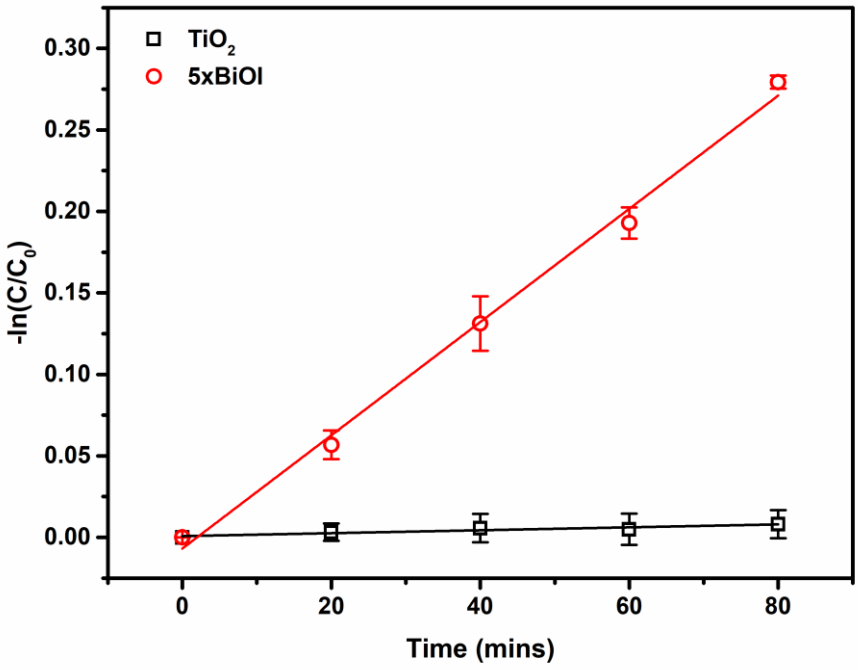

Figure 4.36. Pseudo first order rate plots of TiO_2 and 5xBiOI against 4CP

The initial 1st order rate constants achieved for 5xBiOI and TiO_2 are compared in Table 2. While a similar trend is observed in the activity of the 3x, 5x and 7xBiOI sensitised films (Figure 4.37), the photoactivity of 5xBiOI on 4CP is lower than the same material tested on RhB, attributed to the loss of self-sensitisation.

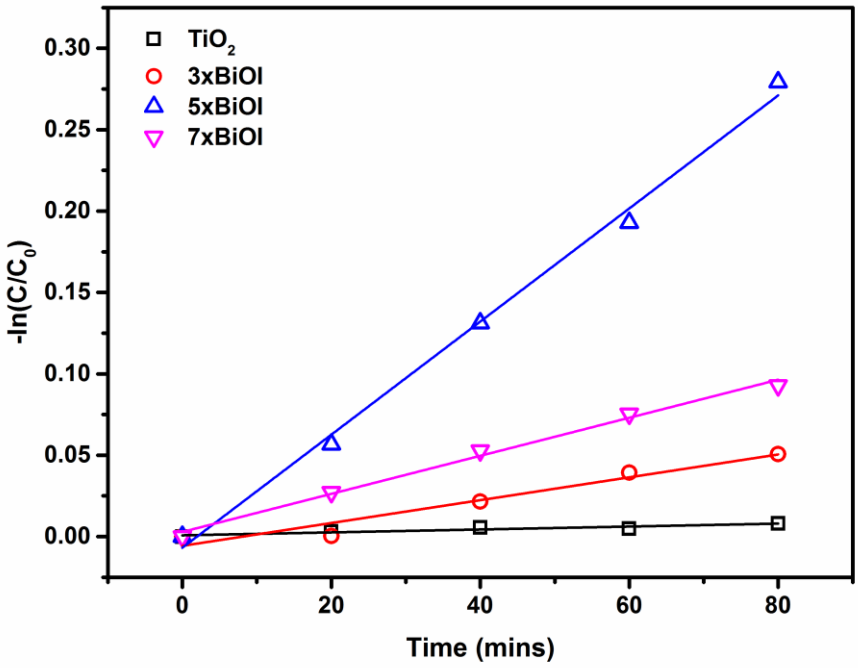

Figure 4.37. Activity trend of the prepared films against 4CP

However, the lack of this effect means that the rate constant achieved for the degradation of 4CP is a much more accurate reflection of the photocatalytic efficiency of BiOI-TiO_2 towards real-world pollutants. In comparison to photocatalytic BiOI-TiO_2 materials which have been reported previously, the SILAR produced material presented here compares very favourably (Table 4.7).

Table 4.7 - Previously reported BiOI-TiO_2 photocatalysts

Preparation	Light Source (filter)	Analyte	Photocatalytic Activity	Reference
Doctor Blading & SILAR	30 W White LED (>400 nm)	Rhodamine B	$23.9*10^{-3}$ min^{-1}	This Work
		4-Chlorophenol	$3.47\pm0.05*10^{-3}$ min^{-1}	
Soft Chemical (80 ^{o}C)	500 W Halogen-Tungsten Lamp (>420 nm)	Methyl Orange	1.3925 hr^{-1} ($23.2*10^{-3}$ min^{-1})	Zhang *et al.*[33]
Electrospinning & Hydrothermal	500 W Xe lamp (>420 nm)	Rhodamine B	92 % degradation in 135 mins	Liao *et al.*[47]
Reverse Microemulsion	250 W Halogen Lamp (>420 nm)	Methyl Orange	0.8699 hr^{-1} ($14.5*10^{-3}$ min^{-1})	Liu *et al.*[48]
Electrospinning & Solvothermal	500 W Xe Lamp (>400 nm)	Methylene Blue	0.015 min^{-1}	Zhang *et al.*[49]
Electrospinning & Hydrothermal	500 W Xe Lamp (>420 nm)	Methylene Blue	83 % degradation in 180 mins	Luo *et al.*[46]

It should be emphasised that direct numerical comparison between these different studies cannot be made since all were performed under different conditions, however

a broad qualitative comparison is worthwhile to understand the context of our findings. We note that our study was performed using an immobilised film suitable for practical recycling and used a much lower-power light source than the other studies. Despite this, 5xBiOI performs either similarly or better than the previously reported materials in the photocatalytic degradation of dyes. Furthermore, to the best of our knowledge no literature precedent for the photocatalytic degradation of colourless pollutants by BiOI-TiO_2 exist, and as such no comparison could be made for the photodegradation of 4CP. As stated previously, the degradation of colourless organics is a better reflection of a materials activity than that of dyes when using visible light, however this has clearly been overlooked for BiOI-TiO_2 composites. It is therefore suggested that this work represents the first accurate reflection of the non-self-sensitised activity of BiOI-TiO_2.

4.3.2.7.2 Recyclability Testing

The long-term stability of the films was assessed by increasing the irradiation time to 4 hours per run and measuring the degradation efficiency of 5xBiOI on 4CP upon successive recycles (Figure 4.38).

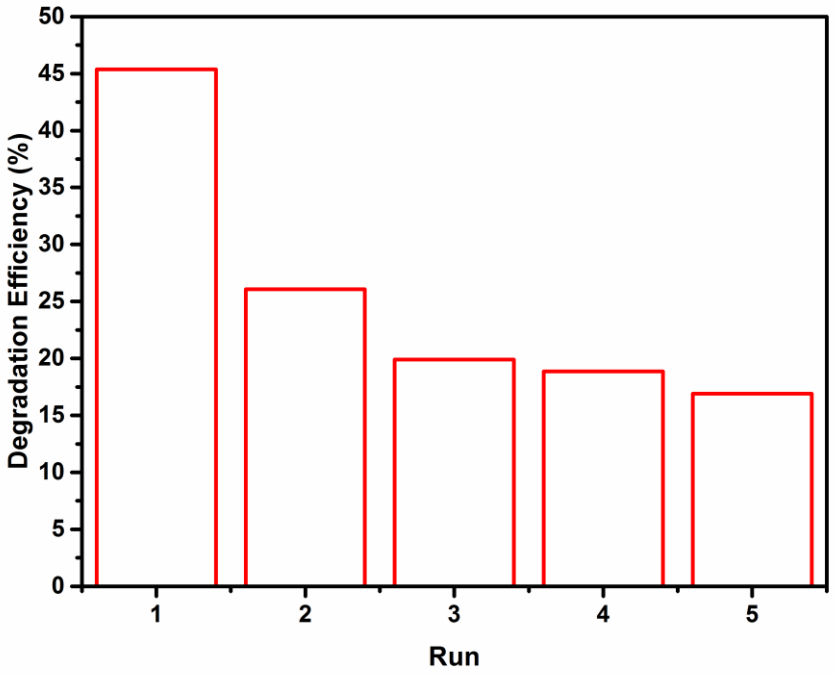

Figure 4.38. DE changes of 5xBiOI against 4CP on successive 4 hour long cycles

It was found that ~45% of the 4CP was degraded in the first 4 hours, but that after the first recycle around half the activity was lost. The activity losses however, became smaller on subsequent recycles. There remained a downward trend in the degradation efficiency up to the 20 hours of irradiation tested. It has been noted that BiOI may be somewhat unstable in water due to the loss of iodine and formation of surface hydroxides[50]. The formation of a surface layer of bismuth hydroxide reduces the visible activity as bismuth hydroxide has no visible absorption, and hence this is a likely reason for the activity losses observed. To probe the changes that occur during photocatalytic testing, X-ray diffraction studies were carried out before and after irradiation (Figure 4.39).

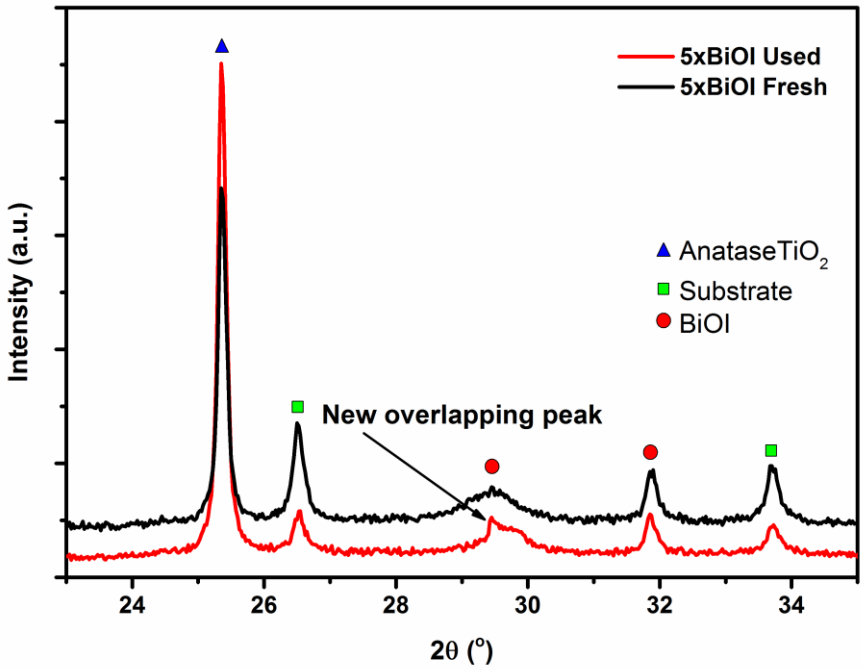

Figure 4.39. XRD traces of 5xBiOI before and after recycle testing

Focusing upon the peaks due to the [012] and [110] planes of BiOI at 2θ values of 29.7° and 33.7°, changes in the relative intensities and peak shapes were observed. Generally, both peaks decreased in intensity when compared to the intense anatase peak (blue triangle in Figure 4.39), indicating a reduction of the concentration or crystallinity of the BiOI. In addition, a distinct change in the shape of the peak corresponding to the [012] plane was noted. Before irradiation a broad symmetric peak was measured, however after irradiation a secondary sharp peak partially overlapping this peak appeared, indicating a secondary phase being present. It is tentatively suggested that this secondary phase to be inactive bismuth hydroxide formed during irradiation.

4.4 Chapter 4 Conclusions

Two bismuth containing materials, $BiVO_4$ and BiOI, have been applied in a composite with TiO_2 immobilised on glass plates. These materials aimed to give superior visible light activity than the previously described BTO and LVO materials, with a view to allowing access to visible only photocatalytic degradation.

$BiVO_4$ has been deposited upon the TiO_2 surface using the SILAR method. Successive deposition cycles were found to sensitise the TiO_2 to visible light up to the band gap of $BiVO_4$ at ~2.5 eV. The band structure of the composites has been determined by spectroscopic and electrochemical methods to provide a thermodynamic drive for charge separation across the interface as a Type II heterojunction. The photocatalytic efficiency of the prepared films has been investigated by the degradation of the model organic contaminant rhodamine 6G under visible light irradiation. The importance of charge separation has been investigated using a new approach in which control films of ZrO_2-$BiVO_4$ were fabricated. These control films were concluded to closely resemble the $BiVO_4$-TiO_2 system in all but charge separation due to mismatching of the conduction and valence band energies, which was found to result in much reduced photocatalytic activity. This provides the first direct photocatalytic evidence between comparable systems, for enhanced performance through interfacial charge separation of a $BiVO_4$-TiO_2 hybrid. The mechanism of action of the composites has been determined to occur via sensitisation by the model organic dye, which has been found to be able to inject charges into the composite conduction band, and hence it can be concluded that charge separation is the main factor in the improvements in activity observed, and that any activity is likely specific to the dye tested against.

To overcome this limitation, a study on BiOI, having a narrower band gap and p-type conductivity complementary to n-type TiO_2 was then carried out. We present the formation of BiOI nanoplate sensitised TiO_2 films for the photocatalytic degradation of organic pollutants. SILAR was used as a simple method to grow BiOI at the surface of TiO_2 allowing control of the size and number of BiOI nanoplates, and as such optimise the photocatalytic properties of the film. The band structure of these composites has again been determined to be that of a type II heterojunction, allowing the migration of excited electrons in BiOI to the TiO_2 conduction band under visible irradiation. This has led the heterojunctions to be effective in the photocatalytic degradation of both the visible active dye RhB and the non-absorbing 4CP under visible light irradiation. Some eventual issues with stability have been uncovered in long term testing, which suggests some further efforts to stabilise the BiOI may be required for the application of this material on a larger scale.

Thus, there is potential for such narrow band gap materials to be used in conjunction with TiO_2 and as such make use of lower energy irradiation or sunlight. However it appears that in doing so the loss of driving force for radical formation can be detrimental to degradation, and can introduce problematic selectivities toward different molecules.

4.5 Chapter 4 Specific Experimental

4.5.1 Sample Preparation

4.5.1.1 Substrate & TiO_2 Film Preparation

FTO glass substrates were cut into 2cm x 2cm squares before being ultrasonically cleaned in a solution of detergent (Decon 90, ~5% in tap water) for 15 minutes. The substrates were then rinsed with tap water, deionised water and finally ethanol. Titania paste (Dyesol 18-NRT was used for $BiVO_4$, Dyesol WER2-O was used for BiOI) was then doctor bladed in 1 cm x 2 cm strips onto the surface of the FTO before heating to 510 ^oC in stages on a controlled hotplate to remove the organic templates, leaving a highly porous TiO_2 film. The temperature profile of the heating regime was as follows: 325 ^oC for 5 minutes, 375 ^oC for 5 minutes, 425 ^oC for 5 minutes, 475 ^oC for 10 minutes, 510 ^oC for 10 minutes. The heating ramp rate between each stage was 10 ^oC min^{-1} apart from the final stage where it slowed to 5 ^oC min^{-1}. The sintered TiO_2 films were then allowed to cool gradually on the hotplate to room temperature. Narrower (0.8 cm x 2 cm) films were also fabricated in the same way for photocatalytic testing and electrochemical characterisation. ZrO_2 films were prepared using the same doctor blading technique, starting from the clean FTO electrodes using a commercially available ZrO_2 paste. After doctor blading the ZrO_2 paste, the films were fired at 400 ^oC for 30 minutes.

4.5.1.2 SILAR Modification

To deposit $BiVO_4$, aqueous solutions of $Bi(NO_3)_3.5H_2O$ (0.01 M) and NH_4VO_3 (0.01 M) were used as the cation and anion precursors respectively. The as-prepared TiO_2 or ZrO_2 films were submerged first in the $Bi(NO_3)_3$ solution for 30 seconds, then washed with water for 30 seconds to remove any loosely bound material before being submerged in the NH_4VO_3 solution for 30 seconds and finally washed once more with

water for 30 seconds. This constitutes one full SILAR cycle, and was repeated 1-6 times to give differing levels of $BiVO_4$ on the substrates. The films were then annealed at 500 ^oC in a furnace for 1 hour.

To deposit BiOI, aqueous solutions of $Bi(NO_3)_3.5H_2O$ (5 mM) and KI (5 mM) were used as the cation and anion precursors respectively. The as-prepared TiO_2 films were submerged first in the $Bi(NO_3)_3$ solution, then washed with water to remove any loosely bound material before being submerged in the KI solution and finally washed once more with water. This constitutes one full SILAR cycle, and was repeated 3, 5 and 7 times to give differing levels of BiOI on the substrates. 600 second immersions were used for each solution and wash.

4.5.2 Photocatalytic Testing

To test the $BiVO_4$ films, narrow films (0.8 cm x 2 cm) were submerged into a solution of Rhodamine 6G (2.5 ml, 6 μmolar) in a quartz glass cuvette. The films were stirred in the dark for 30 minutes to establish an adsorption equilibrium, then irradiated with a white LED (7W applied power) fitted with a UV filter (>400 nm, Thorlabs). The decolourisation of Rhodamine 6G was followed by measuring the absorption at 525 nm at regular time intervals using a JASCO V-670 spectrophotometer. Between recyclability tests the photocatalyst films were left stirring in deionised water overnight and then dried for 30 minutes at 130 ^oC in an oven before re-use.

To test the BiOI films, narrow films (0.9 cm x 2 cm) were submerged into a solution of Rhodamine B (2 ml, 10 μmolar) in a quartz cuvette. The films were stirred in the dark for up to 60 minutes to establish an adsorption equilibrium, then irradiated with a white LED (30 W applied power) fitted with a UV filter (>400 nm, Thorlabs). The degradation of 4-chlorophenol was measured in the same way, using 4-chlorophenol of 156 μmolar concentration followed using the peak at 280 nm. In the assessment of the recyclability of the films, a single measurement after 4 hours irradiation was taken to calculate the degradation efficiency, between runs the film was washed thoroughly with water and dried under a stream of N_2.

4.6 Chapter 4 References

1 S. J. A. Moniz and J. Tang, *ChemCatChem*, 2015, **7**, 1659–1667.
2 G. Chen, S. Ji, Y. Sang, S. Chang, Y. Wang, P. Hao, J. Claverie, H. Liu and G. Yu, *Nanoscale*, 2015, **7**, 3117–3125.
3 S. Li, Z. Zhao, Y. Huang, J. Di, Y. (Alec) Jia and H. Zheng, *J. Mater. Chem. A*, 2015, **3**, 5467–5473.
4 Y. Liu, P. Zhang, B. Tian and J. Zhang, *ACS Appl. Mater. Interfaces*, 2015, **7**, 13849–13858.
5 Y. Kim, D. Shin, W. J. Chang, H. L. Jang, C. W. Lee, H.-E. Lee and K. T. Nam, *Adv. Funct. Mater.*, 2015, **25**, 2369–2377.
6 R. Munprom, P. A. Salvador and G. S. Rohrer, *J. Mater. Chem. A*, 2015, **3**, 2370–2377.
7 J. Sun, X. Li, Q. Zhao, M. O. Tadé and S. Liu, *J. Mater. Chem. A*, 2015, **3**, 21655–21663.
8 M. Zalfani, B. van der Schueren, Z.-Y. Hu, J. C. Rooke, R. Bourguiga, M. Wu, Y. Li, G. Van Tendeloo and B.-L. Su, *J. Mater. Chem. A*, 2015, **3**, 21244–21256.
9 N. Guijarro, T. Lana-Villarreal, T. Lutz, S. A. Haque and R. Gómez, *J. Phys. Chem. Lett.*, 2012, **3**, 3367–3372.
10 S. S. Mali, R. S. Devan, Y.-R. Ma, C. A. Betty, P. N. Bhosale, R. P. Panmand, B. B. Kale, S. R. Jadkar, P. S. Patil, J.-H. Kim and C. K. Hong, *Electrochim. Acta*, 2013, **90**, 666–672.
11 A. Kudo and Y. Miseki, *Chem. Soc. Rev.*, 2009, **38**, 253–278.
12 A. Kudo, K. Omori and H. Kato, *J. Am. Chem. Soc.*, 1999, **121**, 11459–11467.
13 X. Zhang, Z. Ai, F. Jia, L. Zhang, X. Fan and Z. Zou, *Mater. Chem. Phys.*, 2007, **103**, 162–167.
14 H. Huo, S. Wang, S. Lin, Y. Li, B. Li and Y. Yang, *J. Mater. Chem. A*, 2014, **2**, 333–338.
15 L. Chen, E. Alarcón-Lladó, M. Hettick, I. D. Sharp, Y. Lin, A. Javey and J. W. Ager, *J. Phys. Chem. C*, 2013, **117**, 21635–21642.
16 M. D. Rossell, P. Agrawal, A. Borgschulte, C. Hébert, D. Passerone and R. Erni, *Chem. Mater.*, 2015, **27**, 3593–3600.
17 L. Zhang, D. Chen and X. Jiao, *J. Phys. Chem. B*, 2006, **110**, 2668–2673.
18 K. P. S. Parmar, H. J. Kang, A. Bist, P. Dua, J. S. Jang and J. S. Lee, *ChemSusChem*, 2012, **5**, 1926–1934.
19 T. S. Sinclair, B. M. Hunter, J. R. Winkler, H. B. Gray and A. M. Müller, *Mater. Horizons*, 2015, **2**, 330–337.
20 H. Ye, J. Lee, J. S. Jang and A. J. Bard, *J. Phys. Chem. C*, 2010, **114**, 13322–13328.
21 S. Ho-Kimura, S. J. a. Moniz, A. D. Handoko and J. Tang, *J. Mater. Chem. A*, 2014, **2**, 3948.
22 R. Bajaj, M. Sharma and D. Bahadur, *Dalt. Trans.*, 2013, **42**, 6736.
23 D. K. Ma, M. L. Guan, S. S. Liu, Y. Q. Zhang, C. W. Zhang, Y. X. He and S. M. Huang, *Dalt. Trans*, 2012, **41**, 5581–5586.
24 Y. Hu, D. Li, Y. Zheng, W. Chen, Y. He, Y. Shao, X. Fu and G. Xiao, *Appl. Catal. B Environ.*, 2011, **104**, 30–36.
25 M. Xie, X. Fu, L. Jing, P. Luan, Y. Feng and H. Fu, *Adv. Energy Mater.*, 2014, **4**, n/a-n/a.
26 H. Li, H. Yu, X. Quan, S. Chen and H. Zhao, *Adv. Funct. Mater.*, 2015, **25**, 3074–3080.
27 J. Sun, X. Li, Q. Zhao, J. Ke and D. Zhang, *J. Phys. Chem. C*, 2014, **118**, 10113–10121.
28 B. J. Morgan and G. W. Watson, *J. Phys. Chem. C*, 2010, **114**, 2321–2328.
29 M. Wang, Y. Hu, J. Han, R. Guo, H. Xiong and Y. Yin, *J. Mater. Chem. A*, 2015, **3**, 20727–20735.
30 L. Liu, W. Yang, W. Sun, Q. Li and J. K. Shang, *ACS Appl. Mater. Interfaces*, 2015, **7**, 1465–1476.
31 Y. Wang, K. Deng and L. Zhang, *J. Phys. Chem. C*, 2011, **115**, 14300–14308.
32 J. Xia, S. Yin, H. Li, H. Xu, Y. Yan and Q. Zhang, *Langmuir*, 2011, **27**, 1200–1206.
33 X. Zhang, L. Zhang, T. Xie and D. Wang, *J. Phys. Chem. C*, 2009, **113**, 7371–7378.
34 Y. Zhang, Q. Pei, J. Liang, T. Feng, X. Zhou, H. Mao, W. Zhang, Y. Hisaeda and X. M. Song, *Langmuir*, 2015, **31**, 10279–10284.
35 M. Fang, H. Jia, W. He, Y. Lei, L. Zhang and Z. Zheng, *Phys. Chem. Chem. Phys.*, 2015, **17**, 13531–13538.
36 K. Wang, F. Jia, Z. Zheng and L. Zhang, *Electrochem. commun.*, 2010, **12**, 1764–1767.
37 K. Wang, F. Jia and L. Zhang, *Mater. Lett.*, 2013, **92**, 354–357.

38 W. Zhou, F. Sun, K. Pan, G. Tian, B. Jiang, Z. Ren, C. Tian and H. Fu, *Adv. Funct. Mater.*, 2011, **21**, 1922–1930.

39 J. B. Joo, Q. Zhang, M. Dahl, I. Lee, J. Goebl, F. Zaera and Y. Yin, *Energy Environ. Sci.*, 2012, **5**, 6321–6327.

40 S. Huang, Y. Feng, L. Han, W. Fan, X. Zhao, Z. Lou, Z. Qi, B. Yu and N. Zhu, *RSC Adv.*, 2014, **4**, 61679–61686.

41 S. Chou, C. Chen, Y. Dai, J. Lin and W. William, *RSC Adv.*, 2016, **6**, 33478–33491.

42 X. Xiao and W.-D. Zhang, *J. Mater. Chem.*, 2010, **20**, 5866.

43 Y. Lei, G. Wang, S. Song, W. Fan, M. Pang, J. Tang and H. Zhang, *Dalt. Trans.*, 2010, **39**, 3273.

44 X. Zhang and L. Zhang, *J. Phys. Chem. C*, 2010, **114**, 18198–18206.

45 Q. Teng, X. Zhou, B. Jin, J. Luo, X. Xu, H. Guan, W. Wang and F. Yang, *RSC Adv.*, 2016, **6**, 36881–36887.

46 S. Luo, J. Chen, Z. Huang, C. Liu and M. Fang, *ChemCatChem*, 2016, **8**, 3780–3789.

47 C. Liao, Z. Ma, G. Dong and J. Qiu, *Appl. Surf. Sci.*, 2014, **314**, 481–489.

48 Z. Liu, X. Xu, J. Fang, X. Zhu, J. Chu and B. Li, *Appl. Surf. Sci.*, 2012, **258**, 3771–3778.

49 Y. Zhang, S. Liu, Z. Xiu, Q. Lu, H. Sun and G. Liu, *J. Nanoparticle Res.*, 2014, **16**, 2375.

50 N. T. Hahn, S. Hoang, J. L. Self and C. B. Mullins, *ACS Nano*, 2012, **6**, 7712–7722.

Chapter 5 Separating Visible Light Harvesting and Charge Separation

5.1 Overview

Following the difficulties faced in designing a single material with both good visible light harvesting and the ability to separate charges efficiently, these two properties were separated and considered individually. This section aims to describe a simple way in which TiO_2 may be modified in two ways to address both properties, and through the combination of such, give a material with higher activity than each modification individually.

5.2 Carbon Coated TiO_2 with Chlorine Doping

5.2.1 Introduction

Doping is a commonly applied method by which visible light harvesting may be introduced to TiO_2 and other wide band gap semiconductors[1–3]. Excitation from interband dopant states allows a wide band gap material to use lower energy light, and thus for TiO_2 this typically allows visible light sources to be used to drive photocatalysis. Organic-inorganic hybrids have also attracted significant attention, with materials such as graphitic carbon nitride[4–6], light harvesting polymers[7–9] or carbon quantum dots[10,11] being studied in composites with TiO_2 for photocatalytic applications. The coating of inorganic semiconductors with a carbon layer has been investigated in recent years as a method for improving photocatalytic efficiencies by decreasing charge recombination due to the intrinsic high conductivity of the carbon layer[12]. This effect has also been shown to increase the stability of some inorganic semiconductors under irradiation by reducing the likelihood for photo-induced charges to simply reduce or oxidise lattice ions[13,14], and provide a layer of chemical protection to the coated semiconductor.

In this chapter is described the formation of a carbon coated TiO_2 film by pyrolytic treatment of a simply prepared TiO_2-catechol surface complex. We also describe a method by which the activity of this material can be improved by a simple hydrolysis of $TiCl_4$, resulting in the deposition of small (5-10nm) particles. This treatment has

also been found to result in the doping of chlorine into the structure, resulting in a substantial increase in photocatalytic activity for the degradation of organic pollutants. These $TiCl_4$ treated composite materials also are found to exhibit good activity for the photoreduction of Cr(VI) to Cr(III), and bactericidal applications. As such, the prepared films are shown to be multi-functional, with photocatalytic activity against organic, inorganic and biological contamination.

5.2.2 Results & Discussion

5.2.2.1 Sample Preparation

It is well known that catechol binds strongly to the surface of TiO_2[15,16], forming a visible absorbing charge transfer complex indicating intimate contact between the resulting carbonaceous material and the TiO_2 surface. Subsequent hydrolysis of a solution of $TiCl_4$ in a similar manner to that which is typically used in the field of dye sensitized solar cells to deposit small (~5-10nm) particles onto the film surface[17] was found to not significantly affect the films appearance. Upon thermal treatment under N_2 the films were found to turn from the characteristic yellow colour of the surface complex to a light brown, indicating the decomposition of the organic catechol to carbon. The general synthetic procedure is given in Figure 5.1, where the initial TiO_2 film is formed by a doctor blading method (see experimental).

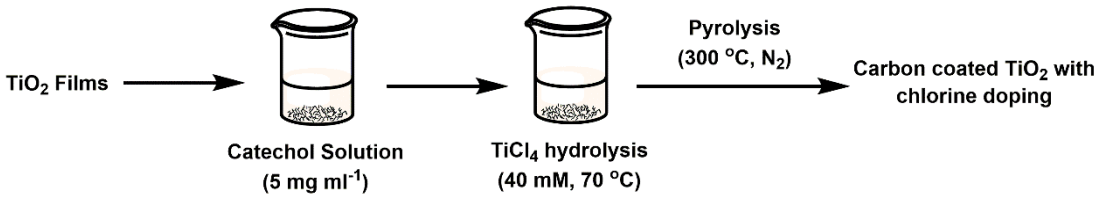

Figure 5.1. General preparation process used to generate the doped & composited films

Hydrolysis of $TiCl_4$ to give TiO_2 is typically followed up with a thermal treatment step in air to give complete conversion to crystalline TiO_2. Here, by using relatively low temperatures and an inert atmosphere, some Cl remains in the lattice as a dopant. This represents a relatively simple method to introduce Cl as a dopant into TiO_2, which to the best of our knowledge has not been reported to date. Chlorine doped TiO_2 as a photocatalytic material is relatively unexplored, with only a few examples existing in the literature[18], where the Cl dopant is often paired with a co-dopant[19,20]. To explore

the various components of the composite films, controls were prepared with only carbon coating (C-TiO_2), only $TiCl_4$ treatment with subsequent heating under N_2 (TiO_2-$TiCl_4$), and with both (C-$TiCl_4$-TiO_2).

5.2.2.2 Structure & Morphology

5.2.2.2.1 X-ray Diffraction

X-ray diffraction traces of the prepared materials are given in Figure 5.2.

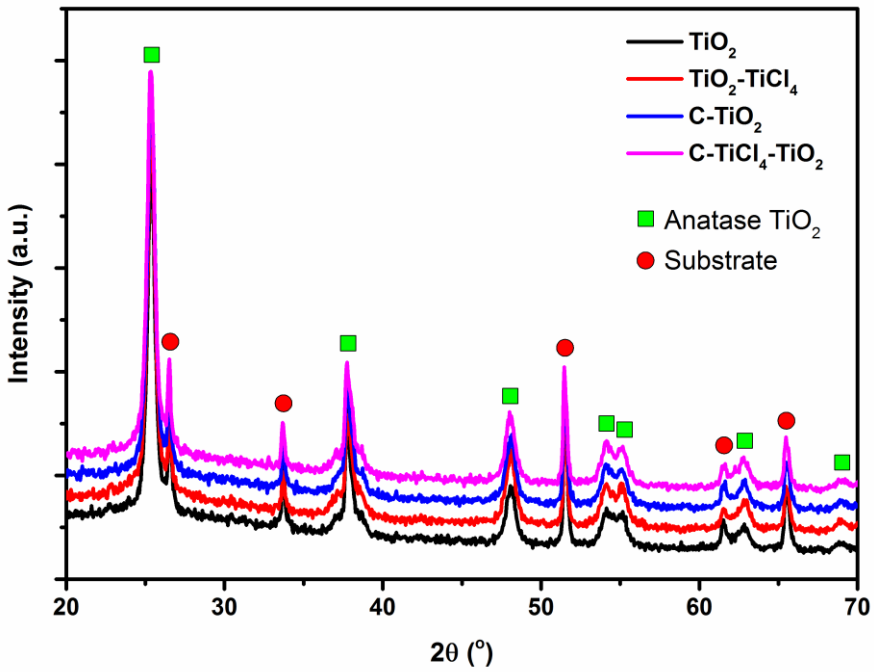

Figure 5.2. XRD traces of the TiO_2 films with various modifications

Several peaks were found which match well with the reported 2θ values for anatase TiO_2 (JCPDS card #21-1272). The remaining peaks are identified as being due to the FTO glass substrate. Upon modification of the film, no new peaks were found, suggesting either amorphous materials and/or their presence being in too low a concentration to be detectable by XRD analysis. The crystallinity of the underlying TiO_2 film is found to be largely unaffected by the modifications made, keeping high crystallinity after modification. This is advantageous as good crystallinity has been noted to be important in ensuring rapid charge migration through the structure, resulting in improved photocatalytic efficiencies[21].

5.2.2.2.2 Electron Microscopies

Scanning electron microscope (SEM) images of the pristine TiO_2 film surface revealed an interconnected porous network of particles of approximately 20nm in size (Figure 5.3).

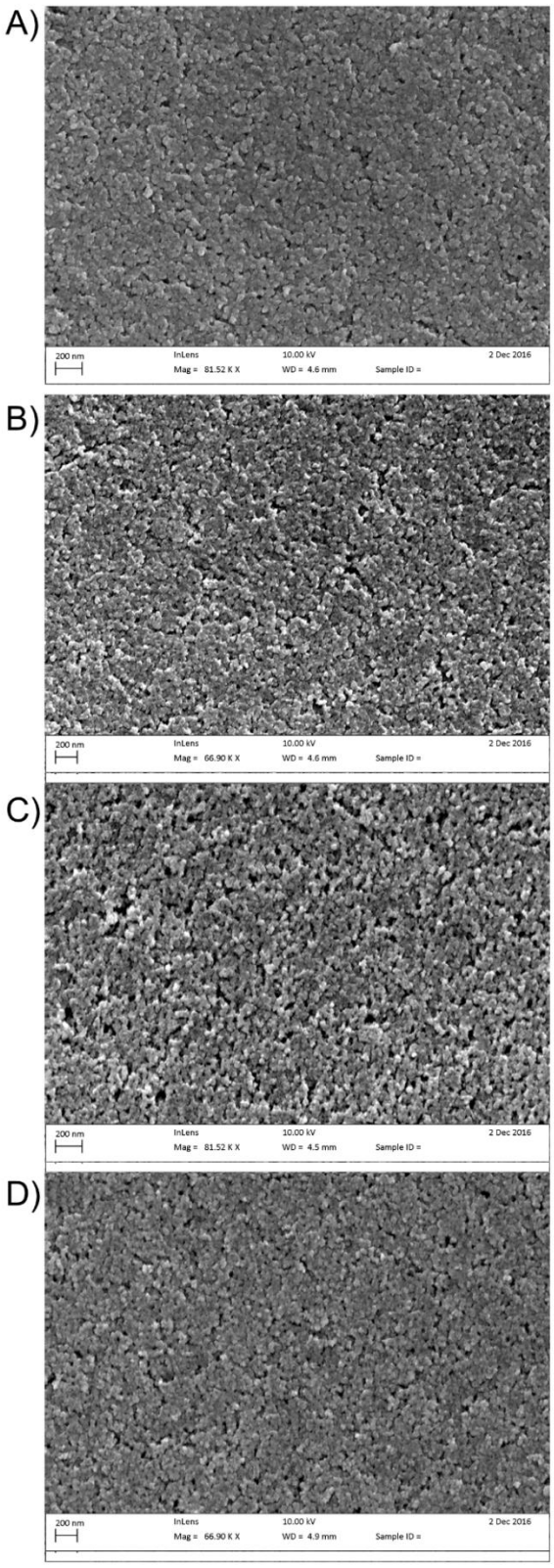

Figure 5.3. SEM images of A) the plain TiO_2 B) TiO_2-$TiCl_4$ C) C-TiO_2 and D) C-$TiCl_4$-TiO_2 film surfaces

However, no discernable differences were noted when the films were subjected to the carbon and/or the $TiCl_4$ treatments. To study the surface at greater magnification transmission electron microscope images were gathered (Figure 5.4).

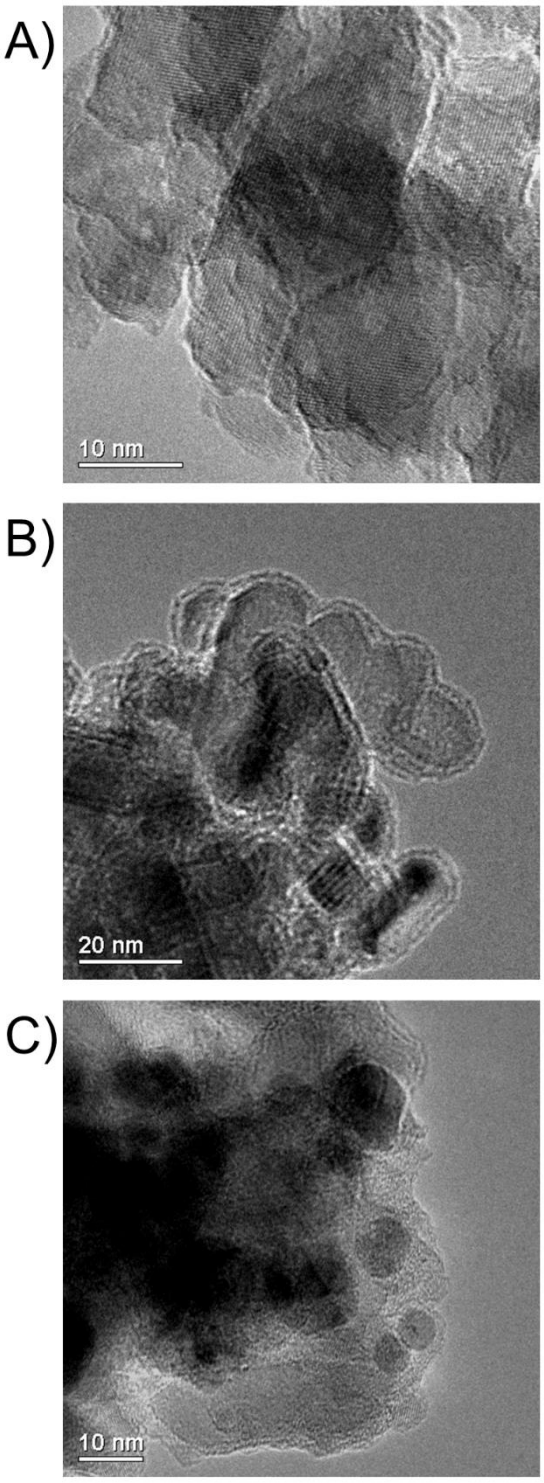

Figure 5.4. TEM images of the A) plain TiO_2 B) C-TiO_2 and C) C-$TiCl_4$-TiO_2 materials.

The unmodified TiO_2 particles were found to be well defined particles of around 20 nm in size. Clear lattice fringes of 0.35 nm were measured (Figure 5.5), which can be indexed to the [100] plane of anatase TiO_2.

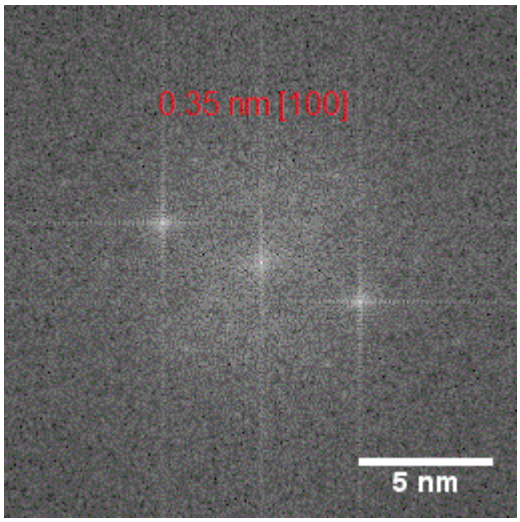

Figure 5.5. TEM lattice fringe measurement of the TiO_2 materials

By contrast, images of the carbon coated sample (C-TiO_2) revealed that the lattice fringes were entirely obscured with amorphous material, with a layer of this material observed around the edges of the particles of around ~2 nm. This material we assign as a carbonaceous layer, formed by the pyrolytic decomposition of catechol. Images of C-$TiCl_4$-TiO_2 revealed smaller particles (5-10 nm) deposited across the surface, which originate from the hydrolysis of $TiCl_4$. It is noteworthy that, upon treatment with $TiCl_4$, the lattice fringes that were previously entirely obscured were now found to be at least partially visible, and the carbon layer was in places much thinner than in the C-TiO_2 sample.

5.2.2.3 Elemental Analysis

5.2.2.3.1 TEM Elemental Mapping

To prove the presence of Cl dopants in the particles originating from the hydrolysis of $TiCl_4$, TEM elemental mapping experiments were carried out upon C-$TiCl_4$-TiO_2 (Figure 5.6).

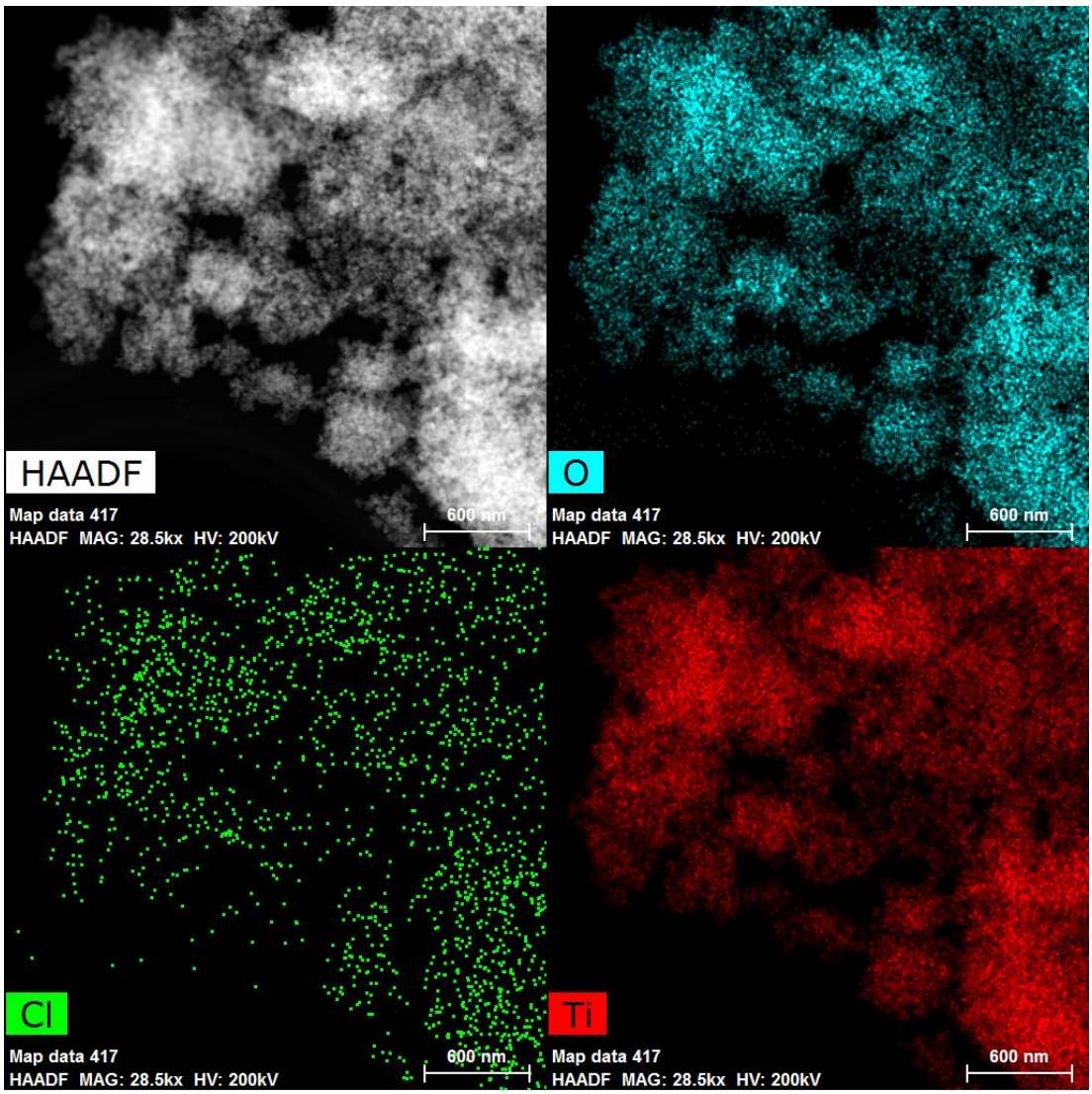

Figure 5.6. Element maps of O, Cl, and Ti in the C-$TiCl_4$-TiO_2 sample material

The presence of Cl was clearly confirmed by the EDS mapping, showing the Cl present across the film. No distinct areas of high Cl concentration were noted, indicating that the doping of chlorine into the structure is applied equally across the entire structure, and is not confined to any particular area.

High resolution X-ray photoelectron spectroscopy (XPS) scans of the carbon and chlorine regions are given in Figure 5.7.

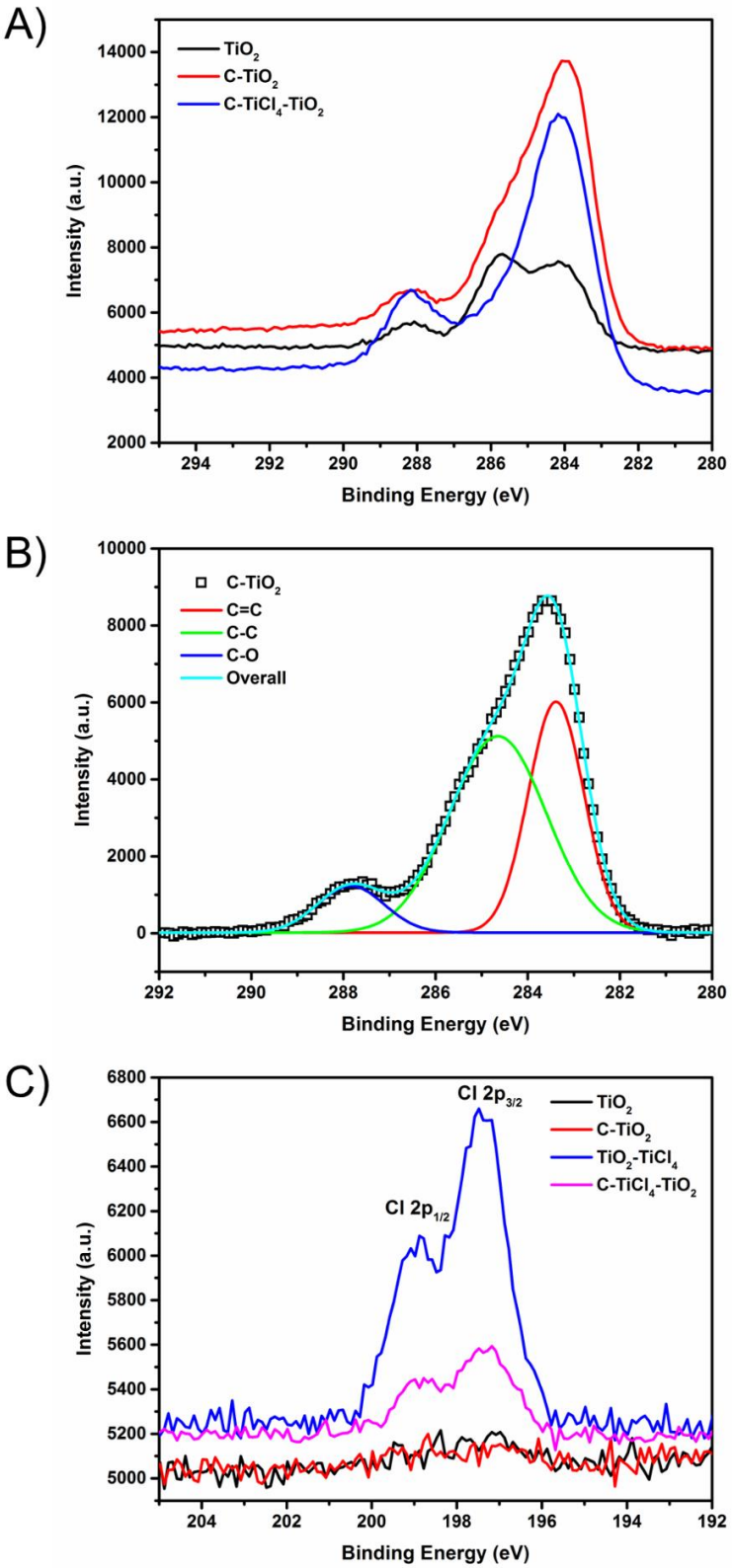

Figure 5.7. XPS scans of the A) C1s region B) C1s region of C-TiO₂ with fittings and C) Cl 2p region for the prepared materials

Carbon is often found in XPS studies due to adventitious carbon introduced in the handling of samples. However, it was found that samples containing pyrolysed catechol had significantly higher peak intensities in the carbon region. Typically, carbon XPS peaks are split into the various chemical states of carbon. Fits of these various chemical states are given in Figure 5.7b. The lowest energy peak (~284 eV) has been previously assigned to sp_2 hybridised carbon in other carbon nanomaterials[22], which sees the greatest increase in intensity over the adventitious carbon in the unmodified sample. This is in keeping with the pyrolytic decomposition of catechol leaving the aromatic features of the catechol intact. The shoulder peak (~285 eV), typically assigned to sp_3 hybridised carbon, sees only a very small increase in intensity when compared to the pristine TiO_2 sample, indicating that the majority of the added carbon exists as planar sp_2 type carbon. The small peak at higher binding energy (~288 eV) is typical of carbon attached to oxygen[23], and sees little difference between C-TiO_2 and pristine TiO_2. High resolution XPS of the chlorine region (Figure 5.7c) revealed the presence of chlorine in the TiO_2-$TiCl_4$ and C-$TiCl_4$-TiO_2 samples, but not the pristine or C-TiO_2 samples. This confirms that the $TiCl_4$ hydrolysis and subsequent heat treatment under N_2 is not converting the deposited material entirely into TiO_2, and that some Cl is retained within the structure as a dopant. The two peaks for chlorine can be assigned to the $2p_{1/2}$ and $2p_{3/2}$ states of chlorine, which appear in positions in accordance with previously reported values for chlorine doped materials[18,19]. No evidence for the introduction of nitrogen into the sample by the heating step under N_2 was found in the nitrogen region of the XPS (Figure 5.8)

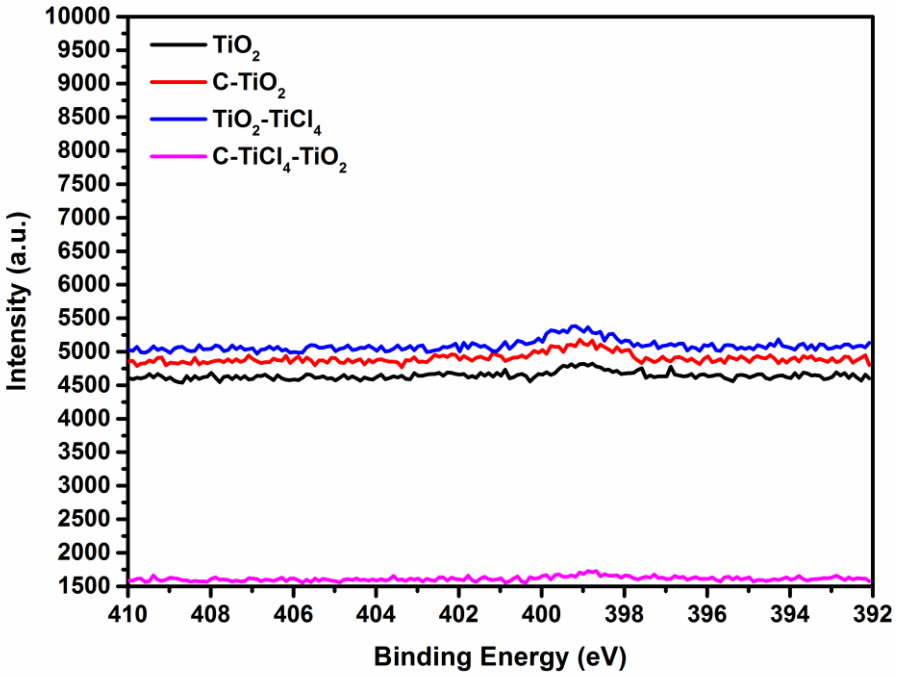

Figure 5.8. XPS scans of the N1s region of the prepared materials

This discounts the presence of N-doped TiO_2, a common strategy for improving photocatalytic activity of TiO_2[24], in the samples which could have caused similar changes in the films' properties.

5.2.2.4 Optical & Electronic Characterisation

5.2.2.4.1 UV-visible Spectroscopy

The as-prepared samples were all found to be semi-transparent, and therefore UV-vis transmission experiments were carried out to ascertain the films absorption characteristics (Figure 5.9).

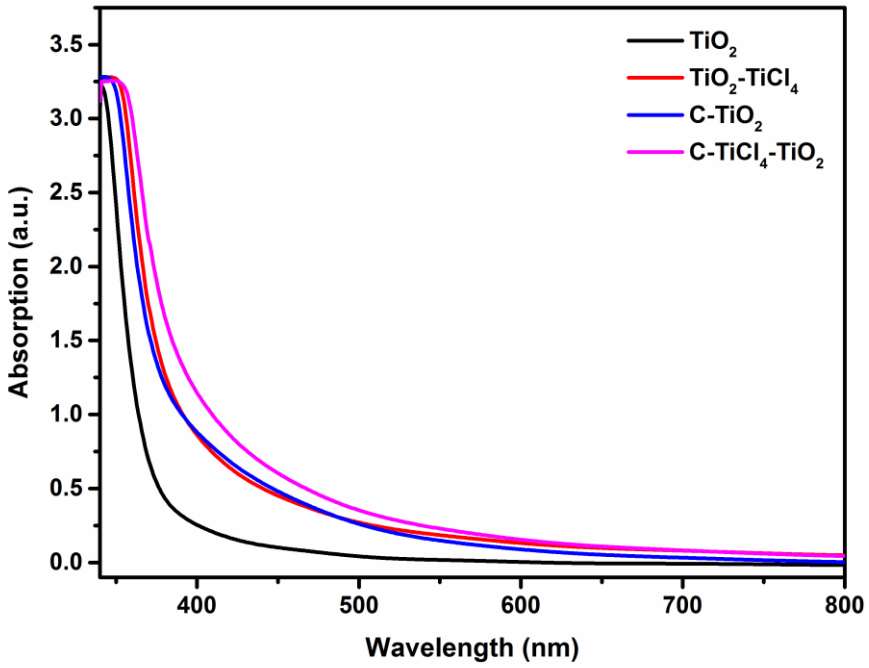

Figure 5.9. UV-visible absorption spectroscopy of the prepared films

It was observed that each of the samples displayed superior visible light absorption when compared with pristine TiO_2. Of note is the absorption characteristics of TiO_2-$TiCl_4$, the visible light absorption of which is in keeping with the presence of Cl-doped TiO_2 being present. As reported by Wang et al[18], the extension of the absorption of TiO_2 into the visible by Cl doping typically leads to a broad absorption up to ~ 700 nm, accounting for the shift in absorption into the visible for TiO_2-$TiCl_4$.

5.2.2.4.2 Mott-Schottky Analysis

The Mott-Schottky plots of the prepared films are given in Figure 5.10.

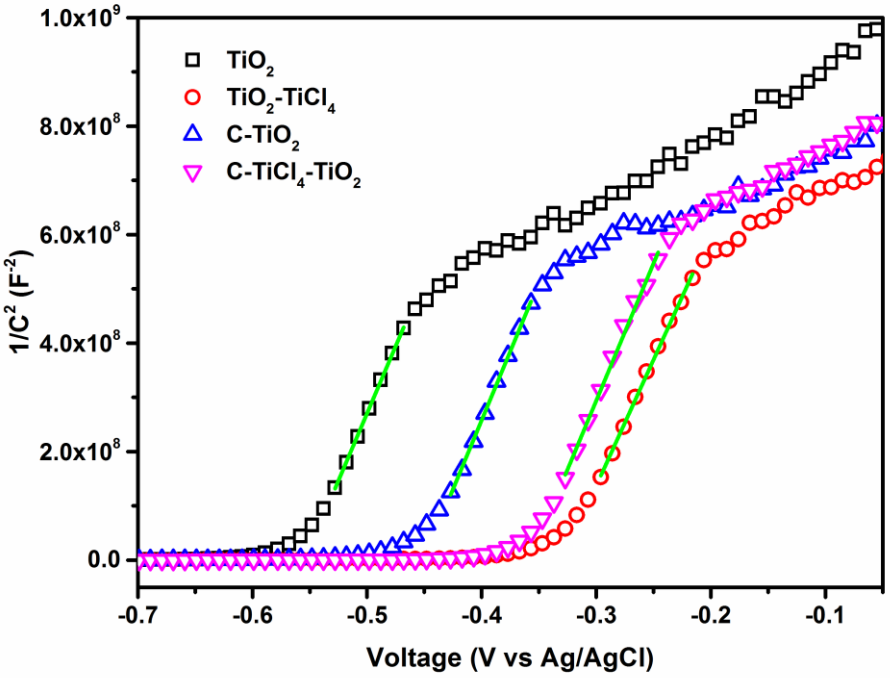

Figure 5.10. Mott-Schottky plots generated from the prepared films. Green lines indicate tangents used to calculate flat band potentials.

All the films exhibit the positive slope associated with n-type materials, meaning that the dominant charge carriers in the films are electrons. Interestingly there appears to be little difference in the slopes of the plots, indicating that the charge carrier density in each film is approximately constant. Flat bands were determined using the fits shown in Figure 10, and are given in Table 5.1.

Table 5.1 – Flat Band Potentials

Sample	Flat Band Potential (V vs Ag/AgCl)
TiO_2	-0.555
TiO_2-$TiCl_4$	-0.330
C-TiO_2	-0.451
C-$TiCl_4$-TiO_2	-0.358

A clear shift is observed in the flat band potential upon going from pristine TiO_2 to C-TiO_2. This is to be expected, as carbon is well known to be a good electron accepting material[14], drawing electrons from electron rich TiO_2 and therefore shifting the flat band to more anodic potentials. The flat band potential of TiO_2-$TiCl_4$ is also found to have shifted anodically. Doping is often found to have pronounced effects upon the flat band of semiconducting materials[25], and a large anodic shift of the flat band is in keeping with dopant states being introduced just above the valence band maximum in a similar fashion to what has been observed in N-doped TiO_2 films[26]. This supports the presence of Cl doped TiO_2 being present upon $TiCl_4$ treatment. It is expected that if some lattice O ions are replaced with less electronegative Cl ions that dopant states would appear above the valence band maximum, and therefore the Fermi level of the semiconductor (and therefore the flat band) would be shifted anodically.

5.2.2.5 Photocatalytic Testing

5.2.2.5.1 Degradation of Organic Pollutants

The films were tested using the same cuvette reactor as described in the experimental section. Methyl orange (MO) was initially chosen as a model pollutant, prior to photocatalytic tests the prepared films were placed in the solution until no change in the absorption was observed (Figure 5.11).

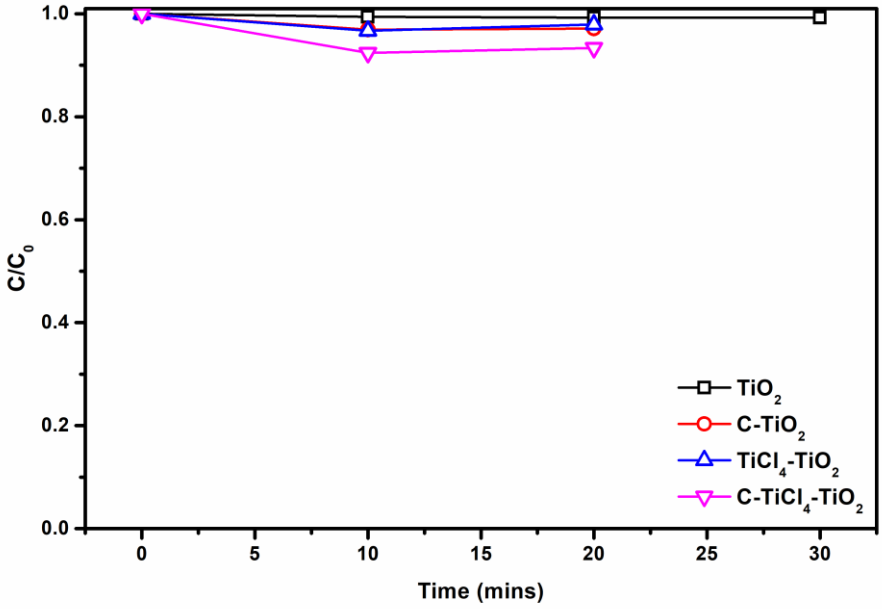

Figure 5.11. Dark adsorption of MO by the doped and carbon coated films

Upon irradiation, the concentration was observed to decrease, and the corresponding rate plots shown in Figure 5.12.

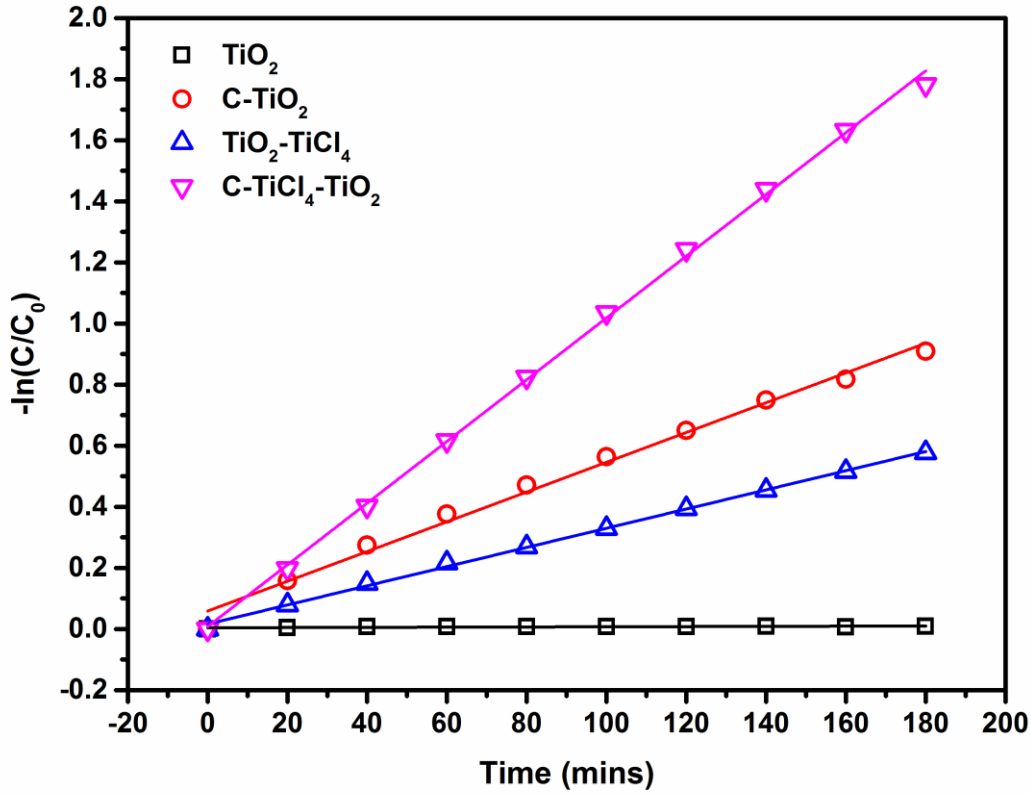

Figure 5.12. Pseudo 1st order rate plot of the degradation of MO by the prepared films

No degradation was observed for plain TiO_2, while TiO_2-$TiCl_4$, C-TiO_2 and C-$TiCl_4$-TiO_2 displayed increasingly rapid decolourisation of MO. As such it can be noted that the introduction of Cl doped TiO_2 improved the photocatalytic rate somewhat, as does the introduction of a carbon layer, while together they produce a highly effective photocatalyst. A summary of the photocatalytic activities of the samples is given in Table 5.2.

Table 5.2 – Photocatalytic Degradation of Methyl Orange

Sample	Pseudo 1st order rate constant ($x10^{-3}$ min^{-1})
TiO_2	0.03
TiO_2-$TiCl_4$	3.14
C-TiO_2	4.87
C-$TiCl_4$-TiO_2	10.11

While an easy way of screening materials, the rates obtained using visible dyes should not be taken as being final. With this thought, further studies upon 4-CP, a colourless, UV absorbing phenolic pollutant, were carried out, beginning with a dark adsorption test (Figure 5.13).

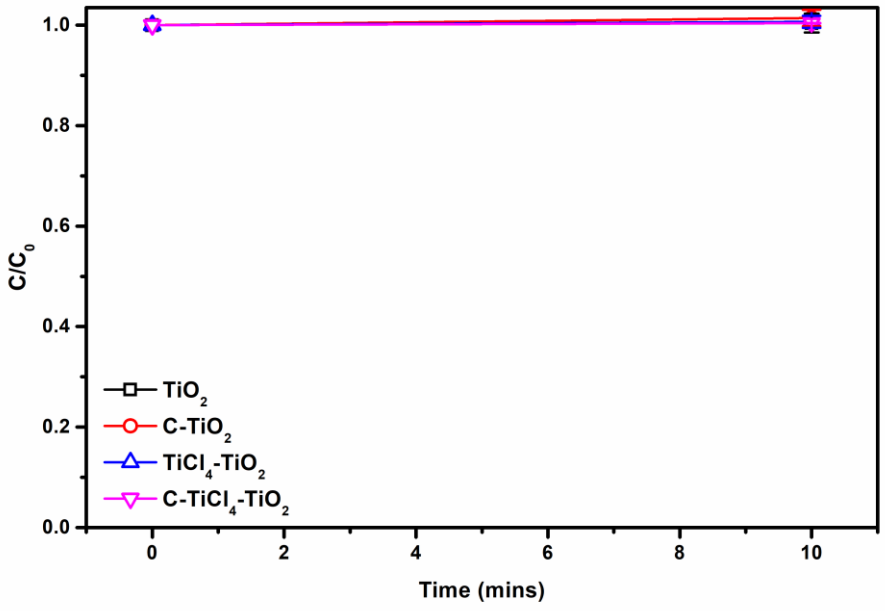

Figure 5.13. Dark adsorption test of 4CP using the prepared films

The set up was then irradiated using a white LED, giving the first order rate plots giving in Figure 5.14.

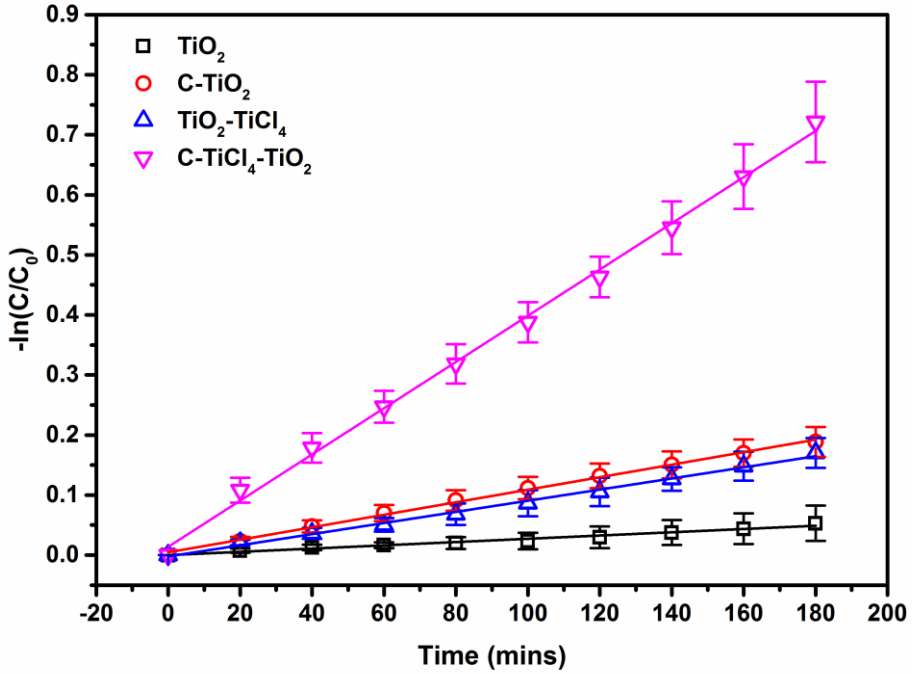

Figure 5.14. Pseudo first order rate plots of the degradation of 4CP by the prepared films

The 1st order rate constants for 4-CP photodegradation are summarized in Table 5.3.

Table 5.3 – Photocatalytic Degradation of 4CP

Sample	Pseudo 1st order rate constant ($x10^{-3}$ min^{-1})
TiO_2	0.27 ± 0.17
TiO_2-$TiCl_4$	0.85 ± 0.13
C-TiO_2	1.00 ± 0.13
C-$TiCl_4$-TiO_2	3.86 ± 0.36

Immediately, a significant loss of activity is noted when comparing the degradation of 4-CP to MO. This can be ascribed to the loss of photosensitization that occurred using the visible dye MO. Otherwise a similar trend was seen in the photocatalytic activities, although the TiO_2-$TiCl_4$ and C-TiO_2 films appeared to be within experimental error of one another, both had superior activity to pristine TiO_2. The C-$TiCl_4$-TiO_2 film produced significantly improved activity over all other samples, confirming that the combination of Cl-doping and a carbon layer is effective as a photocatalytic material.

5.2.2.5.2 Recyclability Test

An advantage of the immobilization of the photocatalytic material as a film is the simplification of re-use. With a view to test this, repeated runs of 3 hours each were carried out upon the photocatalytic degradation of 4-CP (Figure 5.15).

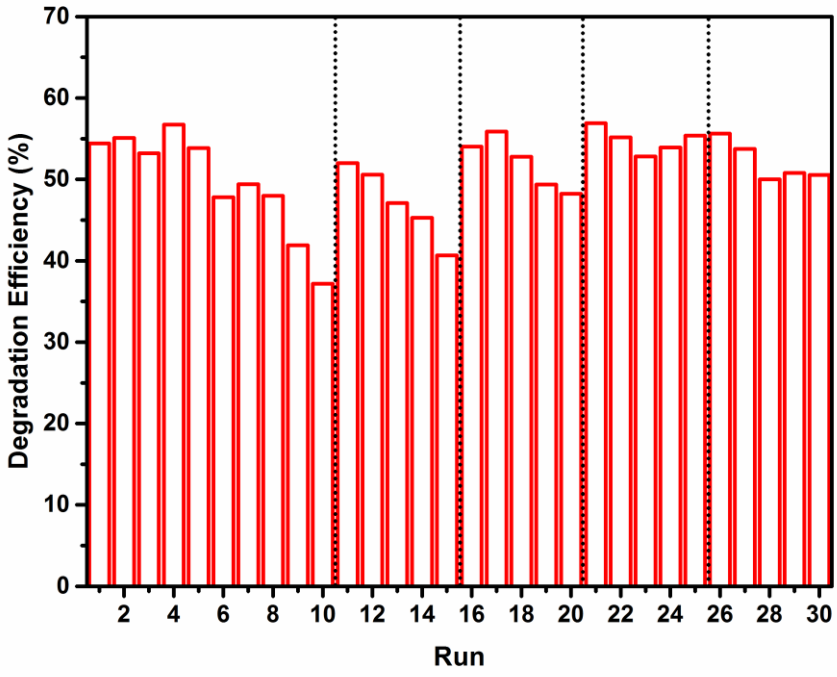

Figure 5.15. Recyclability testing of C-$TiCl_4$-TiO_2 against 4CP, dotted lines indicate regeneration steps

Degradation efficiency is determined as 1-C/C_0, the fractional quantity of 4-CP destroyed in 3 hours. Initially, no losses of activity were noted, however towards 30 hours of irradiation (10 runs) the activity began to decrease. However, it was found that the photocatalyst could be regenerated by simply heating once again under

nitrogen using the same method that was used in the synthesis (dotted lines in Figure 15). Using this method, the photocatalyst could be tested for 90 hours with no losses in activity. After 90 hours of testing, TEM studies revealed that the material in the film appeared to be largely unaffected by the irradiation/regeneration steps that had been applied, with the same ~10 nm particles and carbon layer upon larger ~20 nm particles being observed (Figure 5.16).

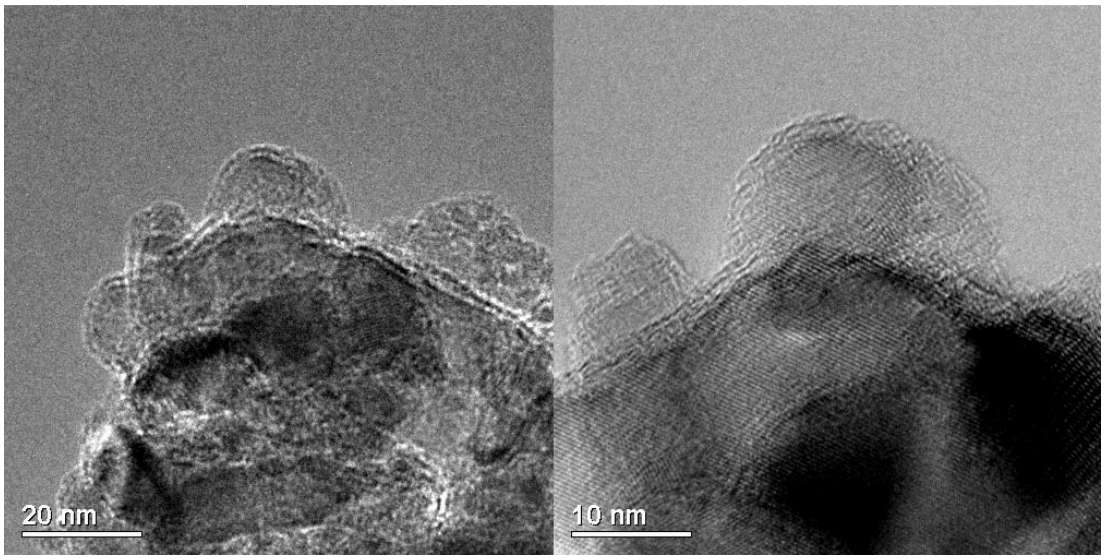

Figure 5.16. TEM images of the C-$TiCl_4$-TiO_2 after 90 hours of use.

Thus, it can be concluded that the C-$TiCl_4$-TiO_2 material retains its structure and activity even after prolonged usage, and that drops in activity are due to surface contamination during the photocatalytic processes rather than any irreversible change in the photocatalyst material.

5.2.2.5.3 Mechanistic Studies

Introduction of a variety of different scavengers in high concentration has been used previously to effectively remove certain key species from the test, and the corresponding change in the degradation efficiency can be used to shed light upon the mechanism. Usually, scavenging experiments are carried out upon dye solutions[27,28]. However, as discussed previously, we believe this to be unreliable, as photosensitization can lead to the production of reactive species which would not occur in the photocatalytic degradation of different analytes, once again making the test an

unreliable method to determine the important reactive species generated. Therefore, scavenging tests upon C-$TiCl_4$-TiO_2 were carried out using the photocatalytic degradation of 4-CP (Figure 5.17).

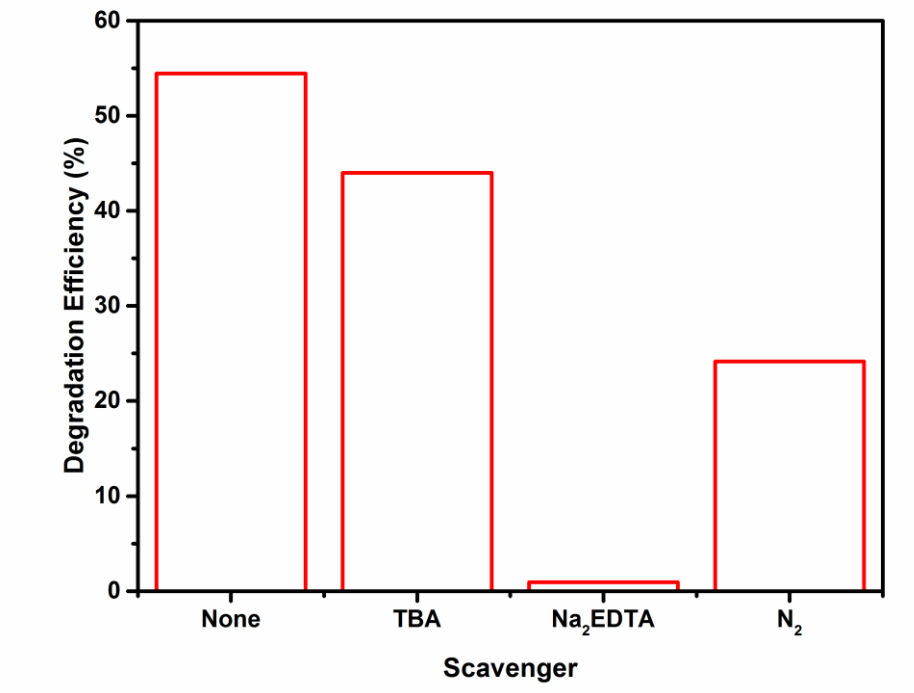

Figure 5.17. Scavenging tests of C-$TiCl_4$-TiO_2 against 4CP

It was found that hydroxyl radicals play a minor role in the degradation of 4-CP, with a small decrease in the degradation caused by addition of TBA. The main oxidizing species however appears to be photogenerated holes, with addition of disodium EDTA causing almost complete loss of activity. The removal of O_2 from the 4-CP solution causes a partial drop in activity, indicating that electron transfer to O_2 to form superoxide is indeed important, which supports the formation of hydroxyl radicals which may be accessed via the superoxide ion[29].

5.2.2.5.4 Photocatalytic Reduction of Cr(VI)

In addition to organic pollution, heavy metal contamination is becoming increasingly common in urban industrialised water sources. Soluble chromium (VI) is a typical toxic metal contaminant resulting from a variety of industrial processes[30], which can be remediated by reduction to less toxic Cr(III). The photocatalytic reduction of Cr(VI)

using C-$TiCl_4$-TiO_2 with phenol as a sacrificial electron donor was chosen as a method by which this may be tested. The dark adsorption of Cr(VI) is shown in Figure 5.18.

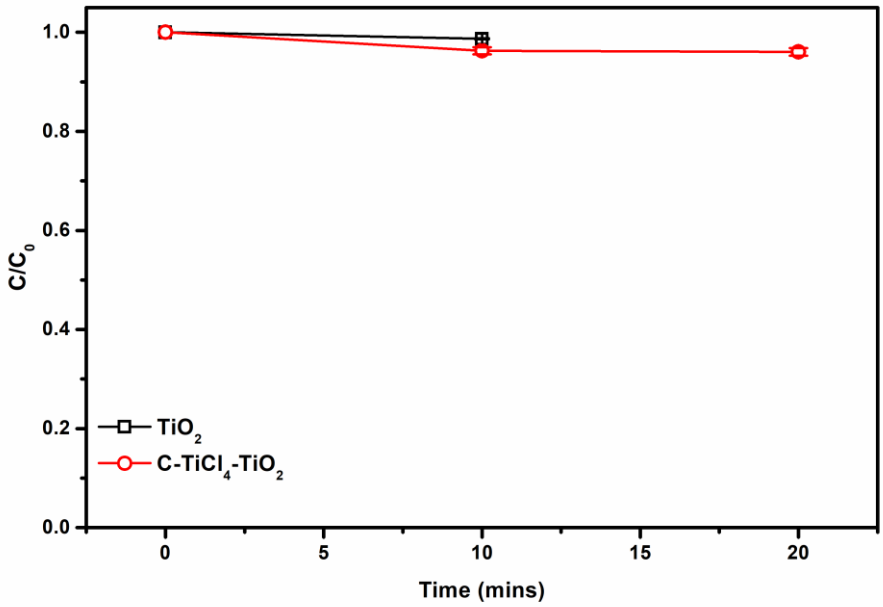

Figure 5.18. Dark adsorption of Cr(VI) by pristine TiO_2 and C-$TiCl_4$-TiO_2

The first order rate plots for degradation under irradiation are given in Figure 5.19.

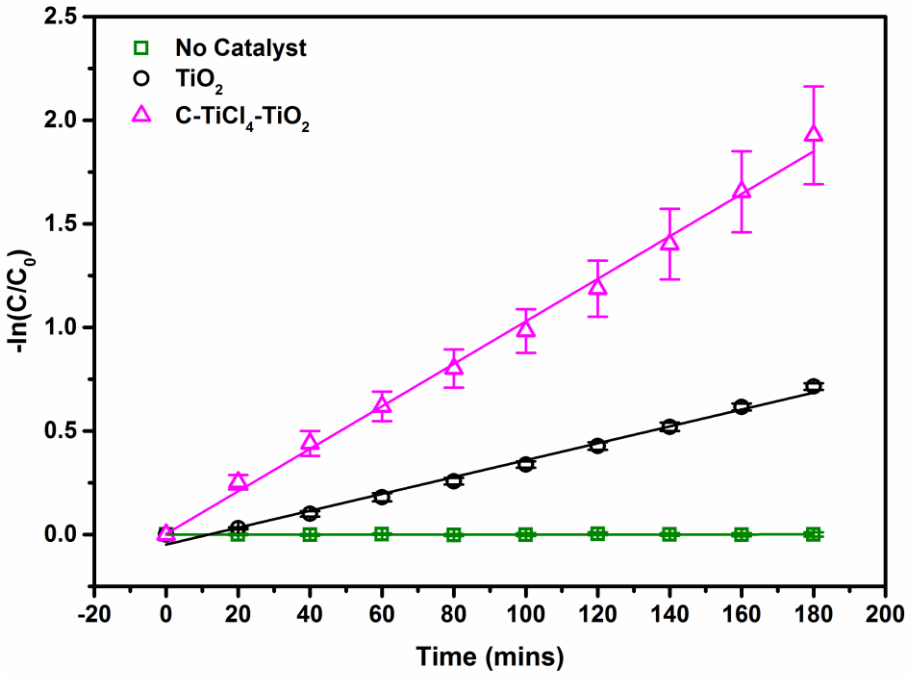

Figure 5.19. Pseudo first order rate plots of the photoreduction of Cr(VI)

Once again C-$TiCl_4$-TiO_2 proved a superior photocatalyst to pristine TiO_2, the rate constants for Cr(VI) reduction are given in Table 5.4.

Table 5.4 – Photoreduction of Cr(VI)

Sample	Pseudo 1st order rate constant ($x10^{-3}$ min^{-1})
No Catalyst	0.00(5) ± 0.06
TiO_2	4.03 ± 0.08
C-$TiCl_4$-TiO_2	10.35 ± 1.15

Interestingly, TiO_2 alone gave some activity, most likely owing to photosensitization of the film by the chromium(VI) source, which has a pale yellow colour in aqueous solution. Solutions used in Cr(VI) photoreduction tests are typically acidified, which

has been suggest to be due to the consumption of H^+ during the reduction[31] as shown in the experimental section of this thesis. The low pHs used in this type of test are often too low to be used with many visible light active semiconductors such as sulfides, which are unstable in highly acidic solutions. Here, the highly stable carbonaceous material allows use of low pH and visible light irradiation, proving the applicability of this type of system for Cr(VI) photoreduction.

On this basis of the photocatalytic action for Cr(VI) and the scavenger tests described previously, the mechanism of action can be determined, and is represented in Figure 5.20.

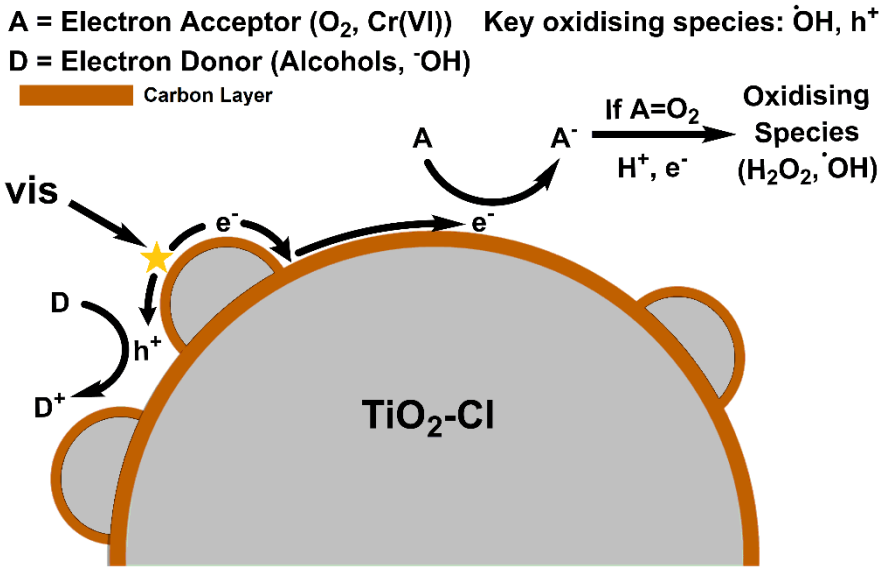

Figure 5.20. Mechanism of action of the carbon coated Cl-doped TiO_2 material against the various pollutants tested

5.2.2.5.5 Bactericidal Activity

Escherichia coli (E. coli) are commonly used as a marker for bacterial content in contaminated of water[32]. Of the UV radiation reaching the earth surface, more than 95 % consists of longer wavelength UV-A component. Thus, in the present study the bactericidal activity of the TiO_2 and C-$TiCl_4$-TiO_2 samples were studied using the standard *E. coli* strain under UV-A exposure. To determine the relationship between UV-A light intensity and efficiency of photocatalytic inactivation, the disinfection kinetic constants were calculated using the classic disinfection model of Chick-Watson

equation[33]. Figure 5.21 shows the linear fitted plots of the photocatalytic disinfection kinetics as per Chick-Watson model.

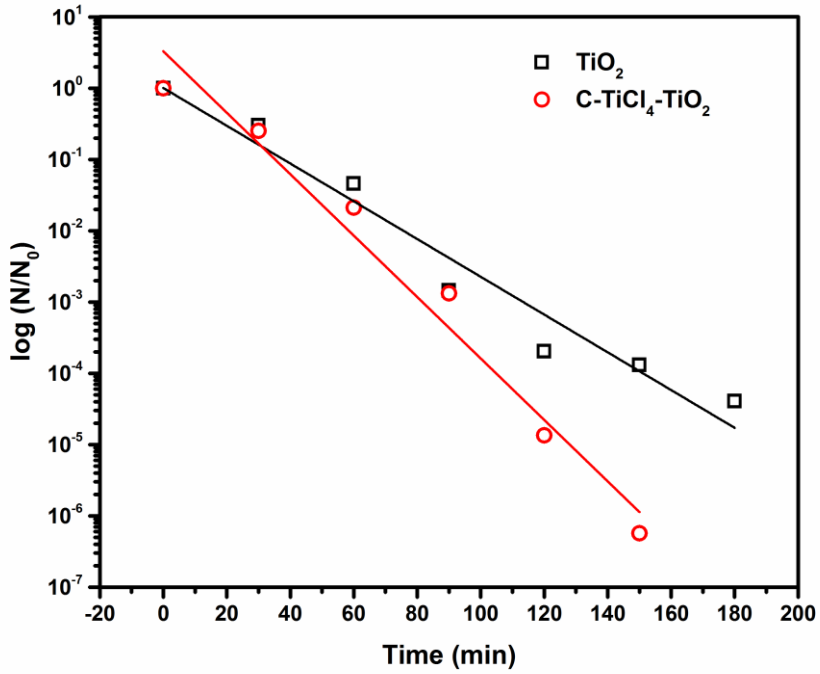

Figure 5.21. Bactericidal efficiency of C-$TiCl_4$-TiO_2 and TiO_2 agains E.coli

The *E. coli* disinfection rate constant for C-$TiCl_4$-TiO_2 sample (k = $4.31\times10^2 \pm 0.36\times10^2$ min^{-1}) was observed to be nearly twice that of the pristine TiO_2 (k' = $2.65\times10^2 \pm 0.24\times10^2$ min^{-1}). Figure 5.22 shows the digital photographs of the Agar plates cultured with water samples spiked with *E coli* with the photcatalyst (TiO_2 and C-$TiCl_4$-TiO_2 samples) after 120 minutes, 150 minutes and 180 minutes of UV exposure.

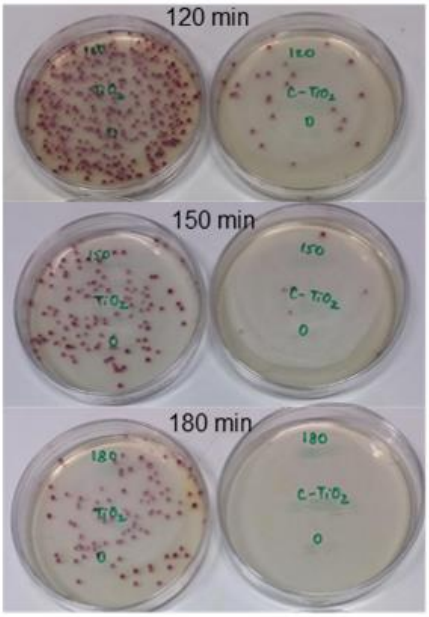

Figure 5.22. Viable colony formation of E.coli after various treatment times with C-$TiCl_4$-TiO_2

Clearly, the C-$TiCl_4$-TiO_2 samples show an enhanced bactericidal activity with total inactivation of *E. coli* observed after 3 hours of UV-A illumination as compared to the pristine TiO_2 sample. TiO_2 and carbon modified TiO_2 including nanocarbon/TiO_2 composite, multi-walled carbon nanotubes coated by TiO_2, TiO_2/carbon nanotubes composites etc have been widely tested for photocatalytic bactericidal activity[34–37]. The prevalent mechanism for the photocatalytic bactericidal activity of *E. coli* consists of oxidative damage of the cell wall and cell membrane and alterations of the internal DNA molecules.

5.3 Chapter 5 Conclusion

C-$TiCl_4$-TiO_2 has been demonstrated as a versatile photocatalyst for environmental water remediation. It has been shown that using simple processing techniques both chlorine doping, and thin carbonaceous layers may be deposited upon TiO_2 films. Together these two modifications are found to produce a very effective photocatalyst for the degradation of dyes, colourless pollutants, the photoreduction of chromium(VI) and the killing of bacteria. Such a comprehensive study of a single material against all of these pollutant types is rarely found in the literature but is important if photocatalytic materials are to be applied beyond the laboratory. The films also display good re-

useability, being able to be regenerated and continually used for 90 hours without significant losses of activity. We believe that this combination of high activity, good re-useability and versatility of activity towards an example of each type of pollutant present in water sources demonstrates that this material is a prominent candidate for real world water purification.

5.4 Chapter 5 Specific Experimental

5.4.1 Photocatalyst Preparation

5.4.1.1 TiO_2 Film Preparation

FTO glass substrates were cut into 2cm x 2cm squares before being ultrasonically cleaned in a solution of detergent (Decon 90, ~5% in tap water) for 15 minutes. The substrates were then rinsed with tap water, deionised water and finally ethanol. Titania paste (Dyesol 18-NRT) was then doctor bladed in 1 cm x 2 cm strips onto the surface of the FTO using scotch tape (3M) as a spacer before heating to 510 ^{o}C in stages on a controlled hotplate to remove the organic templates, leaving a highly porous TiO_2 film. The temperature profile of the heating regime was as follows: 325 ^{o}C for 5 minutes, 375 ^{o}C for 5 minutes, 425 ^{o}C for 5 minutes, 475 ^{o}C for 10 minutes, 510 ^{o}C for 10 minutes. The heating ramp rate between each stage was 10 ^{o}C min^{-1} apart from the final stage where it slowed to 5 ^{o}C min^{-1}. The sintered TiO_2 films were then allowed to cool gradually on the hotplate to room temperature. Narrower (0.9 cm x 2 cm) films were also fabricated in the same way for photocatalytic degradation of methyl orange, 4-chlorophenol and Cr(VI) reduction. Wider films (3.5 cm x 3.5 cm) were also fabricated for the bactericidal testing studies.

5.4.1.2 Modification Procedure

Films were dipped into catechol (5 mg/ml) for 30 minutes during which time the films became yellow in colour. The films were then rinsed thoroughly with de-ionised water before submerging in a solution of titanium tetrachloride (40 mM) and heating at 65 ^{o}C for 30 minutes. Films were washed thoroughly once again with deionised water and allowed to air dry before heating under N_2 (10 minutes at 200 ^{o}C, 30 minutes at 300 ^{o}C), during which time the films turned from yellow to brown, indicating the thermal decomposition of the catechol-TiO_2 surface complex.

5.4.2 Photocatalytic Testing

Narrow films (0.9 cm x 2 cm) were submerged into a solution of methyl orange (2 ml, $4.6x10^{-5}$ molar) in a quartz cuvette. The films were stirred in the dark for up to 30 minutes to establish an adsorption equilibrium, determined as the point at which no further change to the absorbance of the solution occurred, and then irradiated with a white LED (30 W applied power) fitted with a UV filter (>400 nm, Thorlabs). The decolourisation of methyl orange was followed by measuring the absorption at 463 nm at regular time intervals using a JASCO V-670 spectrophotometer. The degradation of 4-chlorophenol was measured in the same way, using 4-chlorophenol of 156 μmolar concentration followed using the peak at 280 nm. In the assessment of the recyclability of the films, a single measurement after 3 hours irradiation was taken to calculate the degradation efficiency, between runs the film was washed with deionised water overnight and dried under a stream of N_2. Where severe losses in activity were observed, the films were regenerated by heating under N_2 (10 minutes at 200 ^oC, 30 minutes at 300 ^oC). Scavenging experiments were carried out on the same 4-chlorophenol solution used in the regular studies, but with the addition of the molecular scavengers (50 mM) tert-butyl alcohol, disodium EDTA, or with constant bubbling of N_2 gas during irradiation. Note: due to interferences between disodium EDTA and 4-chlorophenol in the UV-vis trace, the 4-chlorophenol peak at 280 nm was used to determine the degradation efficiency. Chromium(VI) reduction was carried out in a similar fashion to the degradation of organic pollutants. 2ml of a solution containing Potassium dichromate ($4x10^{-4}$ M) and phenol ($6x10^{-6}$ M) adjusted to pH 1 using H_2SO_4 (4M) was added to a quartz cuvette. A film was then added to the solution and irradiated using the same white LED and filter as was used in the organic photodegradation tests.

5.4.2.1 Bactericidal Testing

The standard *E. coli* ATCC 23716 (American Type Culture Collection, Rockville, MD, USA) were used in this study. The freeze-dried cultures were rehydrated and reactivated according to the manufacturer's instructions. The reactivated *E. coli* were cultured on petri dishes with *Brilliance E. coli/coliform Agar* (Oxoid) selective media using the 'spread plate' technique. The *E. coli* colonies with purple colour appeared

on the petri dishes after incubation at 37 °C for 20-24 h. The freshly cultured *E. coli* colonies were used to spike the deionised water (DI) which was sterilised at 121 °C for 15 mints prior to use.

Substrates coated with TiO_2 and C-$TiCl_4$-TiO_2 layers (3.5 × 3.5 cm^2) were each immersed in 50 ml of sterilised DI water spiked with *E.coli* (with initial concentration of 1.2×10^7 CFU/ml, where CFU is colonies forming unit) and illuminated with UV-A lamp. The lamp was placed on top of the water sample at about 8 cm from its surface. An 11W low-pressure blacklight fluorescent lamp (PLS G23, Casell Lighting) emitting predominantly at 365 nm provided UV irradiation. The photon flux emission of the lamp was determined by potassium ferrioxalate actinometer, as described by Murov et al.[38], and found to be 4.98×10^{-6} Einstein/s. At specific time intervals, 2 ml of the water sample were pipetted out and immediately analysed with respect to viable *E. Coli* cells by the serial dilution culture method. For each dilution, 200 µl of the sample were spread on petri dishes with *Brilliance E. coli*/*coliform Agar* (Oxoid) selective media. The petri dishes were incubated at 37 °C for 20-24 h before viable counts were determined.

5.5 Chapter 5 References

1 M. Pelaez, P. Falaras, V. Likodimos, A. G. Kontos, A. A. de la Cruz, K. O'shea and D. D. Dionysiou, *Appl. Catal. B Environ.*, 2010, **99**, 378–387.

2 H. Zeng, J. Xie, H. Xie, B. Su, M. Wang, H. Ping, W. Wang, H. Wang and Z. Fu, *J. Mater. Chem. A*, 2015, **3**, 19588–19596.

3 J. Reszczyńska, T. Grzyb, J. W. Sobczak, W. Lisowski, M. Gazda, B. Ohtani and A. Zaleska, *Appl. Catal. B Environ.*, 2015, **163**, 40–49.

4 H. Li, L. Zhou, L. Wang, Y. Liu, J. Lei and J. Zhang, *Phys. Chem. Chem. Phys.*, 2015, **17**, 17406–17412.

5 Y. Yang, Y. Li, J. Wang, Y. Zhang, D. He, J. Wu and H. Dai, *RSC Adv.*, 2015, **5**, 50833–50842.

6 Y. Zhang, J. Lu, M. R. Hoffmann, Q. Wang, Y. Cong, Q. Wang and H. Jin, *RSC Adv.*, 2015, **5**, 48983–48991.

7 L. U. Jefferson, A. D. Netchaev, J. a. Jefcoat, A. D. Windham, F. M. McFarland, S. Guo, R. K. Buchanan and J. P. Buchanan, *ACS Appl. Mater. Interfaces*, 2015, **7**, 12639–12648.

8 H. Liang and X. Li, *Appl. Catal. B Environ.*, 2009, **86**, 8–17.

9 N. M. Dimitrijevic, S. Tepavcevic, Y. Liu, T. Rajh, S. C. Silver and D. M. Tiede, *J. Phys. Chem. C*, 2013, **117**, 15540–15544.

10 Y. Huang, Y. Liang, Y. Rao, D. Zhu, J. Cao, Z. Shen, W. Ho and S. C. Lee, *Environ. Sci. Technol.*, 2017, acs.est.6b04460.

11 Y. K. Kim, E. B. Kang, S. H. Kim, S. M. Sharker, B. Y. Kong, I. In, K. Lee and S. Y. Park, *ACS Appl. Mater. Interfaces*, 2016, **8**, 29827–29834.

12 L.-W. Zhang, H.-B. Fu and Y.-F. Zhu, *Adv. Funct. Mater.*, 2008, **18**, 2180–2189.

13 L. Yu, G. Li, X. Zhang, X. Ba, G. Shi, Y. Li, P. K. Wong, J. C. Yu and Y. Yu, *ACS Catal.*,

2016, **6**, 6444–6454.
14 P. D. Tran, S. K. Batabyal, S. S. Pramana, J. Barber, L. H. Wong and S. C. J. Loo, *Nanoscale*, 2012, **4**, 3875.
15 C. Creutz and M. H. Chou, *Inorg. Chem.*, 2008, **47**, 3509–3514.
16 D. Finkelstein-Shapiro, S. K. Davidowski, P. B. Lee, C. Guo, G. P. Holland, T. Rajh, K. A. Gray, J. L. Yarger and M. Calatayud, *J. Phys. Chem. C*, 2016, **120**, 23625–23630.
17 B. C. O'Regan, J. R. Durrant, P. M. Sommeling and N. J. Bakker, *J. Phys. Chem. C*, 2007, **111**, 14001–14010.
18 X. K. Wang, C. Wang, W. Q. Jiang, W. L. Guo and J. G. Wang, *Chem. Eng. J.*, 2012, **189**–**190**, 288–294.
19 H. Xu and L. Zhang, *J. Phys. Chem. C*, 2010, **114**, 11534–11541.
20 H. Luo, T. Takata, Y. Lee, J. Zhao, K. Domen and Y. Yan, *Chem. Mater.*, 2004, **16**, 846–849.
21 W. Zhou, F. Sun, K. Pan, G. Tian, B. Jiang, Z. Ren, C. Tian and H. Fu, *Adv. Funct. Mater.*, 2011, **21**, 1922–1930.
22 Z. Zhu, Y. Xu, B. Qi, G. Zeng, P. Wu, G. Liu, W. Wang, F. Cui and Y. Sun, *Environ. Sci. Nano*, 2017, **4**, 302–306.
23 H. Estrade-Szwarckopf, *Carbon N. Y.*, 2004, **42**, 1713–1721.
24 R. Asahi, T. Morikawa, H. Irie and T. Ohwaki, *Chem. Rev.*, 2014, **114**, 9824–9852.
25 W. Q. Fang, X. L. Wang, H. Zhang, Y. Jia, Z. Huo, Z. Li, H. Zhao, H. G. Yang and X. Yao, *J. Mater. Chem. A*, 2014, **2**, 3513.
26 L. Samiolo, M. Valigi, D. Gazzoli and R. Amadelli, *Electrochim. Acta*, 2010, **55**, 7788–7795.
27 W. Shan, Y. Hu, Z. Bai, M. Zheng and C. Wei, *Appl. Catal. B Environ.*, 2016, **188**, 1–12.
28 L. Chen, M. Chen, D. Jiang and J. Xie, *J. Mol. Catal. A Chem.*, 2016, **425**, 174–182.
29 H. Park, Y. Park, W. Kim and W. Choi, *J. Photochem. Photobiol. C Photochem. Rev.*, 2013, **15**, 1–20.
30 World Health Organisation, *Guidelines for Drinking-Water Quality - Second Edition - Volume 2 - Health Criteria and Other Supporting Information - Addendum*, 1998.
31 L. Fenghui, Y. Jie, T. Guangyuan, Q. Ling, X. Jiacheng, L. Yongdi, L. Wang, L. Juying and J. Zhang, *Appl. Catal. B Environ.*, 2017, **201**, 1–11.
32 O. CARP, *Prog. Solid State Chem.*, 2004, **32**, 33–177.
33 J. Marugán, R. van Grieken, C. Sordo and C. Cruz, *Appl. Catal. B Environ.*, 2008, **82**, 27–36.
34 M. Janus, A. Markowska-Szczupak, E. Kusiak-Nejman and A. W. Morawski, *Environ. Prot. Eng.*, 2012, **38**, 89–97.
35 W. C. Oh, A. R. Jung and W. B. Ko, *Mater. Sci. Eng. C*, 2009, **29**, 1338–1347.
36 O. Akhavan, M. Abdolahad, Y. Abdi and S. Mohajerzadeh, *Carbon N. Y.*, 2009, **47**, 3280–3287.
37 O. Akhavan, R. Azimirad, S. Safa and M. M. Larijani, *J. Mater. Chem.*, 2010, **20**, 7386–7392.
38 S. L. Murov, I. Carmichael and G. L. Hug, *Handbook of Photochemistry, second edition*, 1993.

Thesis Conclusions & Outlook

Water contamination is, and continues to be, a significant problem is much of the modern world, with current water treatment options generally lacking in their ability to provide clean drinking water to much of the global population. Be it in lightly polluted water in developed nations, or relatively highly contaminated wells in remote rural communities, removal of organic and bacteriological contaminants pose problems which vary greatly across the planet. In the drive to bring clean drinking water to a growing population, new technologies must be developed and implemented with a view to their implementation is the near future.

The field of semiconductor photocatalysis is often touted as a key player in the future of water purification, yet complexities exist in bringing it to bear on such a diverse problem. Work in the field of photocatalytic water purification, to date, is by and large ill-suited to operation outside of carefully selected laboratory conditions, which does not facilitate application in a broader context. However, a great number of studies have been carried out to investigate the underlying principles, and materials development and testing under these artificial conditions. Therefore, there remains still a void in the established work to be filled where new materials, fabrication methods and testing conditions are developed with a view to the applicability of the system in mind, and thereby move away from the laboratory.

The work contained within this thesis demonstrates several such materials, photocatalytic systems and testing regimes which have been carried out with the aim of bringing the laboratory and true application in close alignment. Beginning with the favoured material of TiO_2, immobilisation has been investigated as an avenue by which the ease of introduction and operation of a photocatalytic system can be improved. New post-immobilisation modification methods to produce a variety of materials have been investigated, with methods that lend themselves to use in any immobilised system being developed. While attempts have been made to dramatically increase the response of TiO_2 to visible light with these modifications, more promising appears to be the use of relatively wide band gap semiconductors, focusing on overcoming charge recombination with only modest visible light sensitisation where

possible. Throughout the course of this work, more thorough and robust testing methods than those typical of the field have been developed and put into practice. Reliance on artificial dye-based testing has been avoided, and broader model pollutant scopes have been investigated with a view to proving a general baseline of activity against molecules, bacteria and inorganics with some significance in contaminated water sources.

Thus, where does this work leave the field of photocatalytic water purification? It is intended that to some extent the gap between laboratory and real-world application has been lessened by the work contained within this thesis. However, looking ahead further work must be undertaken to encourage the end of poor testing regimes common in the literature, and to promote a shift towards consideration of the applicability of a photocatalyst system to be of the same importance as photocatalytic degradation rate. It is hoped that through the contributions made during this PhD that these factors become a reality somewhat sooner.

With this in mind, efforts have been made towards the end of this work to establish field testing in collaboration with two institutions in India, IIT Kharagpur and ATREE Bangalore. This work is still in early organisation stage, and as such no results have been produced for discussion in this thesis. However, it is intended that these ongoing tests establish the efficacy of the materials detailed within under realistic conditions, to be investigated for the removal of organic and bacterial content from real contaminated water under Indian solar irradiation. Through the work of future students this collaboration will be maintained, and as such it is aimed that the viability of small scale, point-of-use photocatalytic water treatment can begin to be investigated. With a view to making the work contained within this thesis a reality, it is suggested to improve the comparability of the testing methods, and thereby allow better comparability between materials and reactor systems. Development of actinometric methods are currently underway within the Robertson group, which aims to allow improved assessment of material activity and establishment of more standard testing regimes. Going forward to field testing such information is key to ensure that the system and material combination is of the highest efficiency.

It is aimed that the work following that which is contained within this thesis will continue to bring the field of photocatalytic water purification ever closer to workable solutions. Through improved collaboration with end users, improved standardisation of test conditions, reactor designs and development of materials, the gap between laboratory and the real world will be bridged.

Published Work

What follows are the publications prepared in the course of this work, including submitted drafts. The papers are included in chronological order.

Why is Anatase a Better Photocatalyst than Rutile? The Importance of Free Hydroxyl Radicals

G. Odling and N. Robertson, *ChemSusChem*, 2015, **8**, 1838-1840

DOI: 10.1002/cssc.201500298

$BiVO_4$-TiO_2 Composite Photocatalysts for Dye Degradation Formed Using the SILAR Method

G. Odling and N. Robertson, *ChemPhysChem*, 2016, **17**, 2872 – 2880

DOI: 10.1002/cphc.201600443

SILAR BiOI-Sensitized TiO_2 Films for Visible-Light Photocatalytic Degradation of Rhodamine B and 4-Chlorophenol

G. Odling and N. Robertson, *ChemPhysChem*, 2017, **18**, 728 – 735

DOI: 10.1002/cphc.201601417

Improving Carbon-Coated TiO_2 Films with a $TiCl_4$ Treatment for Photocatalytic Water Purification

G. Odling, A. Ivaturi, E. Chatzisymeon and N. Robertson, *ChemCatChem*, 2018, **10**, 234 –243

DOI: 10.1002/cctc.201700867

Sequential ionic layer adsorption and reaction (SILAR) deposition of $Bi_4Ti_3O_{12}$ on TiO_2: an enhanced and stable photocatalytic system for water purification

Immobilised Semiconductors for Photocatalytic Water Purification

G. Odling, E. Chatzisymeon and N. Robertson, *Catal. Sci. Technol.*, 2018, **8**, 829-839

DOI: 10.1039/C7CY02549A

Bismuth titanate modified and immobilized TiO_2 photocatalysts for water purification: broad pollutant scope, ease of re-use and mechanistic studies

G. Odling, Z. Y. Pong, G. Gilfillan, C. R. Pulham and N. Robertson, *Environ. Sci.: Water Res. Technol.*, 2018, Advance Article

DOI: 10.1039/c8ew00568k

Sequential Ionic Layer Adsorption Reaction Formation of $LaVO_4$-TiO_2 Nanocomposites for Photocatalytic Water Purification

G. Odling, R. Bhosale, S. Ogale and N. Robertson, *submitted*

Bridging the Gap Between Laboratory and Application in Photocatalytic Water Purification

G. Odling and N. Robertson, *submitted*

Naturally derived carbon for water purification in rural India

G. Odling, E. Chatzisymeon, P. Karve, S. Ogale, A. Ivaturi, and Neil Robertson, *submitted*
